

REPORT DOCUMENTATION PAGE

19951012 093

1a. REPORT SECURITY CLASSIFICATION Unclassified		1b. RESTRICTIVE MARKINGS None	
2a. SECURITY CLASSIFICATION AUTHORITY DTIC SELECTED		3. DISTRIBUTION / AVAILABILITY OF REPORT Approved for Public Release Distribution Unlimited	
2b. DECLASSIFICATION / DOWNGRADING SCHEDULE OCT 1 6 1995			
4. PERFORMING ORGANIZATION REPORT NUMBER(S) 042-003256500		5. MONITORING ORGANIZATION REPORT NUMBER(S)	
6a. NAME OF PERFORMING ORGANIZATION Drexel University Department of Materials Engin.	6b. OFFICE SYMBOL (If applicable) ----	7a. NAME OF MONITORING ORGANIZATION ONR Representative	
6c. ADDRESS (City, State, and ZIP Code) Drexel University Department of Materials Engineering		7b. ADDRESS (City, State, and ZIP Code) OSU Research Foundation 1960 Kenny Road Columbus, OH 43210	
8a. NAME OF FUNDING / SPONSORING ORGANIZATION Office of Naval Research	8b. OFFICE SYMBOL (If applicable)	9. PROCUREMENT INSTRUMENT IDENTIFICATION NUMBER N00014-91-J4060	
8c. ADDRESS (City, State, and ZIP Code) Materials Division, Code 1131N 800 North Quincy Street Arlington, VA 2217-5000		10. SOURCE OF FUNDING NUMBERS	
		PROGRAM ELEMENT NO.	PROJECT NO.
		TASK NO.	WORK UNIT ACCESSION NO.
11. TITLE (Include Security Classification) In-Situ Metal Matrix Composites - Synthesis and Property Enhancement			
12. PERSONAL AUTHOR(S) Michael J. Koczak and Victoriya Shtessel			
13a. TYPE OF REPORT Final	13b. TIME COVERED FROM 4/1/91 TO 12/30/94	14. DATE OF REPORT (Year, Month, Day) 9/30/95	15. PAGE COUNT 170
16. SUPPLEMENTARY NOTATION			
17. COSATI CODES		18. SUBJECT TERMS (Continue on reverse if necessary and identify by block number)	
FIELD	GROUP	SUB-GROUP	
		In-Situ, Composite Materials, Metal and Ceramic Matrix Composites	
19. ABSTRACT (Continue on reverse if necessary and identify by block number) Metal matrix composites (MMC's) have emerged as a chief class of materials for advanced aerospace, automotive, electronic, thermal management and wear applications. These materials provide superior specific strength and stiffness as compared to the conventional monolithic materials. Traditionally, the development of MMC's has been spurred by aerospace and the defense industry. With the changing political and economic conditions, however, it has become more important for the MMC's to find cost effective industrial applications, e.g. automotive, electronic packaging, and wear resistance applications. This will be facilitated by liquid phase processing of particulate MMC's in larger quantities and in a near net shape form. In addition, the processing should be amenable to tailor the composites to specific structures, e.g., gradient structures and/or reinforcements at the surfaces for better mechanical performance and wear resistance. The final report deals with a combined experimental and modeling program involving reactive processing of metal matrix composites. Initially, it provides for an overview of liquid-gas, liquid-liquid and liquid-solid reactions. The program of study is detailed in the subsequent sections to include: in-situ processing of aluminum matrix composites with carbide and nitride reinforcements; in-situ processing of aluminum matrix composites with mixed carbide and boride reinforcements; modeling of the reactive gas injection process with analytic solutions for carbide reinforcement formation and a process envelope formulation; in-situ processing of nickel matrix composites with carbide via reactive gas infiltration and self propagating synthesis approaches.			
20. DISTRIBUTION / AVAILABILITY OF ABSTRACT <input checked="" type="checkbox"/> UNCLASSIFIED/UNLIMITED <input type="checkbox"/> SAME AS RPT. <input type="checkbox"/> DTIC USERS		21. ABSTRACT SECURITY CLASSIFICATION Unclassified	
22a. NAME OF RESPONSIBLE INDIVIDUAL Dr. Steve Fishman		22b. TELEPHONE (Include Area Code) 703 696 4401	22c. OFFICE SYMBOL

## Table of Contents

<b>Abstract .....</b>	<b>1</b>
 <b>CHAPTER I.</b>	
<b>INTRODUCTION .....</b>	<b>2</b>
A. REVIEW OF THE <i>IN-SITU</i> PROCESSING TECHNIQUES FOR COMPOSITE MATERIAL .....	2
A.1. Liquid-Gas Reactions .....	2
A.1.1. Reactive Gas Injection (RGI) .....	2
A.1.2. Gas-eutectic Reactions .....	4
A.2. Liquid-Liquid Reactions .....	5
A.2.1. Mixalloy .....	5
A.2.2. Osprey™ Spray Deposition .....	5
A.3. Liquid Solid .....	5
A.3.1. SHS-XD™ .....	5
A.3.2. Reactive Infiltration .....	7
B. OUTLINE OF PROGRAM .....	8
B.1. Description of the Scientific Research Goals .....	8
B.2. Significant Results .....	8
B.2.1. Reactive Gas Injection Processing of MMCs .....	9
B.2.1.1 RGI processing of TiC/Al .....	9
B.2.1.2 RGI processing of AlN/Al .....	9
B.2.1.3 RGI processing of TiC/Ni .....	10
B.2.2. SHS Processing of MMCs .....	10
B.2.2.1 SHS processing of (TiC+TiB <sub>2</sub> )/Al .....	10
B.2.2.2 SHS processing of TiB <sub>2</sub> /NiAl and TiC/FeAl .....	11
B.2.3. RGI Process for TiC/Al .....	11
 <b>CHAPTER II</b>	
<b><i>IN-SITU</i> PROCESSING OF ALUMINUM MATRIX COMPOSITES .....</b>	<b>16</b>
A. IN-SITU PROCESSING OF TiC/Al/ COMPOSITES VIA REACTIVE GAS INJECTION. ..	18
A.1. Processing Background .....	18
A.2. Thermodynamic Analysis .....	19
A.3 Experimental Procedure, Results and Discussion .....	19
A.3.1. Methane Decomposition Study .....	20
A.3.1.1 Experimental Procedure and Results .....	20
A.3.1.2 Discussion .....	20
A.3.2 Determination of the Processing Envelope via RGI .....	21
A.3.2.1. Experimental Procedure .....	21
A.3.2.2 Results .....	22
A.3.2.3 Discussion .....	23
A.3.3 Mechanism Study .....	26
A.3.3.1 Experimental procedure .....	26
A.3.3.2 Results .....	26
A.3.3.3 Discussion .....	27
A.3.4 Kinetics of Conversion Study .....	29
A.3.4.1. Experimental procedure .....	29
A.3.4.2. Results .....	29
A.3.5 Feasibility Study of Silicon Carbide Formation via RGI ..	30
A.4. Summary .....	30

B. IN-SITU PROCESSING OF AlN/Al COMPOSITES VIA REACTIVE GAS INJECTION....	37
B.1. Processing Background .....	37
B.2. Thermodynamic Analysis.....	38
B.2.1. Direct Nitridation .....	38
B.2.2. Indirect Nitridation .....	39
B.3. Experimental Procedure and Results .....	39
B.3.1.1 Experimental Procedure .....	39
B.3.1.2. Experimental Results and Discussion .....	40
B.3.2. Indirect Nitridation of Al.....	43
B.3.2.1. Gas-liquid Displacement Reaction.....	43
B.3.2.3 Solid-liquid Displacement Reaction.....	44
B.4 Summary .....	46
C. <i>IN SITU</i> PROCESSING OF TiC/Al, TiB <sub>2</sub> /Al AND (TiC+TiB <sub>2</sub> )/Al COMPOSITES VIA SELF-PROPAGATING SYNTHESIS .....	48
C.1. Processing Background .....	48
C.2. Experimental Procedure .....	49
C.2.1. Self-propagating synthesis .....	49
C.3. Results and Discussion .....	50
C.3.1. Combustion Synthesis .....	50
C.3.2. Microstructure Evaluation .....	50
C.3.3. Mechanical Properties .....	53
C.4. Summary .....	55

### CHAPTER III

RGI PROCESS MODEL.....	91
A. RGI PROCESS MODEL .....	91
A.1.Theoretical Background .....	91
A.2 Estimation of Limiting Stages in Kinetics of TiC Formation .....	91
A.3. The Process Model Development .....	93
A. 3.1. Model Assumptions .....	93
A.3.2. Mathematical Representation.....	93
A.3.3. Analysis of the Analytical Solution .....	96
A.4 Discussion of the Model.....	100
A.5. Summary .....	101

### CHAPTER IV.

IN-SITU PROCESSING OF NICKEL MATRIX COMPOSITES .....	109
A.1. Processing Background .....	109
A.2. Thermodynamic Analysis .....	109
A.2.1 RGI Process.....	110
A.2.2 SHS Process .....	112
A.3.Experimental Procedure .....	114
A.3.1 RGI Process.....	114
A.3.2 SHS Process .....	116
A.4.Results and Discussion.....	116
A.4.1 RGI Process.....	117
A.4.1.1 Carbide formation	
A.4.1.2 Nitride formation	
A.4.2 SHS Process .....	118

A.5. Discussion .....	118
A.5.1 RGI Process .....	119
A.5.1.1 Reaction efficiency .....	119
A.5.1.2 Reinforcement formation .....	121
A.5.1.3 Reinforcement morphology, size and distribution .....	128
A.5.2 SHS Process .....	129
A.6. Summary .....	131
<b>CHAPTER V.</b>	
<b>CONCLUSIONS</b> .....	159
I.A. Reactive Gas Injection Processing of TiC/Al .....	159
I.B. Reactive Gas Injection Processing of AlN/Al .....	160
I.C. SHS Processing of TiC/Al, TiB <sub>2</sub> /Al, (TiC+TiB <sub>2</sub> )/Al .....	161
II. RGI Process Model .....	162
III. <i>In-Situ</i> Processing of Ni-matrix Composites .....	164
<b>Acknowledgment</b> .....	166
<b>References</b> .....	167

Accession For	
NTIS CRABI	<input checked="" type="checkbox"/>
DTIC	<input type="checkbox"/>
Unannounced	<input type="checkbox"/>
Justification	
By	
Distribution /	
Availability Codes	
Dist	Avail and/or Special
A-1	



# **FINAL REPORT TO ONR**

**Drexel University  
Department Of Materials Engineering,  
Philadelphia, Pennsylvania**

## **ABSTRACT**

Metal matrix composites have emerged as a chief class of materials for advanced aerospace, automotive, electronic, thermal management and wear applications. These materials provide superior specific strength and stiffness as compared to the conventional monolithic materials. MMC's have been utilized in aerospace structural applications at elevated and ambient temperatures due to their high specific strength and stiffness. Therefore, traditionally, the development of metal matrix composites has been spurred by aerospace and the defense industry. With the changing political and economic conditions, however, it has become more important for the metal matrix composites to find cost effective industrial applications, e.g. automotive, electronic packaging, and wear resistance applications. This will be facilitated by liquid phase processing of particulate MMC's in larger quantities and in a near net shape form. In addition, the processing should be amenable to tailor the composites to specific structures, e.g., gradient structures and/or reinforcements at the surfaces for better mechanical performance and wear resistance.

The final report deals with a combined experimental and modeling program involving reactive processing of metal matrix composites. Initially, it provides for an overview of liquid-gas, liquid-liquid and liquid-solid reactions. The program of study is detailed in the subsequent sections to include: in-situ processing of aluminum matrix composites with carbide and nitride reinforcements; in-situ processing of aluminum matrix composites with mixed carbide and boride reinforcements; modeling of the reactive gas infiltration process with analytic solutions for carbide reinforcement formation and a process envelope formulation; in-situ processing of nickel matrix composites with carbide via reactive gas infiltration and self propagating synthesis approaches.

## CHAPTER I

### INTRODUCTION

#### A. REVIEW OF THE *IN-SITU* PROCESSING TECHNIQUES FOR COMPOSITE MATERIALS

It is now widely recognized that the mechanical and physical properties of Reaction Processed Metals (RPMs) are controlled by the size and volume fraction of the reinforcement phase, as well as the microstructure and properties of the matrix/reinforcement interface. RPMs have a high potential for advanced structural and thermal applications when a combination of strength and modulus as well as good wear resistance are important (e.g. free standing structural bodies and plasma coatings for thermal, oxidation, or wear resistance; structural ceramics; composites; and thin films for optical or microelectronics devices). In most of the processing techniques, the reinforcement (usually in a particulate form) is combined with the matrix material (either molten or in a powder form) in an isotropic, uniformly incremental or graded manners.

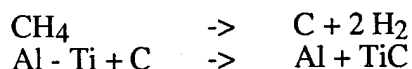
*In-situ* processes are new and promising techniques for composite fabrication and a number of patents have been granted in recent years for the methods developed. These processes involve the formation of reinforcements during the processing period through reactions between the mixed components of the composite. The following section presents an overview of the various composite processing *in-situ* techniques and it is divided on the basis of reaction mechanism, e.g. gas-liquid reactions (Reactive Gas Injection and Gas-eutectic processes), liquid-liquid reactions (Mixalloy, Osprey™) and solid-liquid reactions (SHS, XD™, Reactive Infiltration processes).

#### A.1. Liquid-Gas Reactions

##### A.1.1. Reactive Gas Injection (RGI)

###### a) *Al-Based Alloys*

Reactive Gas Injection (RGI) is a process patented recently [1]. A schematic of this technique is shown in Figure 1-1, it involves the injection of a carbon or nitrogen bearing gas into an alloy melt held at 150-250 °C above its liquidus temperature. The gas decomposes to give carbon or nitrogen on heating, which subsequently react with the ceramic forming alloying element to produce the ceramic reinforcement. For example, the authors [2] have injected an Ar-CH<sub>4</sub> mixture into molten Al-Ti alloy at 1100 °C resulting in the formation of a TiC/Al composite with submicron TiC particulate (0.1-3.0 mm) reinforcements. The reactions are



Extruded samples of this composite exhibited a 130 % increase in yield strength and 65 % increase in tensile strength compared with the base alloy. Furthermore, the composite retained room-temperature strength to 250 °C. A similar reaction using an Ar-C<sub>2</sub>H<sub>4</sub> mixture in air has successfully produced TiC/Al composites [3].

A theoretical analysis of the mechanism of the composite formation reaction has reported that the rate limiting step in the initial stages of the reaction is the supply of C to the alloy melt [4]. This is dependent on the residence time of the gas in the melt and the temperature to which it is heated. During the later stages of reaction, the rate limiting step is the diffusion of Ti to solid C particles trapped in the melt. Further work on the same system revealed that the formation of TiC was not instantaneous, as previously believed [5-6]. In fact, decomposition of the carbon-bearing gas produces carbon, which presumably first dissolves in the melt and then precipitates from the solution as nanometer size C particles during solidification. Homogenization in the liquid or solid state results in the conversion of these particles into carbide particles. Thermodynamically stable TiC particles may be preceded by metastable Ti<sub>3</sub>AlC or Al<sub>4</sub>C<sub>3</sub>.

An in-situ process to form AlN-reinforced Al-alloy composite has been carried out between 700 to 1500°C. Molten-aluminum is partially nitrified by injecting nitrogen-containing reactive gas into the melt. AlN can be formed in the bulk melt only in the presence of Mg and Si, with a mixture of nitrogen and ammonia as reactive gases at above 1000°C. It is found that magnesium serves as a catalyst [7]. Magnesium nitride is formed first by the reaction of vaporized magnesium and nitrogen gas. When magnesium nitride particles are introduced into molten aluminum, a substitution reaction takes place between magnesium nitride and aluminum to form aluminum nitride. The average size of the AlN formed is about 3 µm. Aluminum nitride can be formed from molten Al alloys by injecting the mixture of NH<sub>3</sub>-N<sub>2</sub> at 1000°C. Mg reacts with N<sub>2</sub>-bearing gases in the vapor phase, followed by a substitution reaction with Al to release AlN. Mg serves as "catalyst". Pure molten aluminum cannot form AlN in the bulk because of the passivation effect. However, Al alloys, such as Al-Mg-Si, reduce the passivation effect. Nitrogen along with about 3 v/o ammonia can provide a very reactive source of nitrogen. Examples of the nitridation strategy are shown in Figure 1-2.

#### ***b) Ni-Based Alloys***

The cost-effective processing of high temperature non-ferrous metallic and intermetallic matrix composites is a major challenge. Due to the high temperatures involved in these reactions, the reactive gases used in RGI reactions are readily decomposed, providing carbon or nitrogen for TiC and TiN formation. TiC, NbC, and TiN reinforced Ni-based composites were also processed via the RGI synthesis route. Decomposition of methane produces carbon which

dissolves in the alloy melt at 1600°C. During solidification, the carbides form through the eutectic reaction which precipitates interdendritic lamellar TiC and NbC around primary dendrites. TiC lamellae were thick 1-5 µm while NbC lamellae were 1-3 µm. Exploratory studies in nitridation revealed that a continuous 3-5 µm layer of TiN was formed on the top and sides of the sample by the reaction of Ti in the melt with nitrogen gas at 1550°C. NiAl/TiB<sub>2</sub> and FeAl/TiC composites were synthesized from less than 1.0 µm to 3.0 µm for TiB<sub>2</sub> and 10-40 µm for TiC. The distribution of these particles in the matrix was uniform and demonstrated the potential of TiC/TiB<sub>2</sub> formation in Ni- and Fe- based alloys and intermetallics.

#### **A.1.2. Gas-eutectic Reactions**

Gas-eutectic transformation in metal-hydrogen systems is a relatively recent discovery [8]. In this reaction, the liquid decomposes into a solid and a gas phase:  $L \rightarrow S + G$ . The transformation takes place if the phase diagram for the metal-hydrogen system involves a gas-eutectic equilibrium as in Figure 1-3a. Making the material consists of two steps:

1. Melt charging with hydrogen to reach the eutectic composition, and
2. Melt solidification in a conventional or continuous casting mold.

No melt foaming occurs because the gas is evolved as the melt freezes (Figure 1-3b). The process is in many ways similar to conventional eutectic solidification, the distinction being that the liquid decomposes into a solid and a gas rather than into two solids. The main process variables that govern the amount of porosity, shape, size, and orientation of the pores are the hydrogen level in the melt, gas pressure over the melt in solidification, direction and rate of heat removal, and the alloy chemical composition. The pore structure can be controlled over a wide range by changing these variables.

Materials produced by gas-eutectic solidification are so different structurally from all other porous materials that a new word has been coined for them - GASAR which is an abbreviation of the Russian term for "gas-reinforced". All factors being equal, GASARs are considered to be the strongest porous materials. For instance, at 20% porosity, the strength of a copper GASAR is 1.9 times that of sintered copper, and 4 times stronger at 45% porosity [9]. GASARs can be manufactured in diverse structural variations depending on the processing variables. Figure 1-4. illustrates the main structural types embodied in GASARs. In a GASAR with closed hydrogen-filled pores, convection plays a far more important part. The reason is that hydrogen has high thermal conductivity and low viscosity. When its pressure in the pores is high enough, the contribution of convection increases so that the GASAR's thermal conductivity exceeds that of the similar poreless metal.

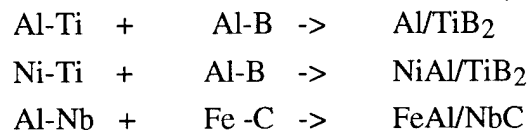
Permeable porous materials have an extremely wide range of applications. These include filters, catalysts, mufflers, flame arresters, heat exchangers, fuel cells, electrolytic cells, fluid

substance separators, fluid flow regulators, ionizers of ionic rocket engines, self-lubricating bearing, thermal screens, silencers, and vibration dampers. Impermeable porous materials are used less extensively. They are limited to applications for lightweight structures capable of absorbing noise, vibrations, and shocks. High-porosity foamed metals, particularly aluminum, are particularly suited for thermal insulation in construction and engineering.

## **A.2. Liquid-Liquid Reactions**

### **A.2.1. Mixalloy**

Another recent process, the Mixalloy™ process of the Sutek Corporation, Hudson, MA [10], has been successful in producing TiB<sub>2</sub>/Cu composites. The process involves melting alloys of Cu-Ti and Cu-B in two separate crucibles and mixing them in a turbulent manner in a third chamber. The vigorous mixing that accompanies turbulent jets causes a fast reaction between the Ti and B to form the ceramic particulates. Further, the vigorous mixing does not allow coarsening or coalescence of the ceramic particles. Electric grade TiB<sub>2</sub>/Cu composites have been produced by this method. The following reactions:



should lead to the formation of metal and intermetallic matrix composites by the Mixalloy™ process for structural, wear, corrosion and thermal applications.

### **A.2.2. Osprey™ Spray Deposition**

In the Osprey™ process, the reinforcement particulates are introduced into a stream of a molten alloy which is subsequently atomized by jets of inert gas. The sprayed mixture is collected on a substrate in the form of a reinforced metal matrix billet. This approach was introduced by ALCAN as a modification of the Osprey process [11-13], see Figure 1-5. The process combines the blending and consolidation steps of the powder metallurgy. It promises major savings in the production of metal matrix composites.

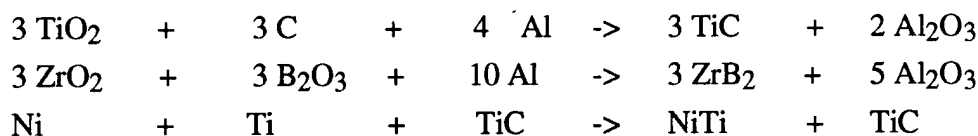
## **A.3. Liquid Solid**

### **A.3.1. SHS-XD™**

The invention of a new process for producing ceramic and intermetallic materials in the former Soviet Union known as Self-propagating High-temperature Synthesis (SHS) by Merzhanov and associates has resulted in considerable activity in recent years [14]. In this process, stoichiometric quantities of elements are blended together and compacted to about 50-70 % of theoretical density. A highly exothermic formation reaction is subsequently initiated in the

compact, which sustains a combustion wave that travels through the sample leaving behind the reacted product. The schematic of the SHS technique is illustrated in Figure 1-6. The SHS process has been used to produce a wide range of ceramic, metallic and intermetallic materials, and more recently, metallic and intermetallic matrix composites. Extensive work has led to the production of intermetallic compounds, shape memory alloys, and ceramic and intermetallic matrix composites [15, 16, 17]. In particular, the feasibility has been demonstrated of producing well dispersed 10 wt.-%-TiC/NiTi composites through reaction between elemental Ni and Ti powders in the presence of solid TiC particles [17]. The reacted compact was subsequently hot-rolled at 800 °C into ribbons that exhibited the shape-memory effect.

The SHS reaction can be initiated in various ways. In one approach Kanthal ribbon connected to a electric power supply was used to react mixed  $\text{TiO}_2\text{-C-Al}$ ,  $\text{ZrO}_2\text{-B}_2\text{O}_3\text{-Al}$  and Ni-Ti-TiC powders [17].  $\text{TiC-Al}_2\text{O}_3$ ,  $\text{ZrB}_2\text{-Al}_2\text{O}_3$  and NiTi-TiC composites were formed by the reactions



An oxyacetylene torch in air was used to initiate a reaction between Ti and Al powders in the presence of SiC or  $\text{Al}_2\text{O}_3$  to form SiC/TiAl and  $\text{Al}_2\text{O}_3\text{/TiAl}$  composites. [18] Other methods of heating have included induction heating, plasma, and electric discharge. In a recent advance, microwave energy was used to initiate and sustain a reaction between Ti-C and Al-C-TiO<sub>2</sub> mixtures to produce TiC and TiC/ $\text{Al}_2\text{O}_3$  composites [19]. The basic difference between conventional and microwave ignition is that in the latter the reaction temperature is first reached at the center of the sample, following which, the combustion wave radiates out to the surface. This reduces the volume change accompanying the release of volatiles during the propagation of the reaction wave. Although this method seems to have many advantages, it is still in an embryonic stage of development.

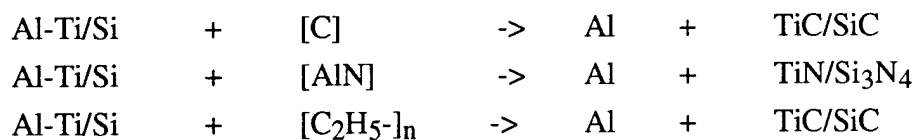
Another process that uses the exothermal heat released during chemical reactions is the widely studied XD™ process of Martin Marietta, Baltimore, Maryland [20]. This process involves the mixing of elemental ceramic precursors with matrix precursors in the form of powders and increasing the temperature of the mixture upto a point where an exothermic reaction is initiated. The combustion temperature is high enough to melt at least one of the components. The ceramic precursors then dissolve in the molten component, react in solution, and form a uniform dispersion of submicron ceramic particles. The composite powders thus formed are subsequently subjected to various forming operations such as casting, rolling, extrusion, forging, etc. The key condition for the successful production of the ceramic reinforcement in the

metallic, ceramic or intermetallic matrix is that the liquid component has extensive solubility for the precursors, but negligible solubility for the solid ceramic particles. The patent literature shows examples of the production of composites with reinforcements of  $\text{TiB}_2$ ,  $\text{ZrB}_2$ ,  $\text{MoSi}_2$ , VC,  $\text{VB}_2$ , TiC,  $\text{AlTi}_2$ , WC,  $\text{TiSi}_2$ ,  $\text{AlZr}_2$ , etc. in matrices of Al, Cu, Fe, Mg, Ni, Co, Si, Ti, NiAl, CoAl, CrAl, TiAl, etc. The wear properties of XD<sup>TM</sup> processed composite powders that have been consolidated to full density are superior to those of conventional powder metallurgy processed composites of the same system without the in-situ formation reaction.

### A.3.2. Reactive Infiltration

The infiltration process involves holding a porous body of the reinforcing phase within a mold and infiltrating it with molten metal that flows through interstices to fill the pores and produce a composite. Two examples of infiltration processes are given in Figure 1-7. Such processes are not new; liquid-metal infiltration has been used for many years in powder metallurgy to strengthen porous metal parts of iron and steel with copper [21]. The major difference between infiltration of a solid metal by a liquid metal and infiltration of a ceramic by a liquid metal regards wetting. In the case, of a ceramic, the liquid metal generally does not spontaneously wet the reinforcement. Therefore, it is often forced into the preform by application of the external force that overcomes the capillary and fluid-drag forces.

Reactive infiltration has the potential for fabricating complex near net shaped metal matrix composite MMC components. This process consists of infiltrating a carbon or polymer precursor preform with a reactive alloy. The possible reactions depend on the relative thermodynamic stability and reaction kinetics of the materials:



(the preform materials are in the parenthesis)

It is possible to tailor the preform to have graded reinforcement and controlled reinforcement volume fractions. The polymeric preforms, e.g., fiber precursor materials, can also be selected to have non-carbide reinforcements, e.g.,  $\text{KBH}_4$  (potassium boro-tetrahydride). The matrix reinforcement, i.e., volume fraction, size, gradient can be controlled by designing the appropriate preform. For example, wear resistant parts can be made by infiltrating a carbon preform that has higher density at the surface. Honda Motor Co. uses a carbon and an alumina-based preform infiltrated with an aluminum alloy to fabricate wear resistant engine blocks [22]. In addition to providing a route for forming tailored near net shaped composites, reactive infiltration shows promise for substantial energy savings, since the exothermicity of the reactions can provide the heat required for the in-situ reaction.

## **B. PROGRAM OF STUDY**

### **B.1 Description of the Scientific Research Goals**

MMC's have been utilized in aerospace structural applications at elevated and ambient temperatures due to their high specific strength and stiffness. It has become, however, more important for the liquid phase processed metal matrix composites to find cost effective industrial applications, e.g. automotive, electronic packaging, and wear resistance applications. This will be facilitated by liquid phase processing of particulate MMC's for non-ferrous alloy systems. In addition, the liquid processing approach should tailor the composites to specific structures, e.g., centrifugal casting or injection molding for enhanced mechanical performance and wear resistance.

The program of study and significant result are detailed in the subsequent sections to include: in-situ processing of aluminum matrix composites with carbide and nitride reinforcements; in-situ processing of aluminum matrix composites with mixed carbide and boride reinforcements; modeling of the reactive gas infiltration process with analytic solutions for carbide reinforcement formation and a process envelope formulation; in-situ processing of nickel matrix composites with carbide via reactive gas infiltration and self propagating synthesis approaches.

### **B.2 Significant Results**

The results of metallic and intermetallic matrix composites produced by two reactive techniques involving in-situ reactions are given below.

#### **B.2.1. Reactive Gas Injection Processing of MMCs**

The RGI process was compared with the other existing in-situ techniques for the synthesis of MMC composite materials. The main advantages of the RGI are thermodynamic stability of the composites, nascent interfaces, fine reinforcement size as well as economical processing due to rapid kinetic of reinforcement formation and nonexpensive starting materials, net shape forming and continuous processing. The disadvantages of the RGI are mainly due to the high melt viscosity, which prevents the fabrication of composites with high volume fractions of reinforcement and causes the formation of inhomogeneties due to the poor mixing of the viscous melts. The selection of reinforcements is also limited due to thermodynamic reasons: in order to produce stable reinforcements there should be a large difference in change of free energy of carbide formation between the matrix metal and reinforcement precursor metal.

##### ***B.2.1.1. RGI Processing of TiC/Al***

The processing envelope for conversion of C and Ti to TiC has been determined. Minimum TiC platelets size is limited by the nucleation process and corresponds to 0.1  $\mu\text{m}$  in



diameter. Maximum size of reinforcement is determined by coarsening kinetics of carbides and the particles vary in size from 10 to 20  $\mu\text{m}$ . Maximum volume fraction of reinforcement is limited by the melt viscosity and does not exceed 40 volume percent. For the range of volume fractions, the average TiC particulate size is 1-3  $\mu\text{m}$ . The average TiC size does not increase significantly with time. TiC particle size increased by 15  $\mu\text{m}$  in 8 hours, which signifies that the process of TiC coarsening is quite slow.

The TiC formation mechanism follows the solution-precipitation route for fine soluble particles and interfacial reaction route for graphitic surfaces. The interfacial reaction of TiC formation at the solid carbon particle is 5 orders of magnitude slower than carbon dissolution process. Thus, the two processes are taking place simultaneously, but since the interfacial reaction is much slower, by the time a significant carbide layer can build up on a carbon particle, the particle may completely dissolve.

#### ***B.2.1.2. RGI Processing of AlN/Al***

Aluminum nitride synthesis in molten aluminum alloy was achieved by two methods, namely, direct and indirect nitridation. Direct nitridation experiments produced AlN/Al-Mg-Si metal matrix composites via nitrogen-bearing gas injection, with the aid of Mg and Si at temperatures above 1000°C. Indirect nitridation included solid-liquid displacement reaction, and reactive gas injection method. The first was by mixing magnesium nitride with molten aluminum at 1000°C. The reaction between magnesium nitride and aluminum is a liquid-solid interfacial reaction. Agitation and/or gas stirring must be carefully employed to develop intimate contact of  $\text{Mg}_3\text{N}_2$  and Al in order to provide for uniform composite. Early gas injection and stirring resulted in segregation of  $\text{Mg}_3\text{N}_2$  from Al, while late gas injection results in agglomeration of AlN particles formed. The second method of forming AlN via *in situ* generated  $\text{Mg}_3\text{N}_2$  was also successful. This approach has the promise of synthesizing micron and submicron sized AlN. Volumetric concentrations of AlN as high as 15% are obtained. Enhanced mechanical and wear properties of aluminum alloy can be achieved with this cost effective liquid-gas phase synthesis route.

#### ***B.2.1.3 RGI Processing of TiC/Ni***

TiC/Ni composites with TiC volume fractions below ~20 % was produced by methane injection into the corresponding Ni-Ti alloy melt. The morphology of TiC in low volume fraction composites is a eutectic lamellar morphology. The thickness of the lamellae vary between 1 and 10  $\mu\text{m}$ . Equilibrium aging experiments (1200 °C / 24 hours / Ar atmosphere) performed on these samples resulted in precipitation of TiC platelets inside the Ni dendrites. These platelets had a thickness of <1  $\mu\text{m}$  and were 1-5  $\mu\text{m}$  long. Higher volume fraction TiC/Ni composites (20-30 vol.%) exhibited non-homogeneous microstructures. TiC was formed in two

morphologies- angular and eutectic lamellar. Angular TiC particles of size 5-20  $\mu\text{m}$  were theoretically found only in the top half of the casting. The bottom half consisted of  $\text{Ni}_3\text{Ti}$  intermetallics and eutectic lamellar TiC. Based on the microstructures observed and examination of available phase diagrams, a reaction mechanism was developed for the formation of TiC in Ni. The reaction sequence is: (i) decomposition of methane to give free carbon; (ii) dissolution of carbon in the Ni-Ti alloy melt and (iii) precipitation of TiC during solidification

## **B.2.2 SHS Processing of MMCs**

### ***B.2.2.1 SHS Processing of TiC/Al, TiB<sub>2</sub>/Al, (TiC+TiB<sub>2</sub>)/Al***

Al matrix *in situ* composites with 30 vol.% of hard ceramic particles (TiC and/or TiB<sub>2</sub>) were successfully fabricated employing SHS technique. This is the first study to report the SHS processing of Al base MMCs with such a low volume fraction of the ceramic reinforcement. The result is significant, and it denotes that, employing SHS, it is possible to obtain Al matrix *in situ* composites with compositions ranging from 30 to 100 vol.% of TiC and/or TiB<sub>2</sub> particles. Very fine-scale ceramic reinforcements ranging from tens of nanometers up to 1-2  $\mu\text{m}$ , were obtained in the Al matrix.

It was shown that, by employing high pressure consolidation at temperatures not exceeding 300°C, full density can be achieved in the porous SHS-processed Al matrix composites containing 30% of TiC and/or TiB<sub>2</sub> particles. High room and elevated temperature mechanical properties (yield stress, microhardness) were obtained in the high pressure consolidated SHS-processed composites, comparable to the best rapidly solidified Al base alloys with the same volume fraction (~30%) of the second phase. Alongside with the high yield strength, appreciable room and elevated temperature ductility was observed in the SHS-processed Al base composites. Al matrix *in situ* composites, with their low SHS combustion velocities (due to the strong heat dissipation in the "inert" metal matrix), as well as MMCs on the whole, may be an alternative processing route for the utilizing low volume fraction (~30%) aluminum MMC's.

### ***B.2.2.2 SHS Processing of TiB<sub>2</sub>/NiAl and TiC/FeAl***

Intermetallic matrix composites of TiB<sub>2</sub>/NiAl and TiC/FeAl were produced by mixing elemental precursors and initiating the exothermic formation reactions. The TiB<sub>2</sub> particle size was between 1 and 3  $\mu\text{m}$  while the TiC particle size was 10-40  $\mu\text{m}$ . The distribution of TiB<sub>2</sub> in NiAl was relatively uniform while TiC in FeAl was formed as large clusters. The reaction mechanism is believed to be the dissolution of the ceramic precursors in a transient molten phase followed by reaction and precipitation of the ceramic particles. Pursuit of the SHS route for intermetallic matrix composites and the RGI process for metal matrix composites should result in the development of economically viable production routes for the respective composites.

### B.2.3 RGI Process Model for TiC/Al

A kinetic model of the process of TiC formation has been developed for a batch operation and can be modified for continuous MMC production. The model predicts the degree of Ti and C conversion to TiC, (i.e.  $V_f$  of TiC) as a function of reaction time. The model revealed three main stages in the kinetics of conversion.

Based on the analytical solution of the model the synthesis should contain two steps:

Steps I: Introduction of carbon into the melt for the required time, which depends on the value of  $[Ti]_0$  and the flow rate of methane.

Steps II: Holding the melt at high temperature to allow the reaction of TiC formation to proceed to completion.

Diffusion limited, TiC formation rate constant was calculated for the processing temperature of 1300°C to be  $1.64 \times 10^2 \text{ cm}^3/\text{g sec}$ .

The results of the theoretical model are in rather good agreement with the experiment. The disagreement between the model and experiment is observed at high volume fractions of reinforcement. It can be explained by the increment of the melt viscosity; to include this effect a correction for reaction rate constant should be made.

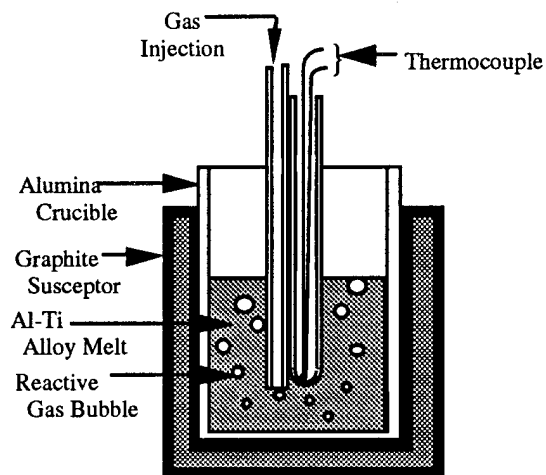


Figure 1-1. Schematic of reaction vessel used for Reactive Gas Injection (RGI) runs.

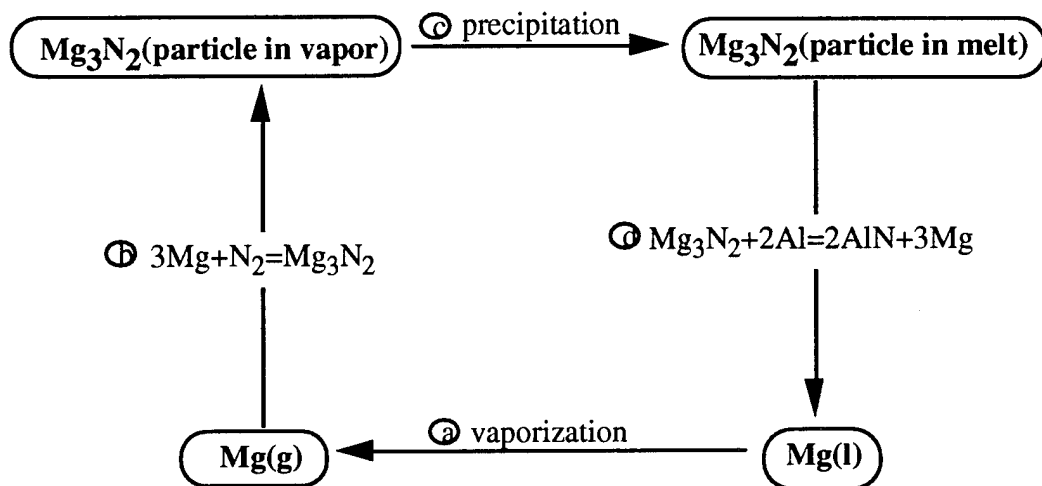


Figure 1-2. Mechanism of "catalytic" nitridation.

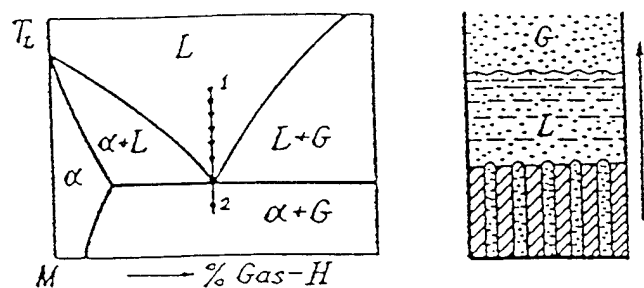


Figure 1-3. (a) Isobaric section of metal-hydrogen system with gas-eutectic equilibrium. (b) Gas-solid eutectic growth in upward directional solidification. [9]

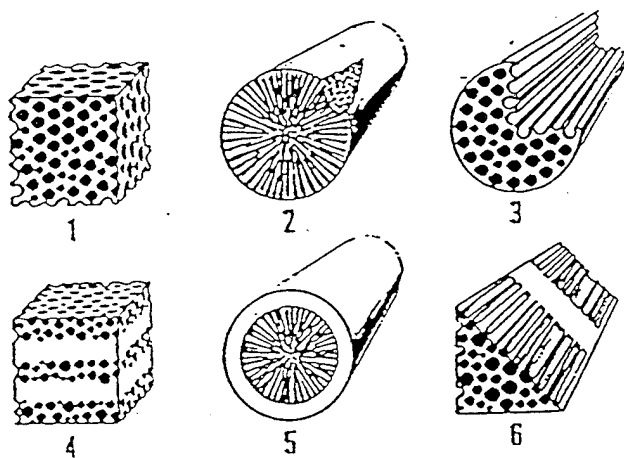
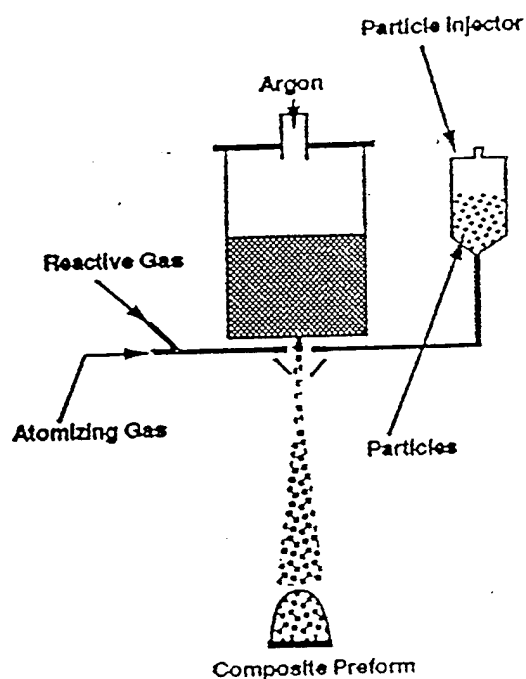
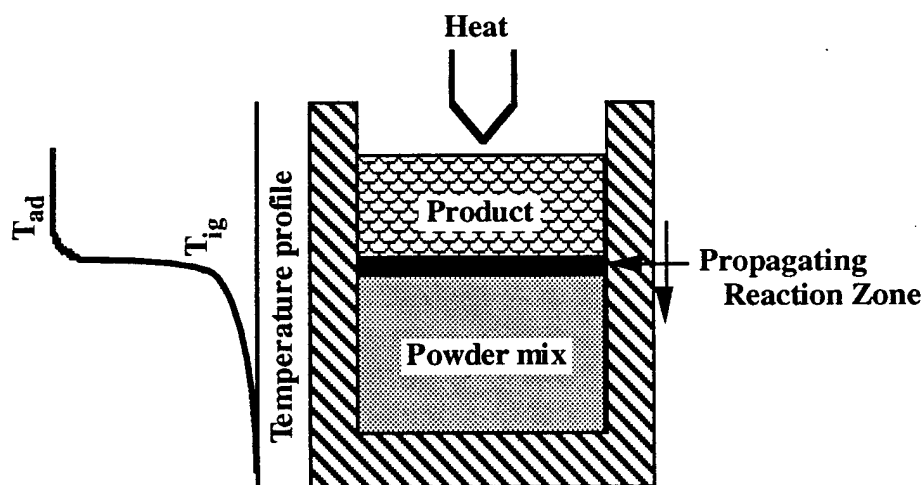


Figure 1-4. Gas-solid structures formed in GASARs under various conditions of gas-eutectic reactions. [9]



**Figure 1-5** Schematic diagram of the modified Osprey technique.



**Figure 1-6** Schematic of experimental setup used for Self-propagating High-temperature Synthesis (SHS) reactions showing temperature distribution during combustion wave propagation.

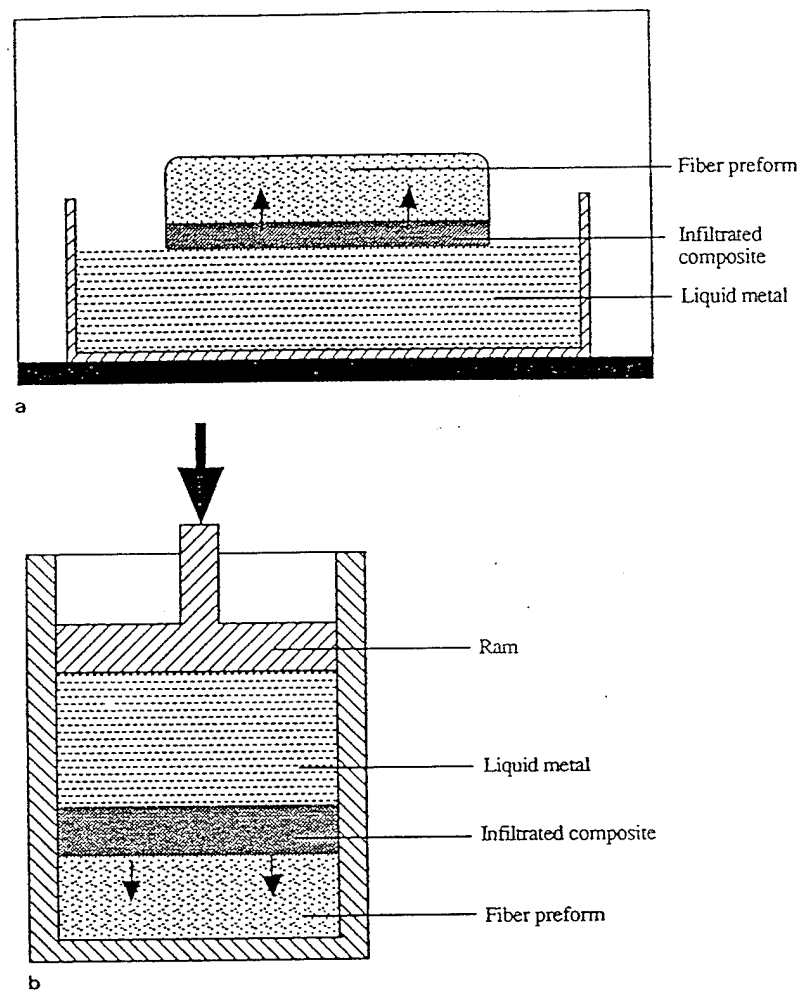


**Figure 1-7** Schematic representations. (a) Spontaneous infiltration and (b) Pressure-driven infiltration. [21]

## CHAPTER II.

### **IN-SITU PROCESSING OF ALUMINUM MATRIX COMPOSITES**

The overall goal of this research has been to fabricate aluminum matrix composites with various reinforcements, namely titanium carbide, aluminum nitride, titanium diboride as well as complex reinforcements using *in-situ* technique. Research of TiC/Al matrix was concentrated primarily on processing of Al matrix with a narrow size distribution of submicron TiC particles. A Reactive Gas Injection (RGI) technique for the synthesis of fine single crystal TiC platelets in Al has been developed. The kinetics of Ti and C conversion to TiC at a temperature range of 1100 - 1300°C has been investigated. Rapid melt cooling after different reaction times allows measurement of the degree of Ti and C conversion as a function of time. Microstructure of the reaction products was characterized by means of XRD, optical and scanning electron microscopy. A kinetic model of titanium carbide formation by RGI has been developed. Predictions of the theoretical model have been compared to the experimental results. Based on the observations, two possible mechanisms for TiC formation in Al matrix have been proposed and compared, namely a liquid state, solution-precipitation mechanism versus a solid-liquid interfacial reaction.

The feasibility of directly forming aluminum nitride by *in-situ* reactive nitrogen gas injection into molten aluminum alloys has been evaluated over a temperature range of 700 to 1500°C. It is shown that aluminum nitride can be melt formed in the presence of Mg and Si, with nitrogen and/or ammonia as the reactive gases at temperatures above 1100°C. In this role, magnesium served as a catalyst. Two methods of indirect nitridation were investigated for synthesizing aluminum nitride, namely (i) by gas injection and reaction to form magnesium nitride *in situ*, followed by the displacement reaction, i.e.  $\text{Al-Mg(l)} + \text{N}_2 \rightarrow \text{Al-Mg(l)} + \text{Mg}_3\text{N}_2\text{(s)} \rightarrow \text{AlN(s)} + \text{Al-Mg(l)}$ , and (ii) by a solid-liquid displacement reaction, i.e.  $2\text{Al(l)} + \text{Mg}_3\text{N}_2\text{(s)} \rightarrow 2\text{AlN(s)} + 3\text{Mg(l)}$ . In the former, aluminum nitride was formed via *in situ* generated magnesium nitride. In this synthesis route, nitrogen bearing gas was bubbled into magnesium-containing aluminum alloy, and up to 15 vol% of aluminum nitride with average particle size of 3µm was formed at 1100°C. In another approach, aluminum nitride was formed in molten aluminum by mixing magnesium nitride powder with molten aluminum at 1000°C. The reaction proceeded via a solid-liquid interfacial reaction. The size of aluminum nitride formed was directly related to the initial size of magnesium nitride particles. The results observed suggest that aluminum nitride/aluminum composites can be made via the molten metal chemical reaction route.



Another *in situ* technique termed Self propagating High temperature Synthesis (SHS) was employed for processing of Al matrix composite materials with 30 vol.% TiC, TiB<sub>2</sub> and (TiC+TiB<sub>2</sub>) ceramic reinforcements. Material synthesis was followed by high pressure consolidation to full density. Nonsteady-state oscillatory motion of the combustion wave was observed during the SHS processing, resulting in a typical layered structure of the reaction products. Very fine-scale ceramic particles ranging from tens of nanometers up to 1-2  $\mu\text{m}$ , were obtained in the Al matrix. Microstructural analysis of the reaction products showed that the TiB<sub>2</sub>/Al and TiB<sub>2</sub>-TiC/Al composites contained Al<sub>3</sub>Ti phase, indicating that full conversion of Ti had not been achieved. In TiC/Al composite, a certain amount of Al<sub>4</sub>C<sub>3</sub> was detected. High room and elevated temperature mechanical properties (yield stress, microhardness) were obtained in the high pressure consolidated SHS-processed TiC/Al and TiB<sub>2</sub>/Al composites, comparable to the best rapidly solidified Al base alloys. These high properties were attributed to the high density of the nano-scale ceramic particles and matrix grain refinement. The potential for these processes permits economical processing of Al-matrix composite reinforced with TiC, TiB<sub>2</sub>, (TiC+TiB<sub>2</sub>) or AlN for structural, thermal and wear applications.

## **A. *IN-SITU* PROCESSING OF Al/TiC COMPOSITES VIA REACTIVE GAS INJECTION.**

### **A.1. Processing Background**

The formation of carbides by the gas-liquid reaction depends on a number of thermodynamic and kinetic factors. Based on the free energy of formation ( $\Delta G_f$ ) of the carbides, metals can be classified into strong and weak carbide formers and this is schematically illustrated in Figure 2-1. The in-situ process is most efficient for systems where the reinforcement carbide is thermodynamically stable compared to the matrix metal carbide at the processing temperature. In RGI experiments involving Ni-Ti [23] alloys as well as Al-Ti alloys, the matrix metals Ni and Al are weak carbide formers compared to Ti.

The sequence of TiC formation in the Al matrix via RGI is outlined below:

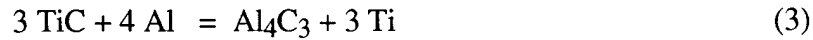
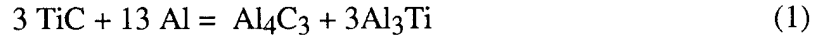
- (1) decomposition of methane in the bubble;
- (2) transport of carbon across the gas-liquid interface into the melt by
  - motion of carbon particles to the inside surface of the bubble,
  - particles incorporation into the melt;
- (3) transport of carbon away from the bubble surface by
  - dispersion of as-decomposed carbon particles in the melt;
  - dissolution of carbon in the alloy,
- (4) carbide formation via two mechanisms illustrated in Figure 2-2:
  - precipitation out of the solution (solution-reprecipitation mechanism)
  - reaction of solid carbon with liquid carbide former at the solid-liquid interface (solid-liquid interfacial reaction).

In the case of solution-reprecipitation, carbon and titanium are present in the Al-Ti-C solution and when the solubility limit of Ti and C in Al is exceeded, they precipitate as TiC. In this case, the size of TiC particulates does not depend on the carbon particle size and can be calculated by nucleation theory. In general this mechanism is expected to yield fine carbides (up to 1  $\mu\text{m}$  in diameter). The alternative process of TiC formation takes place at the solid carbon/liquid melt interface and causes a formation of TiC particulates proportional to the size of the initial carbon particle. Since very fine carbon particles tend to agglomerate, the carbides formed via this route are presumed to be coarser, i.e. 1-10  $\mu\text{m}$ . Thus, the mechanism of TiC formation determines the size and morphology of TiC particulates (see Figure 2-3).

The formation of carbides by the gas-liquid reaction depends on a number of thermodynamic and kinetic factors. Thermodynamics of TiC and  $\text{Al}_4\text{C}_3$  formation is considered first, providing a background for future kinetic analysis.

## A.2. Thermodynamic Analysis

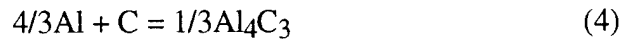
The results of thermodynamic analysis conducted by several authors [24-27] are illustrated in Figure 2-4 and show the free energy versus temperature curves for the reactions:



Reaction (1) proceeds to the right only below 1025 K (752 °C), above which the free energy change for the reaction is positive. Thus the equilibrium presence of  $\text{Al}_3\text{Ti}$  and  $\text{Al}_4\text{C}_3$  below 1025 K is expected.

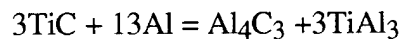
The study on relative  $\text{TiC}$  and  $\text{Al}_4\text{C}_3$  stability over the range of temperatures can be briefly summarized as follows:

- (1) In liquid state, i.e. at any temperature above 1025 K (752°C),  $\text{TiC}$  is stable and  $\text{Al}_4\text{C}_3$  is not expected to form due to thermodynamic reasons (see Figure 2-4a) if Ti and C are present in stoichiometric amounts in Al-Ti-C system. However, since the free energy change for the reaction:



is negative at all the temperatures below 2273K (2000 °C) (see Figure 2-4b), aluminum carbide will form in presence of extra carbon. This is valid for liquid and solid aluminum.

- (2) At the temperatures below 1025 K, reaction:



becomes thermodynamically feasible and as it was shown experimentally by Mirta et. al [24], titanium carbide converts to  $\text{Al}_4\text{C}_3$  and  $\text{Al}_3\text{Ti}$  on isothermal solid state heat treatment at 933 K (660°C).

## A.3 Experimental Procedure, Results and Discussion

The experiments were designed to evaluate five aspects of Al-based composites processing via Reactive Gas Injection, namely:

- (i) methane decomposition efficiency and the morphology of carbon formed during the decomposition under different processing conditions,

- (ii) processing envelope, i.e. range of feasible sizes and volume fractions of TiC processed via RGI,
- (iii) the reaction mechanism of TiC formation in Al,
- (iv) the kinetics of Ti and C conversion to TiC
- (v) the feasibility of SiC formation via RGI.

The experiments conducted over the research period were divided into five types accordingly. Number of successful and unsuccessful runs with the main reasons for the experiment failure and total number of experiments conducted are summarized in Table 2-1. The experimental approach, results of each study and their discussion are presented below.

### **A.3.1. Methane Decomposition Study**

#### ***A.3.1.1 Experimental Procedure and Results***

To investigate the efficiency of methane decomposition, size and structure of the nascent carbon formed from decomposed methane at high temperature, a series of methane decomposition experiments were conducted. A 1:3 CH<sub>4</sub>-Ar mixture was decomposed in a flow reactor at temperatures varying from 900°C to 1200°C and flow rates of 0.1, 0.3 and 0.5 SLPM. The experimental setup used is shown in Figure 2-5. The installation was equipped with two flow meters, which registered the flow rate of the gas mixture entering and exiting the reactor. The increment of the flow rate of the exiting gas was correlated with the degree of methane decomposition and the data is presented in Table 2-2.

In the flow reactor, BeO and Al<sub>2</sub>O<sub>3</sub> substrates were placed for collection and growth of deposited carbon particles. Carbon particles collected on these substrates were examined microscopically. The results are summarized in Table 2-3. Figures 2-6 and 2-7 show deposited carbon on BeO and Al<sub>2</sub>O<sub>3</sub> substrates, respectively. Different time-temperature exposures indicate that the substrate type has a significant effect on the morphology and size of carbon particles.

#### ***A.3.1.2 Discussion***

The study designed to investigate the efficiency of methane decomposition demonstrated that the degree of conversion is lower than that theoretically predicted, especially for the high gas flow rates. The difference between the theoretical and experimental results may be explained as follows. Time required for methane to reach the furnace temperature is longer than the time the methane spends in the reactor. Thus a correction, accounting for the fact that the gas temperature is lower than the furnace temperature, should be made. The actual gas temperature is related to the furnace temperature by the expression:

$$T_{\text{gas}} = f T_{\text{furnace}}$$

where  $f$  is a correction factor,  $f \leq 1$ . The parameter  $f$  is mainly a function of the gas flow rate, i.e. the smaller the flow rate the closer  $f$  to one. This type of behavior is illustrated in Figure 2-8 by the lines, which leads to the conclusion that small flow rates provide a better efficiency of methane decomposition and consequently a higher degree of Ti conversion to TiC. Calculation of  $f$  for each experiment conducted and expression of the actual gas temperature will shift the lines given in Figure 2-8 to the left. Table 2-4 gives the value for the  $f$  factor and actual gas temperature accordingly. The experimental data, corrected for the temperature difference, are represented in Figure 2-8 by dots. The new data representation shows that the efficiency of methane decomposition is somewhat lower than predicted by thermodynamics, but is still within the range of 0.95-0.99 at the typical processing temperatures, i.e. 1000 - 1300°C.

As can be clearly seen from the Figures 2-6 and 2-7, the carbon particle size ranges from 0.1 to 0.3  $\mu\text{m}$ . It is believed that the initial carbon particle size is much smaller, i.e. 50 - 100 nm. After nucleation, the carbon nano-particles undergo agglomeration and coalescence. During injection in the molten aluminum, the growth of carbon particles, however is unlikely, due to the short residence times and fast dissolution of solid carbon in the Al-Ti melt. The above experiments indicated that typical initial carbon particles in the melt are less than 100 nm, which was later substantiated by TEM studies of the Al-C samples with no or very low (<1wt.%) Ti concentration, obtained by bubbling of methane-argon mixture through the melt. Figure 2-9 illustrates an agglomerate of carbon particles, which were trapped in the melt after rapid cooling of the sample.

### **A.3.2 Determination of the Synthesis Processing Envelope via RGI**

The goal of this research was to define the processing envelope, e.g. the range of TiC sizes and volume fractions, which can be produced by the RGI technique. The main processing hurdles are summarized in Table 2-5. The minimum TiC size is limited by the nucleation process; obviously, the particle size cannot be smaller than the TiC nucleus size. Maximum size of reinforcement is determined by diffusion controlled coarsening of carbides and is a function of the processing time and temperature. Maximum volume fraction of reinforcement is limited by the melt viscosity. The melt viscosity increases as the volume fraction of TiC increases. When a high level of reinforcement is reached, e.g. 25-40%, bubbles become suspended in the liquid and can not be liberated. A piston-like motion of the bubbles in a viscous liquid can cause ejection of the melt from the crucible.

#### **A.3.2.1. Experimental Procedure**

The experimental procedure of the RGI process, which is schematically represented in Figure 2-10, consists of five main parts, namely, induction power supply unit; induction furnace

and vacuum chamber with coils, reaction crucible, gas injection system and IBM-based data acquisition and control system.

A schematic of the in-situ synthesis technique was shown in Figure 1-1. An alumina crucible coated with yttria ( $Y_2O_3$ ) was used as the reaction vessel and was placed within a graphite susceptor to ensure uniform heating over the length of the crucible. The power was supplied via water cooled copper coils in a Vacuum Industries, Model 600 induction furnace. A thermocouple placed in contact with the bottom surface of the graphite susceptor was used for temperature monitoring purposes. The gas flow rates were monitored via computer controlled electronic gas flowmeters from Porter Instruments. The titanium was provided in the form of Al-10%wt.Ti (Cabot - KBI Co.) master alloy and commercially pure Ti (Tico Inc.).

Melting was achieved under vacuum at a level of 60 mtorr, and subsequently the chamber was back-filled with purified argon (Airco Company) which also serves as the carrier gas. Upon reaching the appropriate processing temperature, the carbonaceous gas was introduced into the melt via a gas ceramic tube diffuser system. The reaction was conducted at a constant temperature for an appropriate length of time to ensure complete conversion of titanium to titanium carbide. After completion of the reaction, the power was turned off and the melt was allowed to solidify. The processing times and temperature depend upon the gas partial pressure and alloy chemistry. Processing times and temperatures ranged from 2 minutes to 8 hours and 1150 to 1600°C, respectively, depending upon the matrix chemistry as well as the melt quantity and volume fraction desired.

The in-situ processed composites were sectioned and polished for microscopic examination. The composites were examined by means of XRD, optically using a Zeiss microscope and via scanning electron microscope in JEOL Model 35CF. In addition, selected Al-based composites with low volume fraction of reinforcement were electropolished in perchloric acid/methanol solution at -20°C for transmission electron microscopy studies.

#### ***A.3.2.2 Results of the Processing Envelope Study***

##### **a) Maximum Volume Fraction**

Experimental parameters and results of the experiments designed to determine the maximum volume fraction of reinforcement are summarized in Table 2-5. Figure 2-11 (a-c) illustrates the microstructures formed in experiments 1-3 with 7, 19 and 26 v/o of reinforcement, respectively. Experiment 4 did not reach complete carbon conversion. Two different types of carbides were found on the crucible sides: coarse, 10 - 15  $\mu m$  on the melt surface, and very fine and well dispersed carbides within the matrix (Figure 2-12 (a,b)).

### **b) Minimum TiC Size Study**

TEM studies of the samples obtained by melting of Al with low Ti content (up to 6 wt.%) at 1150°C and short bubbling times (up to 14 minutes) with subsequent rapid cooling revealed the presence of very fine carbon particles trapped in the aluminum and single crystal, submicron, carbides. Carbides appear as single crystals with a faceted morphology with a size of 100 to 800 nm, Figure 2-13(a-c). At higher volume fractions, growth and carbide agglomeration will occur.

### **c) Maximum TiC Size**

Figure 2-14 (a-c) shows the incremental change of volume fractions of reinforcement and carbide particles size with the reaction time. The volume fractions observed are 17.5, 35 and 40 volume percent for the reaction times of 2, 6 and 8 hours, respectively, at 1600°C. The sizes and size distribution of carbides formed after each of the experiments were determined by image analysis. The average and maximum sizes of TiC are plotted versus synthesis time in Figure 2-15. The maximum size of TiC, which was achieved after 8 hrs. of gas bubbling is 10 - 15  $\mu\text{m}$ . The particles growth is limited by coarsening.

### **A.3.2.3 Discussion of the Processing Envelope Study**

#### **a) Determination of the Maximum Feasible Volume Fraction**

The gradual increase in volume fraction of reinforcement leads to a significant increase in melt viscosity, which in turn affects the bubble size and motion. As was shown by Richard [27], the presence of very fine solid particles in the melt introduces very high friction due to the small interparticle spacing, <1  $\mu\text{m}$ . The viscosity of the liquid as a function of a volume fraction of solid particles with the size of less than 40 $\mu\text{m}$  can be calculated by the relation below:

$$\frac{\eta_s}{\eta} = \frac{1+0.5f}{(1-f)^4}$$

where  $\eta_s$  and  $\eta$  are the viscosities of the liquids with and without solid particles, respectively, and  $f$  is the volume fraction of solid particles in the liquid. This relation can be applied to the Al-TiC system at the processing temperatures, since the TiC particles formed are much less than 40  $\mu\text{m}$ . Simple calculations show, that 10 volume percent of TiC gives rise to the melt viscosity only 1.5 times<sup>†</sup>, but when volume fraction of reinforcement becomes 50 v/o melt viscosity increases 20 times. That complicates of the processes of bubble formation and rising and increases the bubble size. Relationships between the melt viscosity, the bubble size and the velocity of bubble rise will be given in the next Chapter. As the fraction of particles increases,

---

<sup>†</sup> The viscosity of liquid aluminum is 0.01 poise, the same is water. Mercury is 1.5 times more viscous than liquid aluminum. The car oil viscosity is 1 poise, which is 100 times higher than the liquid aluminum viscosity.

bubbling becomes more and more difficult, and at a high volume fraction (25 - 40 v/o), absolutely impossible, since bubbles get trapped in the bulk of the melt.

The experiments reveal, that the viscosity problem arises as volume fractions exceed 20v/o. For example, a significantly inhomogeneous carbide distribution throughout the melt was observed in the composites with the volume fractions of reinforcement higher than 20v/o (see Table 2-6). Surprisingly, the volume fraction of carbides at the top of the melt was higher than that at the bottom, although density of TiC is 1.8 times higher than the density of Al. An explanation is postulated that when the bubble emerges from the melt, the unreacted carbon falls on the melt surface. If the melt viscosity is low, mixing occurs due to the natural convection inside the crucible. At high volume fractions, the mixing efficiency of the liquid is very low, and the carbides become entrapped at the top of the melt and remain there.

As the volume fraction of reinforcement reaches 40 v/o, the viscosity limitations become critical. At this volume fraction, the bubble diameter becomes equal to the diameter of the crucible and a piston-like motion of the bubbles in the liquid results in the ejection of the melt from the crucible. This phenomena was revealed in experimental series #4 (Table 2-6). Carbides were found only on walls of the crucible. Figure 2-12(a,b) illustrate coarse and fine carbides, which were found on the surface and in the bulk, respectively. Such a difference in size and morphology of the titanium carbides can be explained by the difference in their formation mechanisms. Since carbon was depositing on the melt surface and mixing was absent, the carbon layer reacted with titanium and formed coarse carbides (Figure 2-12a) via interfacial chemical reaction. The rest of the carbon dissolved in aluminum and diffused away with subsequent precipitation of fine carbides (Figure 2-12b). The two different morphologies are similar to those found in the plate dissolution experiments. The details on the two mechanisms of TiC formation are provided in the following sections.

#### **b) Minimum TiC Size Study**

It was shown theoretically before and confirmed by the experiments that TiC particulates can be formed via two routes, namely: solution-precipitation and interfacial chemical reaction. In the case of solution-precipitation the size of TiC particulates does not depend on the carbon particle size and can be calculated by nucleation theory. The alternative process of TiC formation takes place at the solid carbon/liquid melt interface and causes a formation of TiC particulates proportional to the size of the initial carbon particle.

The simple calculations, shown below, demonstrate that the diameter of a TiC particle formed as a result of conversion of a carbon particle to carbide via interfacial chemical reaction is 1.3 times larger than the diameter of the initial carbon particle. Assuming the stoichiometry of



TiC one can conclude that 12 g of carbon is required to form 60 g of TiC (e.g. one mole). Thus, the TiC particulate formed after conversion of carbon particle to TiC is 5 times heavier than the initial carbon particle. Expressing the mass in terms of volume and density we obtain:

$$\frac{R_{\text{TiC}}^3 \rho_{\text{TiC}}}{R_{\text{C}}^3 \rho_{\text{C}}} = 5, \quad (5)$$

from a diameter, D, viewpoint

$$\frac{D_{\text{TiC}}}{D_{\text{C}}} = 1.3 \quad (6)$$

Therefore, according to this calculation, if the minimum size of carbon particles in the melt is of the order of 100 nm, then the minimum TiC particles formed by liquid-solid interfacial reaction route are 30% larger in size.

A size of TiC nucleus formed via solution-precipitation route is determined by a series of thermodynamic factors, such as TiC/melt surface tension, free energy change related to the nucleation process, temperature and melt composition. The classical nucleation theory for homogeneous nucleation gives the following expression for the equilibrium nucleus size:

$$r^* = \frac{2 \sigma_{\text{sl}}}{\Delta G_{\text{v}}}$$

where  $r^*$  is the critical nucleus size,  $\sigma_{\text{sl}}$  is the solid/liquid interfacial free energy, and  $\Delta G_{\text{v}}$  is the free energy change per unit volume related to the nucleation event. Unfortunately, it is very hard to make a reasonable estimation of the critical nucleus size for TiC forming in the Al-Ti solution, since there is no data on  $\Delta G_{\text{v}}$  currently available in the literature.

### c) Determination of the Maximum TiC Size

The alloy system under evaluation contained 60wt.%Ti with an anticipated volume fraction of 51v/o. After a 2 hr. reaction at 1600°C, the carbon supplied was sufficient for titanium to completely convert into TiC. Due to process parameters, the volume fraction observed was only 17.5 v/o (see Figure 2-14a). Additional 4 and 6 hrs. of bubbling led to a conversion of 40 v/o of the reinforcement.

The coarsening study results are shown in Figure 2-15. The average TiC size does not increase significantly with time and varies from 1.7 to 2.8  $\mu\text{m}$ . As coarsening time proceeds, three simultaneous processes are taking place: coarsening of the existing particles, nucleation of new particles and possible agglomeration of particles. Thus, even though the maximum size

increases significantly (from 5 to 15  $\mu\text{m}$  over 6 hrs.), the increase in the average particles size is very small, since fine particles are being continuously nucleated.

### **A.3.3 Mechanism Study**

Two alternative mechanisms of TiC formation in Al matrix were described in great detail in previous sections. Since the formation mechanism determines the size of TiC particles and consequently, mechanical properties of the composite, it is important to determine the mechanism of TiC formation. Thus, a series of model planar interfacial experiments, designed to study the reaction sequence and the process mechanism during carbide formation, was conducted.

#### **A.3.3.1 Experimental procedure**

Continuous plates of structural graphite were inserted for 2 hrs. into the Al-Ti melts containing 10 and 30 wt.%Ti, respectively. The reactive temperatures varied from 1300 to 1400°C. Alloys were heated to the desired temperature at a rate of about 20°C min<sup>-1</sup>. After 2 hrs. at the reaction temperature, the melt was allowed to solidify. The composites obtained were microstructurally characterized by means of XRD, optical and scanning electron microscopy.

#### **A.3.3.2 Results**

The micrographs of the interface at a 5 mm graphite plate dissolution in Al-10wt.%Ti and Al-30wt.% Ti are presented in Figures 2-16 and 2-17. Carbon dissolution in the liquid matrix resulted in the formation of 1-5  $\mu\text{m}$  TiC particles with relatively high volume fraction of reinforcement, e.g. >20 v/o at 5 mm from the interface. Titanium carbides were observed in the 2 cm thick layer along the plate. The TiC distribution through this layer parallels the diffusion profile of C in the melt with the decreasing volume fraction of carbon as the distance from the graphite plate increased. This observation is confirmed by the hardness measurements along the cross section of the sample, Figures 2-18 and 2-19.

The microstructure of the interfacial reaction layer for the alloys with low and high concentration of Ti are different. A 15  $\mu\text{m}$  thick  $\text{Al}_4\text{C}_3$  layer is formed along the graphite - matrix interface at 1350°C. The size and distribution of TiC particles along the  $\text{Al}_4\text{C}_3$  layer varies from Ti-lean to Ti-rich alloy with islands of 15  $\mu\text{m}$  TiC particles in Al-10wt.%Ti alloy (Figures 2-16), and coarser and evenly distributed TiC in Al-30wt.%Ti alloy, Figure 2-17. The XRD analysis confirms the presence of TiC and  $\text{Al}_4\text{C}_3$ , Figure 2-20. The results indicate an ability to establish in-situ reinforced gradient alloys with short time liquid reactions.

### A.3.3.3 Discussion

The behavior of a planar, solid graphite preform in the melt is anticipated to be different from nanolevel carbon particles in terms of morphology, degree of crystallinity and reactivity. A model graphite plate acts as a constant composition carbon source, while the Al-Ti melt serves as an "infinite sink". In this case, carbon dissolution is analogous to the diffusion in a semi-infinite rod, e.g. the saturation is never reached at the opposite end. Thus, carbon dissolves in the liquid matrix and precipitates out as TiC where the solubility limit is reached. With time, the carbon saturation front diffuses away from the carbon plate, resulting in TiC formation at distances proportional to the diffusion distance of carbon in the Al-Ti melt.

Since the reaction of TiC formation is assumed to be a second order chemical reaction, the reaction rate is proportional to the product of both Ti and C concentrations which is a function of reaction time and distance from the carbon plate. The schematic illustration of titanium and carbon concentration distribution in the melt is shown in Figure 2-21. The reaction rate should have a maximum at a certain point  $x_0$ , which also depends on time. The reaction rate maximum corresponds to the points where carbon and titanium concentrations are in a stoichiometric ratio. Reaction is taking place within a relatively narrow zone, corresponding to those regions where Ti and C concentration ratio is within the homogeneity range of TiC. If the chemical reaction rate is much higher than the rate of diffusion of titanium and carbon to the reaction zone, then the concentration profiles of these components will look like those shown in Figure 2-22. It can be seen that a region A, illustrated in Figure 2-22 contains only carbon in the solution, on the other hand, a region B is Ti rich and does not contain any carbon in the melt. The absence of titanium in the region A and carbon in the region B must be a result of the fast kinetics of TiC formation. All titanium and carbon supplied to the reaction zone is consumed there immediately and converted to TiC. The reaction front propagates through the melt in the direction away from the graphite plate. Since the initial concentration of Ti in the melt was constant throughout the volume the rate of reaction front propagation is determined mainly by the rate of carbon diffusion to the reaction zone and may be determined by the following expression:

$$v = \frac{dx}{dt} \sim \sqrt{\frac{D}{t}}$$

where  $v$  is the propagation rate of the reaction front,  $x$  is the diffusion distance,  $D$  is a diffusion coefficient of carbon in the melt and  $t$  is the processing time. The diffusion distance is a function of alloy composition and reaction temperature and time. The diffusion coefficient of carbon in

aluminum at 1300°C is estimated at  $\sim 3 \times 10^{-4} \text{ cm}^2/\text{sec}$ . For a reaction time of 2 hrs., the diffusion distance:

$$x = 2 \sqrt{Dt} \sim 18 \text{ mm} \quad (7)$$

and is consistent with the experimental results, with a presence of TiC particulates at  $\sim 20 \text{ mm}$  from the graphite plate. This observation clearly illustrates the solution - reprecipitation mechanism, however under certain conditions interfacial reaction product also is present.

Along with the solution - reprecipitation process, the chemical reaction of carbides formation on the solid carbon/ liquid melt interface is anticipated. The experiment did not reveal the continuous TiC film on the graphite surface, but it can be suggested that the process of interfacial TiC formation was taking place simultaneously with the solution - reprecipitation process in the early stages of the reaction. In the later stages, when a significant layer of TiC on carbon plate is built up, TiC particles fracture from the carbon preform due to the residual stresses at the carbon/carbide interface. Figure 2-23 illustrates the interfacial layer formed around the graphite plate, showing two types of titanium carbides - coarse and porous, formed as a result of interfacial reaction at the graphite plate and fine single crystal particles which are similar to those found in RGI processed samples, formed via solution-reprecipitation mechanism.

The presence of  $\text{Al}_4\text{C}_3$  directly at the graphite interface, which is clearly seen in Figure 2-24, can be explained as follows. The TiC forms via two processes simultaneously: solution-reprecipitation and interfacial reaction. Thus, by the time when the TiC film breaks away from the carbon interface the titanium concentration in the melt is negligible. The process sequence is illustrated in Figure 2-25. Since the Gibbs free energy change for  $\text{Al}_4\text{C}_3$  formation at 1300°-1400°C temperature range is still negative the reaction occurs. The thickness of  $\text{Al}_4\text{C}_3$  layer in the Al-30wt.%Ti is less than that in Al-10wt.%Ti, which confirms our initial assumption based upon thermodynamic model.

The processes, described above and illustrated in Figure 2-22, which are taking place around a graphite plate placed into an Al-Ti liquid solution are qualitatively similar to those occurring around a spherical nanolevel carbon particle with the only difference being the amount of carbon dissolving in the melt. A massive graphite plate dissolves slowly and can serve as a source of carbon for both: solution-reprecipitation and interfacial reaction, while a fine carbon particle dissolves before any interfacial reaction starts. The assumption of solution-reprecipitation mechanism for TiC formation processed via RGI technique is confirmed by the fact that the size and morphology of titanium carbides found in the bulk of the composite produced via reactive dissolution is identical to that of the RGI processed carbides.

### A.3.4 Kinetics of Conversion Study

During the RGI process, carbon and titanium convert into TiC and concentration of Ti in the melt decreases. To successfully and reproducibly control the process, it is important to determine the time of complete conversion of Ti to TiC. In the following chapter, a kinetic model, expressing the concentration of Ti in the melt as a function of time and predicting the exact moment of complete conversion based on the processing parameters will be developed. The experiments described below were designed to test or validate the model predictions and obtain the kinetic parameters of the conversion.

#### A.3.4.1. *Experimental procedure*

Five experiments with 150 g charges of Al-10wt.%Ti alloy were conducted at the reaction temperature of  $1300^{\circ}\text{C} \pm 10^{\circ}\text{C}$  and 0.1 SLPM methane flow rate, ( $\text{CH}_4$  to Ar flow rate ratio was held at 1:2). Reactions were interrupted by pulling the crucible out of the induction coils after 9, 21, 45, 70 and 140 min, respectively. It is important to note, that the time required to introduce the stoichiometric amount of carbon into the melt was 70 minutes at a given flow rate. The samples were sectioned and subjected to XRD, microstructural and chemical analysis. The amount of total and free carbon in each sample was measured at NSL Analytical Services, Inc., Cleveland, OH. The processing parameters and results of this series of experiments are summarized in the Table 2-7.

#### A.3.4.2. *Results*

The selected XRD patterns and micrographs of the initial Al-10wt.% Ti alloy, showing the presence of  $\text{Al}_3\text{Ti}$  and of the samples processed at 21, 70 and 140 min are presented in Figure 2-26(a, b). It can be clearly seen from the XRD pattern that the height of  $\text{Al}_3\text{Ti}$  peak gradually decreases and the height of TiC peak increases with the increasing processing time. The presence of  $\text{Al}_4\text{C}_3$  was not noticed, which suggests that the assumption that all the reacted carbon is a constituent of titanium carbide is valid. It was shown in thermodynamic analysis that  $\text{Al}_4\text{C}_3$  is unstable in presence of titanium at the processing temperature ( $1300^{\circ}\text{C}$ ), but it becomes stable at the temperatures below 1025 K ( $752^{\circ}\text{C}$ ). Rapid cooling of the samples, thus appear to prevent the formation of the aluminum carbide. Table 2-7 compares the theoretical and actual amount of carbon introduced into the melt over the various periods of time. The difference illustrates that the carbon supply to the melt is not 100% efficient and some carbon escapes from the system. The reason for this phenomena along with the detailed analysis and explanation will be proposed in Chapter III.

### A.3.5 Feasibility Study of Silicon Carbide Formation via RGI

Feasibility of processing of SiC/Al formation was also investigated by injecting 3:7 methane-argon gas mixture at 1250°C in two alloy systems: Al - 50wt.%Si and Al - 45.5wt.%Si - 3wt.%Mg - 6wt.%Zn modifications. No SiC was found in the Al-Si binary while SiC particles of 15 to 60 µm were found near the melt surface in the Mg-Zn modified silicon containing alloy. Silicon carbide particles micrograph and the XRD pattern of the sample are presented in Figure 2-27. Mg and Zn play an important role, possibly through a surface-active mechanism, in the kinetics of SiC formation. Mg and Zn appear to catalyze SiC formation and has also been implicated in DIMOX™ reaction systems with the formation of Al<sub>2</sub>O<sub>3</sub> [28].

### A.4. Summary

The goal of that research was to study the thermodynamics, kinetics and mechanism of the process of TiC formation in Al matrix via Reactive Gas Injection technique. Based on the analysis of the available literature, theoretical studies and results of the experiments conducted the following conclusions are made.

The study on relative TiC and Al<sub>4</sub>C<sub>3</sub> stability over the range of temperatures concludes that in liquid state, i.e. at any temperature above 1025 K (752°C), TiC is stable and Al<sub>4</sub>C<sub>3</sub> is not expected to form in excess of Ti in the Al-Ti-C system. However, since the free energy change for the reaction:  $4/3\text{Al} + \text{C} = 1/3\text{Al}_4\text{C}_3$  is negative at all the temperatures below 2000 °C, aluminum carbide will form in the presence of excess carbon. This is valid for liquid and solid aluminum. At temperatures below 1025 K, the reaction:  $3\text{TiC} + 13\text{Al} = \text{Al}_4\text{C}_3 + 3\text{TiAl}_3$  becomes thermodynamically feasible and titanium carbide converts to Al<sub>4</sub>C<sub>3</sub> and Al<sub>3</sub>Ti on isothermal heat treatment.

The processing envelope for conversion of C and Ti to TiC has been determined. Minimum TiC platelets size is limited by the nucleation process and corresponds to 0.1 µm in diameter. Maximum size of reinforcement is determined by coarsening kinetics of carbides and the particles vary in size from 10 to 20 µm. Maximum volume fraction of reinforcement is limited by the melt viscosity and does not exceed 40 volume percent. TiC particle size increased by 15 µm in 8 hours, which signifies that the process of TiC coarsening is quite slow.

The TiC formation mechanism follows the solution-precipitation route for fine soluble particles and interfacial reaction route for graphitic surfaces. The interfacial reaction of TiC formation at the solid carbon particle is 5 orders of magnitude slower than carbon dissolution process.

**Table 2-1: Summary of the Experiments Conducted**

Type of Experiment	# of Successful Experiments	Total # of Experiments
1. Methane Decomposition Study	12	19
2. Determination of the Synthesis Envelope		
Maximum $V_f$ of TiC	7	16
Minimum TiC Size	8	15
Maximum TiC Size	5	13
3. Mechanism Study	7	10
4. Kinetics of Conversion Study	9	11
5. SiC Formation Feasibility Study	4	5
Total # of Experiments	52	88

**Table 2-2: Efficiency of Methane Decomposition in the Flow Reactor**

Number	Decomposition Temperature, °C	Gas Flow Rate before Decomposition, SLPM	Gas Flow Rate after Decomposition, SLPM	Degree of Decomposition, %
1	900	0.5	0.6	60
	1075		0.84	84
	1100		0.87	87
	1200		0.94	94
2	900	0.3	0.46	78
	1075		0.55	92
	1100		0.55	92
	1200		0.57	95
3	900	0.1	0.18	90
	1075		0.19	95
	1100		0.19	95
	1200		0.19	95



**Table 2-3: Gas Decomposition and Carbon Synthesis**

Decomposition time	Temperature, °C	Carbon Size, $\mu\text{m}$	Carbon Morphology
<b>BeO substrate</b>			
1h 25 min	900	-	Gray amorphous film
1h 30 min	1075	3 - 5	Film is thicker, with particles partially embedded in it
1h 30 min	1200	3 - 5	The same film + amorphous carbon fibers with the layered fracture surface*
<b>Al<sub>2</sub>O<sub>3</sub> substrate</b>			
1h	1100	0.15 - 0.2	Spherical graphite particles*
2h 30 min	1100	0.2 - 0.7	Agglomerates of 2 to 20 graphite particles. Agglomeration size - 1 - 7 $\mu\text{m}$ .
4h 30 min	1075	1.2	Fine graphite powder ~ 100nm covers the surface of large graphite spheres. Spheres form chains 50 $\mu\text{m}$ long.*

**Table 2-4: Methane Decomposition Efficiency with the Correction Factor**

Number	Furnace Temperature, $T_{\text{fur}}, ^\circ\text{C}$	Gas Flow Rate before Decomposition, SLPM	Correction Factor, $f = \left( \frac{T^* - T_{\text{in}}}{T_{\text{fur}} - T_{\text{in}}} \right)^a$	Actual Gas Temperature, $T_{\text{gas}}, ^\circ\text{C}$
1	900	0.5	0.62	580
	1075			670
	1100			685
	1200			748
2	900	0.3	0.81	729
	1075			871
	1100			891
	1200			972
3	900	0.1	0.93	837
	1075			1000
	1100			1023
	1200			1080

- a.  $T^*$  - average gas temperature in the flow reactor  
 $T_{\text{in}}$  - initial gas temperature at the reactor entrance, room temperature  
 $T_{\text{fur}}$  - furnace temperature

**Table 2-5: Summary of Reactive Gas Injection Processing Limitations**

Process Parameter	Limitation	Function of
Maximum Volume Fraction of Reinforcement	Melt Viscosity	Temperature and Melt Chemistry
Minimum TiC Particle Radius	Nucleation	Nucleus Size ( $r_{\min} \geq r_{\text{nucl}}$ )
Maximum TiC Particle Radius	Coarsening, $r_{\text{av}}^3 = r_o^3 + kt$	TiC Formation Mechanism, Reaction Time, Temperature

**Table 2-6: Experimental Details on Al/TiC Composites Produces by Reactive Gas Injection**

#	Alloy Composition.	Expected Vf of TiC, v/o	Temp, °C	CH <sub>4</sub> flow rate, l/min	Fraction of Carbon*	Expected conversion, v/o of TiC	Conversion observed, v/o of TiC
1	Al-10wt.%Ti	7	1300	0.1	1	7	top ~ 8 bot. ~ 6
2	Al-27wt.%Ti	20	1500	0.1	0.8	16	top 22±3 bot. 14±3
3	Al-38wt.%Ti	31	1550	0.1	0.7	21.7	top 33±6 bot. 13±4
4	Al-60wt.%Ti	51	1600	0.5	1	51	~ 40

\* Fraction of Carbon = 
$$\frac{\text{vol. of CH}_4 \text{ injected}}{1.5 \times (\text{vol. of CH}_4 \text{ needed for complete conversion})}$$

**Table 2-7: Summary of Results on Conversion Kinetics of Ti and C to TiC**

Reaction Time, min	Theoretical Amount of C Introduced via RGI, wt. %;	Total Amount of Carbon Observed wt. %	Total Amount of Reacted Carbon, wt. %	Calculated <sup>a</sup> V <sub>f</sub> of TiC, v/o
9	0.32	0.28	0.224	0.61
21	0.75	0.72	0.692	1.91
45	1.57	1.42	1.389	3.84
70 <sup>b</sup>	2.44	1.96	1.922	5.32

<sup>a</sup> Calculated on the basis of chemical analysis data on the amount of reacted carbon, assuming that all the reacted carbon formed TiC and no Al<sub>4</sub>C<sub>3</sub> present.

<sup>b</sup> Time required to introduce the stoichiometric amount of carbon into the melt

## **B. *IN-SITU* PROCESSING OF Al/AlN COMPOSITES VIA REACTIVE GAS INJECTION.**

### **B.1. Processing Background**

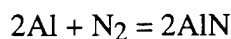
The in-situ nitridation process, under consideration, produces discontinuously-reinforced composites by forming ceramic particles directly in the molten metal. In the recent years, however, AlN-Al composite has received considerable attention. Not only can AlN enhance the modulus, strength, hardness, wear resistance and refractory nature of aluminum alloy matrix, but also AlN is much more wettable to aluminum vs. conventional Al<sub>2</sub>O<sub>3</sub>. From a stability viewpoint, the AlN reinforcement does not react or decompose in the presence of molten aluminum.

Even with the prominent advantages mentioned above, AlN-Al composite has not yet been widely commercialized, due to two challenging problems of AlN. Firstly, although crystallized AlN is very stable, AlN powders are relatively reactive. They hydrolyze in moisture to form hydrated alumina and ammonia[29]. Secondly, fine AlN powders are expensive, as a result, a cost effective particulate reinforcement is not envisioned. Thus, the production of AlN-Al composite, usually starting with ceramic powders, is very costly and less attractive. The in-situ process, if shown to be feasible in forming AlN-Al composite, will eliminate these economic and technical boundaries.

The object of the nitridation research was to determine the feasibility of forming of AlN in molten aluminum alloys by reactive gas injection methodology. The starting materials were aluminum alloys and nitrogen-bearing gases such as nitrogen and/or ammonia. Since nitrogen bearing gases are plentiful and relatively inexpensive, the processing of AlN-Al composite via AlN *in-situ* formation is considered desirable.

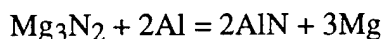
Two approaches for forming AlN reinforcement in molten aluminum, namely direct nitridation and indirect nitridation have been evaluated. Direct nitridation of aluminum consists of aluminum reacting with nitrogen-bearing gases directly to form precipitate AlN. It is a direct gas-liquid reaction that produces solid particles. Indirect nitridation involves Mg in the melt and consists of formation of an intermediate nitride, Mg<sub>3</sub>N<sub>2</sub>, followed by a substitution or replacement reaction to produce AlN.

The aluminum nitride forming reaction from nitrogen and molten aluminum, i.e.



is energetically favorable and is strongly exothermic. The theoretical adiabatic temperature is more than 6300°C for the stoichiometric nitridation reaction [30]. However, direct nitridation of molten aluminum is not practical, because of the following three factors. First, bubbling nitrogen-containing gases into molten aluminum results in solid shell of passivation that prevents good contact of reactants [7]. Second, the solubility of nitrogen in molten aluminum is very low [31], making the solution reaction kinetics negligible. Finally, the formation kinetics of aluminum nitride is very slow. Alternative approaches, such as using ammonia instead of nitrogen, does not resolve the problem, since recombination of nitrogen atoms is more rapid than the formation of aluminum nitride [7].

Therefore there is a strong incentive for investigating the feasibility of forming AlN using a solid nitrogen source. Since magnesium is a common alloy component of aluminum,  $Mg_3N_2$  is a potential nitriding agent. The feasibility of forming AlN from  $Mg_3N_2$  in molten aluminum by the following displacement reaction is the primary focus of the paper.



Magnesium nitride is highly reactive with air, and handling of its powder must be made in an oxygen-free environment. Magnesium nitride is also readily formed by reacting magnesium with nitrogen [32]. It has been reported that the addition of magnesium nitride into aluminum alloys increases the hardness of the latter [33] which is probably due to the substitution reaction.

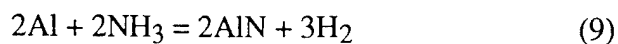
## B.2. Thermodynamic Analysis

### B.2.1. Direct Nitridation

Figure 2-28 shows the temperature dependence of enthalpy and Gibb's free energy changes for the nitridation reactions. Thermodynamically, the nitridation of aluminum is an exothermic process and is energetically very favorable over an extensive temperature range. At 700°C, for example, the enthalpy changes are (-330KJ/mole AlN) and (-274KJ/mole AlN) for nitrogen and ammonia respectively, whereas the free energy changes are (-215KJ/mole AlN) and (-218KJ/mole AlN). With aluminum as a starting material, AlN can be formed with aluminum in either solid or molten state.



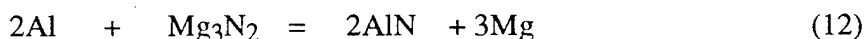
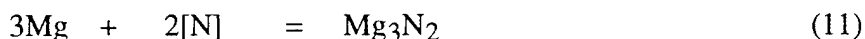
Ammonia can also be used as a reactive nitrogen-bearing source. It is more reactive than nitrogen, because it dissociates at high temperatures. The nitridation reaction with ammonia is given by:



### B.2.2. Indirect Nitridation

Apart from the direct nitridation of molten aluminum, the reaction pathway was studied theoretically and experimentally. Figure 2-29 shows the Gibb's free energy change vs. temperature for the reactions occurring in Al-Mg-N system based on a similar nitrogen content. From thermodynamic viewpoint, nitridation of either Al or Mg is very favorable and strongly exothermic. Also AlN has higher thermal stability than magnesium nitride over the entire temperature range. Kinetically, however, the formation of magnesium nitride is a much more favorable reaction than that of aluminum nitride, above 1100°C, in the vapor phase. In nitridation Experiments 2, 4, 5 and 6, conducted in the presence of 2.1 - 8.7 mole% Mg (see Table 2-8), Mg vaporized during the gas injection and melting. The greenish-yellow powder was found on the chamber wall which was later confirmed to be  $\text{Mg}_3\text{N}_2$ .

The thermodynamics and kinetics are favorable and conform the formation of  $\text{Mg}_3\text{N}_2$ . Since AlN is more stable than  $\text{Mg}_3\text{N}_2$  at high temperatures, molten aluminum reacts with  $\text{Mg}_3\text{N}_2$  to form the more stable ceramic phase AlN. The reaction steps are as follows:



Regardless of the loss of Mg by vaporization, AlN is formed during the cycling of magnesium. In the whole process, Mg serves as a recyclable catalytic nitrogen carrier. It is very important to introduce  $\text{Mg}_3\text{N}_2$  formed into molten aluminum alloy to ensure that Reaction (13) will proceed to form AlN.

## B.3. Experimental Procedure and Results

### B.3.1. Direct Nitridation

#### B.3.1.1 Experimental Procedure

The starting reagent materials were pure aluminum with Si, Mg or Mn as alloying elements. Commercially pure aluminum, magnesium, 50wt% Si-Al alloy, 75wt% Mn-Al alloy were ultrasonically cleaned in acetone before being placed in  $\text{Y}_2\text{O}_3$ -coated crystalline alumina crucible (99.9%, Coors). Two kinds of nitrogen-containing reactive gases were used in the experiments: nitrogen gas (Grade 5, Airco) and dehydrated ammonia (Airco). Argon (Grade 5,

Airco) was used as the carrier gas to dilute reactive gases. The overall material systems studied are shown in Figure 2-30. In this paper, emphasis is placed on the final composition of the mixture and the experimental processing conditions listed in Table 2-8.

The experiments were conducted in a vacuum induction furnace (Vacuum Industries Model 600) using graphite as a susceptor. The reactor is schematically illustrated in Figure 1-1 and was described in the previous sections. A vertically mounted sliding injected tube ( $\phi \approx 6\text{mm}$ ) was used to inject the reactive and inert gases into the molten alloy. The melt temperature was measured with a K-type thermocouple (e.g. Chromel and Alumel, Omega) embedded in an alumina tube which was immersed in the aluminum alloy melt. It was monitored and controlled via an IBM PC based control system.

The furnace was evacuated to 60 millitorr and backfilled with argon to 200 millitorr. This evacuating-backfilling process was repeated three to four times prior to filling the furnace with argon at atmospheric pressure. Before the gas injection, induction heating was initiated. When the temperature of the melt reached the desired value, the gas injection tube was lowered into the melt. Argon was injected into the melt first, to provide for mixing the molten alloy for several minutes. Then nitrogen-bearing gases, diluted with argon, were injected into the melt to initiate the nitridation reactions. The reactions were carried out for several hours, depending on melt size, volume fraction of AlN desired, and chemistry of bubbling gases. After a desired period of time of bubbling, the melt was furnace-cooled to room temperature in  $\text{N}_2\text{-Ar}$  atmosphere. The final ingot was sectioned and analyzed macroscopically and microscopically.

#### ***B.3.1.2. Experimental Results and Discussion***

The experimental conditions used are summarized in Table 2-8, and represents a selected group of injection experiments. There were many processing kinetic and thermodynamic aspects considered responsible for nitridation, such as, passivation effect, the wettability of AlN by molten aluminum, the solubility of nitrogen in molten aluminum or aluminum alloy, the reactivity of nitrogen-bearing gases and reaction kinetics, etc. The discussion will consider three aspects, namely, (i) passivation effect, (ii) solubility of nitrogen in molten aluminum and (iii) reactivity of nitrogen-bearing gases.

##### **(1) Passivation Effect**

The extent of passivation due to nitridation can be determined with the Pilling-Bedworth Ratio (PBR) which is the molar volume ratio of product to reactant. If PBR is greater than one, passivation effect exists[33]. For nitridation of molten aluminum, PBR is greater than one at a certain temperature range (e.g. about 1.14 at the melting point of aluminum), which means that a coherent skin of AlN will be formed, similar to oxidation of aluminum at room temperature.



Initially pure aluminum was used, with nitrogen or ammonia as a reactive gas, over a wide temperature range (from the melting temperature of aluminum to 1500°C). In Experiments 1 and 3, during bubbling, it was observed that a stable cavity around the gas injection tube was formed. When the tube was lifted out of the melt, the cavity did not collapse and a stable shell was visible even though the melt surrounding it was molten.

It is postulated that the cavity was caused by the passivation effect. That is, for a solid-gas or a liquid-gas reaction, the product takes more surface area than condensed reactant itself, so the product covers the interfacial area and prevents condensed reactant from further reacting. Thus, under these experimental conditions, AlN was formed as a coherent solid skin around the gas injection tube. This protective skin isolated the reactive gas from aluminum melt, making bulk nitridation impossible.

Further experimental refinements (Experiments 2 and 4 in Table 2-8) showed that the strength of the passivation shell can be reduced by adding Mg and Si to the melt. Mg and Si can reduce the surface tension of molten aluminum on the gas-liquid surface. Also Mg can be nitrided to form non-protective and porous  $Mg_3N_2$ . Since PBR of  $Mg_3N_2$  is less than one (about 0.77 at 900°C), the shell is porous, and does not maintain its integrity. The formation of  $Mg_3N_2$  and the reduction of surface tension is responsible for the reduction of aluminum passivation. Occasionally in the presence of Mg, passivation effect still existed in local regions in the form of porosity. However, even though passivation effect did not exist, AlN was only found on the entire ingot surface. No nitridation in the bulk was observed.

## **(2) Solubility of Nitrogen in Molten Aluminum**

One possible reason for lack of nitrides in the bulk was the low solubility of nitrogen in molten aluminum alloy. Nitrogen is practically insoluble in either liquid or solid aluminum. At the melting point of aluminum, the solubility of nitrogen in aluminum is  $0.66\text{cm}^3/100\text{g}$ , which is almost 3.7 times lower than that of hydrogen. It does not change significantly with temperature[34]. It was believed that longer contact times between nitrogen and aluminum would enhance the reaction. In order to accomplish this, nitrogen should be soluble in the melt. Since the solubility of nitrogen is very low, alloying elements of aluminum which enhance nitrogen solubility were considered. Mn was found to have favorable characteristics because (1) it is a compatible alloying element for aluminum; (2) pure Mn can dissolve about 0.4-0.5 at% or 0.1-0.13 wt% nitrogen at 1300-1400°C, which is significantly higher than in pure aluminum at the same temperature (about 7ppm). In the commercial aluminum alloy containing Mn at about 1.25 at%, the solubility of nitrogen is increased by a factor of about 7 at 1100°C.

Experiment 5 in Table 2-8 was conducted at a very high fraction of Mn (19wt%). The experimental results showed that the addition of Mn did not improve bulk nitridation

significantly. AlN was found again only on the ingot surface. It is therefore reasonable to conclude that the solubility of nitrogen in molten aluminum alloy was not a dominant factor in direct nitridation reaction. One possible reason hypothesized was that the dissolved nitrogen and the gaseous nitrogen in contact with aluminum melt was not reactive due to kinetic limitations which must be overcome by gas and/or matrix chemistry modification.

### **(3) Reactivity of Nitrogen-Bearing Gas**

Since ammonia decomposes at high temperature, as indicated in Figure 2-28, it was expected to be a good source of reactive nitrogen. In addition, the kinetics of nitridation with ammonia could be more favorable than via nitrogen because of lower activation energy for nitridation. Therefore, more AlN was expected to be formed using ammonia vs. using nitrogen for the same period of gas injection time. Experiments 1 and 3 were conducted with nitrogen as a reactive gas while Experiments 2 and 4 utilized ammonia. However, experimental results showed that comparing Experiments 1 and 3 with 2 and 4, there was no significant difference in using different reactive gases. AlN was again formed on the ingot surface, which was typical of all the unsuccessful bulk nitridation experiments. It is believed that the nitrogen atom competes more successfully with available nitrogen atoms rather than with aluminum atoms. Ammonia is dissociated into atoms and nitrogen atoms more rapidly combine before AlN formation. The typical microstructure of the area close to the surface of the ingot in Figure 2-31, shows that AlN-rich region is about 1mm thick. AlN formed is not a solid film on the ingot surface, but rather an interconnected AlN structure, which seems to have been disrupted by liquid agitation.

During Experiment 6, a mixture of 3vol%  $\text{NH}_3\text{-N}_2$  was used to inject into molten Mn-Mg-Si-Al alloy. The gas injection tube was blocked after bubbling for 10 minutes due to AlN formation. X-ray diffraction (XRD) analysis confirmed that the material inside the tube, as well as at the area around the end of the tube, contained very high fraction of AlN formed (>50vol%). AlN was formed and simultaneously grew out of the melt with the matrix alloy. The rate of outward nitridation inside the gas injection tube was much higher than that in the bulk nitridation.

In summary, direct bulk nitridation of molten aluminum alloy by bubbling nitrogen-containing reactive gases is not feasible. This results from the intrinsic kinetics of nitridation, which is unfavorable, even though the thermodynamics is favorable. Thus, our effort was redirected to find an alternate and a more rapid reaction pathway which is feasible both thermodynamically and kinetically. The basic idea was to form an intermediate, catalytic nitride (e.g. Mg, Si or Zn) which could donate its nitrogen to aluminum in molten state to form AlN. For this approach to be practical, it is required, that the kinetics of the first nitride formation, and the second substitution reaction, have to be favorable. Searches for the intermediate nitride were limited to common aluminum alloying elements, such as Mg, Si and Zn.

### B.3.2. Indirect Nitridation of Al

Two experimental approaches to form AlN were investigated. In the first method,  $\text{Mg}_3\text{N}_2$  was formed *in situ*, which subsequently reacted with molten Al to form AlN. In the second method,  $\text{Mg}_3\text{N}_2$  particles were added to molten Al.

#### B.3.2.1. Gas-liquid displacement reaction

##### Experimental Procedure

Based on the kinetic nitridation limitation detailed previously, a process modification had been conceived in the reactor configuration to facilitate a closed reactor system in Experiments 7a, 7b and 7c in Table 2-8, see Figure 2-32. In this modification, the thermocouple was located between the crucible and the susceptor, versus inside the crucible. The crucible was wrapped with insulating sheet (alumina fiber) and fastened with a refractory wire to the crucible. A gas port was placed through the insulating sheet for inserting the gas-injection tube. In addition, several semi-circular crystallized alumina plates were placed on top of the insulating sheet to reduce the magnesium and magnesium nitride loss. Nitrogen or a mixture of 3vol%  $\text{NH}_3\text{-N}_2$  was used as reactive gases (see Table 2-8, Experiments 7a, 7b and 7c).

##### Results and Discussion

With the addition of Mg and the experimental modification, AlN was synthesized in copious amounts and similar results were obtained in Experiments 7b and 7c, although the extent of AlN formed varied. These combined experiments demonstrated the feasibility of the indirect nitridation scheme. The final ingot consisted of two parts which were separated by a large gas void. The upper part (e.g. 2/3 of the ingot) contained high fraction of AlN, while the lower part (e.g. 1/3) did not contain any AlN. Figure 2-33 is XRD pattern for the polished cross-section area of the upper-part sample from Experiment 7a. It confirmed the generation of AlN in aluminum alloy. Based on the intensity ratio of the (100) line for AlN and (200) line for aluminum, the weight fraction of AlN was estimated[36] to be about 17%.

Figure 2-34 is the macrostructure of the upper portion of the Sample 7a. There was also a high level of porosity which are not shown in the micrograph. For use as a master alloy and in order to study the microstructure, Sample 7a was remelted and well mixed with an equivalent weight of pure aluminum. Figure 2-35 shows the microstructure of the cross-section area of the mixed and diluted sample. It suggests that agglomeration of AlN particles occurs during solidification. The average size of individual AlN particles was  $3\mu\text{m}$  with finer nitrides observed in the submicron range. Other indirect nitrided samples had similar microstructures. Comparing these three experiments, the following conclusion can be made: a higher fraction of AlN can be produced via indirect nitridation with higher Mg levels at longer bubbling times.

The details of the proposed process are schematically shown in Figure 2-36. Magnesium vaporizes and then reacts with nitrogen-containing gases to form  $Mg_3N_2$  particles. The initial particles of  $Mg_3N_2$  are believed to be very small (i.e. submicron) because they are formed in gas phase. When  $Mg_3N_2$  particles precipitate into the molten alloy, the substitution reaction (Reaction 13) occurs. In the liquid-solid interfacial reaction, the size of AlN particles formed is dependent on the size of the precursor  $Mg_3N_2$  particles. AlN particles are formed initially in submicron sizes, and later agglomerate based upon coarsening kinetics. As the  $Mg_3N_2$  particles migrate in the melt, the fraction of AlN formed is higher in the upper portion of the melt which increases the viscosity of the melt in this region. As a result, the melt traps more bubbles, decreasing its average density. With the aid of gas injected from the bottom, the melt separates into two parts. The upper portion of the melt has a higher fraction of AlN and a higher porosity, while the lower part has no AlN.

#### ***B.3.2.3 Solid-liquid displacement reaction***

The proposed nitridation reaction mechanism has been also elucidated by the following experiments. When there was bulk nitridation, there was always greenish-yellow powder on the ingot top surface, which is a characteristic color of magnesium nitride. Other experiments (e.g. Experiment 8a-c) was also conducted to demonstrate the substitution or displacement reaction, i.e. Reaction 13.

#### **Experimental Procedure**

In order to avoid exposure of magnesium nitride to air,  $Mg_3N_2$  powder (from Alfa AESAR, Ward Hill, MA, typical size from 0.1 mm to 10 mm) was encased into a machined capsule of pure aluminum under argon atmosphere with a pure aluminum cover seal (see Figure 2-37). Typical charge was ~60 grams of aluminum and ~7 grams  $Mg_3N_2$ . The capsule was placed in a crystalline  $Al_2O_3$  crucible. The vacuum induction furnace was purged with argon several times prior to melting. The heating was at a rate of ~20°C per minute. The crucible content was maintained at ~1000°C for a fixed period of time (0 to 1 hour), followed by bubbling of argon up to 3 hours in order to obtain an uniform composite sample. Experimental conditions investigated are summarized in Table 2-8. The goal of these experiments was to understand the factors that govern full conversion of  $Mg_3N_2$  to AlN and formation of an uniform composite.

#### **Results and Discussion**

The results of the experiments where  $Mg_3N_2$  particles were added to molten Al are summarized schematically in Figure 2-37. The solidified sample obtained in Experiment 8a (e.g., holding at 1100°C without gas injection), showed three distinct regions. The first region was pure aluminum, the second in the center was a hard material, and the third was unreacted  $Mg_3N_2$  powder. The X-Ray diffraction analysis (XRD) showed that the hard material consisted

of a mixture of AlN and Al. Microstructurally, a distinct interface between Al-AlN region and pure Al region is visible and is shown in Figure 2-38. The dark gray region is AlN-Al and the visible particles are AlN. AlN particles converted from  $Mg_3N_2$  maintain the geometry and size as that of the initial  $Mg_3N_2$  particles and is shown in Figure 2-39. In Figure 2-40, the indentation of the different phases indicate significant microhardness differences. The microhardness was about  $818 \text{ kg/mm}^2$  for the AlN particulate while it was about  $66 \text{ kg/mm}^2$  for the Al-Mg matrix, confirming the formation of AlN.

In Experiment 8b, the charge was maintained at  $1000^\circ\text{C}$  for 30 minutes, and was followed by a three hour period of argon-bubbling to mix the reinforcement and the matrix. Micrograph of the final sample is shown in Figure 2-41. The particles were identified as AlN. There were many unreacted  $Mg_3N_2$  particles at the bottom of the sample. Since density of  $Mg_3N_2$  ( $2.7 \text{ g/cm}^3$ ) is higher than that of molten Al ( $2.3 \text{ g/cm}^3$ ), these particles tended to reside in regions of low mixing and to settle at the bottom of the crucible.

In Experiment 8c, the experimental conditions were the same as those used in Experiment 8b, except that stirring was started right after the temperature of the melt had reached  $1000^\circ\text{C}$ . The experimental results were completely different from those of Experiments 8a and 8b. Magnesium nitride powder floated to the surface of the melt and was never mixed into the melt, even though the melt was agitated quite vigorously. The final sample consisted of two parts, namely, Al in the bottom, and black-yellow powder on the top. The latter is believed to be  $Mg_3N_2$  combined with vaporized Al from the melt and carbon from the susceptor.

The formation of AlN from magnesium nitride, is kinetically feasible as shown in the Figures 2-38 to 2-41. However, the manner of operation, e.g., holding and stirring time periods, is very important for the contact and reaction between  $Mg_3N_2$  and molten Al. For example, if the mixture is not held for a sufficient period of time prior to stirring, as in Experiment 8c, almost no AlN was formed. The  $Mg_3N_2$  particles are transported to the melt surface by the action of gas bubbles. Poor wetting of  $Mg_3N_2$  by molten aluminum prevents entrainment of  $Mg_3N_2$  into the melt. In addition, any aluminum nitride formed at the melt surface also prevents re-entrainment of  $Mg_3N_2$  particles in the melt because the nitride forms a coherent layer. We have previously shown[7] that AlN formed at the surface of a pure Al melt is quite tenacious and prevents further nitridation reaction from taking place.

In experiments which argon stirring was initiated after a prolonged holding period, e.g., Experiment 8b, significant amount of AlN was formed from  $Mg_3N_2$ , and the nitride particles were found as aggregates (Figure 2-41). It would appear that a shorter holding time might reduce aggregate formation and produce more finely dispersed AlN. The size of the initial AlN particles formed can be controlled by the  $Mg_3N_2$  particle size.

When no stirring was employed, a distinct vertical interface between  $Mg_3N_2$  region and Al region was visible (see Figure 2-37). The top cover of the encasement melted and infiltrated into the packed  $Mg_3N_2$ , forming AlN. However, penetration from the side of the encasement did not occur. It is believed that  $Al_2O_3$  layer prevented  $Mg_3N_2$  from contacting molten Al. In the region where Al penetrated, full conversion to AlN occurred. Wave length dispersion X-ray analysis (WDX) and XRD showed only trace Mg to be present in this reacted region (Figures 2-37 and 2-38), suggesting that Mg was removed due to vaporization.

From the foregoing discussion, it is clear that argon stirring is useful in mixing the charge only after the reaction is initiated but not completed. Early initiation of stirring can result in incomplete conversion of  $Mg_3N_2$ . It is also worth noting that a holding period of 30 minutes was adequate for complete conversion of  $Mg_3N_2$ . It is reasonable to expect that the reaction is particle size dependent. Since shorter holding time experiments were not conducted, the reaction may have been completed in less than 30 minutes. We are currently characterizing the kinetics of the reactions and the dependency of particle size on the reaction time.

## B.4 Summary

Aluminum nitride synthesis in molten aluminum alloy was achieved by two methods, namely, direct and indirect nitridation. Direct nitridation experiments produced AlN/Al-Mg-Si metal matrix composites via nitrogen-bearing gas injection, with the aid of Mg and Si at temperatures above  $1000^{\circ}C$ . Indirect nitridation included solid-liquid displacement reaction, and reactive gas injection method. The first was by mixing magnesium nitride with molten aluminum at  $1000^{\circ}C$ . The reaction between magnesium nitride and aluminum is a liquid-solid interfacial reaction. The second method of forming AlN via *in situ* generated  $Mg_3N_2$  was also successful. This approach has the promise of synthesizing micron and submicron sized AlN. Volumetric concentrations of AlN as high as 15% are obtained. Enhanced mechanical and wear properties of aluminum alloy can be achieved with this cost effective liquid-gas phase synthesis route.

**Table 2-8. Selective List of Nitridation Experiments**

Exp.	Purpose	Al-Alloying Element(mole%)			Melt Temperature (°C)	Time (hr)	Reactive Gases		
		Mn	Mg	Si			N <sub>2</sub>	NH <sub>3</sub>	Ar
1	Al+N <sub>2</sub>				1135	1.0	X		
2	Al(Mg+Si)+N <sub>2</sub>		8.7	0.55	1175	3.0	X		
3	Al+NH <sub>3</sub>				950	3.5		X	
4	Al(Mg+Si)+NH <sub>3</sub>		6.1	0.52	920	4.0		X	
5	Al(Mg-Si-Mn)+N <sub>2</sub>	19	2.1	2.10	1000	2.5	X		
6	NH <sub>3</sub> -N <sub>2</sub> mixture	.84	5.0	0.51	1430	10/60		X	
7a	Al[Mg+Si]+mix		15.5	2.40	1130	7.0	X	X	
7b	Al[Mg+Si]+N <sub>2</sub>		7.8	2.40	1100	1	X		
7c	Al[Mg+Si]+N <sub>2</sub>		3.9	2.40	1100	4	X		
8a	Mg <sub>3</sub> N <sub>2</sub> +Al				1100	1.0+0*			
8b	Mg <sub>3</sub> N <sub>2</sub> +Al				1000	0.5+3*			X
8c	Mg <sub>3</sub> N <sub>2</sub> +Al				1000	0+1.0*			X

\*The first number is the time of melt holding prior to bubbling; the second number is the bubbling time.

## C. IN SITU PROCESSING OF TiC/Al, TiB<sub>2</sub>/Al AND (TiC+TiB<sub>2</sub>)/Al COMPOSITES VIA SELF-PROPAGATING SYNTHESIS

### C.1. Processing Background

SHS is an innovative processing technique which allows to produce a wide range of refractory compounds from powder mixtures utilizing the heat released during the exothermic reactions of their formation [14,37-39]. The ignition of a lightly compacted powder blend initiates a combustion wave that propagates through the blend leaving behind the reaction products. The technique is extremely attractive, its main advantages being the self generation of energy required for the process and the high productivity due to very high reaction rates. Originally employed for the production of single phase ceramic compounds, SHS can be a feasible way for the *in situ* fabrication of composites, since both techniques utilize exothermic chemical reactions. The advantages of this processing route include sub-micron reinforcement size, nascent interfaces, economical processing, thermodynamic stability coupled with rapid reaction kinetics, and the ability to produce high volume fractions of ceramic reinforcements. Despite their intrinsic advantages, SHS-produced powders or porous bodies must be further processed to form dense materials. For SHS-processed MMCs, high pressure consolidation at the room or slightly elevated temperatures (*e.g.* cold sintering) [40,41] may become a feasible consolidation technique. In cold sintering, full density net shape parts are obtained utilizing plastic deformation of powders under high pressure. By this technique, compositions with up to 80 vol.% of hard particles can be consolidated to full density [42,43].

Reports on *in situ* SHS processing of metal and intermetallic matrix composites (MMCs and IMCs) are scarce [44-48]. In all these works, except [44], composites with very low fractions of a matrix material (*i.e.* high fractions of reinforcing phases) were synthesized. In [44], NiAl and FeAl matrix composites with 10-20 vol.% TiC, TiB<sub>2</sub>, TiN and AlN particles were successfully fabricated employing *in situ* SHS synthesis. In principle, SHS processing should be much more problematic for MMCs than it is for IMCs: for IMCs, both the reaction of the reinforcement and of the matrix formation are exothermic, whereas for MMCs the "inert" matrix acts as a diluent that may cause the damping of the combustion wave. Therefore, only ceramic reinforcements with high heats of formation are suitable for SHS processing of MMCs. Another basic requirement is the high fraction of a ceramic reinforcement (*i.e.* low fraction of a metal matrix). This ensures that the reaction will not be extinguished due to excessive dilution by the matrix material. For Al base MMCs, TiC and TiB<sub>2</sub> seem to be feasible reinforcements, both from the point of view of the exothermicity of the reactions of their formation, and from the point of view of their stability in Al. In [48], TiC/Al composites were produced from a blend of Al and Ti



powders and carbon fibers employing SHS and subsequent consolidation with HIP. It was reported that, at room temperature, the self-propagating reaction front could not be sustained when more than 0.1 mole ratio of Al was added to the TiC mixture. Even with preheating of the starting mixture up to the melting point of Al, the authors did not succeed in fabricating composites with more than 0.3 mole ratio of the matrix phase (Al). The TiC/Al composite material obtained had a rather poor density (92%), even after the HIPing operation. In the present work, *in situ* SHS processing coupled with high pressure consolidation was successfully employed for the fabrication of dense Al base MMCs reinforced by ~30 vol.% of TiC, TiB<sub>2</sub> or (TiC+TiB<sub>2</sub>) particles.

## C.2. Experimental Procedure

### C.2.1. Self-propagating synthesis

SHS processing of the Al matrix composites was performed by Exotherm Corporation, Camden, NJ. High purity (99.9%) titanium (< 44  $\mu\text{m}$ ), aluminum (< 44  $\mu\text{m}$ ) and boron (1-5  $\mu\text{m}$ ) from Atlantic Metals, carbon black (< 0.2  $\mu\text{m}$ , agglomerated) and boron carbide, B<sub>4</sub>C (1-7  $\mu\text{m}$ ) powders were used. Powder blends of four different compositions: Al-34 w/o Ti-8.5 w/o C (1:1, Ti:C), Al-28.5 w/o Ti-12.9 w/o B, (1:2, Ti:B) Al-30.6 w/o Ti-11.8 w/o B<sub>4</sub>C (1:1, Ti:C; 1:2, Ti:B) and Al-30.6 w/o Ti-2.6 w/o C-9.2 w/o B (1:1, Ti:C; 1:2, Ti:B), were prepared by ball milling. Very small amounts (< 1%) of halogenide-based gas transport agents were added to the starting powder mixture for the activation of the combustion process. Cylindrical compacts (32 mm diameter  $\times$  100 mm height) with ~ 36-38% theoretical density were placed into a reactor with thermally insulated walls, Figure 2-42. On top of each compact, 15 g of an igniting Ti-C mixture (1:1 mole ratio) were placed. The mixture was ignited by passing electric current through a tungsten wire. All SHS experiments were performed in argon at an atmospheric pressure.

The temperature in the reaction zone was measured by two W-Re thermocouples placed at a distance apart, the upper thermocouple placed at a distance 40 mm from the igniting mixture, Figure 2-42. Time of the wave front propagation between the two thermocouples was measured and the combustion wave velocity was calculated. After the combustion, cylindrical samples with 30-40% porosity were obtained.

The measured, calculated and estimated combustion parameters of different powder mixtures (starting composition, final composition based on thermodynamic equilibrium, adiabatic temperature,  $T_{\text{ad}}$ , combustion temperature,  $T_{\text{exp}}$ , combustion wave velocity,  $u$ , and cooling time from  $T_{\text{exp}}$  to the freezing (melting) temperature of Al,  $t_{\text{cool}}$ ) are listed in Table 2-9.

### C.2.2. Consolidation, mechanical testing and microstructure characterization

For consolidation, two types of specimens were prepared:

- square specimens with cross-sections close to that of the high pressure cell ( $\sim 18 \times 18 \times 3$  mm) were cut from as-received porous material;
- as-received material was milled into powder ( $\sim 100$   $\mu\text{m}$ ) that was subsequently compacted into  $\sim 70\%$  dense green compacts.

Both types of specimens were treated in vacuum ( $\sim 10^{-5}$  Torr) at  $300^\circ\text{C}$  for 1 h in order to remove the hydrate layer from Al surface, and high pressure consolidated (cold sintered) at  $P = 3$  GPa at the room or slightly elevated ( $\leq 300^\circ\text{C}$ ) temperature. (It was previously reported that rapidly solidified Al alloy powders containing  $\sim 30$  vol.% of fine intermetallic precipitates can be consolidated to the full density by high pressure consolidation [49].) As a result of cold sintering, practically 100% density was achieved.

Microhardness of the as-received and cold sintered materials was measured using Vickers diamond pyramid under the load of 200 g. For the cold sintered materials, yield stress in compression,  $\sigma_y$ , and transverse rupture strength (in three point bending),  $\sigma_{\text{TRS}}$ , were measured. Specimens for mechanical testing ( $\sim 3 \times 3 \times 10$  mm for compression and  $3 \times 4.5 \times 18$  mm for bending) were polished and annealed ( $500^\circ\text{C}$ , 1 h) prior to testing in order to minimize the possible strain hardening effects caused by high pressure consolidation.

The phase composition of the SHS materials was studied employing x-ray diffraction (XRD). The materials microstructure (polished samples, fracture surfaces) was investigated by optical microscopy, scanning electron microscopy (SEM) in a secondary electron and backscattered electron modes, and transmission electron microscopy (TEM).

## C.3. Results and Discussion

### C.3.1. Combustion Synthesis

For all the four compositions investigated, very low combustion velocities (at least one order of magnitude lower than those of pure TiC or TiB<sub>2</sub>) were observed, Table 2-9. The propagation of the combustion wave was unstable, indicating that the rate of heat dissipation into the "inert" Al matrix was approaching the rate of heat generation. The nonsteady-state oscillatory motion of the wave during combustion resulted in a typical layered structure of the reaction products. The heat required to maintain the propagation front of these reactions with the formation of 30 vol.% of TiC and/or TiB<sub>2</sub>, appears to be close to the lower limit required for the self-sustaining synthesis process.

### C.3.2. Microstructure Evaluation

XRD spectra of the as-received after SHS material for all four starting mixtures are presented in Figures. 2-43a, 2-44 and 2-45. It can be seen that the phase compositions of the synthesized MMCs closely fit the predictions based on the thermodynamic equilibrium, *i.e.* the materials contain high fractions of TiC, TiB<sub>2</sub> and (TiC+TiB<sub>2</sub>), respectively. Representative micrographs demonstrating TiC and TiB<sub>2</sub> ceramic particles in the synthesized Al matrix composites are shown in Figures 2-46 - 2-48. However, in all the systems except Al-Ti-C, strong additional peaks of Al<sub>3</sub>Ti are observed, indicating that full conversion of Ti into TiC or TiC/TiB<sub>2</sub> has not been achieved. A representative micrograph of Al<sub>3</sub>Ti needles in Al-Ti-C-B system is shown in Figure 2-49. It is assumed that, for all the compositions investigated, the combustion reactions are preceded by the melting of Al, followed by the capillary spreading of the molten Al along the solid Ti and carbon or boron or B<sub>4</sub>C powder particles. This ensures intimate contact between Al and Ti, while there are only occasional points of contact between Ti and carbon or boron or B<sub>4</sub>C. Upon heating, Al<sub>3</sub>Ti is the first phase to be formed by a direct reaction between Ti particles and molten Al. The Al<sub>3</sub>Ti formed is solid and it remains solid throughout the combustion process ( $T_m$  of Al<sub>3</sub>Ti (1340°C) is higher than  $T_{exp}$ , see Table 2-9). According to the thermodynamic equilibrium, Al<sub>3</sub>Ti should further react with carbon or boron forming the more thermodynamically stable TiC or TiB<sub>2</sub>. The appreciable amounts of Al<sub>3</sub>Ti phase in the final products (for Al-Ti-B, Al-Ti-B-C and Al-Ti-B<sub>4</sub>C starting mixtures) show that, under the conditions of a propagating combustion wave, the dwell time of the material in the combustion zone is not long enough to achieve the equilibrium compositions. An interesting observation is that the relative intensities of the Al<sub>3</sub>Ti x-ray peaks do not match the standard intensities and differ from spectrum to spectrum. A possible explanation, suggested by the layered structure of the SHS reaction products, is that the Al<sub>3</sub>Ti needles have a certain preferred orientation with respect to the direction of the combustion wave propagation. Since Ti is partly converted to Al<sub>3</sub>Ti instead of the expected TiC or TiB<sub>2</sub>, some of the carbon, boron or B<sub>4</sub>C should either remain unreacted or form carbides/borides other than TiC/TiB<sub>2</sub>. However, no peaks of Al carbide, Al borides or B-rich Ti borides were detected in the x-ray spectra of the as-received TiB<sub>2</sub>/Al and TiB<sub>2</sub>-TiC/Al materials. The unreacted amorphous carbon or boron, if present, will not give detectable peaks in x-ray diffraction spectra; x-rays are also insensitive to small amounts of B<sub>4</sub>C.

The x-ray spectrum of the material as-received after SHS of Al-Ti-C starting mixture, Figure 2-43a, shows that, for this composition, there is practically no Al<sub>3</sub>Ti phase in the final product. However, the micrographs in Figure 2-50a,b reveal the presence of some needle-like formations resembling Al<sub>3</sub>Ti. There is no contrast difference between these needles and the matrix in the backscattered electron image, suggesting that their composition is similar to that of the matrix. According to the WDX map, Figure 2-50c, the needles, as well as the matrix, contain

both Ti and Al, whereas the darker phase surrounding the needles contains only Al. Since the only two phases detected in the polished Al-Ti-C sample are Al and TiC, Figure 2-43b, the dark phase must be pure Al, and the brighter phase (both the needles and the matrix) - a very fine mixture of Al and TiC. In our opinion, the needles in the final microstructure indicate that a transient  $\text{Al}_3\text{Ti}$  phase was present in the course of the SHS processing. It is possible that, similarly to the previous compositions, the SHS process in the Al-Ti-C starts with the formation of  $\text{Al}_3\text{Ti}$ . These  $\text{Al}_3\text{Ti}$  needles further react with carbon to form  $\text{Ti}_2\text{AlC}$  ternary carbide (H phase) finally decomposing into fine-scale precipitates of TiC (*e.g.*  $\text{Ti}_2\text{AlC} + \text{C} = \text{Al} + 2\text{TiC}$ ). Thus, no  $\text{Al}_3\text{Ti}$  phase is present in the final product. Such a reaction path would be in agreement with the ternary Al-Ti-C system phase equilibria [50]. A similar sequence of events leading to the formation of TiC reinforcements in aluminum was suggested in [6, 51]. This mechanism, however, accounts only for the formation of a relatively small amount of secondary TiC.

It is assumed that solid state reactions at the Ti/carbon or Ti/boron powder particle interfaces, as well as surface reactions between carbon or boron particles and Ti dissolved in the molten Al are important mechanisms of the ceramic reinforcements formation during the SHS processing. These reactions should yield relatively coarse TiC and  $\text{TiB}_2$  particles, comparable in size to the starting powder particles. Indeed, 1-2  $\mu\text{m}$  size TiC and  $\text{TiB}_2$  dispersion can be clearly seen in SEM micrographs in Figures 2-46a, 2-47 and 2-48. However, the micrograph in Figure 2-46b reveals the existence of the whole population of considerably finer-scale ( $\sim 0.1 \mu\text{m}$ ) TiC particles. Very fine TiC and  $\text{TiB}_2$  particles can also be seen on the fracture surfaces of TiC/Al and  $\text{TiB}_2/\text{Al}$  composites, Figure 2-51. TEM micrograph in Figure 2-52 bears evidence to the very fine microstructure of the TiC/Al material obtained: grains as fine as 30 nm are clearly seen, though it is difficult to distinguish between different phases due to the high volume fraction of fine TiC dispersions. Their size, shape and homogeneous distribution suggest that these TiC particles were not formed by an interfacial reaction, but rather by precipitation from the solution. Though very fine  $\text{TiB}_2$  particles are not seen as clearly as TiC particles, their existence will be further confirmed by the high mechanical properties of the Al- $\text{TiB}_2$  composite. As a matter of fact,  $\text{TiB}_2$  particles are more likely to be formed by the solution-reprecipitation mechanism, than TiC particles. Since the concentration of boron and Ti in molten Al at 1260°C ( $T_{\text{exp}}$  for Al- $\text{TiB}_2$  composite processing) can be as high as  $\sim 1.7$  and  $\sim 17$  w/o, respectively [52], the reaction between dissolved Ti and B atoms with precipitation of solid  $\text{TiB}_2$  ( $T_{\text{m}}$  of  $\text{TiB}_2$  (2790°C)  $\gg T_{\text{exp}}$ ) is highly probable. At the same time, the solubility of carbon in liquid Al at 1100°C ( $T_{\text{exp}}$  for TiC/Al composite processing) is very limited (800 ppm as extrapolated from [53], or even 45 ppm [54]), making precipitation of TiC from the melt much less likely. Clearly, the mechanism of formation of the nano-scale TiC particles during the SHS processing of Al matrix composites requires further investigation.

In the case of Al-Ti-C system, relatively large ( $< 0.5$  mm) "islands" of unreacted carbon black are visually observed in the specimens after the SHS treatment. The presence of unreacted carbon implies that the ball milling operation was not effective in disintegrating and distributing the agglomerates of the otherwise fine starting carbon black powder. Under the conditions of the rapidly propagating combustion wave, there is not enough time for the relatively coarse carbon agglomerates neither to dissolve nor to be fully consumed by interfacial reaction with the surrounding metal. Since the ratio of C to Ti in the starting mixture was 1:1 (by moles), some unreacted Ti is expected to be found in the final material. However, no peaks of Ti metal are detected in the x-ray spectrum, Figure 2-42. It is possible that in this case TiC is slightly hyperstoichiometric (TiC has an extremely wide range of homogeneity). It is evident from the x-ray spectrum that the amount of  $\text{Al}_4\text{C}_3$  in the as-received after SHS TiC/Al material is well above the expected 0.15 w/o. This aluminum carbide may have been formed either by a direct reaction between carbon and the molten Al, or by the reaction of TiC with the Al melt during cooling down after the combustion. Indeed,  $\text{Al}_4\text{C}_3$  was reported to be formed on TiC in Al-Ti liquids containing carbon at temperatures below 1273 K [55]. It was assumed that  $\text{Al}_4\text{C}_3$  is formed by the following reaction:  $3\text{TiC} + 13\text{Al}_{\text{liq}} = \text{Al}_4\text{C}_3 + 3\text{Al}_3\text{Ti}$  [26]. In our case, the cooling time from the combustion temperature (1373 K) to  $T_m$  of Al is relatively long (45 min.) and may be sufficient for an appreciable amount of  $\text{Al}_4\text{C}_3$  to be formed. If the formation of  $\text{Al}_4\text{C}_3$  at temperatures below 1273 K is of the equilibrium origin, as it is claimed in [26], one can not expect to fabricate, by SHS processing,  $\text{Al}_4\text{C}_3$ -free Al/TiC composites due to the conversion of TiC to  $\text{Al}_4\text{C}_3$ . It should be mentioned that determining the exact location of the  $\text{Al}_4\text{C}_3$  phase by studying the SHS-processed TiC/Al composite in optical microscope or in SEM could be helpful in establishing whether  $\text{Al}_4\text{C}_3$  is formed by the direct reaction between Al and carbon, or at the TiC/Al interface during cooling. Unfortunately enough,  $\text{Al}_4\text{C}_3$ , being a hygroscopic compound, was completely dissolved in water used during the preparation of the metallographic samples. (The x-ray spectrum of the polished samples contains no peaks of  $\text{Al}_4\text{C}_3$ , Figure 2-43b).

### C.3.3. Mechanical Properties

The results of the mechanical testing of the cold sintered SHS processed Al matrix composites are encouraging. (No difference in the mechanical properties was observed for samples consolidated from pulverized or directly from as-received after SHS materials.) In the bending test, relatively high values of  $\sigma_{\text{TRS}}$  - 550 and 740 MPa for TiC/Al and  $\text{TiB}_2/\text{Al}$  composites, respectively, were obtained. The results of the compression test at different temperatures for the cold sintered TiC/Al and  $\text{TiB}_2/\text{Al}$  materials are presented in Figure 2-53. High values of the yield stress,  $\sigma_y$ , have been obtained for both compositions ( $\sigma_y = 430$  and 560 MPa at room temperature for TiC/Al and  $\text{TiB}_2/\text{Al}$  composites, respectively). For the  $\text{TiB}_2/\text{Al}$

composite, the dependence of  $\sigma_y$  on temperature is similar to the tensile strength behavior of materials fabricated from rapidly solidified aluminum alloy powders with the similar volume fraction ( $\sim 30\%$ ) of intermetallic phases [56]. Correspondingly high microhardness numbers were achieved: VHN =  $225 \pm 5$  for TiC/Al and VHN =  $245 \pm 5$  for TiB<sub>2</sub>/Al composite.

A wide range of controversial viewpoints is currently available on the strengthening of metal matrix composites. Different workers have proposed that the mechanical behavior of MMCs can be understood either on the basis of continuum mechanics models (e.g. shear lag, Eshelby and numerical models [57, 58]), or, alternatively, by considering modifications to the initial dislocation microstructure and including the effects of processing induced residual stresses (e.g. incompatibility dislocation approach [59]). The continuum mechanics models are valid for MMCs reinforced by relatively large (at least several micron size) particles [58], and predict only a very modest increase in  $\sigma_y$  with increasing volume fraction of reinforcement. It is apparent that these models cannot explain the high values of yield strength in the present work, and, therefore, dislocation related models should be addressed. The incompatibility/dislocation approach leads, for fine particles and spacing, to an Orowan-type relation of stress to both particles size and spacing [59]. For the  $\sim 0.1\ \mu\text{m}$  size particles with the interparticle spacing of the same order of magnitude, Figure 2-46b, Orowan-type strengthening of Al will be  $\Delta\sigma_y = 150\ \text{MPa}$  [42]. However, for the larger particle size and spacing ( $1\text{--}2\ \mu\text{m}$ ), Figures 2-46a, 2-47 and 2-48, the single dislocation, Orowan-type hardening will be completely negligible. Nevertheless, these particles may contribute to the overall strengthening by another dislocation related mechanism, namely the formation of dislocation tangles around particles resulting in a dislocation cell structure [59]. Similarly to Orowan-type hardening, the flow stress in this case is inversely proportional to interparticle spacing. Unfortunately, since no reference as to the value of the proportionality constant was given by the authors, no estimations of the relative importance of this mechanism could be done in the present work. In addition, considering the fine microstructure of the composites obtained, Figure 2-52, grain boundary strengthening may also be operative in these systems. We assume, therefore, that superposition of the above dislocation related strengthening mechanisms accounts for the high values of the yield stress of the SHS-processed *in situ* TiC/Al and TiB<sub>2</sub>/Al composites. It should be mentioned that the fine microstructure obtained in these composites seems to be very stable: no decrease in the room temperature yield stress of TiC/Al and TiB<sub>2</sub>/Al specimens was observed after annealing at  $500^\circ\text{C}$  for 10 h. (Compare to rapidly solidified Al base alloys, where coarsening of the fine intermetallic phases accompanied by the corresponding decrease in  $\sigma_y$  and  $\sigma_{\text{UTS}}$  is observed already at  $350^\circ\text{C}$  [60]). The presence of the coarser  $1\text{--}2\ \mu\text{m}$  size hard TiC or TiB<sub>2</sub> particles should also result in a higher wear resistance. Preliminary pin-off on-disc wear resistant tests have demonstrated a

much better performance of the SHS processed Al base composites compared to rapidly solidified Al base alloys having otherwise similar room temperature mechanical properties [61].

It should be mentioned that, in spite of the high volume fractions of ceramic particles, the SHS processed TiC/Al and TiB<sub>2</sub>/Al composites exhibited pronounced ductility in compression: plastic strains,  $\epsilon_p$ , of 10-15 % (at room temperature) up to > 25 % (at the elevated temperatures) were measured for both compositions. (Usually, the room temperature plasticity in compression of Al matrix composites reinforced with 20-30 vol.% hard particles does not exceed ~4 % [59, 62].) In three point bending tests, too, a certain plastic deformation of the above materials was registered prior to the failure. The high levels of elevated temperature ductility observed in the SHS synthesized Al matrix composites provide the possibility for more conventional (compared to cold sintering) densification routes, *e.g.* hot extrusion or forging. Thus, during high pressure consolidation at 300°C, small amounts of TiC/Al and TiB<sub>2</sub>/Al materials were extruded in a gap between the die wall and the punch, forming dense foils ~0.1 mm thick and ~5-6 mm long, indicating reasonable levels of composite ductility.

#### C.4. Summary

In the present research, Al matrix *in situ* composites with 30 vol.% of hard ceramic particles (TiC and/or TiB<sub>2</sub>) were successfully fabricated via SHS technique. Employing SHS processing route, very fine-scale ceramic reinforcements ranging from tens of nanometers up to 1-2  $\mu\text{m}$ , were obtained in the Al matrix. The mechanism of formation of the nanometer-scale TiC and TiB<sub>2</sub> precipitates remains to be elucidated but may be postulated to involve solution and reprecipitation.

It was shown that, by employing high pressure consolidation at temperatures not exceeding 300°C, full density can be achieved in the porous SHS-processed Al matrix composites containing 30% of TiC and/or TiB<sub>2</sub> particles.

High room and elevated temperature mechanical properties (yield stress, microhardness) were obtained in the high pressure consolidated SHS-processed composites, comparable to the best rapidly solidified Al base alloys with the same volume fraction (~30%) of the second phase. SHS-processed Al matrix MMCs exhibit wear resistance superior to the rapidly solidified Al base alloys with the similar room temperature mechanical properties, apparently due to the presence in the former of the dispersion of micron-scale hard ceramic particles. Alongside with the high yield strength, appreciable room and elevated temperature ductility was observed in the SHS-processed Al base composites.

Al matrix *in situ* composites, with their low SHS combustion velocities (due to the strong heat dissipation in the "inert" metal matrix), as well as MMCs on the whole, may be an ideal choice for the utilizing of the continuous manufacturing process approach.

**Table 2-9. Combustion Parameters of the Powder Mixtures Used**

Starting powder mixture (w/o)	Equilibrium combustion products (w/o)	Volume fraction of ceramic particles	Adiabatic temperature $T_{ad}$ (°C)	Combustion temperature $T_{exp}$ (°C)	Combustion velocity $u$ ( $10^{-3}$ m/s)	$t_{cool}$ (min.)
Al - 57.5 Ti - 34.0 C - 8.5	Al - 57.4 TiC - 42.45 Al <sub>4</sub> C <sub>3</sub> - 0.15	0.29	1128	1100	0.9	45
Al - 58.6 Ti - 28.5 B - 12.9	Al - 58.6 TiB <sub>2</sub> - 41.4	0.30	1327	1260	1.9	54
Al - 57.6 Ti - 30.6 B <sub>4</sub> C - 11.8	Al - 57.6 TiB <sub>2</sub> - 29.6 TiC - 12.8	TiB <sub>2</sub> - 0.22 TiC - 0.09	1176	1155	0.8	42
Al - 57.6 Ti - 30.6 B - 9.2 C - 2.6	Al - 57.6 TiB <sub>2</sub> - 29.6 TiC - 12.8	TiB <sub>2</sub> - 0.22 TiC - 0.09	1297	1240	1.4	48



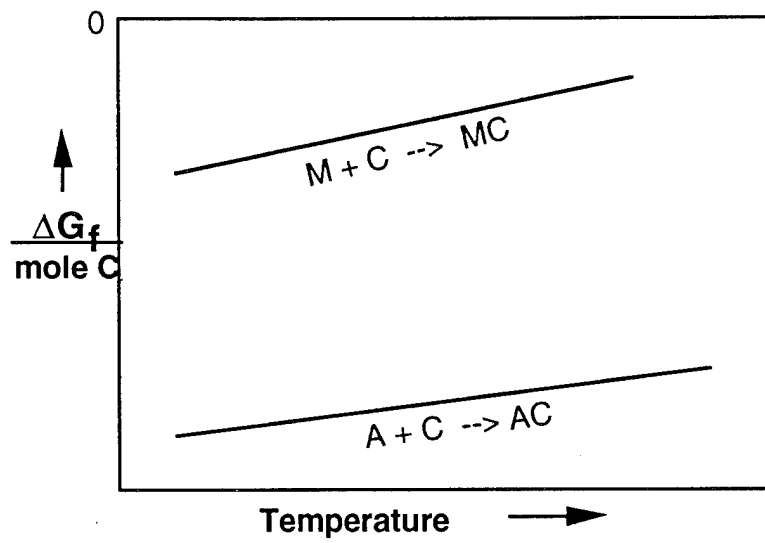


**Figure 2-1** Schematic of free energy vs. temperature curve. MC - strong carbide former; AC - weak carbide former.

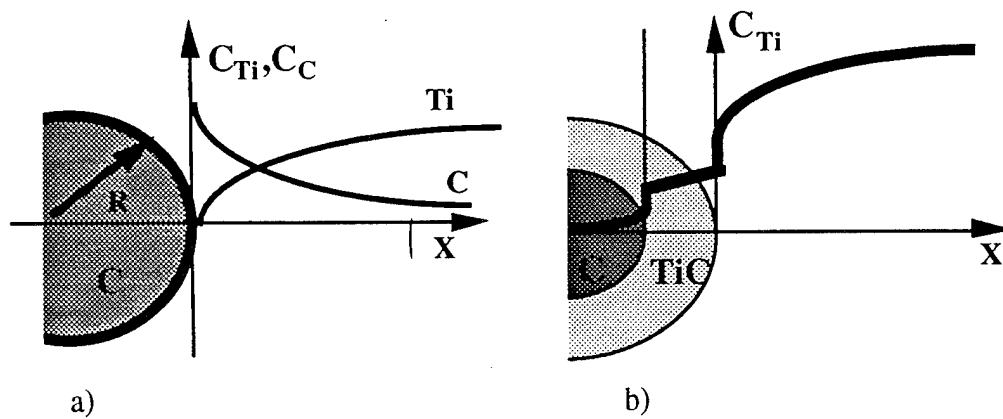


**Figure 2-2** Schematic illustration of two mechanisms of TiC formation, showing the concentration profiles around a carbon particle: (a) solution-reprecipitation mechanism, (b) solid-liquid interfacial reaction.

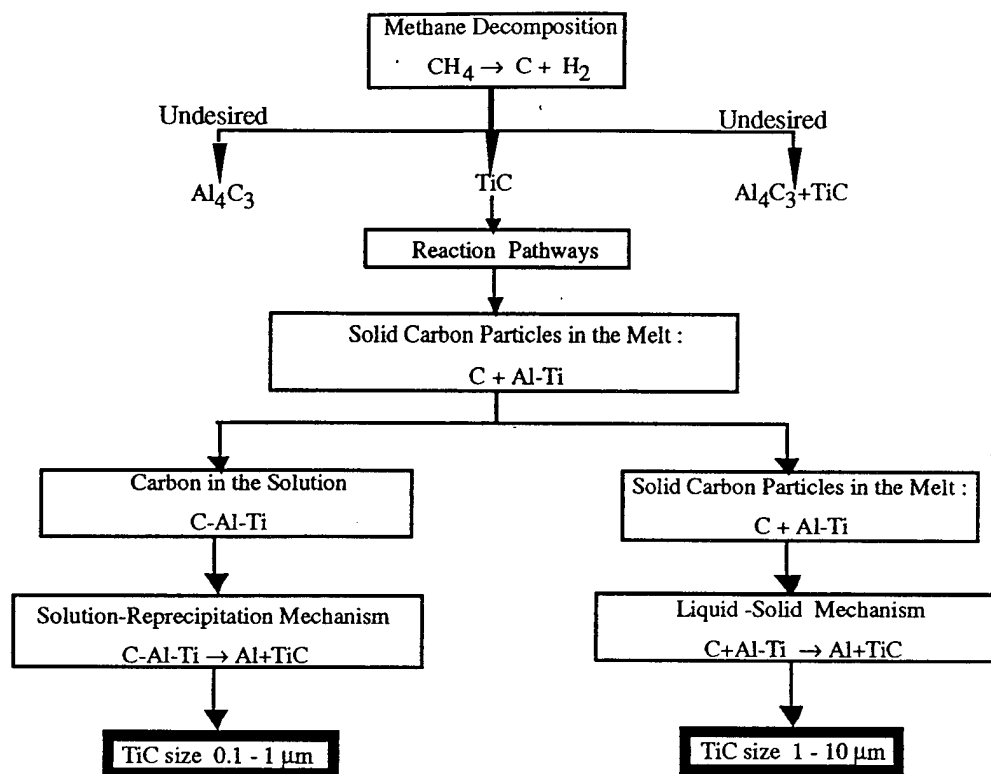


**Figure 2-3** Flow chart of TiC formation in Al matrix via RGI reaction technique.

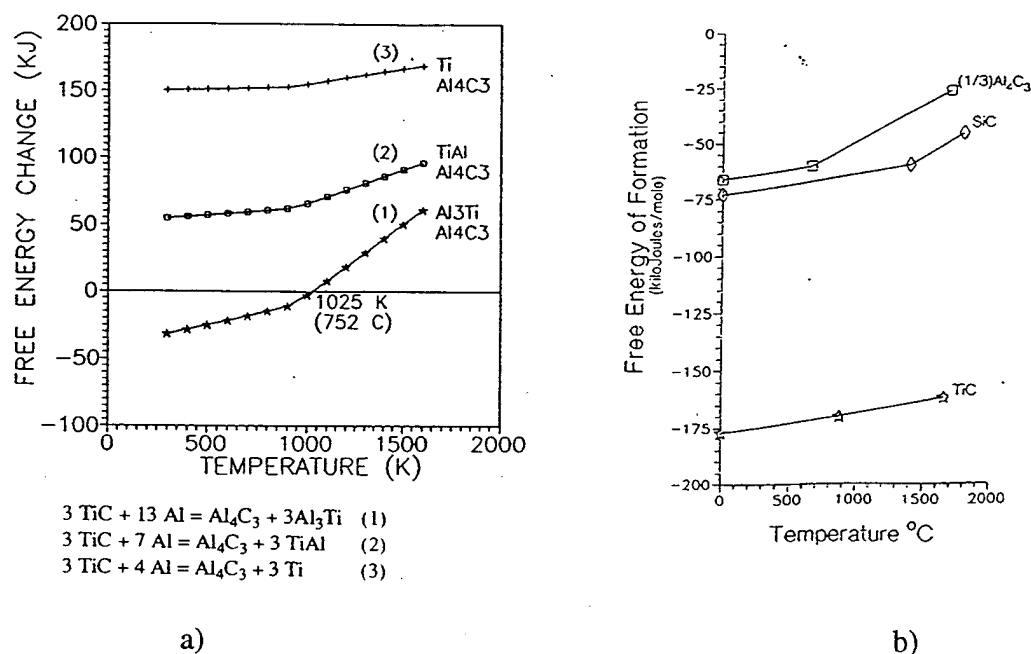


**Figure 2-4** Free energy of formation as a function of temperature.  
a) for reactions (1-3) [24]; b) for SiC, TiC and  $(1/3) \text{ Al}_4\text{C}_3$  [25].

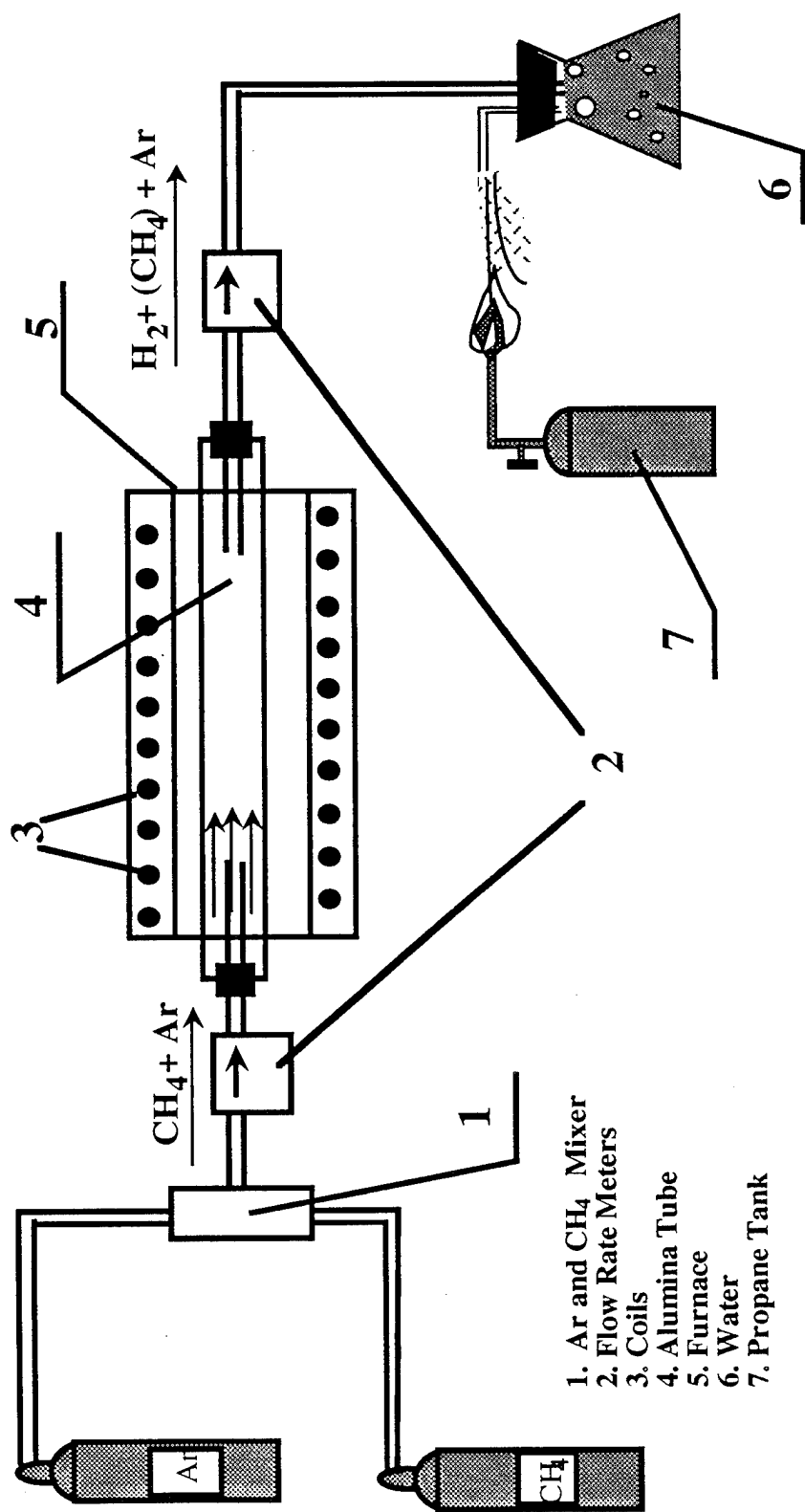
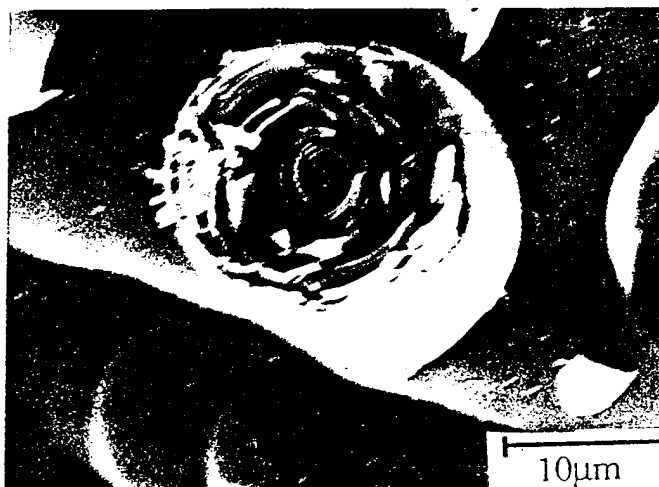
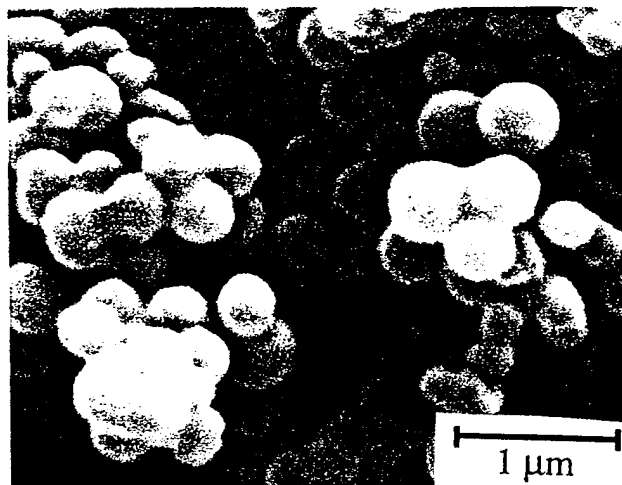
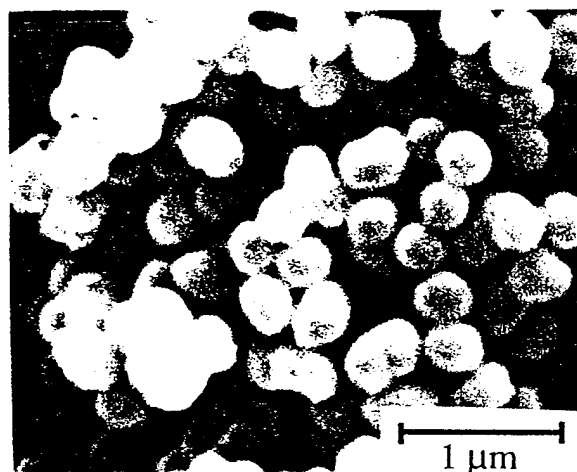


Figure 2-5 Schematic of experimental setup used for methane decomposition efficiency and carbon morphology study.



**Figure 2-6** Carbon fiber formed on the BeO substrate after 1.5 hour methane decomposition at 1200°C.



**Figure 2-7** Carbon particles formed on the Al<sub>2</sub>O<sub>3</sub> substrate after 1 hour (left side) and 2.5 hours (right side) methane decomposition at 1100°C.

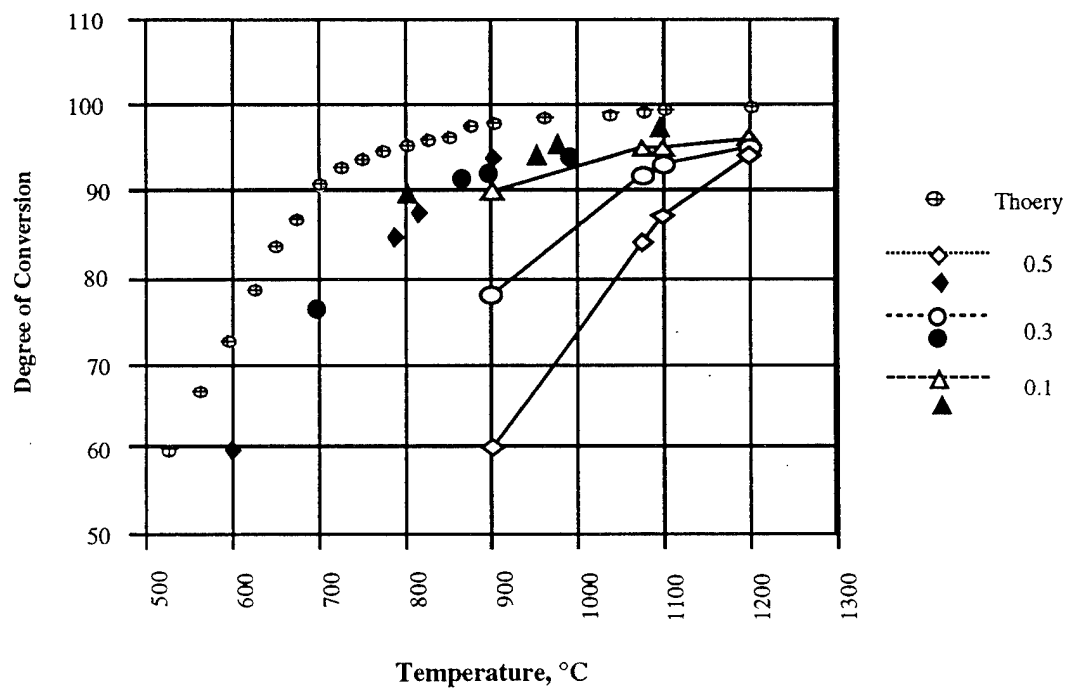


**Figure 2-8** Methane decomposition efficiency versus temperature. Lines illustrate the raw data; dots represent the data, corrected for the temperature difference between the gas and the furnace.

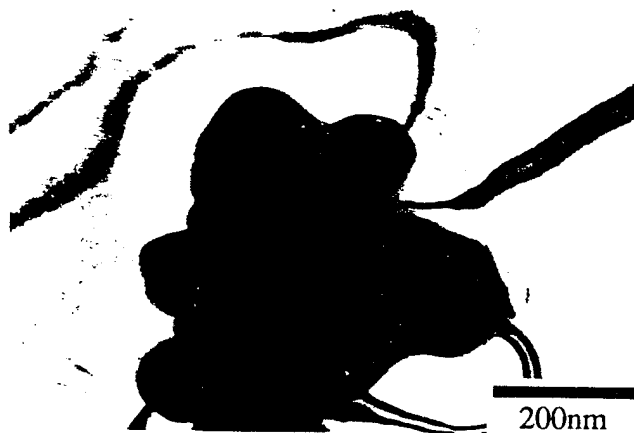
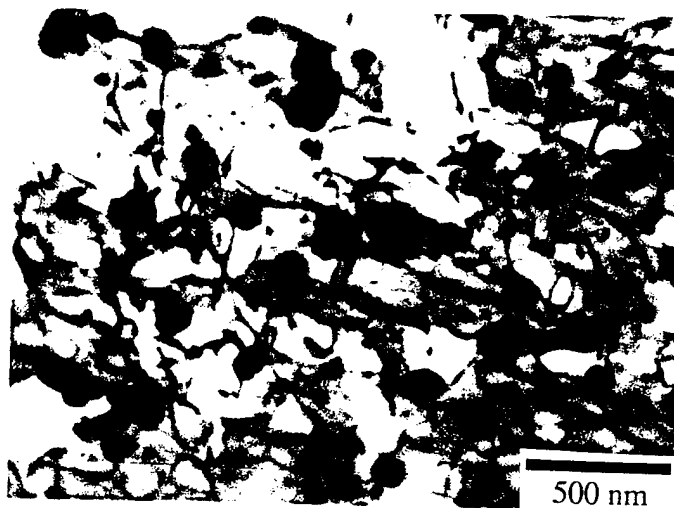


**Figure 2-9** TEM micrograph of carbon particles trapped in the Al matrix after rapid cooling of the sample, showing that the particles size is about 50 nm.

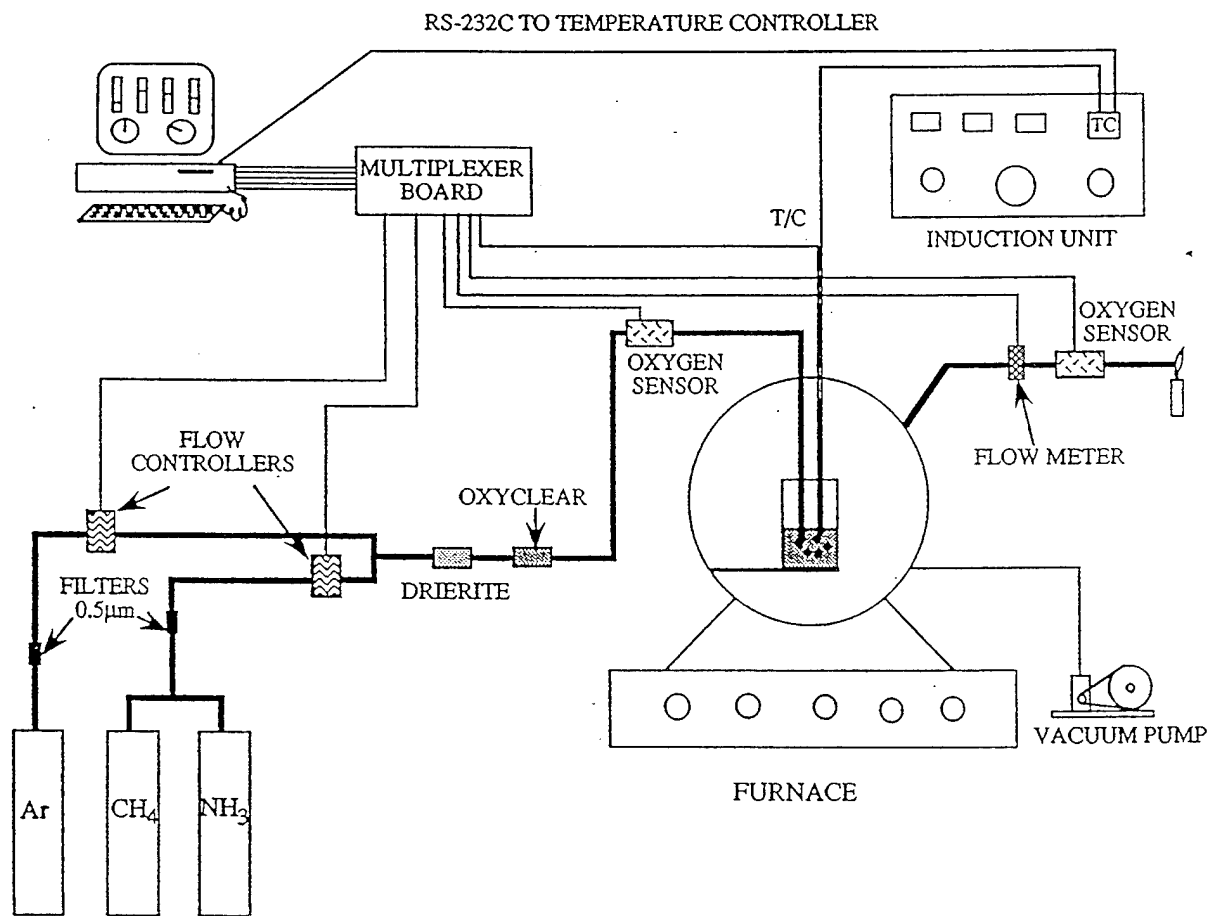
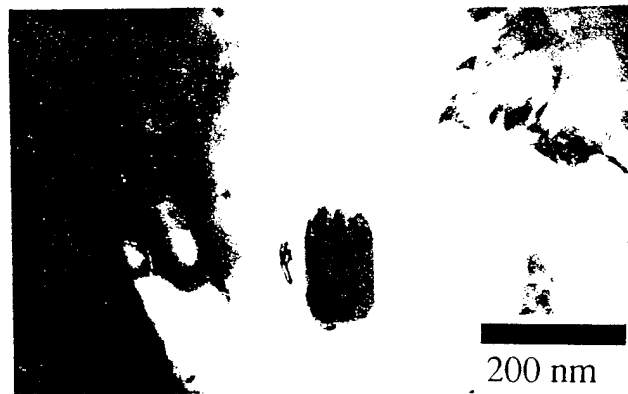


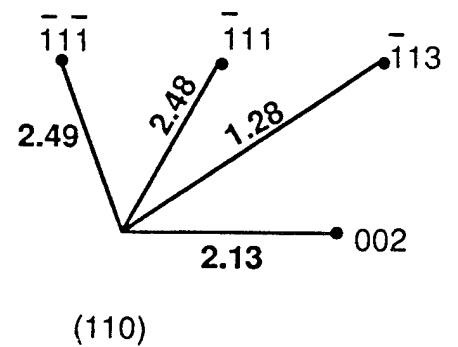
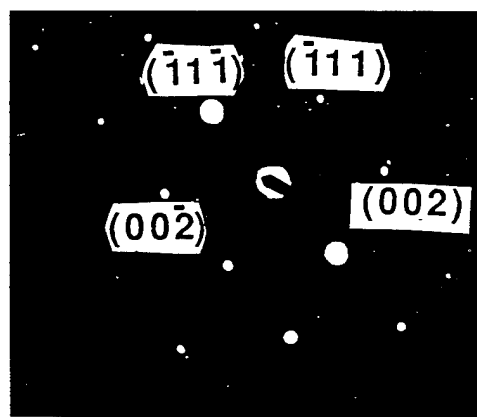
**Figure 2-10** Schematic of experimental system for RGI processes with various control features.







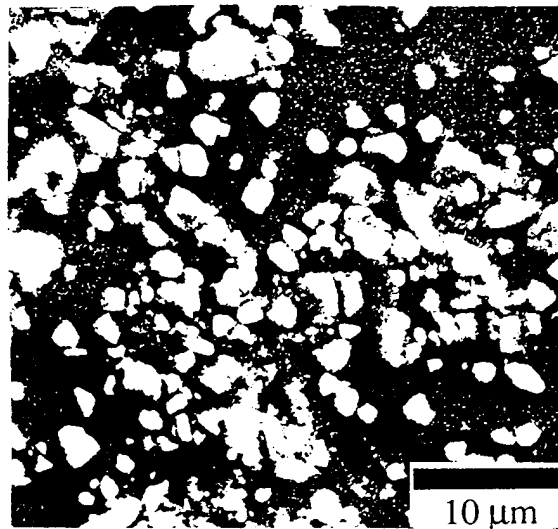
a)



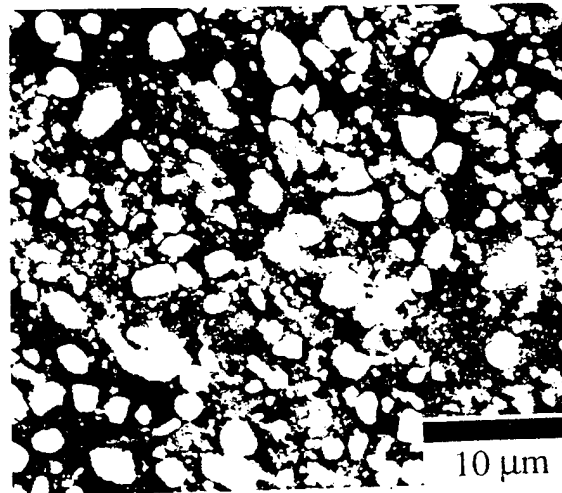
b)

**Figure 2-13**

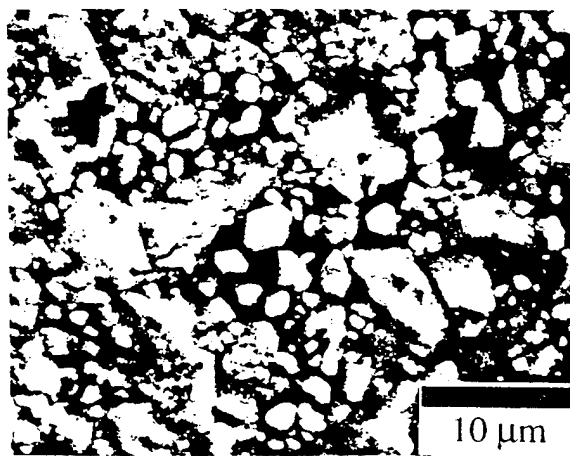
TiC rectangular particle: (a) TEM micrograph, (b) electron diffraction pattern



a)



b)



c)

**Figure 2-14**

Micrograph of Al-60%Ti sample processed for various time periods, showing the increment in volume fraction of TiC: (a) 2 hours, 17.5 v/o TiC (b) 6 hours 35 v/o TiC. (c) 8 hours, 40 v/o TiC.

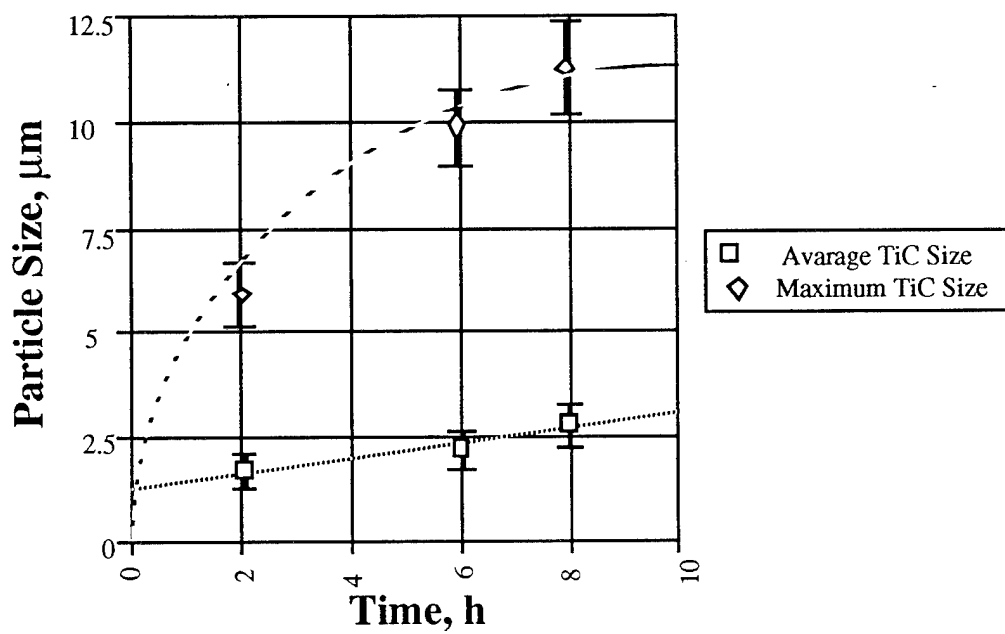


**Figure 2-15** The variation of average and maximum TiC particle size with processing time at 1600°C.

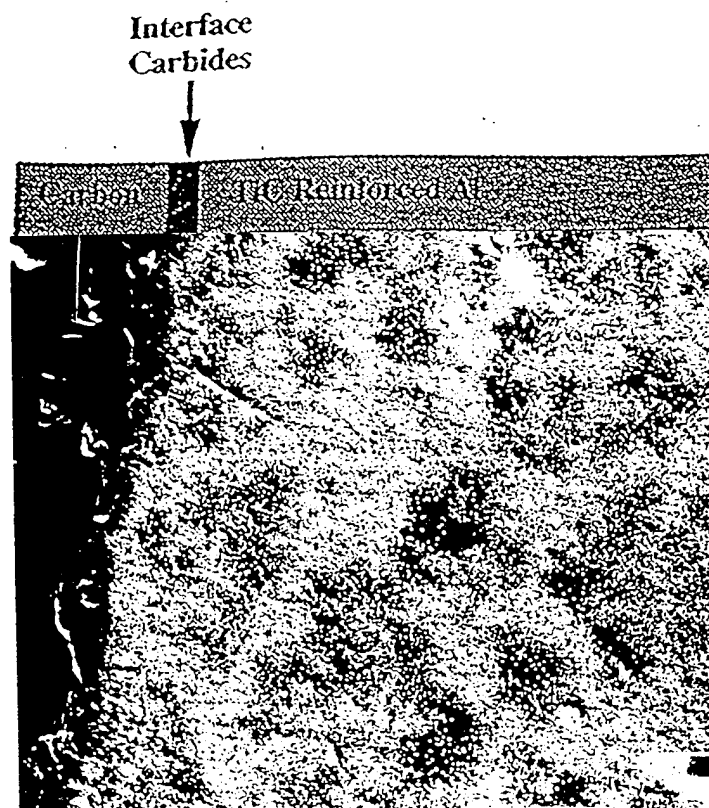


**Figure 2-16**

Planar reaction of Al-10 wt.% Ti sample after immersing graphite plate in the melt at 1300 °C



**Figure 2-17**

Planar reaction of Al-30 wt.% Ti sample after immersing graphite plate in the melt at 1400 °C

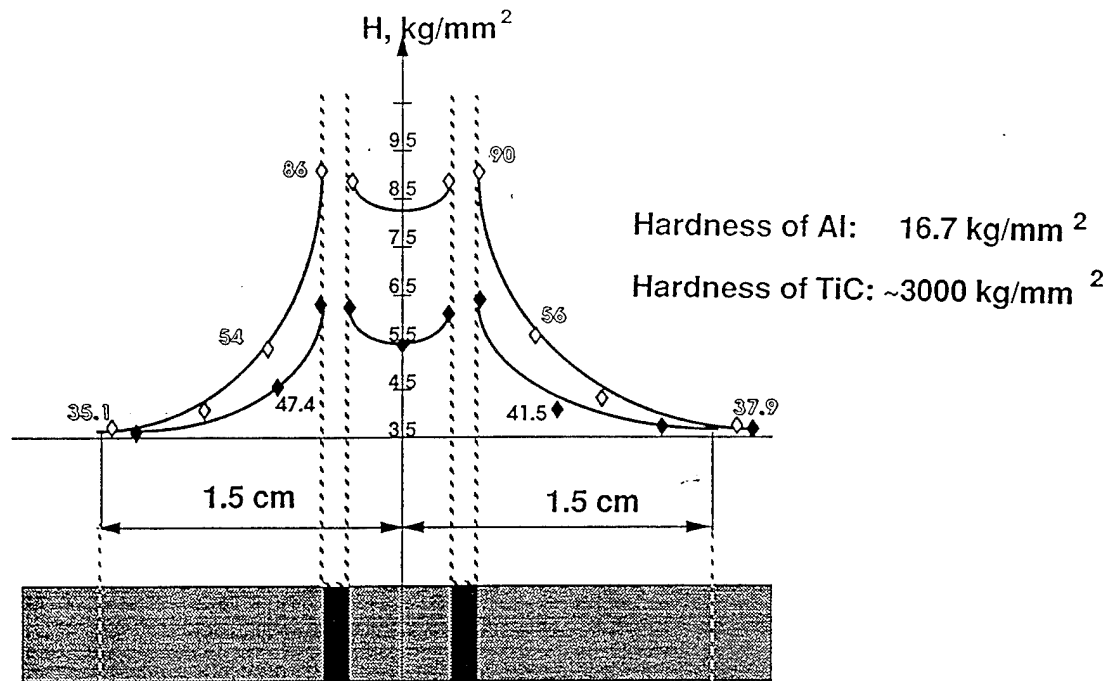


**Figure 2-18** Variation of hardness in the sample across the graphite plates illustrating the carbon diffusion profile in the melt.

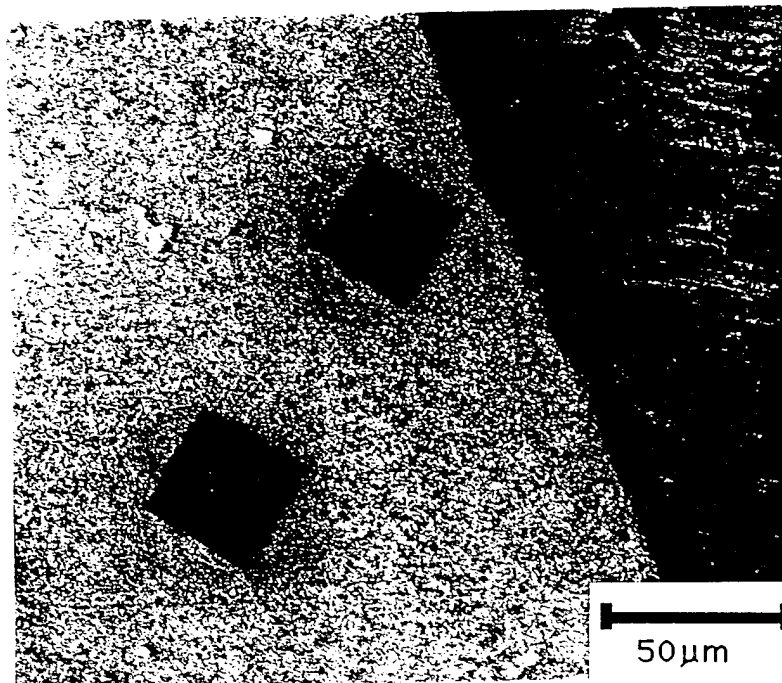


**Figure 2-19** Optical micrograph, illustrating the increasing indentation size with the increasing distance from the carbon plate.

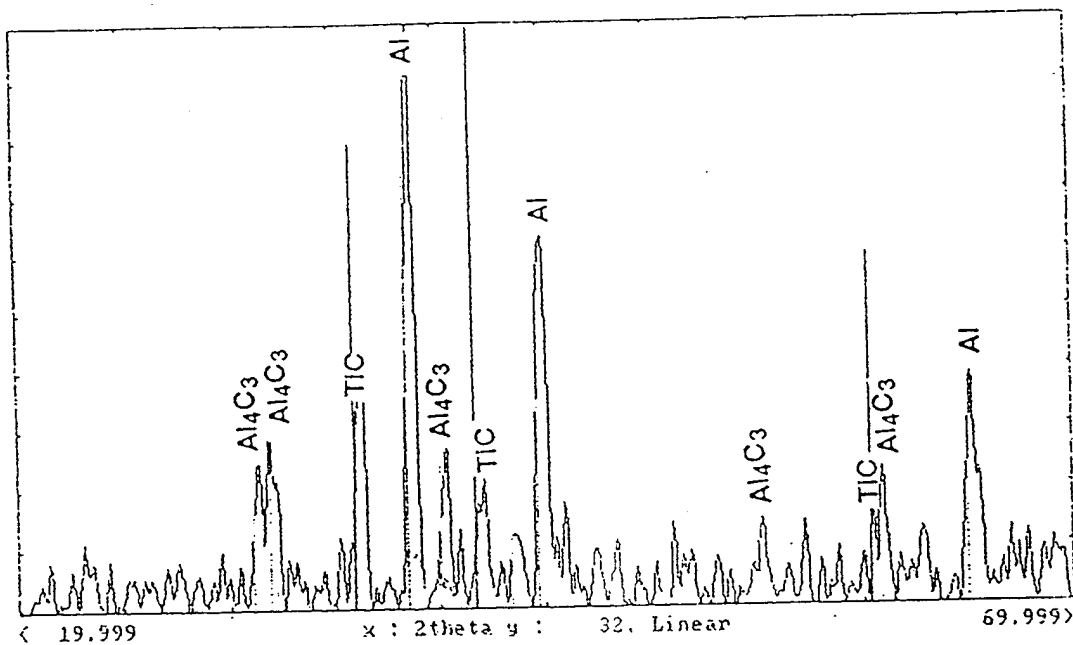


**Figure 2-20** X-ray diffraction pattern showing the presence of TiC and Al<sub>4</sub>C<sub>3</sub> in the Al matrix.

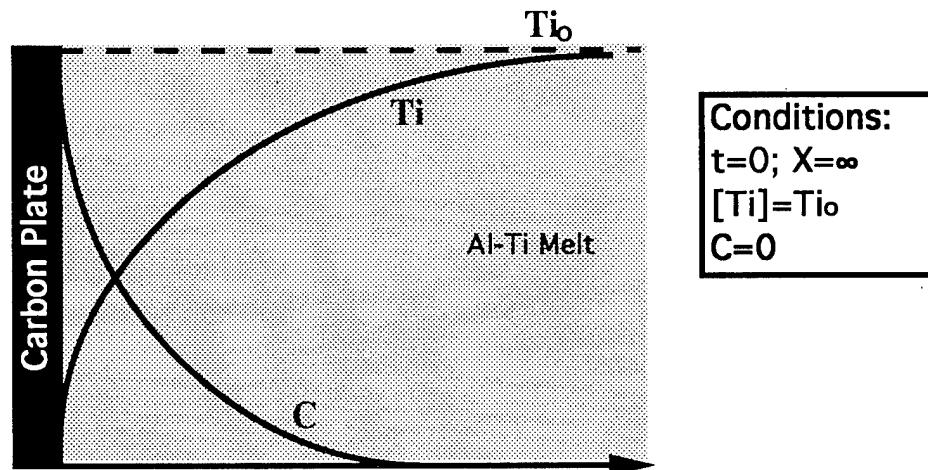


**Figure 2-21** The schematic illustration of titanium and carbon concentration distribution in the melt during the process of carbon plate dissolution in Al-Ti liquid solution.

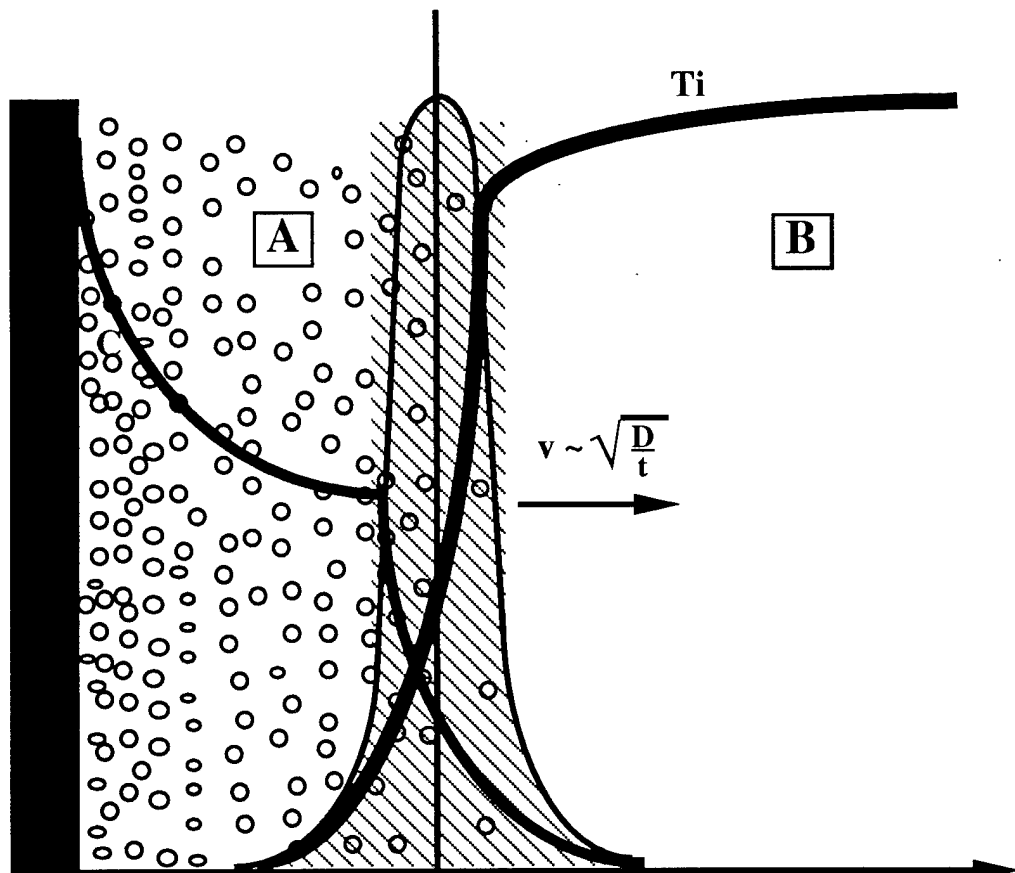


**Figure 2-22** Titanium and carbon concentration profiles in the melt near the carbon plate, showing two regions:

Region A: Carbon reach region;

Region B: Ti reach region

The shaded area corresponds to the reaction zone. A high rate of Ti and C consumption by the reaction  $Ti+C=TiC$  in this zone leads to a drastic Ti and C concentration drop. The direction of the reaction front propagation is indicated.



**Figure 2-23**

SEM micrograph of the interfacial layer formed around the graphite plate, showing two types of titanium carbides - coarse and porous, formed as a result of interfacial reaction at the graphite plate and fine single crystal particles which are similar to those found in RGI processed samples, formed via solution-reprecipitation mechanism.

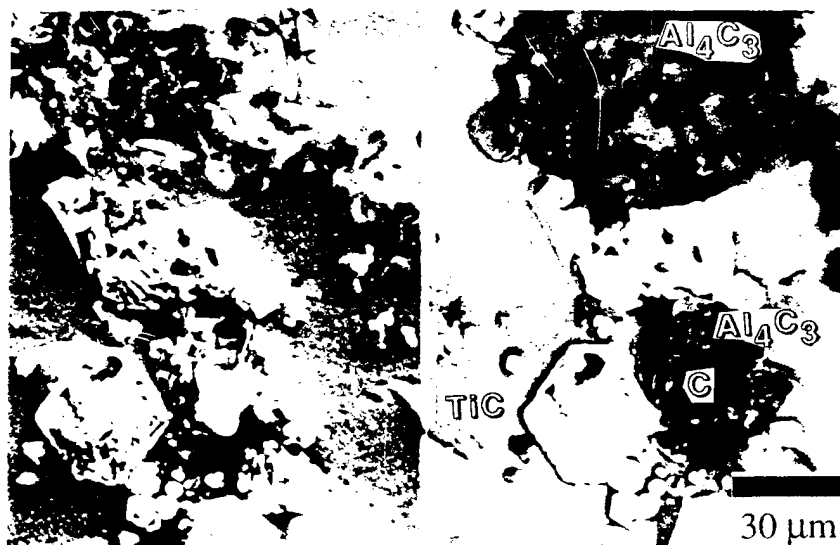


**Figure 2-24**

SEM micrograph of coarse titanium carbides formed as a result of interfacial reaction at the graphite plate, separated from the graphite surface with the Al<sub>4</sub>C<sub>3</sub> layer.



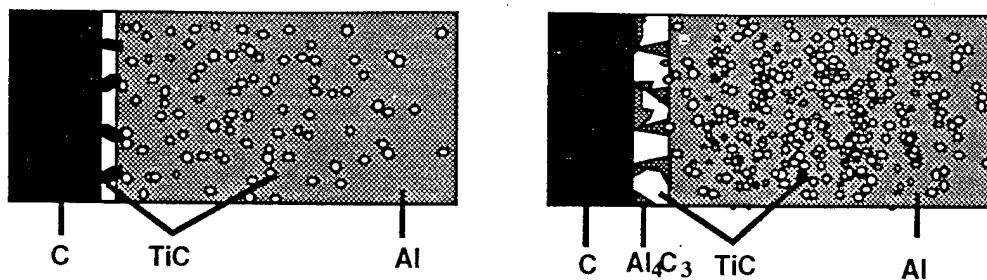


**Figure 2-25** Schematic illustration of the microstructure evolution during carbon plate dissolution in the Al-Ti melt.

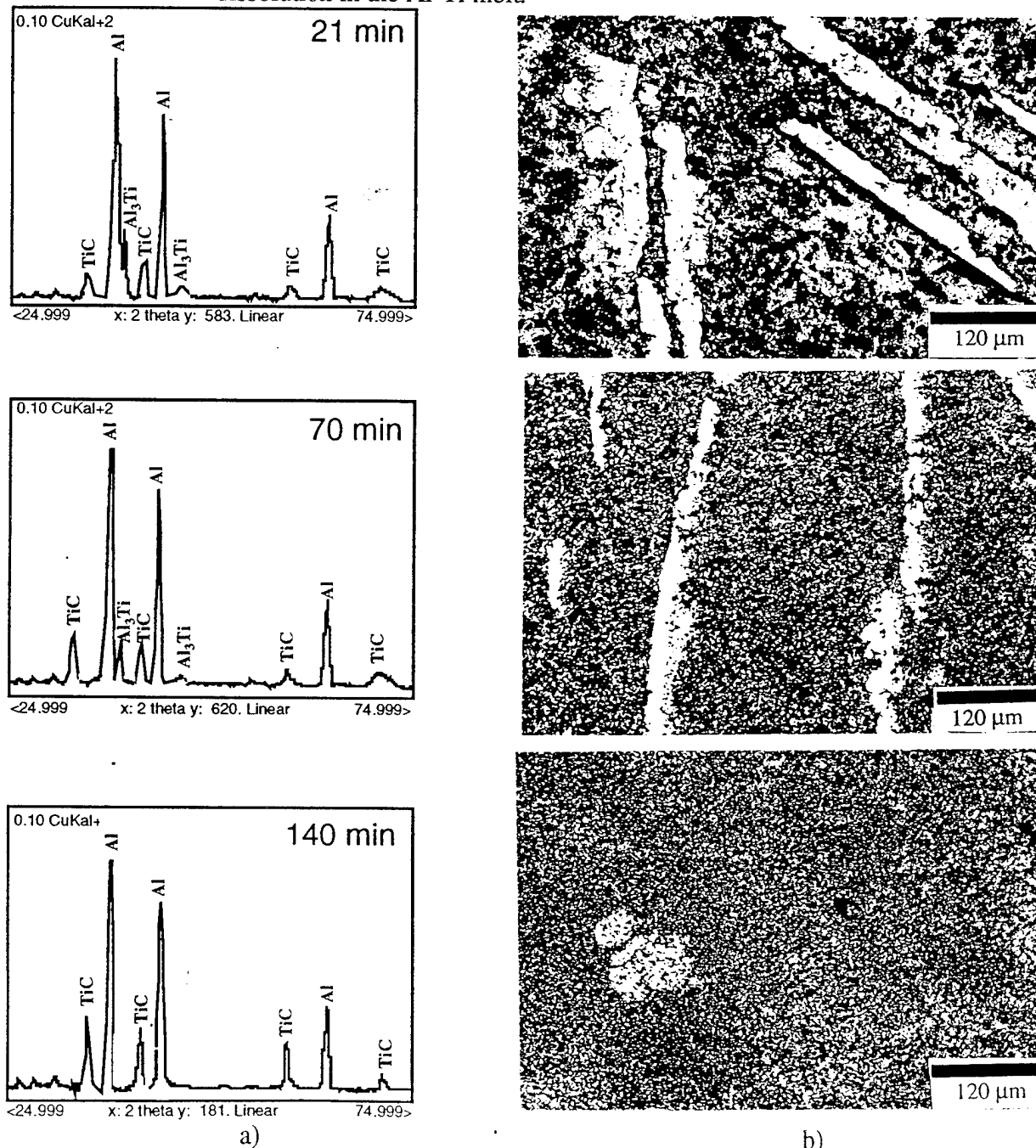


**Figure 2-26** Characteristics of the samples obtained after 21, 70 and 140 minutes of reaction, respectively. a) XRD patterns; b) Optical micrographs

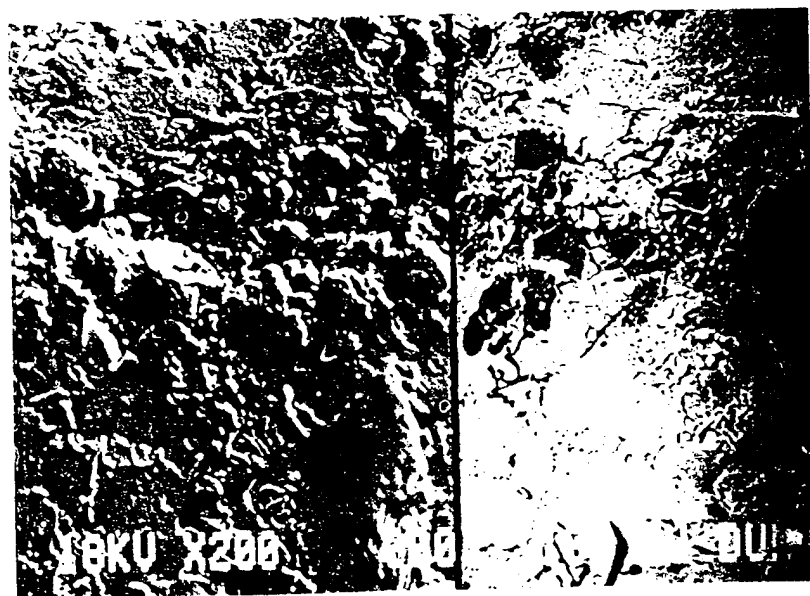
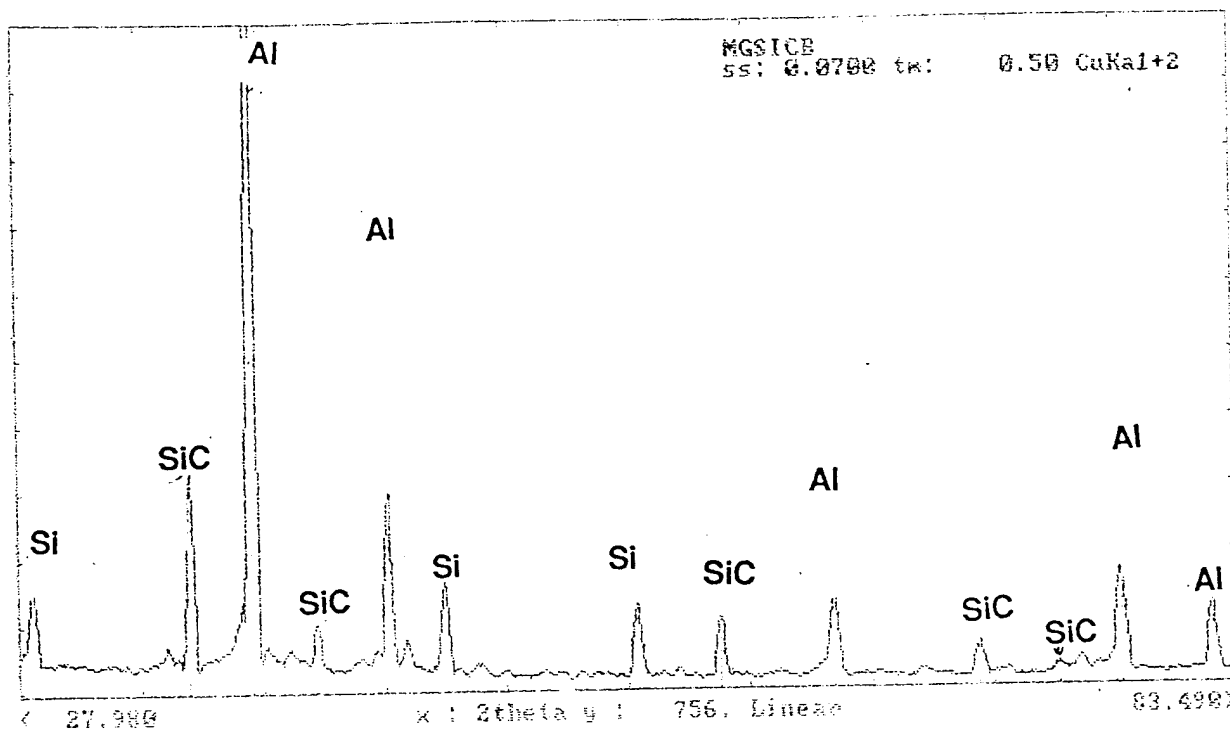


**Figure 2-27**

XRD and SEM micrograph showing the presence of SiC particles in Al matrix

## Part II-B.

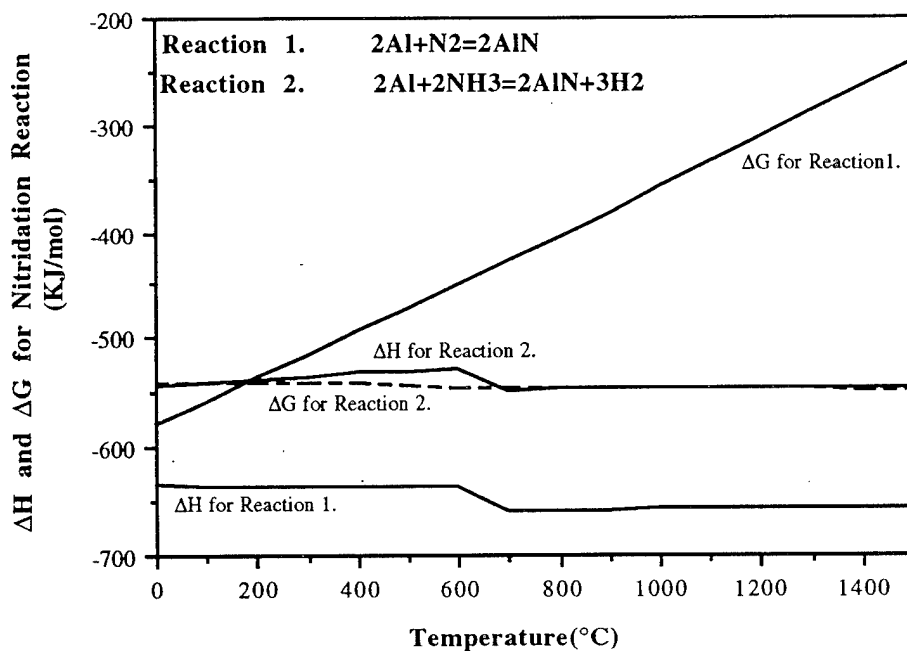


**Figure 2-28** Enthalpy and Gibbs's free energy change for the formation of AlN vs temperature, with nitrogen or ammonia as reactive gas.

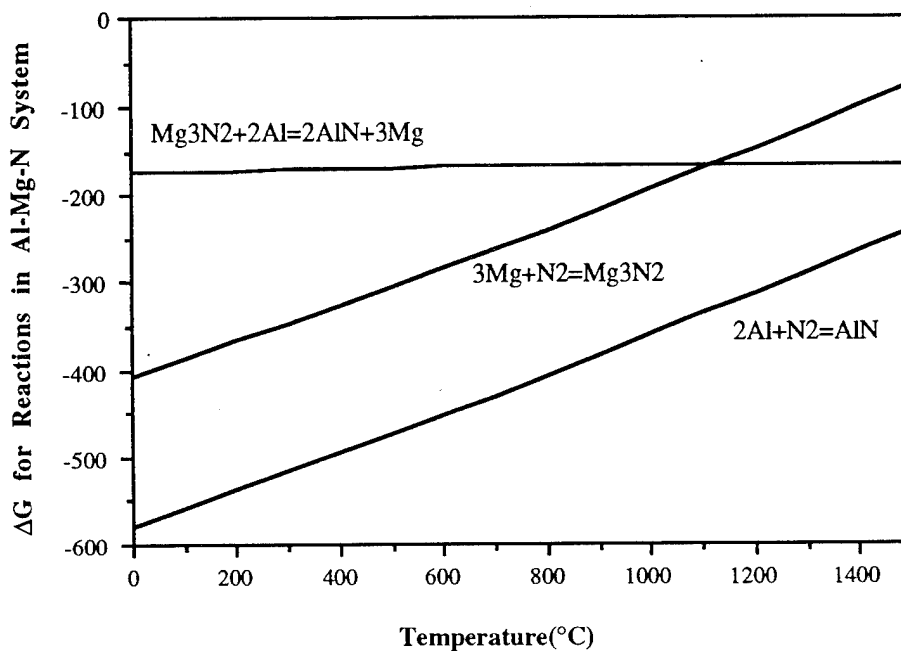


**Figure 2-29** The Gibbs's free energy change vs temperature for the reactions occurring in Al-Mg-N system based on the same amount of nitrogen.

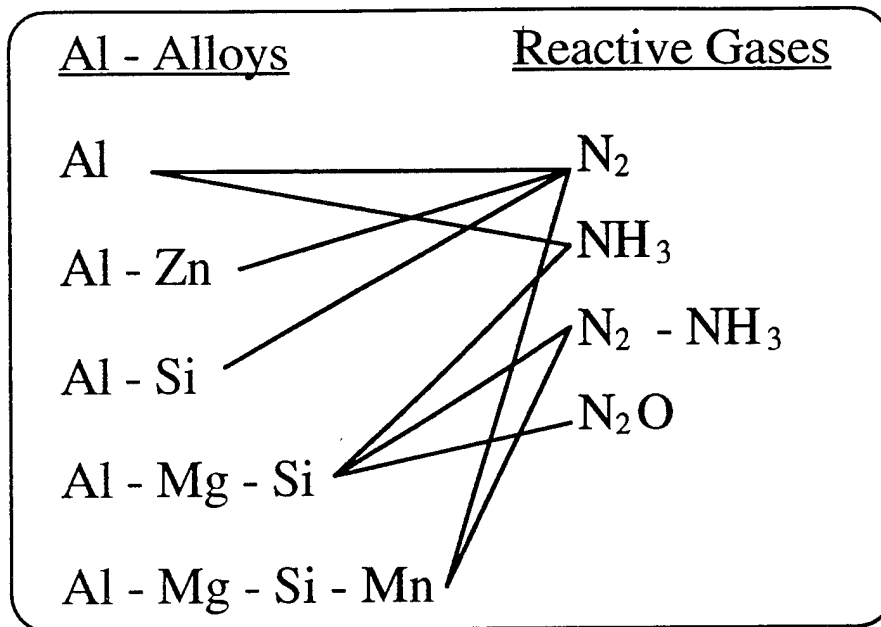


Figure 2-30 Material systems studied.

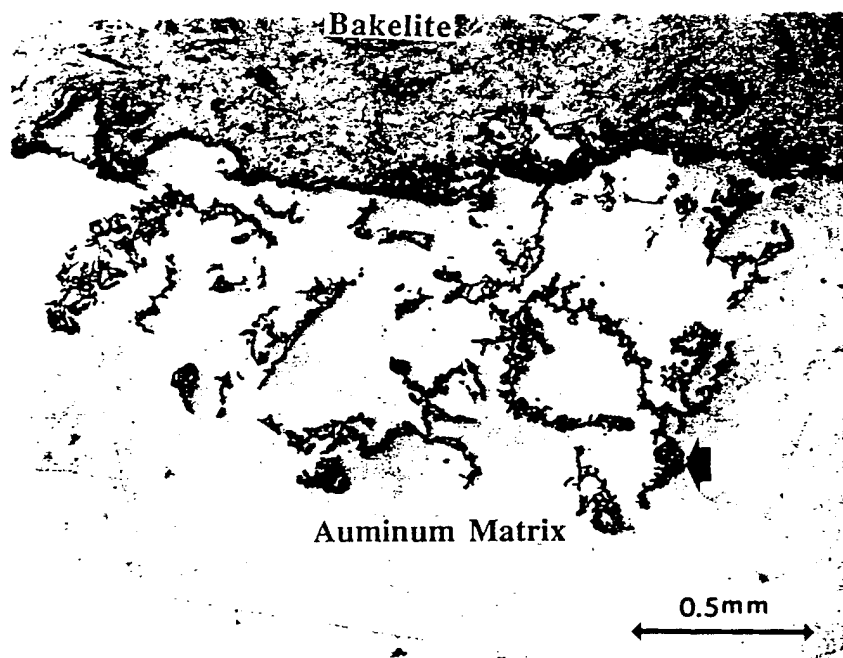
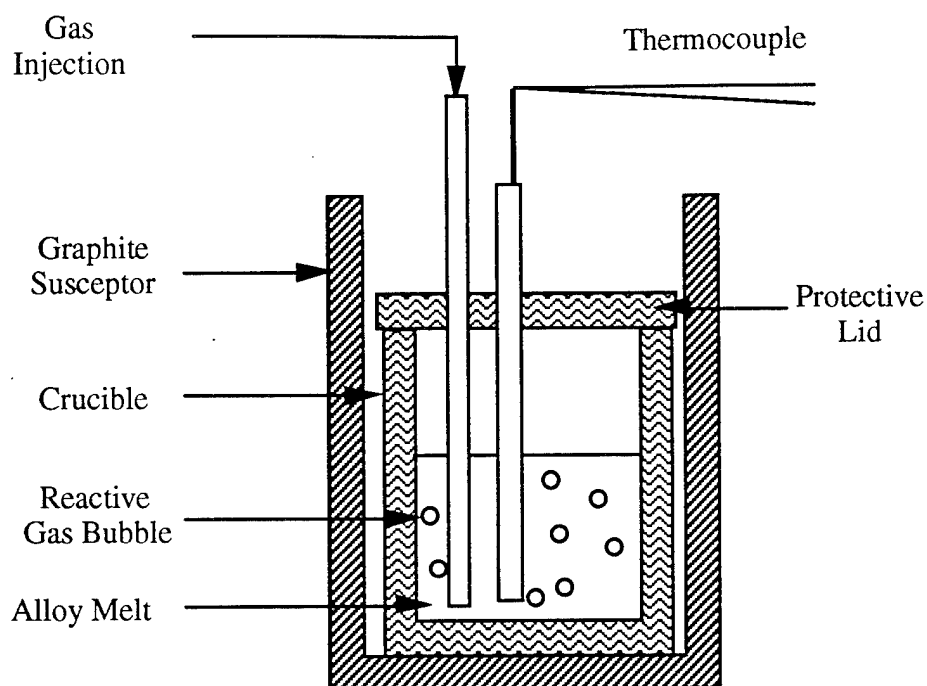
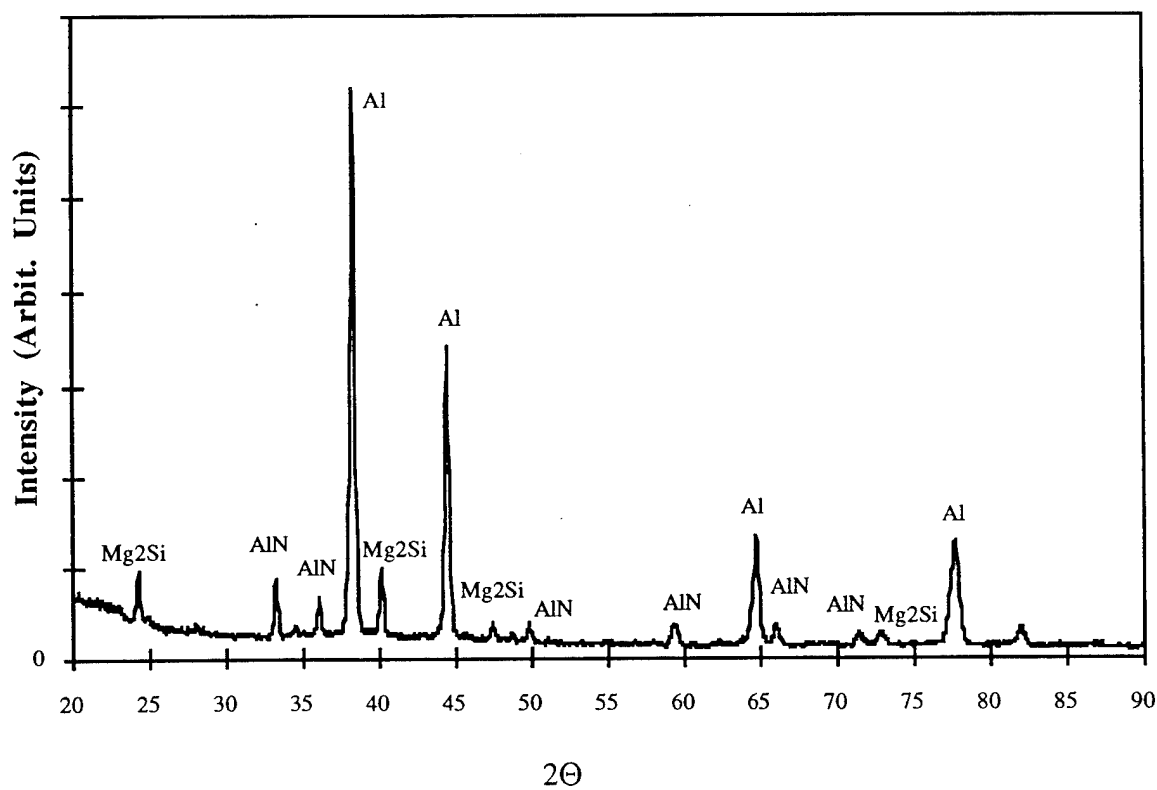


Figure 2-31 The microstructure of the area close to the surface of the ingot shows that AlN-rich region is about 1mm (Sample from Experiment 3).



**Figure 2-32** Schematic reactor geometry.



**Figure 2-33** X-ray diffraction pattern for the cross-section of the Experiment 7a.

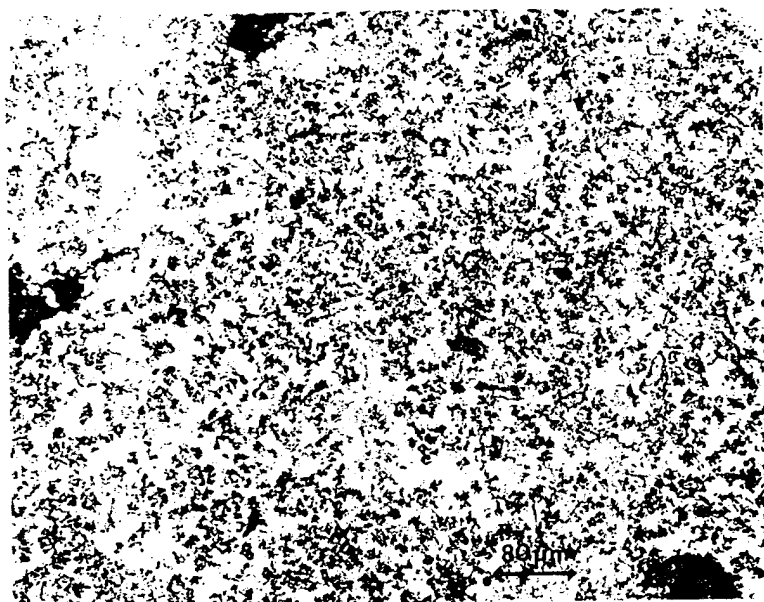


**Figure 2-34** Microstructure of Experiment 7a sample (Al -1.5Mg - 2.4Si - N).

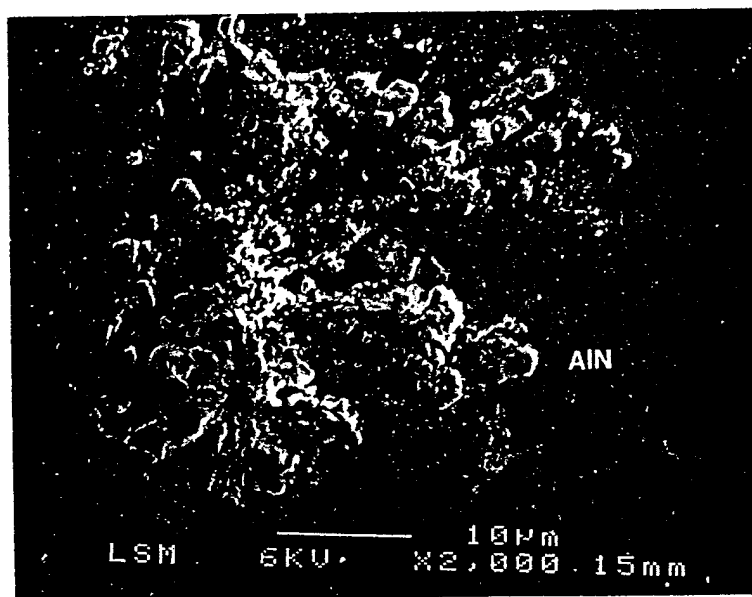


**Figure 2-35** Microstructure of Experiment 7a sample (remelted with the same amount of pure aluminum and homogenized).

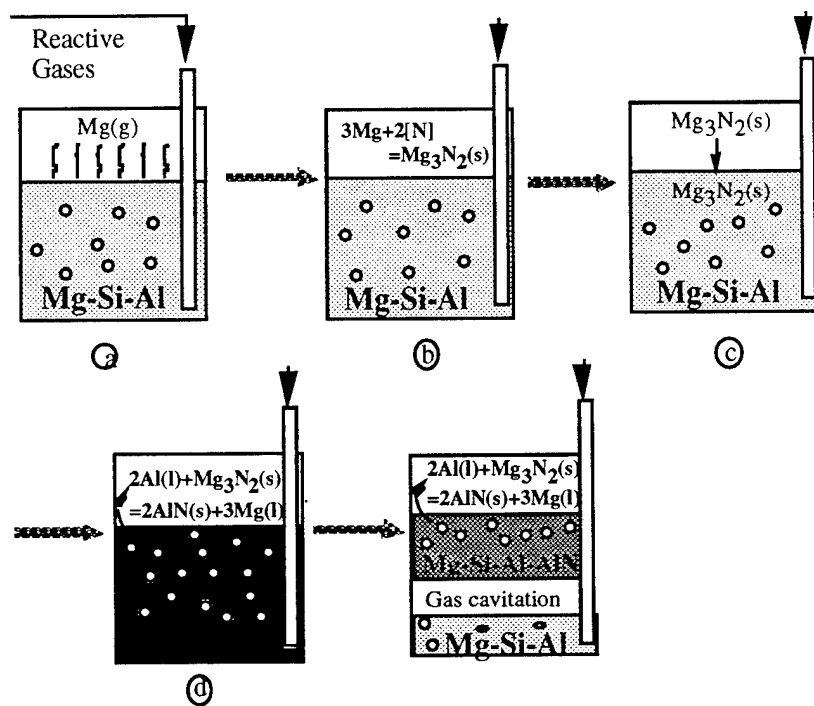
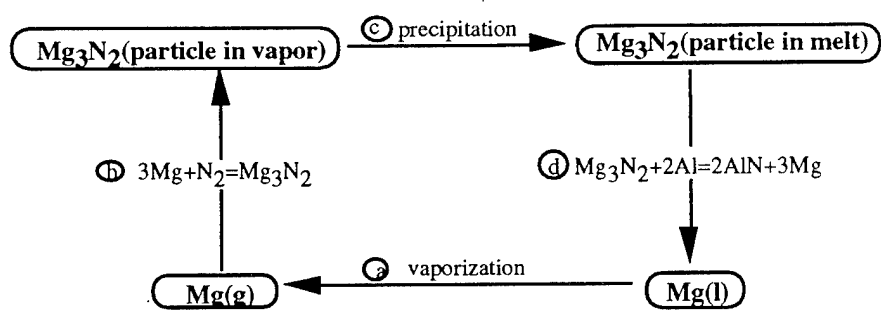


**Figure 2-36** The proposed mechanism of indirect nitridation (gas-liquid substitution reaction).

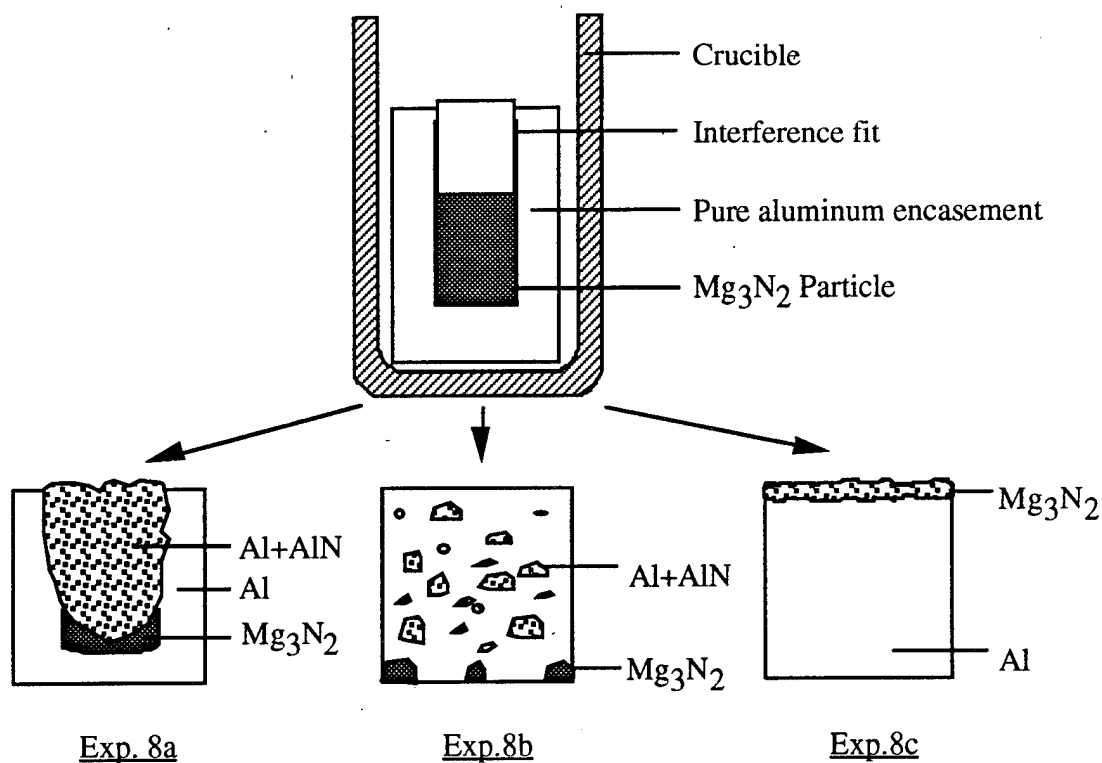


**Figure 2-37** Results from Experiments 8 a,b and c in schematic form.

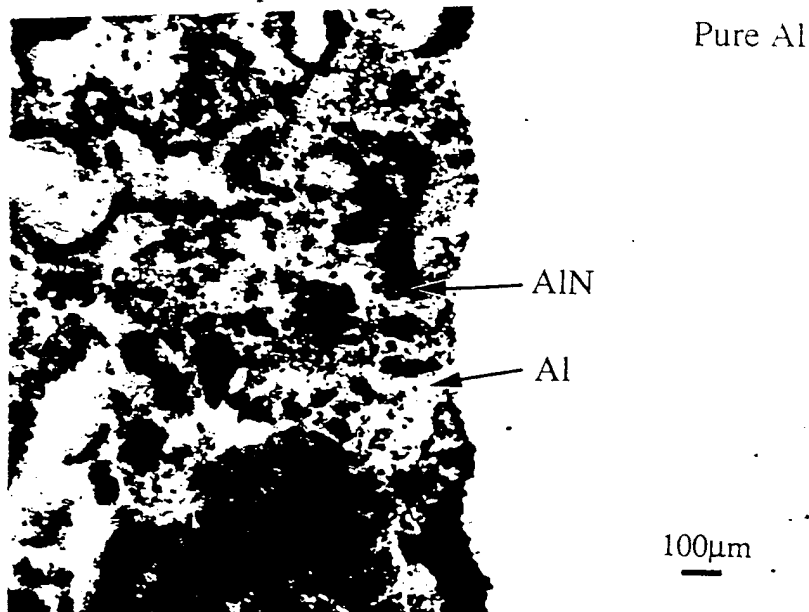


**Figure 2-38** Micrograph from Experiment 8a shows the interface between unreacted Al and AlN-Al region. The aluminum in the AlN-Al region originated from the top cover.



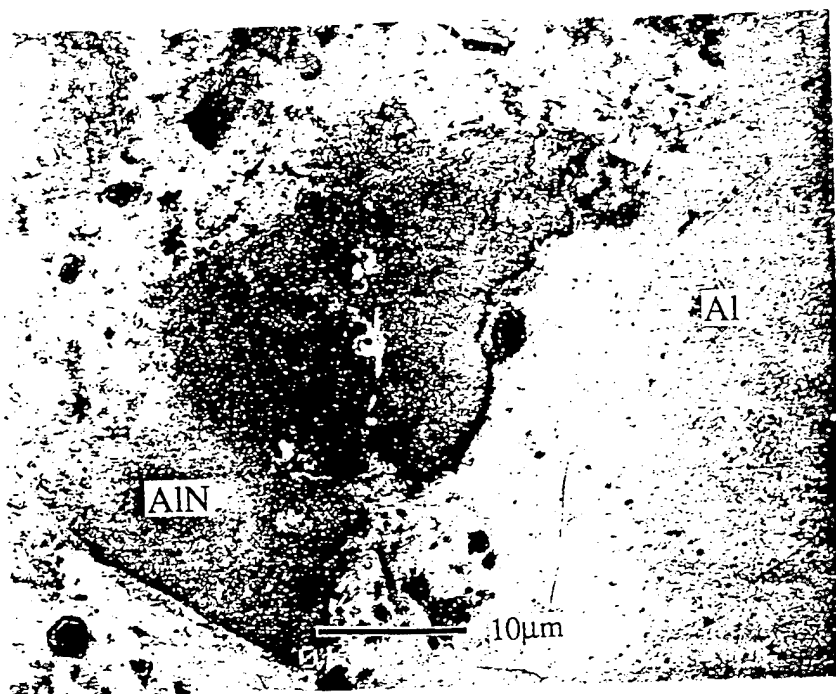


**Figure 2-39** Micrograph from Experiment 8a shows the size and shape of AlN particle which was converted from  $\text{Mg}_3\text{N}_2$ .

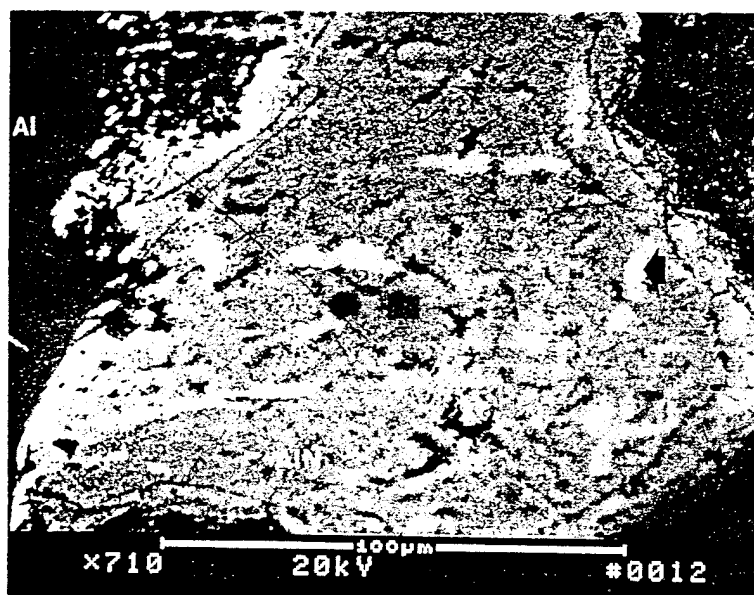


**Figure 2-40** Microstructure of Experiment 8a sample (demonstration of reaction  $2\text{Al} + \text{Mg}_3\text{N}_2 = 2\text{AlN} + 3\text{Mg}$ )



**Figure 2-41** Micrograph from Experiment 8b shows the agglomeration of AlN particles.

## Part II - C

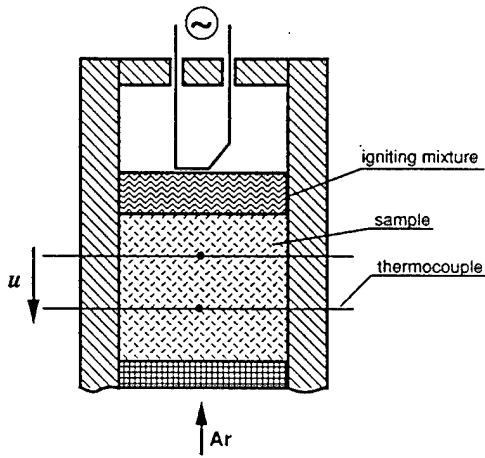
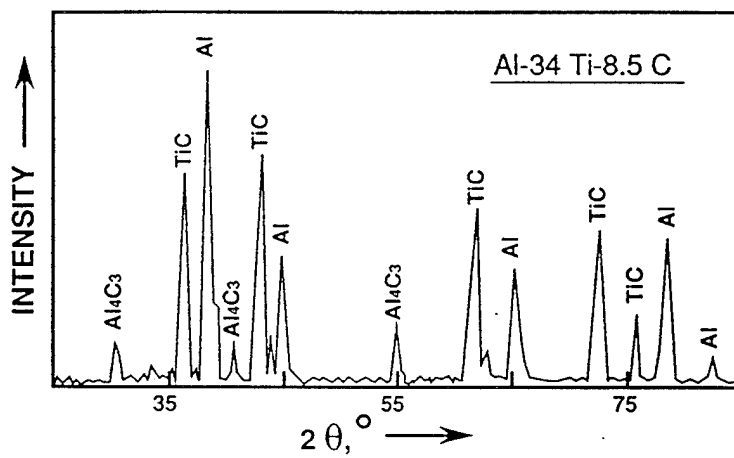
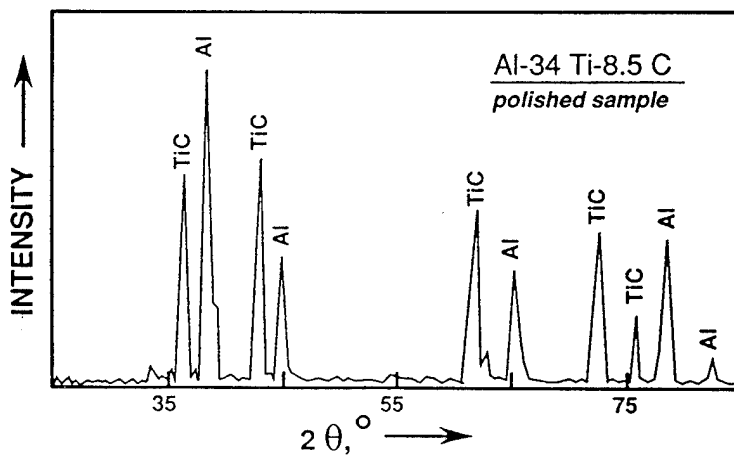


Figure 2-42 Schematic of the SHS experiment.



a)



b)

Figure 2-43 X-ray diffraction patterns of the SHS-processed TiC/Al composite: (a) as-received; (b) after polishing.

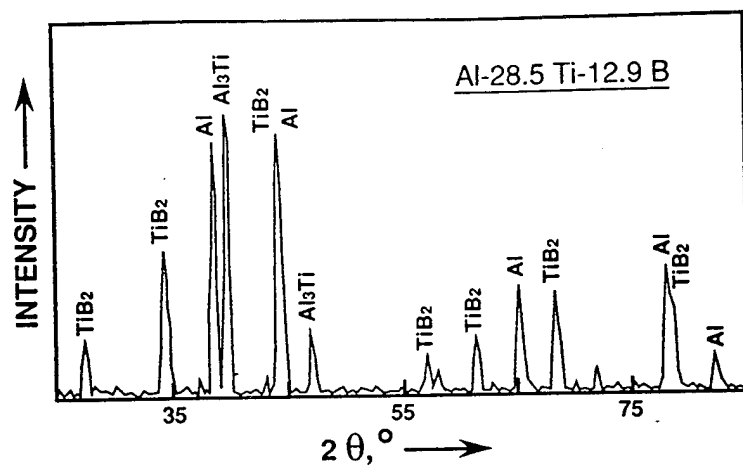
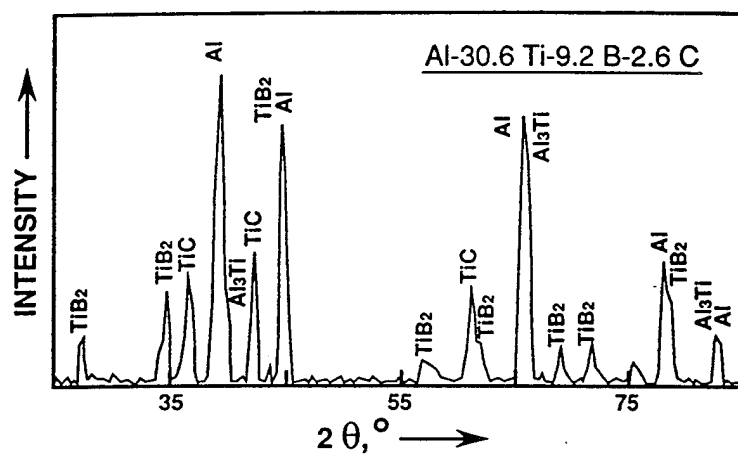
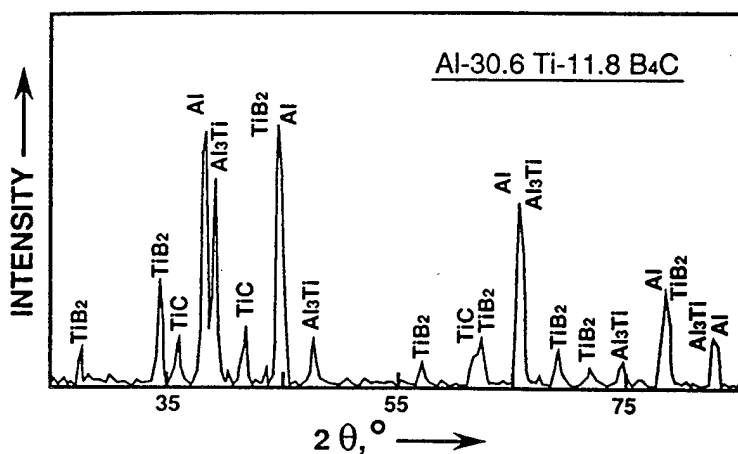


Figure 2-44 X-ray diffraction pattern of the SHS-processed  $\text{TiB}_2/\text{Al}$  composite.

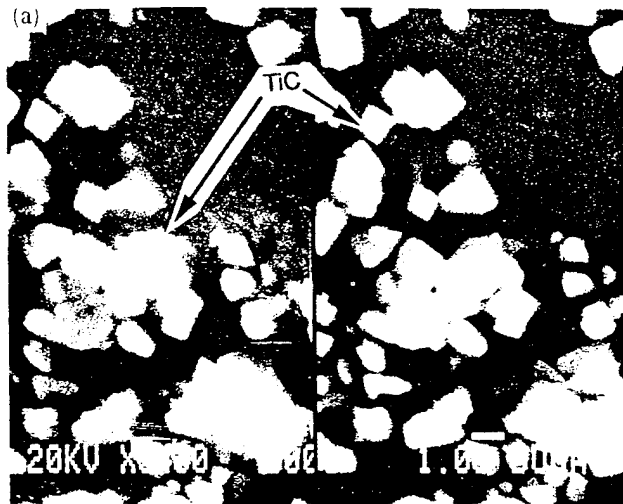


a)

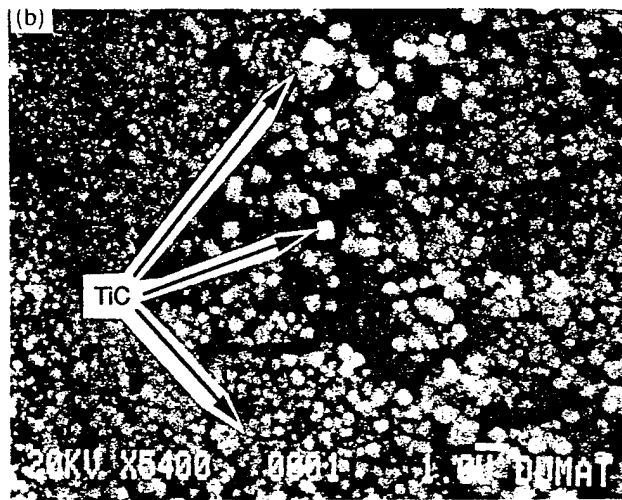


b)

Figure 2-45 X-ray diffraction patterns of the  $\text{TiC-TiB}_2/\text{Al}$  composites SHS-processed from: (a)  $\text{Al-Ti-B-C}$  starting mixture and (b)  $\text{Al-Ti-B}_4\text{C}$  starting mixture.



a)



b)

**Figure 2-46** Representative microstructures of the TiC/Al *in situ* composite (as-received after SHS): (a) relatively coarse TiC particles, left - secondary electron image, right - backscattered electron image; (b) fine TiC particles. SEM.

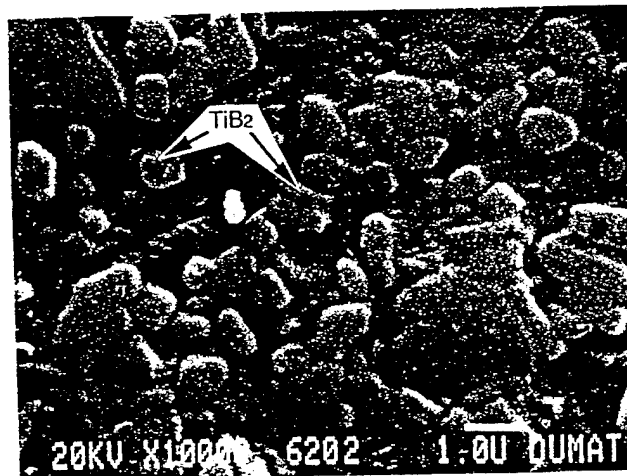


**Figure 2-47** Representative microstructure of the SHS-processed TiB<sub>2</sub>/Al *in situ* composite (cold sintered). SEM.

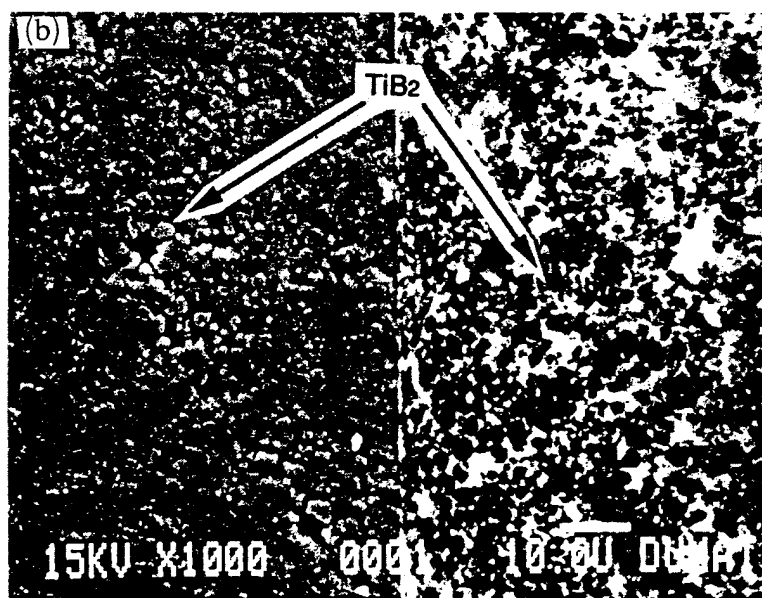
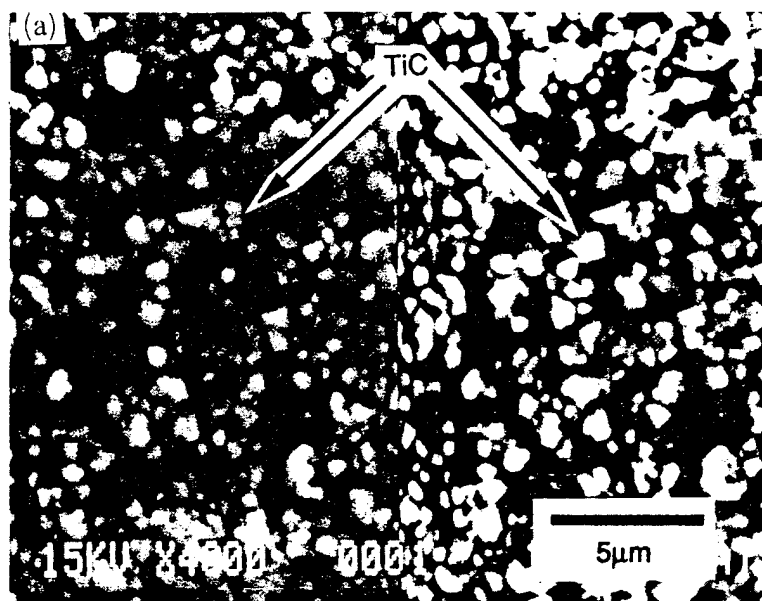
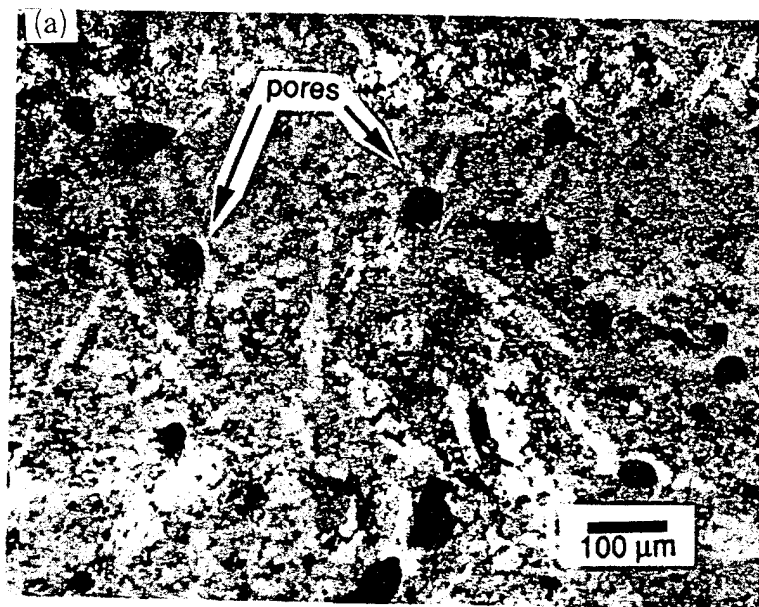
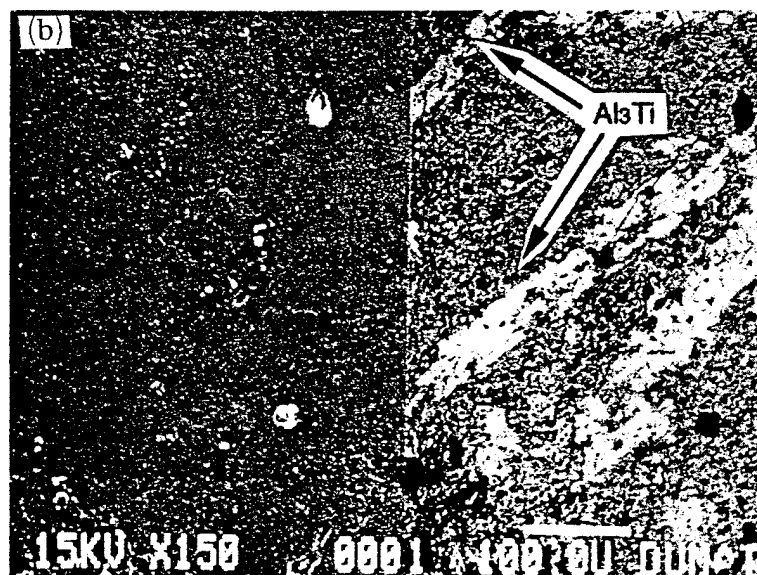


**Figure 2-48** Representative microstructure of the TiC-TiB<sub>2</sub>/Al *in situ* composite (as-received after SHS of Al-Ti-C-B mixture): (a) TiC particles; (b) TiB<sub>2</sub> particles, left - secondary electron image, right - backscattered electron image. SEM.

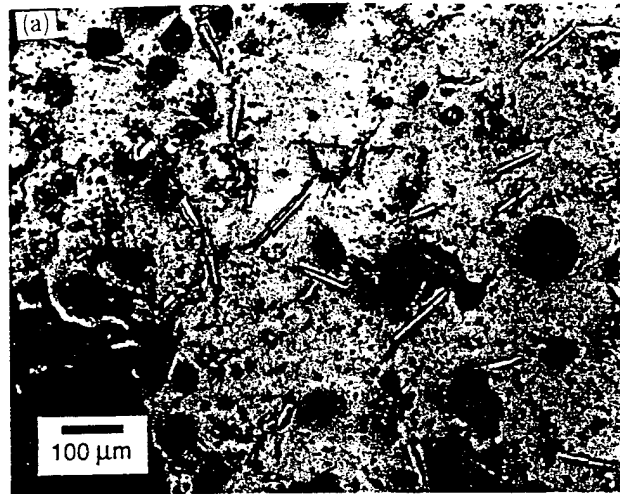


a)

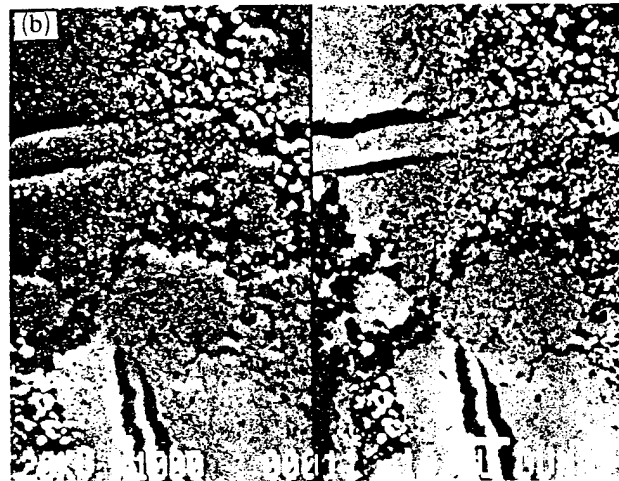


b)

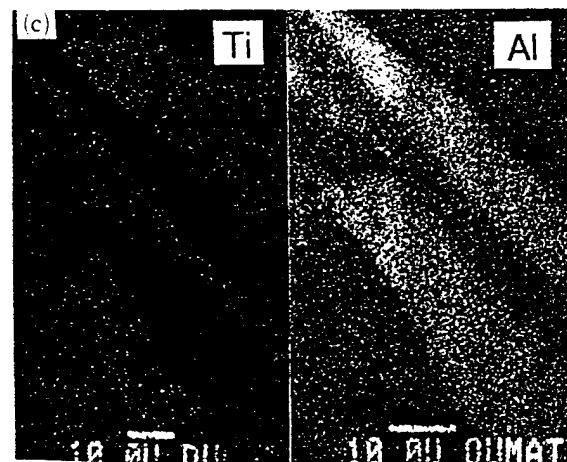
**Figure 2-49**  $\text{Al}_3\text{Ti}$  needles in the microstructure of  $\text{TiC-TiB}_2/\text{Al}$  composite SHS-processed from  $\text{Al-Ti-C-B}$  mixture: (a) optical micrograph; (b) SEM micrograph, left - secondary electron image, right - backscattered electron image.



a)



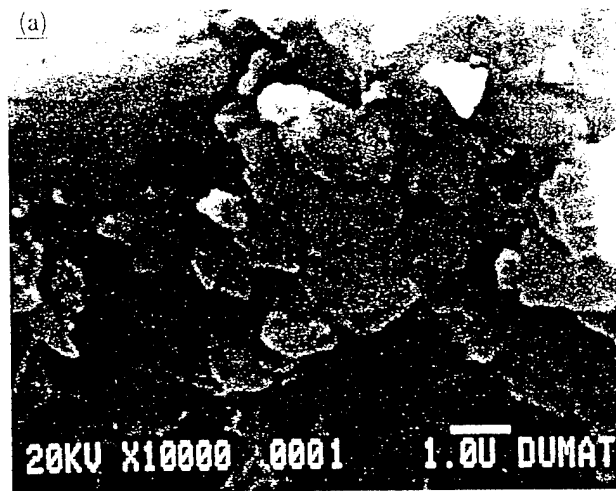
b)



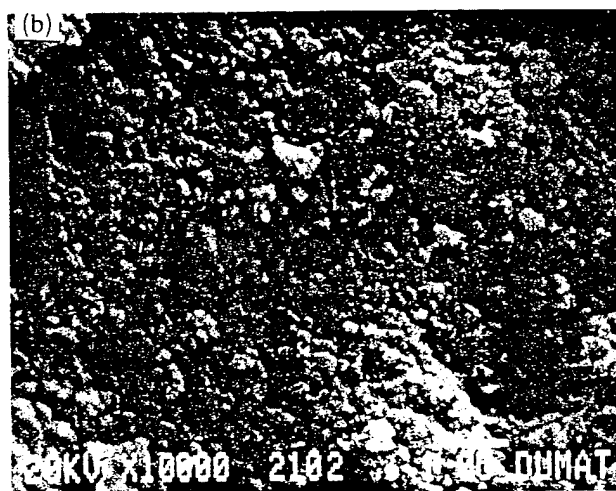
c)

**Figure 2-50**  $\text{Al}_3\text{Ti}$ -like needles in the microstructure of the *in situ* SHS-processed TiC/Al composite: (a) optical micrograph; (b) SEM micrograph, left - secondary electron image, right - backscattered electron image; (c) Al and Ti WDX maps of the needle and the surrounding area.





a)



b)



c)

**Figure 2-51** Fracture surfaces (in bending) of the SHS-processed *in situ* composites: (a)  $\text{TiB}_2/\text{Al}$ ; (b) and (c)  $\text{TiC}/\text{Al}$ . SEM.

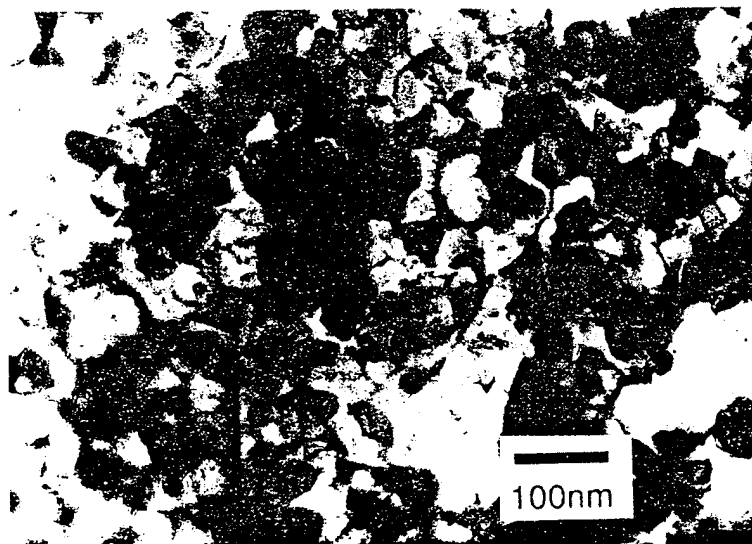


Figure 2-52 TEM micrograph of the SHS-processed TiC/Al *in situ* composite.

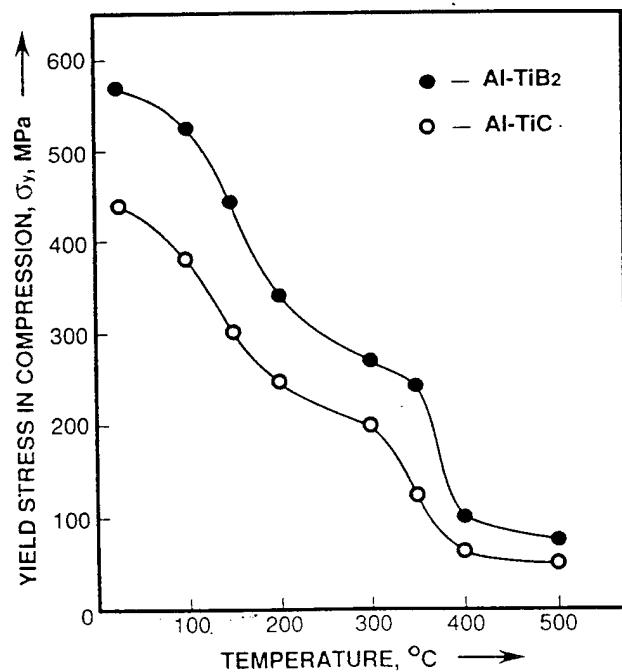


Figure 2-53 Yield stress in compression of the cold sintered ( $P = 3$  GPa,  $T = 300^{\circ}\text{C}$ ) SHS-processed TiC/Al and TiB<sub>2</sub>/Al *in situ* composites as a function of temperature.

## CHAPTER III.

### RGI PROCESS MODEL

#### A. RGI PROCESS MODEL

##### A.1. Theoretical Background

As the reaction proceeds, carbon and titanium convert into TiC and the concentration of Ti in the melt decreases. One of the important processing parameters is the time of complete conversion of Ti to TiC. To accurately predict the moment of complete conversion it is required to develop a kinetic model, expressing concentration of Ti in the melt as a function of time and then to compare the model with the experimental results.

There are two alternative mechanisms of TiC formation, namely the solution-reprecipitation mechanism and the solid-liquid interfacial reaction. The nature of these mechanisms is explained and illustrated in Figure 2-2. It was shown that the mechanism of TiC formation determines the size and morphology of TiC particulates, with solid-liquid interfacial reaction leading to the formation of coarser carbides than those formed via solution-reprecipitation mechanism. A brief discussion of the process mechanism, provided in this section leads to the conclusion that both processes are taking place simultaneously with solution-reprecipitation being dominant due to its fast kinetics. Thus, in order to control the synthesis process and repeatedly fabricate high quality MMCs, it is important to develop the kinetic model of the process and determine the mechanism of carbide formation.

##### A.2 Estimation of Limiting Stages in Kinetics of TiC Formation

The process of in-situ TiC formation in Al matrix via the RGI technique can be divided into seven steps, which can be grouped into two stages (see Figure 3-1):

Stage I. Efficiency of methane decomposition and carbon transfer to the reactive melt

1. Methane residence in the injection tube
2. Methane decomposition
3. Bubble rising
4. Diffusion of carbon particle to the bubble surface

Stage II. Mechanisms of carbide formation.

5. Carbon particle dissolution versus interfacial chemical reaction
6. Reaction of TiC formation in the solution
7. Titanium carbide nucleation in the solution

Comparison of characteristic times of these steps will reveal the limiting ones and provide a better insight to the mechanism of carbide formation. For example, comparison of the characteristic times of steps 1, 2 and 3 answers the question on where the complete methane decomposition occurs. The decomposition process starts in the heated part of the injection tube at temperatures higher than 900°C. Methane will completely decompose in the tube if the decomposition time is less than the time of gas residence in the heated zone. Complete decomposition will occur in the melt, while the bubble is rising, if the decomposition time is longer than the time of gas presence in the heated tube, but shorter than time of bubble residence in the melt. If methane decomposition happens even slower than that, then methane never fully decomposes in the melt and some carbon gets lost, decreasing the efficiency of carbide formation.

The calculations conducted are approximate, due to the lack of some required data in the literature. However, the missing constants were estimated to within an order of magnitude using the available information. This type of estimation is sufficient for qualitative analysis and understanding of the process kinetics, but cannot be used for precise calculations. All the characteristic times were estimated and summarized in Table 3-1 and the conclusions are listed below.

Time required for the gas mixture to reach the methane decomposition temperature (1300 K) is estimated to be about 0.3 sec. The argon-methane gas mixture spends about 0.4 sec in the heated zone of injection tube and 0.5 sec in the melt before the bubble erupts (the numbers can slightly vary depending on the system geometry - the tube length and the melt height). The decomposition time, however, was estimated to be about 0.2 seconds. Thus, by the time the Ar-CH<sub>4</sub> gas mixture approaches the injection tube nozzle it reaches the decomposition temperature and starts to decompose. The decomposition process continues in the melt and by the time a bubble reaches the melt surface, methane is fully decomposed. The analysis of step 4 - carbon motion to the bubble surface shows that it takes 10 - 50 seconds for 20 nm carbon particles, homogeneously nucleated in the bubble, to come in contact with the melt. By the time bubble comes to the melt surface not all the carbon in the bubble would reach the bubble/melt interface and react with Ti; thus some carbon gets lost in the surrounding atmosphere during the bubble eruption and deposits on the furnace walls.

The interfacial reaction of TiC formation at the solid carbon particle is 5 orders of magnitude slower than carbon dissolution process. Thus, the two processes are taking place simultaneously, but since the interfacial reaction is much slower, by the time a significant carbide layer can build up on a carbon particle, the particle may completely dissolve. It leads to the

conclusion that the TiC forms predominantly via solution-reprecipitation mechanism, i.e. carbon goes in the Al-Ti solution, reacts with Ti (reaction time of TiC formation in the solution is estimated to be 0.2 seconds) and then precipitates out. Due to the lack of data it was not possible to estimate the nucleation time and the nucleus size, but it is logical to assume that nucleation is not a limiting stage in the process of TiC formation.

The estimations conducted above reveals the limiting stages of in-situ TiC formation process via RGI and enables us to construct the quasi-homogeneous process model, which is presented below.

### **A.3. The Process Model Development**

Let's outline the simplified process sequence, considered in the model. Solid carbon particles, formed as a result of methane decomposition are introduced to the Al-Ti melt, where they dissolve immediately. The dissolved carbon first reacts with the melt components and subsequently the formation and precipitation of solid titanium carbide and aluminum carbide occurs.

#### **A. 3.1. Model Assumptions**

Let's designate  $C(t)$  to be the instantaneous carbon concentration in the melt, which is the same throughout the whole volume of the system;  $[Ti]$  and  $[Al]$  - are titanium and aluminum concentrations in the melt respectively. The process of TiC ( $Al_4C_3$ ) formation is described using the following assumptions:

- methane decomposition, carbon dissolution and TiC nucleation do not limit the process
- all points of the volume are equivalent, i.e. there are no temperature or concentration gradients throughout the melt and diffusion and convection are absent
- the interfacial solid carbon/liquid melt reaction can be neglected, because it was shown that the reaction time is much longer than the carbon dissolution time
- titanium carbide formation reaction:  $Ti + C = TiC$  is a second order chemical reaction and depends on both Ti and C concentrations
- aluminum carbide formation reaction:  $4Al + 3C = Al_4C_3$  is taken to be a first order chemical reaction with carbon being a limiting element

#### **A.3.2. Mathematical Representation**

Change of carbon, titanium and aluminum concentrations in the melt with time is expressed by the following equations with the initial conditions:

$$\frac{dC}{dt} = \frac{q}{V\rho_{melt}} - k_1[Ti]C\rho_{melt} - k_2C \quad C=0 \text{ at } t=0 \quad (14)$$

$$\frac{d[\text{Ti}]}{dt} = -nk_1[\text{Ti}]C\rho_{\text{melt}} \quad [\text{Ti}] = [\text{Ti}]_0 \text{ at } t=0 \quad (15)$$

$$\frac{d[\text{Al}]}{dt} = -mk_2C \quad [\text{Al}] = [\text{Al}]_0 \text{ at } t=0 \quad (16)$$

where

$q$  - the rate of carbon supply, g/sec (calculated from the rate of methane supply);

$V$  - the system volume,  $\text{cm}^3$ ;

$[\text{Ti}]_0$  and  $[\text{Al}]_0$  - initial concentrations of Ti and Al in the melt;

$k_1(\text{cm}^3\text{g}^{-1}\text{sec}^{-1})$ , and  $k_2(\text{sec}^{-1})$  - the rate constants for the reactions of TiC and  $\text{Al}_4\text{C}_3$  formation;

$n$  and  $m$  - the ratios of masses of components participating in stoichiometric reactions:

$\text{Ti} + \text{C} = \text{TiC}$  and  $4\text{Al} + 3\text{C} = \text{Al}_4\text{C}_3$ ;  $n = \frac{\mu(\text{Ti})}{\mu(\text{C})} \sim 4$ ,  $m = \frac{4\mu(\text{Al})}{3\mu(\text{C})} \sim 3$

Dividing (14) by (16) in the system (14 - 16) we obtain:

$$\ln [\text{Ti}] = \frac{n}{m} \frac{\rho_{\text{melt}} k_1}{k_2} [\text{Al}] + I, \text{ or } [\text{Ti}] = I \exp\left(\frac{n}{m} \frac{\rho_{\text{melt}} k_1}{k_2} [\text{Al}]\right)$$

where  $I$  is the integration constant and can be calculated from the initial conditions.

Let's  $\alpha = \frac{n}{m} \frac{\rho_{\text{melt}} k_1}{k_2}$ , then at  $t=0$   $[\text{Ti}]_0 = I \exp(\alpha[\text{Al}]_0)$  and  $I = [\text{Ti}]_0 \exp(-\alpha[\text{Al}]_0)$ . Thus we can express:

$$\frac{[\text{Ti}]}{[\text{Ti}]_0} = \frac{\exp(\alpha[\text{Al}])}{\exp(\alpha[\text{Al}]_0)} \quad \text{or} \quad \ln \frac{[\text{Ti}]}{[\text{Ti}]_0} = \alpha ([\text{Al}] - [\text{Al}]_0)$$

The parameter  $\alpha$  describes the ratio of rate constants for the reactions of carbon with Ti and Al. Since  $k_1$  is expected to be larger than  $k_2$ , then  $\alpha$  is larger than one.

Equations (14-16) are nonlinear differential equations and have to be solved numerically. However, since  $\alpha \gg 1$ , then it is possible to assume, that the product  $k_2C$  is much smaller than  $k_1[\text{Ti}]C$  and it can be neglected. For this to be true, the condition:  $\alpha[\text{Ti}] > 1$  has to be obeyed. This means that the reaction of  $\text{Al}_4\text{C}_3$  formation can be taken out of the consideration, until the concentration of Ti in the melt decreases to the value of  $[\text{Ti}] \sim 1/\alpha$ . Physically, it does not mean that the reaction of  $\text{Al}_4\text{C}_3$  formation does not take place at all, it occurs very slowly in presence of Ti and becomes significant only when Ti concentration in the melt becomes small. Now the system of equations (14 - 16) can be rewritten as follows:

$$\frac{dC}{dt} = \frac{q}{V\rho_{\text{melt}}} - k_1[\text{Ti}]C\rho_{\text{melt}} \quad (17)$$

$$\frac{d[Ti]}{dt} = -nk_1[Ti]C\rho_{melt} \quad (18)$$

Multiplying (17) by  $n$  and subtracting (18) out of (17) we obtain:

$$n\frac{dC}{dt} - \frac{d[Ti]}{dt} = n\frac{q}{V\rho_{melt}}$$

Taking  $\Theta = n\frac{q}{V\rho_{melt}}$  (sec<sup>-1</sup>), the rate of carbon supply per unit of melt mass, we can rewrite the previous equation as  $\frac{d}{dt}(nC - [Ti]) = \Theta$ . Subsequent integration and determination of integration constant from the initial conditions leads to the expression for carbon concentration as a function of time in the melt:

$$C = \frac{\Theta t - ([Ti]_0 - [Ti])}{n} \quad (19)$$

From (19) rate of Ti consumption is expressed form (17):

$$\frac{d[Ti]}{dt} = -k_1[Ti]^2\rho_{melt} + k_1[Ti]\rho_{melt}([Ti]_0 - \Theta t) \quad (20)$$

Solution of the equation (20), provides the expression of Ti concentration in the melt as a function of time, reaction rate constant and carbon supply rate.

Let's input the dimensionless parameters. The first one is a dimensionless concentration of titanium in the melt with respect to initial titanium concentration:  $x = [Ti]/[Ti]_0$  and the second one being dimensionless time  $\tau = t \Theta$ .

Rewriting the equation (20) in terms of dimensionless parameters we get:

$$\frac{1}{F} \frac{dx}{d\tau} = -x^2 + x - \frac{\tau x}{[Ti]_0} \quad (21)$$

$$\text{where } F = \frac{k_1[Ti]_0\rho_{melt}}{\Theta} = \frac{\text{Ti+C} \rightarrow \text{TiC reaction rate}}{\text{Rate of carbon supply}}$$

to simplify (21) let's input a new variable  $z = 1/x$ , then (21) becomes a linear equation:

$$\frac{1}{F} \frac{dz}{d\tau} = 1 - z - \frac{\tau z}{[Ti]_0}$$

The equation obtained now can be easily solved. Expressing  $z$  out of this equation and returning to the dimensionless concentration  $x$  and time  $\tau$  results in the following:

$$x = \frac{\exp F(-\frac{\tau^2}{2[Ti]_0} + \tau)}{1 + \sqrt{\frac{\pi F[Ti]_0}{2}} \exp(\frac{F[Ti]_0}{2}) \left\{ \operatorname{erf} \sqrt{\frac{\pi F[Ti]_0}{2}} + \operatorname{erf} \left[ \sqrt{\frac{\pi F[Ti]_0}{2}} \left( \frac{\tau}{[Ti]_0} - 1 \right) \right] \right\}} \quad (22)$$

This equation describes the dependence of dimensionless titanium concentration on time. Carbon concentration as a function of time, with account for the chemical reaction of carbon with Ti, can be now expressed from (19):

$$y = \frac{\tau}{[Ti]_0} - 1 + x(\tau) \quad (23)$$

where  $y = \frac{C}{C_0} = \frac{C_n}{[Ti]_0}$  is the ratio of instantaneous carbon concentration to the stoichiometric amount of carbon required for the complete conversion of titanium to the titanium carbide;  $x(\tau)$  can be taken from the equation (22). Figure 3-2 represents the plots of  $x(\log \tau)$  and  $y(\log \tau)$  for various values of  $F$ .

The above model enables the optimization of the process, but the knowledge of the reaction rate constant is required. However, some general regularities of the process can be obtained.

### A.3.3. Analysis of the Analytical Solution

As it is seen from the Figure 6, titanium concentration has a weak dependence on the value of  $F$  at large  $F$ 's. In addition, a dependence of titanium concentration on dimensionless time plotted in log scale:  $x=f(\log \tau)$  shows three main stages in the kinetic of conversion, as demonstrated in Figure 3-3.

Stage I (Initial). The stage is characterized by insignificant change in Ti concentration due to the lack of carbon in the system. Thus the reaction of TiC formation in this stage can be considered to be a first order chemical reaction with carbon being a limiting element. Analyzing the equations (17) and (18) at  $x \leq 1$  the width of this region ( $\tau_1$ ) can be easily expressed:  $0 < \tau_1 \ll 1/F$ .

Stage II (Intermediate). Here the rate of TiC formation depends on both - Ti and C concentrations, i.e. the reaction of TiC formation becomes a second order chemical reaction. The rate of Ti conversion reaches its maximum in this stage. The maximum rate correspond to the



inflection point on the  $x(\log\tau)$  curve  $(\bar{x}, \bar{\tau})$ . The value of  $(\bar{x}, \bar{\tau})$  can be determined analytically or from the plots  $x(\tau, [\text{Ti}]_0, F)$ . The width of this region can be determined by drawing a tangent through the inflection point  $(\bar{x}, \bar{\tau})$  till the intersection with the  $\tau$  axis. The intersection gives the value of  $\tau = \tau_2$ .

Stage III ( Final). At this stage the reaction of TiC formation again becomes a first order chemical reaction, with titanium being a limiting element due to the lack of titanium in the system.

As is seen from the Figure 3-2 carbon concentration starts to increase drastically when the titanium concentration drops significantly. Practically it corresponds to the beginning of the final stage III. The excess of carbon in the system leads to the formation of the undesired  $\text{Al}_4\text{C}_3$ , as was shown before. Thus the methane supply should be stopped after the stoichiometric amount of carbon was introduced to the melt.

For a given Ti concentration in the melt and a given methane flow rate the bubbling time required to provide the stoichiometric amount of carbon in the melt can be calculated:

$t = \frac{[\text{Ti}]_0 V \rho_{\text{melt}}}{nq}$ , or since  $\tau = t\Theta$ ,  $\tau = [\text{Ti}]_0$ . However, even though the amount of carbon introduced to the melt for the time corresponding to  $\tau = [\text{Ti}]_0$  is enough to provide the complete conversion, titanium may not completely convert to TiC, because the reaction of TiC formation is not instantaneous and some time is required for the reaction to occur. It can be clearly seen from equation (22), where  $x = [\text{Ti}]/[\text{Ti}]_0$  is calculated after accounting for the reaction rate of TiC formation, that at  $\tau = [\text{Ti}]_0$

$$x = \frac{\exp\left(\frac{F[\text{Ti}]_0}{2}\right)}{1 + \sqrt{\frac{\pi F[\text{Ti}]_0}{2}} \exp\left(\frac{F[\text{Ti}]_0}{2}\right) \left\{ \text{erf} \sqrt{\frac{F[\text{Ti}]_0}{2}} \right\}} \quad (24)$$

i.e.  $x \neq 0$ . The amount of unreacted titanium strongly depends on the value of  $F$ . Let's briefly analyze it:

(1)  $F \gg 1$ . The reaction rate is much faster than the rate of carbon supply to the melt. Since

$$\text{erf} \sqrt{\frac{F[\text{Ti}]_0}{2}} \rightarrow 1 \text{ at large } F; \text{ thus from (24)}$$

$$x \cong \sqrt{\frac{2}{\pi F[\text{Ti}]_0}}$$

For example at  $F=100$  and  $[Ti]_0=0.1$   $x(\tau=[Ti]_0)=0.252$ , i.e. at  $\tau=[Ti]_0$  there is still 25% of unreacted Ti. For  $F=1000$  the amount of unreacted titanium reduces to 8%. Thus  $x(\tau=[Ti]_0) \rightarrow 0$  at  $F \rightarrow \infty$ , which corresponds to the case of instantaneous reaction.

- (2)  $F \ll 1$ . The reaction rate is much slower than the rate of carbon supply to the melt. At small  $F$ ,  $x$  can be expressed from (24):

$$x \approx \frac{1}{1+2F[Ti]_0} \approx 1,$$

i.e. reaction still did not occur at  $\tau=[Ti]_0$ . In this case the melt cannot be cooled immediately after the methane supply is stopped, and should be exposed to a high temperature for a long time to allow the reaction of carbide formation to occur.

The equation (23) enables to express the amount of unreacted carbon at the time  $\tau=[Ti]_0$ :

$$y = x(\tau=[Ti]_0) \quad (25)$$

and for  $F=100$  there is 25wt.% of unreacted carbon.

On the basis of analytical solution of the model we can draw the following conclusions useful for the processing technology:

1. Injection of the stoichiometric amount of carbon into the melt is not sufficient condition for achievement of the complete conversion of Ti to TiC.
2. For each combination of reaction rate and rate of carbon supply, i.e. for each value of  $F$ , there are the best processing conditions leading to the highest degree of Ti conversion and the least content of free carbon in the melt.

The ideal processing should contain two steps:

Steps I: Introduction of carbon into the melt for the required time, which depends on the value of  $[Ti]_0$  and the flow rate of methane.

Steps II: Holding the melt at high temperature to allow the reaction of TiC formation to proceed to completion.

Equations (22) and (23) describe the first stage of the process. Expressions for the Ti and C concentration changes during the second stage can be easily obtained from the equations (17) and (18), where starting with the certain time corresponding to  $\tau=\tau^*$ ,  $q$  is taken to be zero. Calculations lead to the expressions for  $x$  and  $y$  at the time corresponding to  $\tau \geq \tau^*$ :

$$x = \frac{\frac{An}{[Ti]_0} \exp\left(-\frac{FAn(\tau-\tau^*)}{[Ti]_0}\right)}{1 - \exp\left(-\frac{FAn(\tau-\tau^*)}{[Ti]_0}\right) + \left(\frac{An}{x^*[Ti]_0}\right)} \quad (26)$$

$$y = x + A \frac{n}{[Ti]_0} \quad (27)$$

where  $\tau^*$  - corresponds to the time when methane supply was stopped,  $A = y^* - x^*$  is the integration constant and  $x^*$  and  $y^*$  are Ti and carbon concentrations corresponding to the moment of time  $\tau^*$ . The stoichiometric amount of carbon will be introduced to the melt at  $\tau = [Ti]_0$ , thus let's take  $\tau^* = [Ti]_0$ , in this case  $x^* = y^*$ , thus  $A = 0$ . Equations (26) and (27) now can be rewritten for  $\tau > [Ti]_0$ :

$$x = \frac{x^*}{1 + x^* F (\tau - \tau^*)} \quad (28)$$

$$y = x \quad (29)$$

Figure 3-4 illustrates the behavior of the curves, corresponding to the equations (28) and (29), i.e. plots the concentration of Ti and C versus the reaction time for different values of F. For any value of F, time required for a given degree of conversion of Ti to TiC by holding the melt at the processing temperature (processing step 2) can be obtained from the equation (28):

$$\tau = [Ti]_0 + \frac{(1 - \frac{x}{x^*})}{xF}$$

When the complete conversion is attained, titanium concentration in the melt becomes equal to zero, which gives an infinite value of t. It means that a 100% conversion is impossible, however, practically the degree of conversion of about 98% is feasible in the reasonable processing time frame. For example, in order to achieve 98% of conversion at  $F=100$  time of the melt holding after termination of methane supply is five times longer then the bubbling time, i.e. for titanium concentration of 10 wt.%, total sample weight of 150 g, and the methane flow rate being 0.1 SLPM, the duration of step 1 ( bubbling time ) is 70 minutes and the duration of step 2 (isothermal melt holding) is 350 minutes.

Therefore, the model enables us :

- (1) to express the concentration of Ti and C in the melt at any moment of time and for any relation between the TiC formation reaction rate and the rate of carbon supply;
- (2) to reveal three kinetic stages for the reaction of TiC formation
  - initial stage - a first order chemical reaction with carbon being a limiting element
  - intermediate stage - a second order chemical reaction
  - final stage - a first order chemical reaction with titanium being a limiting element, and
 the time frames for each stage
- (3) to determine two processing steps:

- introduction of carbon into the melt,
  - holding the melt at high temperature after termination of the carbon supply, to allow the reaction of TiC formation to proceed to the completion.
- and the time of the second step, required to achieve a high degree of conversion.

## A.4 Discussion of the Model

The carbon plate dissolution experiments, conducted to reveal the TiC formation mechanism and discussed in previous works [5,63] showed that TiC particles form via the solution-reprecipitation mechanism. Titanium carbide particulates found in the composites after the bubbling experiments conducted at the over a wide range of temperatures (1150-1600°C) demonstrate the same morphology and size range as the particles formed as a result of carbon dissolution experiments. It supports the hypothesis of solution-reprecipitation mechanism and suggests the assumption that the limiting stage of the process is not the reaction between Ti and C atoms in the solution, but the Ti and C diffusion or recombination and subsequent precipitation of solid TiC from the solution. This observation is in a good agreement with the results of the experiments conducted by Shteinberg and Knyazik [64]. The authors studied the reaction rate of TiC formation from pure Ti and C powders at the various temperatures. They found that at the temperatures higher than the Ti melting temperature the dependence of reaction rate on temperature becomes very weak. The dependence of the reaction rate of TiC formation on temperature corresponds to that of the diffusion coefficients of the components in the melt. In this case the process of TiC formation in the **liquid** solution is not an activated process and does not obey the Arrhenius law. Thus the process rate is determined by the diffusion of Ti and C in the melt as well as nucleation and growth kinetics. Therefore it can be assumed that a reaction rate constant for the reaction of TiC formation in Al matrix via RGI technique can be measured at only one temperature and applied to the reactions occurring at the other processing temperatures. Using this assumption let's calculate the reaction rate constant at 1300°C.

The experimental data on the degree of conversion of Ti to TiC as a function of time at 1300°C can be compared with the results of the theoretical model. To do that, the actual experimental time should be converted into the dimensionless time  $\tau = t \Theta$ , where  $\Theta = n \frac{q}{V \rho_{\text{melt}}}$  is the rate of carbon supply per unit of melt mass. For the given processing conditions:  $V \rho_{\text{melt}} = 150 \text{ g}$ ,  $n=4$ ,  $q=8.89 \times 10^{-4} \text{ g/sec}$ ,  $\Theta$  becomes  $2.37 \times 10^{-5} \text{ sec}^{-1}$  and dimensionless time is  $\tau = 2.37 \times 10^{-5} t$ . Figure 3-5 shows the experimental dependence of Ti concentration on time presented in the dimensionless coordinates  $x-\tau$ . It is clear from the Figure 3-5 that experimental data are in good agreement with a theoretical curve corresponding to  $F=200$ . Maximum

deviation from the theoretical curve is 5%. Such a comparison allows us to conclude that the actual reactions are second order chemical reactions, where the reaction rate of TiC formation depends on both titanium and carbon concentration as was illustrates in Figure 3-3. Comparison of the experimental and theoretical results enables one to determine the value of the reaction rate constant.

Using the relation between F and  $k_1$  :

$$F = \frac{k_1 [Ti]_0 \rho_{melt}}{\Theta} = \frac{\text{TiC formation reaction rate}}{\text{rate of carbon supply}}$$

if  $F=200$ ,  $[Ti]_0=0.1$ ,  $\rho_{melt}=2.88 \text{ g/cm}^3$ , we obtain the value for  $k_1=1.64 \times 10^{-2} \text{ cm}^3/\text{g sec}$ .

Now, knowing  $k_1$ , the initial Ti concentration, melt weight and the methane flow rate, we can obtain the parameter F, which was used in the model in calculation of the degree of conversion. Ability to determine the parameter F enables us to check the applicability of the model predictions to experimental reaction kinetics.

Table 3-2 summarizes results of the comparison the model predictions and the experimental results, which were shown in Table 2-7. It can be seen from Table 3-2, that the results of the theoretical model are in good agreement with the experiment, assuming that the rate constant does not strongly depend on temperature. The disagreement between the model and experiment is observed at high volume fractions of reinforcement. It can be explained by the increment of the melt viscosity; to include this effect a correction for a reaction rate constant should be made.

## A.5. Summary

1. Two competitive processes are taking place:

- dissolution of C with subsequent precipitation as TiC from the Al-Ti melt, and
- simultaneous interfacial reaction of TiC formation at the C/Al-Ti melt interface.

Titanium carbide, however, forms predominantly via solution-reprecipitation mechanism in the melt due to its fast kinetics.

2. A kinetic model of the process of TiC formation via RGI technique has been developed.

The model predicted the degree of Ti and C conversion to TiC, (i.e.  $V_f$  of TiC) as a function of reaction time.

3. Three kinetic stages for the reaction of TiC formation have been revealed:

- initial stage - a first order chemical reaction with C being a limiting element
- intermediate stage - a second order chemical reaction

- final stage - a first order chemical reaction with Ti being a limiting element

4. Two ideal processing steps have been determined:

- introduction of the stoichiometric amount of carbon into the melt
- holding the melt at high temperature after termination of carbon supply, to allow the reaction of TiC formation to proceed to completion.

5. Diffusion limited, TiC formation rate constant has been measured.

**Table 3-1. Comparison of the Characteristic Times of the Steps of TiC Formation**

Step #	Name of the Step	Characteristic time, sec	Concluding remarks
<b>Stage I. Methane decomposition efficiency</b>			
1	Methane residence in the injection tube	0.4	• Methane reaches the decomposition temperature inside the injection tube.
	(time required to reach decomposition temperature 900°C)	0.3	• Once the decomposition temperature is reached  CH <sub>4</sub> starts to decompose immediately in the tube.
2	Methane decomposition	0.2	• Decomposition is continued in the bubble and by the time
3	Bubble residence	0.5	when bubble reaches the melt surface methane is fully decomposed.
4	Diffusion of 50nm carbon particle to the bubble surface	120	• Only a fraction of carbon inside the bubble comes into contact with the bubble/ melt surface during the bubble rising time, which leads to carbon losses
<b>Stage II. Mechanisms of TiC formation</b>			
5	Carbon particle dissolution vs interfacial chemical reaction	10 <sup>-3</sup> –	• Interfacial reaction of TiC formation is 5 orders of magnitude slower than carbon particle dissolution. Thus a small carbon particle dissolves before any significant TiC layer forms around it.
6	Reaction of TiC formation in the solution	0.2	• TiC forms predominantly via solution-precipitation reaction in the melt
7	Titanium carbide nucleation in the solution	–	• Assumed that nucleation does not limit the process of TiC formation

**Table 3-2 Comparison of the Experimental Results and Model  
Predictions for Al/TiC Composites Produces by  
Reactive Gas Injection**

Alloy Composition.	Temp, °C	CH <sub>4</sub> flow rate, l/min	Calculated Value of Parameter F	Model Prediction for v/o of TiC at $\tau=1.5[\text{Ti}]_0$	Conversion observed, v/o of TiC
Al-10wt.%Ti	1300	0.1	200	6.7	top ~ 8 bot. ~ 6
Al-27wt.%Ti	1500	0.1	628	18.4	top 22±3 bot. 14±3
Al-38wt.%Ti	1550	0.1	977	28.5	top 33±6 bot. 13±4
Al-60wt.%Ti	1600	0.5	275	49.5	~40



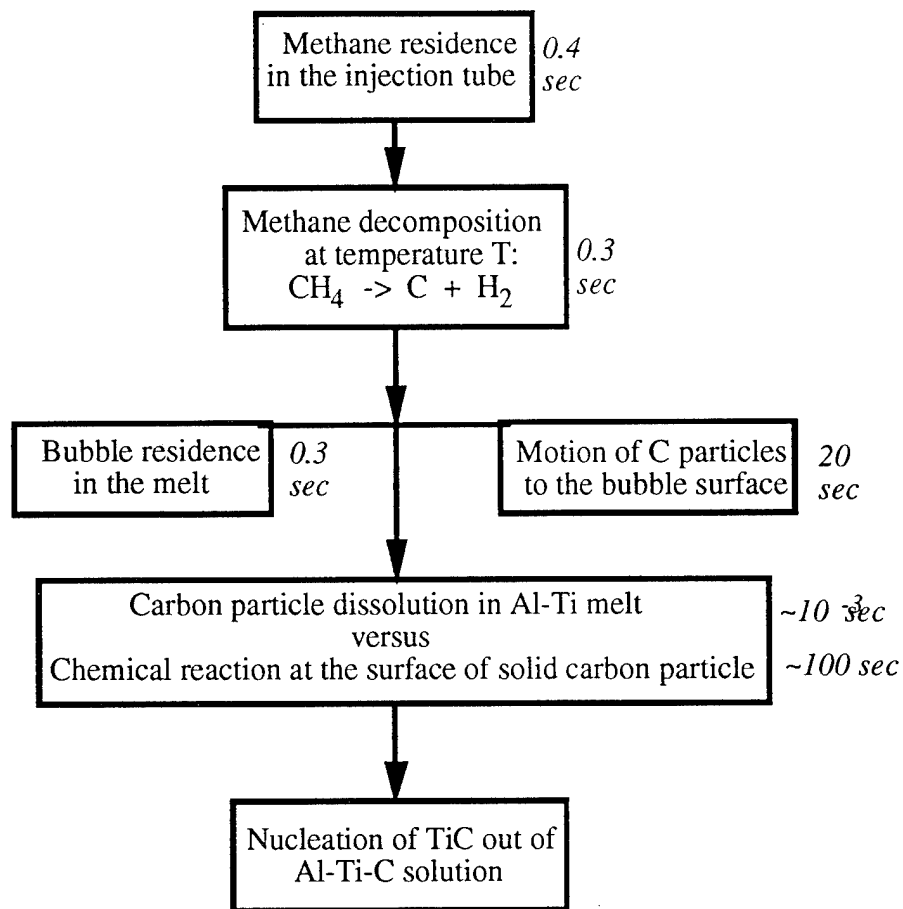


**Figure 3-1** Schematic representation of the processing steps.

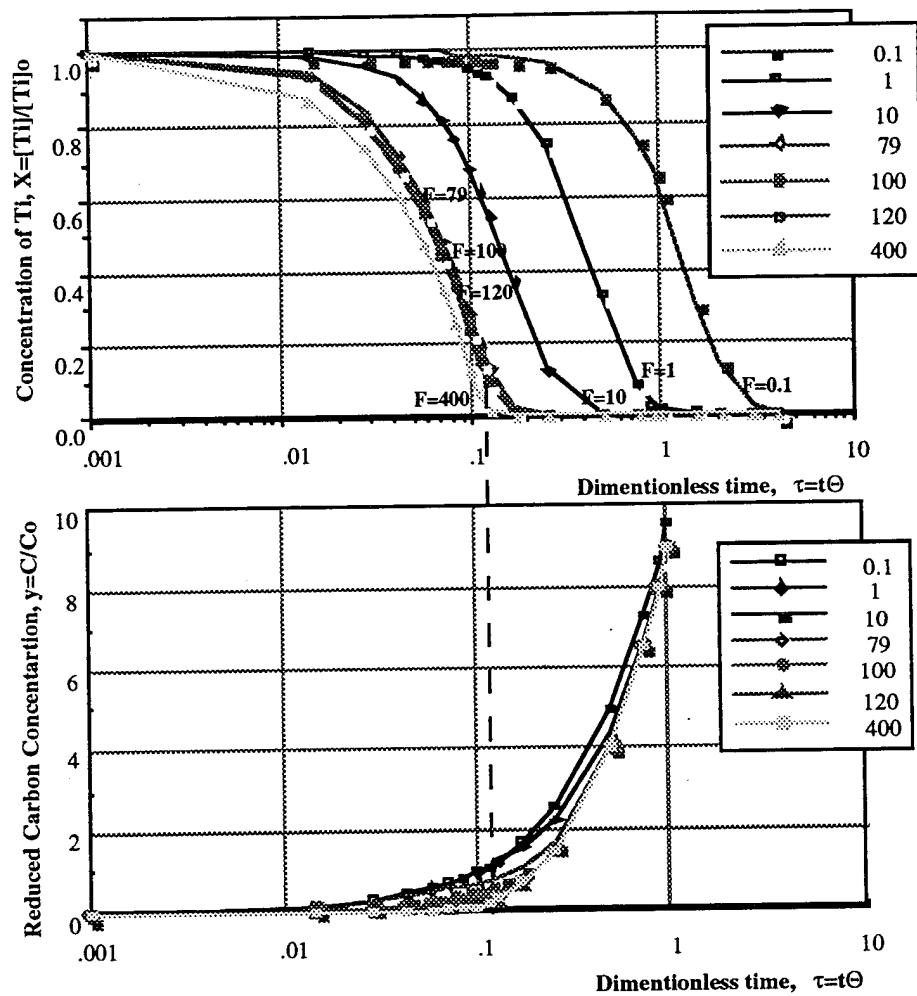


**Figure 3-2** Titanium and carbon concentrations expressed in terms of dimensionless parameters  $x$  and  $y$  versus the dimensionless time,  $t=tQ$  (in log scale).

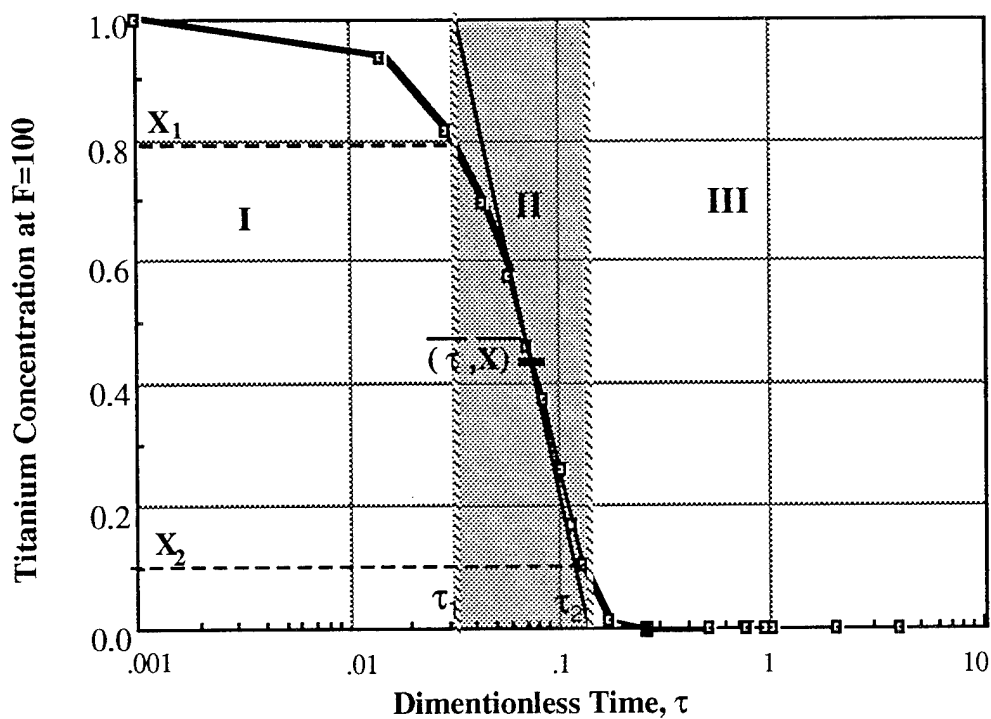


**Figure 3-3** Dimensionless Ti concentration vs. dimensionless time (log scale), illustrating three kinetic regions of TiC formation.

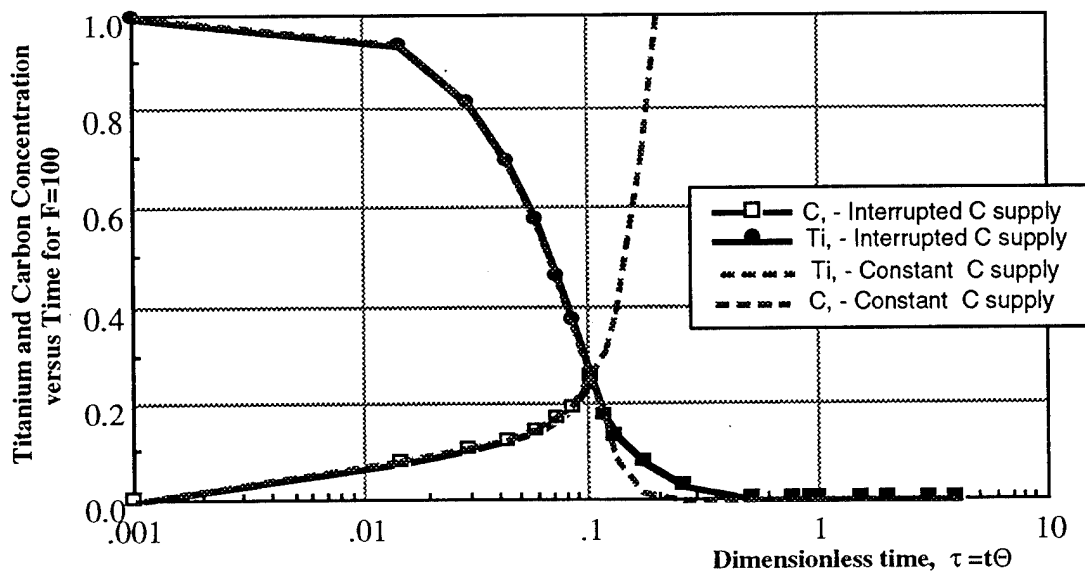


**Figure 3-4** Dimensionless titanium and carbon concentrations versus the dimensionless time, (in log scale), showing the change of Ti and C concentration during the RGI process before and after carbon supply termination.

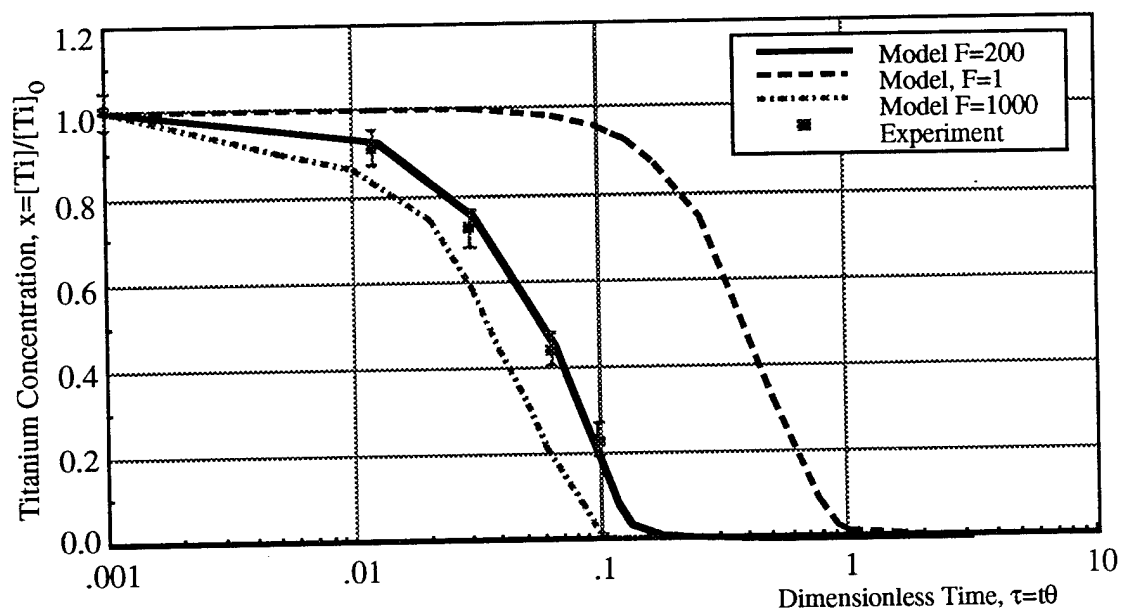


**Figure 3-5** Comparison of experimental results with the theoretical predictions for  $F=1, 200, 1000$ .

## CHAPTER IV.

### A. *IN-SITU* PROCESSING OF NICKEL MATRIX COMPOSITES

#### A.1. Processing Background

In the present work, two in-situ processing techniques:

- (1) Reactive Gas Injection (RGI), and
- (2) Self-propagating High-temperature Synthesis (SHS)

were used to produce Ni-based metallic and intermetallic matrix composites (MMC's and IMC's respectively). The RGI process involves injection of a reactive carbon or nitrogen bearing gas into an alloy melt held at 150-250 °C above its liquidus. Decomposition of the gas on contact with the melt produces carbon or nitrogen which reacts with the alloying element and forms the carbide or nitride reinforcement. TiC/Ni and NbC/Ni composites were produced by injection of methane into the corresponding alloy melts. Two TiC morphologies were found:

- a) faceted particles of size 5-20  $\mu\text{m}$ , and
- b) eutectic lamellae of thickness 1-10  $\mu\text{m}$ .

Microstructural examination supported by phase diagram data suggests that the reaction mechanism is dissolution of carbon into the alloy melt followed by precipitation of the carbide through a eutectic reaction. Attempts to produce nitrides resulted in the production of a layer of TiN on the top and side surfaces of the casting. SiC/Ni and Si<sub>3</sub>N<sub>4</sub>/Ni composites were also attempted but were not produced.

The SHS process is based on the local initiation of a highly exothermic reaction between mixed elemental powders and the propagation of the resultant reaction wave through the compact. In-situ reinforcement formation reactions were incorporated in the combustion synthesis of TiB<sub>2</sub>/NiAl and TiC/FeAl composites. Reinforcement particle sizes depended, among other things, on the reaction front temperature and were of the order of 10  $\mu\text{m}$ . The mechanism of reaction is believed to be formation of a transient liquid phase, dissolution of the ceramic precursor elements in the liquid phase, exothermic ceramic particle formation reaction followed by precipitation of the ceramic particles in the matrix.

#### A.2. Thermodynamic Analysis

The following section discusses the thermodynamics of in-situ reactions and considers the sequence of steps that determine the kinetics of the reactions. Wherever available, binary and ternary phase diagrams of the alloys used in this work are provided, along with a description of the important features.

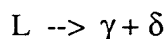
### A.2.1 RGI Process

In previous in-situ experiments involving Al-Ti alloys as well as in the ones described in the present work with Ni-Ti alloys, the matrix metals Al and Ni are weak carbide formers compared to Ti. A look at the Ellingham diagram for carbides (Figure 4-1) gives a good idea of the stability of carbides with respect to each other [65]. Note that the  $\Delta G_f$  of TiC, NbC and SiC are much lower than that of  $Ni_3C$ , which is positive at all temperatures, indicating that it is unstable at all temperatures. Thus, Ni-based carbide composite systems are an ideal choice for illustrating the RGI process for high temperature composites.

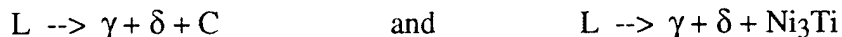
It must be noted that the Ellingham diagram shows the  $\Delta G_f$  of the carbides taking the standard state of the metal as 1 mole of pure metal reacting with pure carbon, which implies an activity of 1 for the metal. In the in-situ RGI process, we are dealing with metallic melts, and the activities of the carbide forming elements can be very different from 1. TiC-Ni is a candidate material for cemented carbides. It is of importance to know the solubility of TiC in Ni and vice versa for information on phase stability during processing and service. Thus, there has been some activity in the past to determine the ternary Ni-Ti-C phase diagram. Stover and Wulff have studied the Ni-rich region of the Ni-Ti-C system since that is important in liquid phase sintering of cemented carbides [66]. They have presented isothermal sections of the ternary diagram at 870 °C and 1200 °C. Some vertical sections, which will be discussed below, have also been given. In addition, solubility of Ti and C in solid Ni has been presented in the form of projections on the basal plane.

Before discussing the ternary Ni-Ti-C system, we shall consider the binary systems Ni-C, Ni-Ti and Ti-C [67]. Figure 4-2 (a)-(c) show the three binary diagrams along with a list of the phases present and their compositions. Examination of these shows that solid Ni is capable of dissolving upto 0.6 wt.% C at the eutectic temperature of 1326.5 °C. However, more than 2 wt.% C is dissolved by liquid Ni at 1600 °C. The Ni-Ti system is characterized by several intermetallic phases, notably  $Ni_3Ti$ , NiTi and  $NiTi_2$ . Solid Ni dissolves a maximum of 11.6 wt.% Ti at 1304 °C. The intermetallic phase  $Ni_3Ti$  forms at a composition of 21 wt.% Ti and melts congruently at 1380 °C. Liquid Ni at 1600 °C has an extensive solubility for Ti. The main characteristic of the system Ti-C is the highly non-stoichiometric compound, TiC (~10-19. wt.% C). The highest melting compound has a composition of Ti-16 wt.% C and melts at 3067 °C. A second carbide  $Ti_2C$  is seen between ~10 and 12.4 wt.% C. The TiC phase is joined on either side by eutectics with Ti and C at 1650 and 2776 °C respectively.

The isothermal section of the ternary Ni-Ti-C system at 1200 °C reported by Stover and Wulff is given in Figure 4-3.  $\gamma$  phase is the Ni solid solution and the  $\delta$  phase is TiC. No ternary compounds are reported at this temperature. The solubility of C in TiNi and Ni<sub>3</sub>Ti is negligible, while Ti<sub>2</sub>Ni dissolves a few atomic percent. There is a quasi-binary eutectic reaction



at a temperature of 1307 °C. This region is flanked by ternary eutectic reactions



at temperatures of 1270 and 1295 °C respectively. Note that both  $\gamma$  and  $\delta$  phases have a wide composition range. However, it is of advantage to produce stoichiometric TiC, since it exhibits the best properties.

In the RGI process, the starting Ni-Ti alloy composition is determined according to the required TiC volume fraction and carbon is added progressively through gas decomposition. For example, for a 20 vol.% TiC/Ni composite, the starting alloy composition is Ni-11.85 at.% Ti and the final composition is Ni-10.6 at.% Ti-10.6 at.% C. It must be noted that both Ti and C go into solution in Ni at the processing temperatures used in the RGI process. The expected final compositions of the different alloys used in the present work are marked in Figure 4-3 with filled circles.

To illustrate the sequence of reactions that occur in the Ni-Ti-C system as the temperature is decreased from 1600 °C to room temperature, consider the vertical section shown in Figure 4-4. This section has been drawn between Ni-20 at.% C alloy and Ni-20 at.% Ti alloys. Suppose that the final alloy composition after completion of gas injection is given by the point A (12 at.% Ti and C). On cooling below 1350 °C, a primary TiC phase precipitates. This is followed by a ternary phase field  $\gamma + \delta + L$ . The liquid region finally solidifies to give  $\gamma + \delta$  through the eutectic reaction mentioned earlier. The above alloy composition gives 22.5 vol.% TiC on complete conversion. The primary carbide precipitates as angular grains while the eutectic carbide precipitates as plates.

Further work on the Ni-Ti-C ternary has been reported by Ballamy and Hucke, who studied the liquid Ni-titanium carbide equilibrium[68]. They have presented liquidus curves showing the solubility of Ti and C in liquid Ni at 1300, 1400 and 1500 °C. Micrographs included by them reveal two kinds of carbide morphologies- angular and lamellar. A clear demarcation is seen between the top and bottom halves of the micrographs, the angular carbides

being present only in the top half. In addition, they have calculated the activities of the three components and the excess free energy as a function of Ni content at 1500 °C. Their data suggests that the system exhibits strongly negative deviation from ideality, as can be predicted from the existence of compounds in the respective binaries.

The phase diagrams of the other alloy systems used in the RGI experiments are briefly discussed below. The binary Ni-Nb system is shown in Figure 4-5(a)[67]. Three intermetallic compounds - Ni<sub>8</sub>Nb, Ni<sub>3</sub>Nb and Ni<sub>6</sub>Nb<sub>7</sub> are reported at compositions of 16.5, 33.1-38, and 60.9-65.5 wt.% Nb respectively. The highest melting intermetallic compound is Ni<sub>3</sub>Nb and it melts congruently at 1399 °C. As in the Ni-Ti case, Ni has an extensive solubility for Nb, especially in the liquid state. The Nb-C phase diagram is shown in Figure 4-5 (b) [69]. The diagram shows a wide region of non-stoichiometry for the equimolar phase from NbC<sub>0.7</sub> to NbC<sub>1.0</sub>. A second carbide phase Nb<sub>2</sub>C is also present.

Figure 4-6 (a) and (b) show binary diagrams Ni-Si and Si-C. The Ni-Si system shows a large number of intermetallic compounds, all of which are stable. Liquid Ni at 1600 °C has an unlimited solubility for Si. The Si-C system shows one compound SiC at a composition of 30 wt.% C. This is a relatively simple system compared to the previous carbide phase diagrams since Si does not show any solubility for carbon.

### A.2.2 SHS Process

The SHS reaction occurs in a very short interval of time (of the order of milliseconds); hence the system can be considered adiabatic. Thus, the enthalpy of formation of the products is a measure of the feasibility of the reaction. To initiate the reaction, the reactants are raised to an ignition temperature  $T_{ig}$ , which triggers an exothermic reaction in a thin layer at that temperature. The heat generated by the reaction is used to increase the temperature of the products to the adiabatic temperature,  $T_{ad}$ , i.e. the temperature of the propagating reaction front.

Figure 4-7 is a schematic representation of the enthalpy-temperature relationship of reactants and products involved in the SHS reaction. The heat balance can be written as follows:[70]

$$\Delta H_{f,T_{ad}} = \Delta H_{f,T_{ig}} + \int_{T_{ig}}^{T_{ad}} C_p(T) dT = 0$$



and so

$$-\Delta H_{f,T_{ig}} = \int_{T_{ig}}^{T_{ad}} C_p(T) dT$$

where  $C_p$  is the combined heat capacity of the products. The above equations describe the heat balance in the narrow reaction zone in Figure 1-6. Actually, a part of the heat of reaction is utilized to raise the reactant layer just below the reaction zone to  $T_{ig}$ , thus ensuring the propagation of the reaction front. The reaction front temperature in this case is lower than the adiabatic temperature. Depending on the exothermicity of the reaction and the temperature of the reactants, the final temperature can be greater than the melting point of at least one of the components. Since diffusion coefficients are of the order of  $10^3$  greater in a liquid than in a solid, the formation of a liquid phase during the propagation of the reaction front gives a more efficient conversion of reactants to products.

In the SHS reactions described below, elemental graphite or boron powder was mixed with metal powders. The formation of carbide or boride reinforcement ( $TiC$ ,  $TiB_2$ ) occurred by diffusion of Ti to the surface of the carbon or boron particle through a liquid film. The form and composition of the product depends on many factors. Finer initial carbon particle size results in finer ceramic reinforcement particle. The initial metal powder particle size is important in solid state SHS reactions because of the shorter diffusion distances involved. In general, a higher green density results in products of higher final density. Higher reaction front temperatures give a cleaner product but may also result in particle coarsening. The formation of a liquid phase accelerates diffusion and favors the kinetics of the process. To summarize, the controlling process parameters for SHS reactions are:

- final temperature of reaction front,
- formation of liquid phase at the reaction front,
- initial powder particle size,
- green density of initial compact,
- initial powder alloy composition.

Further details of modeling of SHS reactions can be obtained from [71]. The SHS process has been used to produce intermetallic matrix composite powders. The above factors are used to explain the microstructures of the composite powders obtained and the sizes of the reinforcements obtained.

### A.3.Experimental Procedure

In-situ metallic and intermetallic composites were processed by two methods: (1) Reactive Gas Injection; and (2) Self propagating High temperature Synthesis. The following section describes the experiments carried out by both methods and any post-processing analysis that the samples were subjected to. The section is divided into two parts and provides an experimental matrix for each method.

#### A.3.1 RGI Process

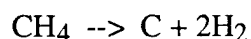
The in-situ Reactive Gas Injection (RGI) method was used to produce Ni-based high temperature MMC's. The schematic of the process control system for carrying out the in-situ reactions by the RGI process is shown in Figure 2-10 and described in Chapter II, (section A3.2.1).

A schematic of the reaction crucible is shown in Figure 1-1. The metallic elements in solid or powder form (Ni, Ti, Nb, Si) were melted in an alumina crucible which was placed in a graphite crucible. Graphite is used regularly in induction furnaces as it readily interacts with induction fields and increases heating efficiency of the furnace. The alumina crucible was wrapped in graphite cloth to reduce the temperature gradient from the susceptor to the crucible and thus prevent crucible cracking due to thermal shock. Gas injection into the melt was done through a 3 mm diameter alumina tube whose open end was ~10 mm from the bottom of the crucible. Melt temperature was monitored via a W-Re, C-type thermocouple placed in a closed end alumina tube attached to the gas injection tube. Ti, Ni, and Nb used were in the form of commercial purity rod, 10 mm diameter spherical shot and -325 mesh powder respectively. Si was used in both powder and bulk form. The amounts of Ti, Nb and Si were calculated based on the level of carbide and nitride reinforcement desired. The alloy compositions used are given in Table 4-1 along with the expected reinforcement level.

The gases used during the experimental runs ( $\text{CH}_4$ , Ar,  $\text{N}_2$ ) were carried to the furnace chamber through stainless steel tubes. The flow rate of the gases were regulated by electronic flow controllers supplied by Porter Instruments. Flow rate variation was in steps of 0.1 SLPM (Standard Liters Per Minute). Microscopic filters, e.g. 0.5  $\mu\text{m}$ , were used before the flow controllers to remove dust particles from the gas. After passing through the flow controllers, the inert and reactive gases ( $\text{Ar}/\text{CH}_4$ ) were mixed and passed through Drierite and Oxyclear to remove water vapor and oxygen. The amount of reactive gas required for complete conversion of the carbide forming elements was determined assuming that the formation reaction was 100

%. The amount of gas actually injected was intended to be ~1.5 times this amount. The thermocouple and gas flow controllers were connected to an IBM-based data acquisition and control system that allowed continuous monitoring and control of these process parameters.

The alloys used were melted under argon atmosphere. The molten alloy was homogenized for ~30 minutes at 150-250 °C above the liquidus of the particular alloy composition used (this was about 1600 °C for most alloys). The reactive gas was then injected into the melt along with argon which served as the carrier gas. The combined gas flow rate was kept below 0.5 SLPM so as to prevent splashing of the molten alloy. When the gas came in contact with the molten alloy, the methane underwent decomposition by the reaction,

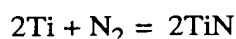
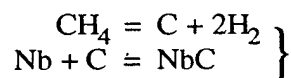
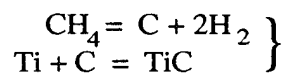


and released carbon into the melt. Subsequent reaction of carbon with Ti, Nb or Si was expected to form the carbides. The hydrogen generated during the reaction was burnt at the outlet. After the requisite amount of gas was injected, the reactive gas was shut off. Inert gas injection was continued for about 15 minutes to degas the melt and to homogeneously distribute the carbides in the melt by agitation. Power to the induction coils was then shut down and the composite allowed to solidify in the crucible.

The cast ingot was sectioned using an alumina wheel and mounted in bakelite. Metallographic specimens were oriented in such a way that the variation of microstructure through the depth of the ingot could be viewed. The samples were polished with silicon carbide paper and diamond paste and etched with a mixture of 1 part nitric acid and 3 parts acetic acid for 15 s. Characterization methods used were: (1) optical microscopy; (2) X-ray diffraction and (3) scanning electron microscopy. Optical micrographs were obtained on a Zeiss microscope. Scanning electron microscopy was performed in a JEOL JSM-35CF machine with a WDX attachment for Ni and Ti detection and generation of elemental maps. X-ray diffraction patterns were obtained on a Siemens D-500 diffractometer.

Some samples (marked with a \* in Table 4-2) were aged in order to determine the equilibrium microstructure. The specimens were aged at 1200 °C for 24 hours in an argon atmosphere. The specimens showed negligible weight changes due to the annealing. These samples were prepared and examined in the same way as above.

The reactions carried out by the VLS process were:



### A.3.2 SHS Process

The Self-propagating High-temperature Synthesis (SHS) process was used to produce aluminum and aluminide matrix composite powders. The composites were produced in collaboration with Exotherm Corporation. Table 4-3 lists the different reactions carried out along with the expected products. The SHS composites were made by mixing elemental powders of the metals (e.g. Ni, Al and Ti) and carbon or boron in stoichiometric ratios to produce various volume fractions of carbide or boride reinforcements. The powder mix was compacted to 55% of theoretical density and placed in a chamber to carry out the combustion reaction. Figure 1-6 is a schematic of the experimental setup used in the SHS process. The reaction was initiated by igniting the compact at the top with a Mg ribbon. The heat of reaction generated in the thin reacting layer causes the layer below it to reach the reaction temperature and sustain a reaction front. This reaction front travels through the sample leaving behind the product. The highest temperature reached at the reaction front was measured by a thermocouple. A representation of the temperature profile along the depth of the sample during the propagation of the wave is also shown in Figure 1-6. A typical SHS reaction is shown below for the formation of NiAl/TiB<sub>2</sub> composite powders:



Phase identification was done by X-ray analysis in a Siemens D-500 X-ray diffractometer for all samples. The samples that incorporated an in-situ reinforcement formation reaction were examined microstructurally. Specimens were mounted in bakelite and examined using a Zeiss optical microscope and a JEOL JSM-35CF scanning electron microscope.

### A.4. Results and Discussion

Reactive Gas Injection (RGI) and SHS processing routes were used to produce nickel based metallic and intermetallic matrix composites. The following section presents the results of the experimental runs. The results obtained were in the form of X-ray diffraction patterns and micrographs of the composites and sizes and morphologies of the reinforcement phases.

#### A.4.1 RGI Process

Composites produced by reactive gas injection into an alloy melt are listed in Table 4-1. The table also gives the expected volume fractions of the reinforcements calculated from the amount of reinforcement precursor alloyed into the matrix metal assuming full conversion. The process details of the experiments carried out using the RGI process are tabulated in Table 4-4. This table provides the following information:

- **Reaction Temperature (°C):** This is the temperature at which injection of the reactive gas into the molten alloy was started. This temperature was usually about 150-250 °C above the liquidus of the alloy being melted. Such high temperatures were warranted due to the expected increase in melt viscosity during gas injection.
- **Reactive Gas Flow Rate (SLPM):** The flow rates of the gases was measured in Standard Liters Per Minute, i.e. the volume of gas flowing through the flow controllers measured at STP (Standard Temperature and Pressure). The flow rate was controlled to moderate the highly exothermic nature of the carbide and nitride formation reactions.
- **Injection Time (min):** This is an important experimental process parameter since it determines the amount of carbon or nitrogen being supplied to the melt. This, in turn, determines the amount of carbide or nitride formed. In case of runs NTC2, NTN and NSN, the amount of gas injected was greater than that theoretically required, assuming complete dissociation of the gas and complete conversion to the carbide/nitride.
- **Theoretical Vol.% Reinforcement:** This value was calculated by assuming that all the carbon/nitrogen injected into the melt or alloying element in the melt was converted to the corresponding carbide or nitride.

Figure 4-8 shows the temperature and flow rate history of a typical RGI run from which the experimental data of melt temperature and gas injection time were derived. The details of the curve are discussed in the next section. The subsections below present the results of microstructural characterization of the RGI samples.

##### ***A.4.1.1 Carbide formation:***

The samples obtained on sectioning the cast RGI composites (TiC/Ni, NbC/Ni, SiC/Ni) were analyzed by X-ray diffraction, optical and scanning electron microscopy. The aim was to determine the phases present in the cast samples and to determine the morphology and size of the in-situ produced reinforcement particles. These results are tabulated in Table 4-5.

Two distinct morphologies of carbides - faceted and interdendritic lamellar - are seen in the cast composites. The lamellar carbides surround the primary dendrites of Ni and are seen distinctly in the low-Ti experiments (Figure 4-9). The thickness of the lamellae lie between 1

and 5  $\mu\text{m}$  and form a more or less continuous layer around the Ni dendrites. The faceted carbides are seen only in high-Ti experiments and have sizes ranging from 1 to 40  $\mu\text{m}$  depending on the chemistry of the sample (Figure 4-10). Alloys where higher volume fraction reinforcements were attempted showed a preference for forming intermetallic phases. In addition to this, there was usually a clear demarcation between the top and bottom halves of the sample, faceted carbides being present in the top half alone. It was not possible to form composites of SiC/Ni, presumably due to insufficient thermodynamic driving force in addition to kinetic limitations. An NbC/Ni composite was produced with a microstructure similar to that one of the TiC/Ni composite, though on a finer scale (Figure 4-11). The significance of these results are discussed in detail in the following chapter.

#### ***A.4.1.2 Nitride formation:***

Preliminary studies in the production of nitride-reinforced composites were done on TiN/Ni (NTN) and  $\text{Si}_3\text{N}_4/\text{Ni}$  (NSN) composites. A layer of TiN was formed on the surface of sample NTN (Figure 4-12). There were, however, no nitrides in the bulk of the sample. The experiment to produce  $\text{Si}_3\text{N}_4/\text{Ni}$  composite was not successful; there were no nitrides anywhere in the sample. Examination of the gas injection times (Table 4-5) for these two runs shows that the amount of  $\text{N}_2$  injected into the respective alloy melts was far in excess of the theoretical amount required. The above observations suggest that the nitride formation reaction (in the case of NTN) was a surface contact reaction between the  $\text{N}_2$  atmosphere and the Ni-Ti melt. This is discussed further in the following chapter.

#### **A.4.2 SHS Process**

The various combustion reactions carried out to produce metallic and intermetallic matrix composites are listed in Table 4-3. The reaction products were in the form of loose powders. Characterization of these powders by X-ray diffraction for the samples listed revealed that the products were indeed what were expected. Furthermore, the patterns are sharp and free of undesirable phases. The maximum temperature reached by the reacting powder mixture is directly related to the exothermicity of the SHS reactions and ranged from 1700 to 1920  $^{\circ}\text{C}$ . The samples that incorporated in-situ reactions to form the reinforcement were analyzed microstructurally. The TiC and  $\text{TiB}_2$  particle sizes range from less than 1  $\mu\text{m}$  in the Al-matrix composite powders to  $\sim 40$   $\mu\text{m}$  in the FeAl-matrix composite powder. In general, the sizes ranged from 1 to 10  $\mu\text{m}$ . The results of the microstructural analysis of the SHS processed powders is presented in Table 4-2. The mechanism of the in-situ SHS reactions is discussed in greater detail later.

## A.5. Discussion

The following chapter discusses the results presented in the preceding chapter and traces the development of the composite microstructures. The focus of the discussion is thermodynamic. A mechanism for the in-situ reactions is proposed on the basis of the observed microstructures and examination of available binary and ternary phase diagrams. As before, the chapter is divided into two parts, each dealing with a single processing scheme.

### A.5.1 RGI Process

Some of the main issues that are of concern in the RGI process are listed below:

- (1) Reaction efficiency
- (2) Reinforcement formation
- (3) Reinforcement morphology, size and distribution

Though these issues are of a general nature, the following discussion is focused on the production of carbide reinforcements through methane decomposition. The conclusions drawn will help in designing future experiments.

#### A.5.1.1 *Reaction efficiency*

The reactions that lead to the formation of the carbide are:

- a) methane decomposition
- b) carbon dissolution in the Ni-Ti melt
- c) TiC formation

The efficiency of carbide formation can be quantified by the ratio of the amount of Ti converted into TiC to the maximum carbide amount obtainable due to equilibria and composition. The methane flow rate determines the rate of carbon supply to the melt. The second step listed above determines the mechanism of carbide formation and is based on thermodynamic and kinetic considerations. The third step essentially determines the efficiency of the overall reaction. Each of the above steps will be considered in the following discussion. The analysis of methane decomposition is considered below, while the other two are elaborated in the next section.

Methane decomposes to an appreciable extent at temperatures in excess of 800 °C. Since the end of the gas injection tube is dipped into the melt at a temperature of ~1600 °C, we may assume that the methane entering the melt reaches the decomposition temperature before exiting. This assumption can be supported by the observation that the cause for tube blockage in some of the experiments was the formation of a carbon plug inside the injection tube.

To assess the gas bubble size and its residence time in the melt, the correlation reported by Szekely and Themelis was used [72]. The most important factor governing the size and

behavior of the gas bubble in a liquid is the Reynolds number of the orifice through which the gas is injected. This is given by,

$$N_{Re,o} = \frac{d \bar{u} \rho}{\mu}$$

where  $N_{Re,c}$  is the orifice Reynolds number;  $d$  is the characteristic length, in this case, the diameter of the orifice;  $\bar{u}$  is the average velocity of the gas inside the tube;  $\rho$  is the gas density and  $\mu$  is the gas viscosity. The term  $\bar{u} \rho$  is the mass flow rate of the gas per unit area and is independent of temperature. Methane viscosity is of the order of  $10^{-5}$  P and the diameter of the injection tube is 0.3 cm. At a flow rate of 0.2 SLPM of methane, the value of  $N_{Re,c}$  is  $\sim 1000$ . In this range of Reynold's number, experiments in the air-water system give the relation,

$$d_b = 0.286 d_o^{0.5} N_{Re,o}^{0.33}$$

for gas bubble diameter. On the basis of the above equation, the average gas bubble diameter is  $\sim 1.5$  cm. In metallic melts, gas bubbles of this size have a spherical cap shape and rise through the melt at a velocity given by the relation,

$$u_t = 1.02 \sqrt{\frac{1}{2} g d_b}$$

where  $g$  is the acceleration due to gravity. The bubble rise velocity is estimated at  $\sim 27$  cm/s. Since the depth of the melt is  $\sim 2$  cm, the residence time of the methane gas bubble in the melt is  $\sim 0.075$  s. For a highly efficient reaction, it is required that all the methane in the injected gas bubble be given a chance to reach the decomposition temperature and release carbon within the residence time.

A thorough analysis of the heat transfer from the melt to the gas will aid in estimating the efficiency of the RGI process. It must be kept in mind that each mole of decomposing methane gives 2 moles of hydrogen gas; thus, heat transfer and decomposition kinetics inside the bubble are very dynamic in nature.

To estimate the time required for supplying the theoretical amount of carbon to an Ni-Ti melt, consider a 100 g Ni-Ti melt containing 10 wt.% Ti. At a flow rate of 0.2 SLPM, the injection of methane should be carried out for  $\sim 25$  min to supply the stoichiometric amount of carbon. In actuality, the efficiency of carbon supply is low, due mainly to the incomplete



decomposition of the gas. The RGI process is expected to be more efficient in deeper melts, since the residence time of the bubble is higher.

#### **A.5.1.2 Reinforcement formation**

**1. Carbide formation:** The primary focus of the present work was the production of carbide reinforced Ni composites. Thus, TiC/Ni was chosen as a model high temperature composite system. Various experiments were attempted in order to produce a uniform distribution of micron-sized carbide particles in the Ni matrix. The interest in the Ni system grew out of initial attempts to produce intermetallic matrix composites of TiC/TiNi. Experiments that attempted to produce TiC/TiNi composites always resulted in incomplete runs due to crucible cracking, making it difficult to isolate the effect of gas injection on composite microstructure. In addition, the microstructures of the composite were too complicated to draw meaningful conclusions regarding the mechanism and efficiency of the in-situ reactions. Apart from the expected phases, there were other intermetallic phases of the Ti-Ni system (TiNi<sub>3</sub>, Ti<sub>2</sub>Ni) with a non-homogeneous distribution through the composite.

The first experiment that produced TiC/Ni composites (NTC1) was done by melting the Ni-Ti alloy in a graphite crucible. The as-cast sample showed a change in microstructure from top to bottom. Large bubbles (0.25-1 mm) were entrapped in the matrix near the top of the sample, as shown in Figure 4-13. These bubbles were surrounded by of faceted carbide particles of sizes ranging from 2 - 10  $\mu$ m. This could be due to one of two reasons:

- the bubbles are methane bubbles that contained a surface layer of carbon through methane decomposition. Titanium diffusion to the surface of the bubble subsequently resulted in reaction with the carbon to produce the carbide particles.
- the rising of the bubbles through the melt caused the flotation of the carbide particles from the bulk of the melt to the top. The rapid cooling rates obtained in the graphite crucible on shutting off the power supply caused the entrapment of these bubbles in the top regions of the melt.

The intervening regions of the matrix contained a network of carbide lamellar of thickness  $\sim$ 1  $\mu$ m. The bottom section of the sample did not contain any bubbles; however, there were large (0.1-0.3 mm long) flakes of carbon distributed randomly. These were believed to have been incorporated into the melt from the graphite crucible. In addition to these, the two carbide morphologies mentioned above were also present. Figure 4-14 shows a Ti elemental map of a region in the bottom of the sample along with the corresponding secondary electron image. The figure shows the carbon and carbide particles.

The next run (NTC2) was done to reproduce NTC1 in an alumina crucible. Figure 4-8 illustrates the various aspects of the process. The events that occur during processing are:

- discontinuities in gas flow

- blocking of injection tube
- increase in melt viscosity due to dispersed particles.

These situations were remedied by

- increasing the melt temperature to counter viscosity increase
- periodically lifting the tube out of the melt and clearing it using argon.

The variation of the temperature with time clearly tracks the application of the remedial actions mentioned above. During lowering and raising of the thermocouple from the melt, inductive effects on the temperature reading can be seen. Figures 4-9 and 4-15 show the results of the sample analysis for the run NTC2. An optical micrograph of the sample is shown in Figure 4-9. The carbide formed is in the interdendritic lamellar form. The plates are 1-5  $\mu\text{m}$  thick and surround the primary Ni dendrites completely. Figure 4-15 is an X-ray diffraction pattern showing high intensity TiC peaks. Note that there are no peaks of the elemental Ti and C or of the intermetallic  $\text{Ni}_3\text{Ti}$  upto the limits of resolution of X-ray diffraction.

Subsequent experiments with the TiC-Ni system were designed to produce TiC/Ni composites with higher volume fractions (~30 vol.%) of the carbides. Thus, run NTC3 was done in an alumina crucible to theoretically produce 22.2 vol.% TiC on full conversion of Ti in the melt to carbide. During the later stages of the experiment, however, the alumina crucible cracked and the Ni-Ti melt flowed out into the graphite susceptor. The sectioned sample was analyzed microstructurally and revealed carbides with two morphologies. The region of the melt in contact with the susceptor contained large (10-40  $\mu\text{m}$ ) faceted particles of TiC (Figure 4-16). The top of the melt contained carbides of lamellar eutectic morphology that contained TiC plates of thickness 1-4  $\mu\text{m}$ .

Run NTC4 and NTC5 were aimed at producing 30 and 25.5 vol.% of carbides in the Ni matrix respectively. High Ti-content alloys such as the ones used in these runs resulted in the formation of intermetallic phases, as was indeed seen on examination. The samples had clearly demarcated regions of carbides in the top half and intermetallic  $\text{Ni}_3\text{Ti}$  in the bottom half. According to the phase diagram, the intermetallic phase should be  $\text{Ni}_3\text{Ti}$ , which was confirmed by X-ray diffraction (Figure 4-17). Figure 4-10 shows an optical micrograph of the top region of NTC4. The micrograph shows faceted carbides in a matrix of Ni- $\text{Ni}_3\text{Ti}$  with sizes ranging from 5-20  $\mu\text{m}$ . The intervening regions also show the interdendritic lamellar morphology.

The bottom half of the sample contained minimal faceted carbides, as seen in Figure 4-18. However, the lamellar carbide morphology is seen in a distinctly intermetallic matrix. The interfacial region between the top and bottom of the sample was made up of large, faceted carbide particles of size 10-60  $\mu\text{m}$ . These particles probably grew to such sizes through coalescence and coarsening, since the middle part of the casting sees the slowest cooling rate. Similar results were obtained for the casting in run NTC5.

The great difference in carbide morphology seen between the top and bottom sections of the melt suggests that:

- there is significant chemical inhomogeneity along the depth of the sample. The concentration of Ti and C increase as we approach the top of the melt.
- the density difference between the carbide particles (4.91 g/cc) and the matrix (8.9 g/cc) causes flotation of the carbide particles.
- the amount of C supplied to the melt was not sufficient to convert all the Ti to TiC, thus leading to the formation of Ni<sub>3</sub>Ti.

We shall now discuss the microstructures obtained in relation to the known phase diagram data as reported by Stover and Wulff and Ballamy and Hucke.

Ni-Ti melts are capable of dissolving a large amount of carbon (~2 wt.%) at the processing temperatures used in the above experiments (1600 °C). Addition of carbon to the starting Ni-Ti alloy thus leads to dissolution of carbon in the liquid up to the solubility limit at that temperature. An increase in dissolved carbon at this stage causes the composition point to penetrate the liquidus, thereby precipitating the carbide. As a result, the liquid is depleted of both Ti and C, and the composition point moves towards the Ni corner of the ternary diagram. Depending on the final carbon percentage in the alloy melt, the final composition can fall within the ternary  $\gamma + \text{Ni}_3\text{Ti} + \text{TiC}$  region, the binary  $\gamma + \text{TiC}$  region or the ternary  $\gamma + \text{C} + \text{TiC}$  region ( $\gamma$  is the Ni solid solution). Figure 4-19 shows a schematic of the Ni-Ti-C ternary on which the paths of the composition points for different initial Ti contents are superimposed. Each of these is discussed in greater detail below and are related to the observed microstructures.

The phase diagram can be divided into two regions based on the amount of Ti in the initial composition. Ti contents lower than that required for the formation of intermetallic Ni<sub>3</sub>Ti (10-15 at.% Ti, depending on temperature) give a composition path that avoids the ternary  $\gamma + \text{Ni}_3\text{Ti} + \text{TiC}$  region. The composition follows Path I in Figure 4-19. The open circle represents the final composition of the melt before solidification commences. A final composition below Ni-13 at.% Ti-4 at.% C (the quasi-binary eutectic at 1307 °C) will first precipitate Ni solid solution,  $\gamma$ , on solidification. The liquidus composition follows the arrow to the eutectic point, where the precipitation of interdendritic lamellar TiC starts. This is the microstructure seen in Figure 4-9.

In contrast, a hyper-eutectic composition results in the precipitation of TiC particles as the primary phase followed by the eutectic reaction giving lamellar TiC (Path II). The eutectic reaction giving interdendritic TiC cannot be eliminated except through rapid solidification techniques. The formation of TiC particles is followed by rapid growth in the liquid phase to sizes greater than a micron. Thus, under the present processing conditions, it is not possible to eliminate the lamellar carbide or obtain submicron carbide particles.

Starting compositions with Ti contents higher than 15 at.% lead to a composition path that goes through the  $\gamma + \text{Ni}_3\text{Ti} + \text{TiC}$  on addition of carbon. This means that a greater amount of carbon has to be injected into the melt to eliminate the formation of  $\text{Ni}_3\text{Ti}$ . In the ternary region, the primary phase to precipitate can be the  $\gamma$  solid solution, the intermetallic  $\text{Ni}_3\text{Ti}$  (Path III) or  $\text{TiC}$ , depending on the amount of carbon injected. The liquidus composition is again given by the arrowed line. When the composition reaches the ternary eutectic point, we get co-precipitation of  $\text{TiC}$  and  $\gamma$ . As before, the formation of  $\text{TiC}$  particles in the liquid is followed by rapid growth to sizes greater than a micron. A combination of the two Paths II and III are present in the solidification of run NTC4 which was a high-Ti run. Since there was an inhomogeneous distribution of the alloying elements in the melt, the top and bottom regions followed different solidification paths. Examination of the phases present lead to the conclusion that the top half of the casting (Figure 4-10) followed Path II and the bottom half (Figure 4-18) followed Path III.

To minimize the segregation of the  $\text{TiC}$  particles to the top of the sample, presumably due to density differences between the matrix and the carbide, an  $\text{NbC/Ni}$  composite was processed by methane injection into an Ni-9.1 wt.% Nb alloy melt (run NNC). The microstructure of the casting was similar to that of NTC2, except for the fact that the carbide plates surrounding the primary Ni dendrites were finer. The carbide lamellae had a thickness of 1-3  $\mu\text{m}$ . An optical micrograph of the composite microstructure is presented in Figure 4-11. In contrast to the  $\text{TiC/Ni}$  composite microstructures, there are no angular carbide particles. The XRD pattern of the composite (Figure 4-20) shows the absence of any Ni-Nb intermetallic phases. The pattern also shows two carbide chemistries,  $\text{NbC}$ , and a mixed carbide,  $\text{Nb}_4\text{Ni}_2\text{C}$ . Thermodynamic properties or crystal structure data for this compound were not found in the literature. In addition, there is no report of a ternary Ni-Nb-C phase diagram. Thus, it is difficult to draw conclusions about the formation of this phase. However, from the binary Ni-Nb phase diagram [Figure 4-5 (a)], and comparison with the binary Ni-Ti phase diagram [Figure 4-2 (b)], it is proposed that the carbide formation reaction in the case of  $\text{NbC/Ni}$  is the same as that of  $\text{TiC/Ni}$ , i.e. solution-reprecipitation. In other words, the carbon formed by methane decomposition dissolves in the melt and the carbide is precipitated through a eutectic reaction during solidification.

Since the previous run (NNC) showed the formation of intermediate phases, it was decided to anneal some samples at a temperature of 1200  $^{\circ}\text{C}$  for 24 hours to determine the thermodynamically stable microstructure. The samples that were aged are marked in Table 4-5 with an asterisk. Figure 4-23 is an optical micrograph of the aged  $\text{NbC/Ni}$  sample. The continuous network of the intermediate carbide phase is broken up into discrete particles of size 1-5  $\mu\text{m}$ . Also, the width of the interdendritic zone is much reduced. This leads to the conclusion

that the carbide phases redissolved into the Ni matrix at 1200 °C. Comparison of the as-cast and aged X-ray diffraction patterns support this conclusion.

Similar ageing experiments were done on the TiC/Ni samples NTC2 and NTC4. The ageing temperature was chosen keeping in mind the ternary eutectics in the Ni-Ti-C system as reported by Stover and Wulff. These are  $\gamma + \delta + C$  at 1270 °C and  $\gamma + \delta + Ni_3Ti$  at 1295 °C. Given that the diffusion coefficient of Ti in Ni at 1200 °C is  $7 \times 10^{-10} \text{ cm}^2/\text{s}$ , and the average dendrite size is  $\sim 100 \text{ }\mu\text{m}$ , the time taken for Ti to diffuse to the center of the dendrite is  $\sim 3$  hours. Thus, the annealing time of 24 hours used is sufficient to bring out the equilibrium microstructure. During the ageing treatment, dissolution of the TiC lamellae occurs to some extent and the Ti diffuses to the region of greater carbon concentration in the center of the dendrite.

The XRD pattern of NTC2 shows an increase in TiC peak intensity (Figure 4-22). Microstructural examination revealed that precipitation of TiC platelets occurred inside the primary Ni dendrites. Figure 4-23 is a scanning electron micrograph of a region in the middle of a dendrite of sample NTC2. The TiC platelets were precipitated far from the initial lamellar carbides in the center of the dendrites and had regular morphologies. The precipitated TiC platelets ranged in length from 1 to 5  $\mu\text{m}$  and had a thickness of  $< 1 \text{ }\mu\text{m}$ . The difference between the morphology of the precipitated carbides and the lamellar carbides at the top of the micrograph is clearly seen. The figure on the right is a backscattered electron image of the region shown on the left and demonstrates the similarity between the two carbide phases. Ageing of sample NTC4 showed the development of both Ni and  $Ni_3Ti$  peaks. Microstructural examination showed the dissolution of the lamellar carbides in the matrix. This was supported by the XRD pattern of the aged sample (Figure 4-24).

The above results indicate that solid-state precipitation of TiC results in the formation of carbide platelets of much finer dimensions than the lamellae. Thus, it is postulated that a uniform distribution of TiC particles can be obtained in a Ni matrix by ageing a rapidly solidified Ni-Ti-C alloy melt. This can be achieved by rapid solidification techniques, in which the velocity of the interface is of the order of the diffusion rate,  $D_i / \delta_i$ , where  $D_i$  is the interface diffusion coefficient (which is less than the bulk liquid diffusion coefficient) and  $\delta_i$  is the width of the interface (of the order of the interatomic distance). This condition ensures that the solute atoms do not have time to diffuse and form the carbide during solidification, effectively freezing the solute atoms in their positions prior to solidification. Substituting representative values of  $10^{-10} \text{ m}^2/\text{s}$  for  $D_i$  and  $10^{-9} \text{ m}$  for  $\delta_i$ , we obtain an interface velocity of  $\sim 10 \text{ cm/s}$  for solidification

with no change in composition. This order of interface velocity can be achieved through rapid solidification, through techniques such as Osprey™ forming or Plasma spraying.

An attempt was also made to produce SiC/Ni composites through methane injection into a Ni-11.7 wt.% Si melt (run NSC). This composition was chosen since it was a low melting alloy and had a eutectic at 1143 °C. The resulting sample was examined and the XRD pattern did not show any SiC. However, intermetallic phases of the form Ni<sub>3</sub>Si and NiSi were formed along with the matrix, Ni. The micrograph of the sample showed a dense network of these intermetallic phases around the primary Ni dendrites. Ageing treatment performed on this sample showed that the NiSi phase was a kinetically stable phase but was not thermodynamically stable. The XRD pattern of the aged sample showed only the Ni<sub>3</sub>Si phase (Figure 4-25). This was supported by examination of the Ni-Si phase diagram. It can be concluded that the formation of the intermetallic Ni<sub>3</sub>Si phase is thermodynamically more favorable than the formation of the carbide. This is in contrast with the Ni-Ti case, where the TiC formation reaction is considerably more favorable than the formation of the Ni<sub>3</sub>Ti phase. It is possible that this composite can be prepared using an alloy with a higher amount of Si.

**2. Nitride formation:** Attempts to produce uniformly dispersed nitride particulate reinforcements in a Ni matrix were largely unsuccessful. In both the runs NTN (to produce TiN/Ni composite) and NSN (to produce Si<sub>3</sub>N<sub>4</sub>/Ni composite), the amount of N<sub>2</sub> gas supplied was far in excess of that required for complete conversion of Ti or Si into the nitride. In spite of this, the sample NSN showed no trace of nitride anywhere in the casting. Thus, it was concluded that the nitride formation reaction in the Ni-Si system was kinetically unfavorable in the present situation.

The sample NTN showed a layer of TiN of thickness 3-5 µm on the top surface and sides of the casting (Figure 4-12). The bulk of the casting was free of nitrides. The above observations suggest that the nitride formation reaction was mainly a surface reaction between the N<sub>2</sub> containing gas atmosphere above the melt and the Ti containing melt. It is important to transport the nitride formation reaction into the bulk of the sample to be able to produce nitride reinforced composites. The formation and uniform dispersion of nitrides is obviously a more difficult problem to handle than that of carbides. Using a gas such as ammonia may promote formation of the nitride particles, though dispersion of these particles in the matrix might still be a concern. The decomposition of nitrogen can also be accelerated by the use of a plasma, where the nitrogen molecules are readily dissociated and are formed in a highly activated state. This would further promote the formation of the nitrides. Further work is required to determine the

exact mechanism of the nitride formation reaction and to utilize this knowledge to tailor the reaction sequence and produce a uniform dispersion of the nitride particles in the Ni matrix.

Several problems were encountered during the experimentation. Principal among these was the necessity of stopping the run before the requisite amount of carbon could be injected into the melt in the form of methane. Insufficient carbon injection resulted mainly due to blockage of the injection tube with carbon particles. This problem can be circumvented by:

- decreasing the processing temperature leading to a decomposition of methane in the melt rather than in the tube;
- using a higher gas flow rate in order to blow out any blockage that may occur;
- cooling the gas before injection to suppress methane decomposition until it is in the melt;
- periodically lifting the injection tube out of the melt and clearing any obstacles to gas flow that may develop into a block.

Experimentally, the other problem encountered was in the processing of TiC/TiNi composites that preceded this work. This is described below along with remedial measures that should be taken in future attempts.

The cracking of alumina crucibles with Ti contents of greater than 20 wt.% was a problem that plagued all the RGI experiments (the initial TiNi-TiC runs had ~40 wt.% Ti). A survey of the available literature did not reveal any information on the interaction of Ni-Ti melts with alumina. However, there was some information on thermodynamics and kinetics of the Ti-Al<sub>2</sub>O<sub>3</sub> and the Al(Ti)-Al<sub>2</sub>O<sub>3</sub> reactions [73,74]. Misra has reported experiments with diffusion couples composed of Ti or Ti-Al alloys and single crystal alumina [73]. The results indicated that alloys with Ti content greater than 50 at.% were not compatible with alumina. Tressler *et al* reported results on diffusion couples similar to the ones used by Misra [74]. They report that the reaction depends on the diffusion of Ti through the interfacial Ti<sub>3</sub>Al layer is the rate-controlling step. Though these results are not directly applicable to the observations in the high Ti content Ni-Ti runs, it is possible that the activity of Ti in these melts was high enough to cause corrosion of the alumina crucibles, leading to cracking. This situation can be remedied by applying a suitably dense coating on the surface of the crucible prior to melting an alloy containing >20 wt.% Ti.

Microstructurally, the TiC/Ni composites showed massive segregation of angular carbide particles to the top half of the melt, similar to the results of Stover and Wulff [66] and Bellamy and Hucke [67]. This microstructure could be the result of insufficient injection of carbon into the melt. Thus, it is important to carry out a complete reaction before any conclusions about the microstructural inhomogeneity can be drawn.

### A.5.1.3 Reinforcement morphology, size and distribution

The effect of reinforcement size on strength is well known from the work of Orowan; effective strength increases can only be obtained through a uniform distribution of submicron particles. The TiC/Ni composites processed in the present work failed to achieve these goals. The following discussion seeks to explain this and to suggest means of overcoming the obstacles.

It must be pointed out that TiC formed through methane gas injection is no different from that formed through addition of solid carbon particles to an Ni-Ti melt. This can be seen by comparing the present micrographs with those obtained by Stover and Wulff and Ballamy and Hucke, who mixed solid elements (Ni, Ti, and C) for their experiments. Thus, the advantages of submicron carbide formation (due to submicron carbon particle formation) and uniform distribution of the particles through gas stirring were not realized. The reasons for this are two-fold: (1) the alloy system and (2) the experimental conditions. The previous section discussed the various means of TiC formation through examination of the projected ternary phase diagram. TiC formation was found to occur through:

- 1) eutectic reaction - interdendritic lamellar,
- 2) primary precipitation on cooling - particle,
- 3) primary precipitation at processing temperatures - particle, and
- 4) secondary precipitation through solid-state ageing - platelet.

Only the last technique yielded submicron dimensions in at least one dimension. The means to achieve this were also discussed in section A 5.1.2., which involved rapid solidification. A carbon content that leads to only the lamellar carbide is not economical since the volume fraction of reinforcement is theoretically limited to ~10 %. Since the size effect on strengthening is not achieved, only a volume fraction effect can make an impact on the strength levels (based on the Rule of Mixtures). Thus, TiC volume fractions of >25 % should be aimed at in future experiments. This requires starting alloy compositions with Ti contents greater than 15 at.%. The projected composition path on carbon injection is marked as Path II in Figure 4-19.

The decomposition of methane gives carbon particles of ~ 100 nm. Assuming that this particle is completely converted to TiC as soon as it is formed, its size increases to ~ 130 nm. The growth of TiC particles in solid Ni has been studied by Chermant and Coster [75], who demonstrated that the growth kinetics was second order interface reaction controlled. The kinetic equation that determines the growth is given by,

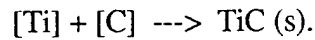
$$D^3 = D_0^3 + k \cdot t$$

where D is the current diameter,  $D_0$  is the diameter at some time  $t_0$ , k is the growth rate constant and t is the time elapsed. k is in turn given by the relation,



$$k = k_R \frac{16}{9} \frac{\sigma^2 V^3 (MC) C_\infty}{R^2 T^2} = 3 \times 10^{-14} k_R$$

where  $k_R$  is the rate constant for the reaction,



The experimentally determined value of  $k_R$  is  $8.3 \times 10^{-8}$  at a temperature of 1350 °C, which gives a value of  $2.49 \times 10^{-22}$  m<sup>3</sup>/s for  $k$ . For the growth of a TiC particle of 130 nm to a size of 1 µm, the time required is then ~ 60 min. Since the present experiments were carried out in the liquid state at a temperature of ~ 1600 °C, the observed particle sizes of 2 - 5 µm seem reasonable. Thus, the extended reaction time required for methane injection is not conducive to the formation of submicron TiC particles in the Ni alloy melt.

The morphology of the carbide particles is faceted. Experiments by Stover and Wulff and Ballamy and Huckle with the TiC/Ni system, where they have used spherical TiC particles, also show that ageing of the composite leads to a faceting of the particles. The faceting of round TiC particles depends on the oxygen content of the annealing atmosphere. Thus, ageing in an oxygen-free atmosphere will retain the spherical shape of TiC particles to a certain extent. The faceted morphology, however, could be useful for wear and abrasive materials applications. Since the density of TiC is about half that of Ni, the production of TiC particles is followed by their floating to the top of the melt. An additional effect could be the flotation of the particles caused by the presence of gas bubbles in the melt. Thus, a uniform distribution of the particles was not obtained in the preceding experiments. This situation can probably be overcome by introducing turbulent mixing in the melt, similar to the vortex stirring approach taken in cast composite processing.

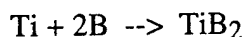
Given the low efficiency of carbon capture by the melt and the fact that particulate carbon can be used without effecting the final microstructure, it is suggested that future experiments utilize a solid source of carbon to provide the bulk of the carbon and methane injection to obtain finer carbide sizes and better distribution. Since there is an effect of the carbon particle size on the TiC particle size, and keeping in mind that a large carbon particle would form a shell of TiC on its surface, thus leading to inefficient conversion, it seems reasonable to inject fine carbon particles along with methane into the alloy melt. This should also help reduce the reaction time considerably.

### A.5.2 SHS Process

The SHS process was used to produce intermetallic matrix composite powders by an in-situ reaction between elemental powders. Characterization of the powder samples using X-ray diffraction revealed the cleanliness of the product. There were no intermediate or undesirable phases detectable by XRD. Intermetallic matrix composite powders that incorporated an in-situ reinforcement formation reaction were examined under the microscope. Figure 4-26 shows an optical micrograph of  $\text{TiB}_2/\text{NiAl}$  powder. The accompanying XRD pattern is shown in Figure 4-27.  $\text{TiB}_2$  particles are evenly distributed in the matrix and range in size from 1 - 3  $\mu\text{m}$ . The formation of the product occurs through two highly exothermic reactions,



and



A possible reaction mechanism is proposed below. Due to the high temperatures encountered at the reaction front (1500-1700  $^{\circ}\text{C}$ ), a transient liquid phase is formed, presumably of Al, which dissolves Ti and Ni.  $\text{TiB}_2$  particle formation then occurs through diffusion of Ti and B through the liquid and subsequent reaction. Simultaneously, the NiAl matrix is formed due to the intermetallic composition being reached. No intermetallic phases other than NiAl were found in the X-ray pattern. Furthermore, no elemental powders were detected by the XRD analysis. The SHS reaction is thus highly efficient in forming both the matrix and the reinforcement phases.

A similar reaction was used to produce  $\text{TiC}/\text{FeAl}$  composite powders. Figures 4-28 and 4-29 show the corresponding optical micrograph and the XRD pattern. As in the previous case, the product contains only the predicted phases. The carbide size, however, is significantly larger than the  $\text{TiB}_2$  particles in the  $\text{TiB}_2/\text{NiAl}$  composite. This is probably due to the higher reaction temperatures used for this composite (1920  $^{\circ}\text{C}$  vs. 1850  $^{\circ}\text{C}$  for  $\text{TiB}_2/\text{NiAl}$ ).

Comparison of the above observations with those for Al-matrix composites is particularly meaningful. Figure 4-30 shows the XRD pattern of the  $\text{TiB}_2/\text{Al}$  composite powders. As before, the peaks of both Al and  $\text{TiB}_2$  are sharp, with no extra phases or elemental Ti or B detectable. An optical micrograph of the  $\text{TiB}_2/\text{Al}$  composite is shown in Figure 4-31. The size of the  $\text{TiB}_2$  particles is  $\sim 1 \mu\text{m}$ . The distribution of the  $\text{TiB}_2$  particles is more or less uniform. The micrograph also shows some large particles of Al. This could be due to the presence of larger Al particles in the initial mixture. Melting of these particles would take more time and so give lesser time for the diffusion of Ti and B into the particles prior to precipitation of  $\text{TiB}_2$ .

Particle sizes comparable to the ones observed in the  $\text{TiB}_2/\text{Al}$  composite were seen in the  $\text{TiC}/\text{Al}$  composite powders (Figure 4-32). However, the distribution of these particles is very

non-uniform. This can be traced back to the processing technique used to prepare the composite powders. Carbon added was in the form of carbon black, which was probably in an agglomerated condition even after mixing. The carbide formation reaction would therefore occur locally. In addition, the solubility of carbon in aluminum is very low (0.32 wt.% at 1500 K). Thus, it is believed that it is the diffusion of Ti through the molten Al particles to the surface of the carbon that leads to the carbide formation reaction. The reaction is thus controlled by the diffusion of Ti to the carbon rather than solution reprecipitation, as in the case of  $\text{TiB}_2/\text{Al}$ .

Of the SHS experiments undertaken, there were few where only the matrix was produced by the reaction; commercially available ceramic powders were blended with elemental metallic powders before initiating the SHS reaction. Of these, the  $\text{TiC}/\text{NiAl}$  composite powder was the only one examined microstructurally. Figure 4-33 shows an optical micrograph of the powder showing carbide particle sizes of 1-3  $\mu\text{m}$ . The micrograph also shows the matrix to be two-phase; however, XRD pattern did not reveal the identity of the second phase. The second phase is thus probably either below the detection level of X-ray diffraction or is a local occurrence.

## A.6. Summary

Reactive Gas Injection technique was used to produce carbide and nitride particulate reinforcements in an Ni alloy melt through methane injection. Composites of  $\text{TiC}/\text{Ni}$ ,  $\text{NbC}/\text{Ni}$  and  $\text{SiC}/\text{Ni}$  were either produced or attempted. The reaction mechanism was developed based on experiments with the  $\text{TiC}/\text{Ni}$  system, leading to the conclusions below:

- (a) the mechanism of carbide formation in a Ni matrix is primarily carbon dissolution followed by carbide formation through a eutectic reaction during solidification.
- (b) regions that have a high concentration of carbon show formation of faceted carbide particles that were probably in equilibrium with the alloy melt.
- (c) the injection of methane into an alloy melt becomes more difficult as time increases due to (1) blocking of the injection tube and (2) an increase in the melt viscosity.

The SHS processing technique was used to produce intermetallic matrix composites ( $\text{NiAl}$ ,  $\text{FeAl}$ ) reinforced with carbides, nitrides and borides. This technique is very successful in producing chemically clean intermetallic and metallic matrix composites. This is evidenced by the absence of any intermediate or undesirable phases in the corresponding XRD patterns. The work on production of SHS composite powders can be summarized as follows:

- (a) it is possible to produce intermetallic matrix composite powders that are homogeneous and chemically clean.

- (b) reinforcement particle size range from 1 - 3  $\mu\text{m}$  in the  $\text{TiB}_2/\text{NiAl}$  case to 10 - 40  $\mu\text{m}$  in the  $\text{TiC}/\text{FeAl}$  case.
- (c) a possible reaction mechanism is the dissolution of reacting elements in a transient liquid phase followed by precipitation.

**Table 4-1 : Composites Processed by Reactive  
Gas Injection**

<b>Run</b>	<b>Alloy (wt. %)</b>	<b>Reinforcement (vol. %)*</b>
<b>Carbides</b>		
NTC1	Ni - 5.7 Ti	TiC : 12.2
NTC2	Ni - 5.8 Ti	TiC : 12.2
NTC3	Ni - 11.1 Ti	TiC : 22.2
NTC4	Ni - 16.0 Ti	TiC : 30.0
NTC5	Ni - 15.9 Ti	TiC : 25.5
NNC	Ni - 9.1 Nb	NbC : 11.4
NSC	Ni - 11.7 Si	SiC : 34.4
<b>Nitrides</b>		
NTN	Ni - 7.7 Ti	TiN : 17.9
NSN	Ni - 8.6 Si	Si <sub>3</sub> N <sub>4</sub> : 28.9

\* expected volume % on full conversion

**Table 4-2 : Results of SHS Combustion Synthesis Experiments**

Composite	Vol.% Reinforcement	Reaction Front Temperature (°C)	Reinforcement Size (μm)
NiAl - TiB <sub>2</sub>	15	1850	1 - 3
FeAl - TiC	20	1920	10 - 40
NiAl - TiC	10	1700	1 - 3
NiAl - TiN	15	1590	-
NiAl - AlN	10	1650	-
Al - TiB <sub>2</sub>	20	1780	<1
Al - TiC	10	1700	<1

**Table 4-3 : Composites Processed by SHS Combustion Synthesis**

Reactant Mixture	Expected Products	
	Matrix	Reinforcement
Ni + Al + Ti + B <sup>*,a</sup>	NiAl	TiB <sub>2</sub>
Fe + Al + Ti + C <sup>*,a</sup>	FeAl	TiC
Ni + Al + TiC <sup>a</sup>	NiAl	TiC
Ni + Al + TiN	NiAl	TiN
Ni + Al + AlN	NiAl	AlN
Al + Ti + B <sup>*,a</sup>	Al	TiB <sub>2</sub>
Al + Ti + C <sup>*,a</sup>	Al	TiC
TiAl <sub>3</sub> + C	Al	TiC

\* incorporated in-situ reinforcement formation reaction

a microstructurally analyzed

**Table 4-4 : Experimental Details of RGI Runs**

Run	Reaction Temperature (°C)	Reactive Gas Flow Rate (SLPM)	Injection Time (min)	Theoretical vol. % Reinforcement #
NTC1	1500	0.3	27	8.9
NTC2	1650	0.1	26	12.2 <sup>x</sup>
		0.2	29	
NTC3	1600	0.2	8.3	11.5
		0.1	24	
NTC4	1600	0.1	6	13.5
		0.2	2	
NTC5	Data acquisition unsuccessful			
NNC	1650	0.1	26	9.3
NSC	1500	0.1	44	12.6
NTN	1450	0.136	75	17.9 <sup>y</sup>
NSN	-	0.136	23	28.9 <sup>z</sup>
		0.272	85	

# : assuming 100 % decomposition and 100 % conversion into reinforcement  
x : 41.6 % excess C supplied                      y, z : 246 % excess N<sub>2</sub> supplied



**Table 4-5 : Microstructural Results of Ni-Based Samples**

Experiment	Matrix	In-situ Phases	Morphology	Size
NTC1	Ni	TiC	Top : Faceted Lamellar Bottom : Faceted	1 - 5 $\mu$ m 2 - 10 $\mu$ m thick 1 - 5 $\mu$ m
*NTC2	Ni	TiC	Lamellar	1 - 5 $\mu$ m thick
NTC3	Ni	TiC	Top : Lamellar Bottom : Faceted	1 - 4 $\mu$ m 10 - 40 $\mu$ m
NTC4	Ni/Ni <sub>3</sub> Ti	TiC	Top : Faceted Lamellar Bottom : Lamellar	5 - 20 $\mu$ m 1 - 4 $\mu$ m thick 2 - 10 $\mu$ m thick
NTC5	Ni/Ni <sub>3</sub> Ti	TiC	Top : Faceted Lamellar Bottom : Lamellar	5 - 20 $\mu$ m 1 - 4 $\mu$ m thick 2 - 10 $\mu$ m thick
*NNC	Ni	Nb <sub>4</sub> Ni <sub>2</sub> C + NbC	Lamellar	1 - 3 $\mu$ m
*NSC	Ni	Ni <sub>3</sub> Si + NiSi	-	-
NTN	Ni	TiN	Continuous layer covering top and sides of melt	3 - 5 $\mu$ m
NSN	Ni	Ni <sub>3</sub> Si + NiSi	-	-

\* samples subsequently annealed at 1200 °C for 24 hours.

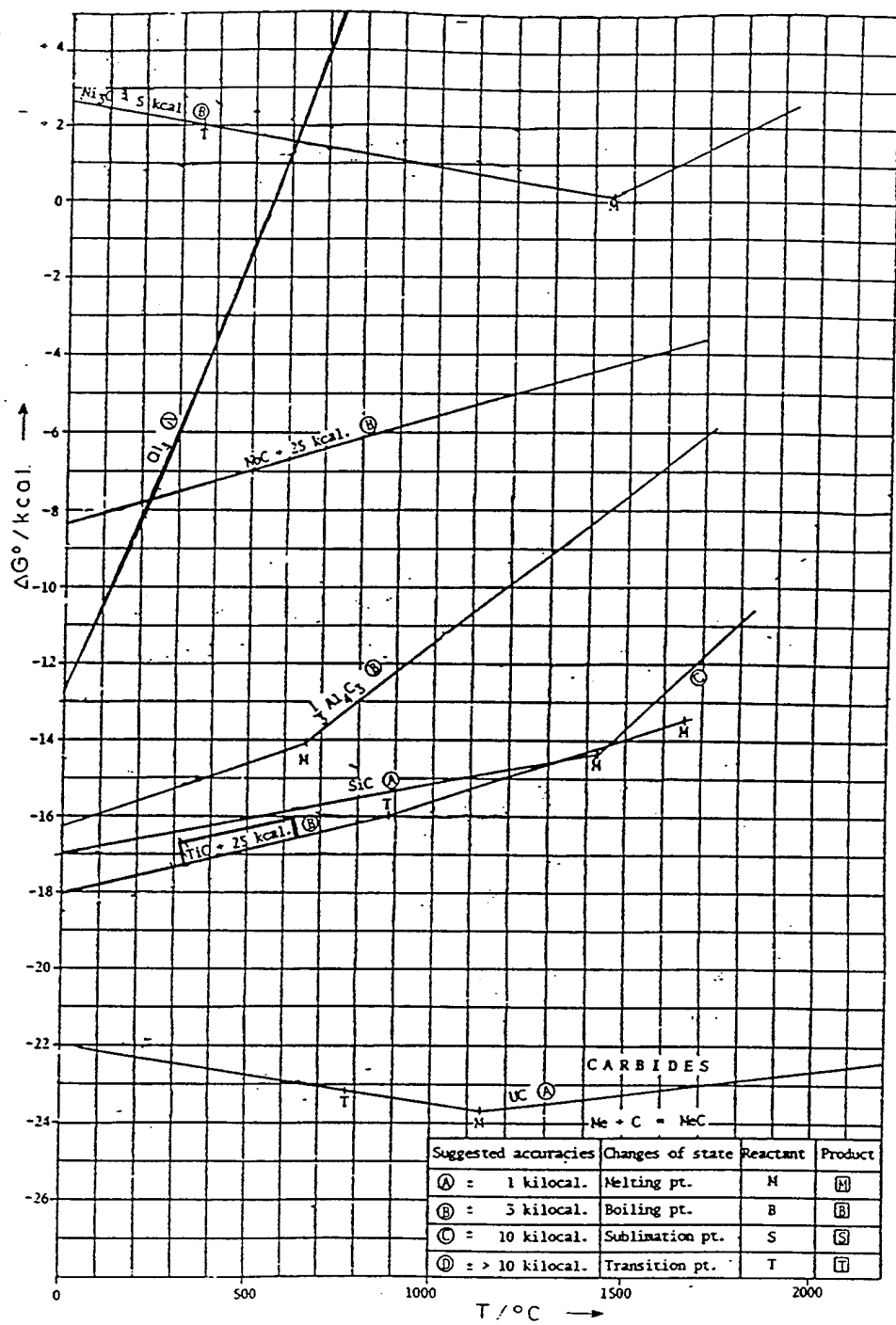
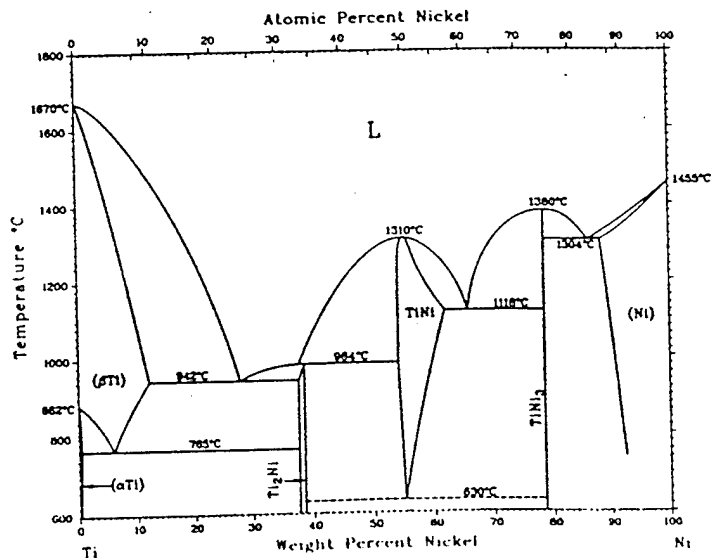


Figure 4-1 Ellingham diagram for selected carbides.

# Ni-Ti

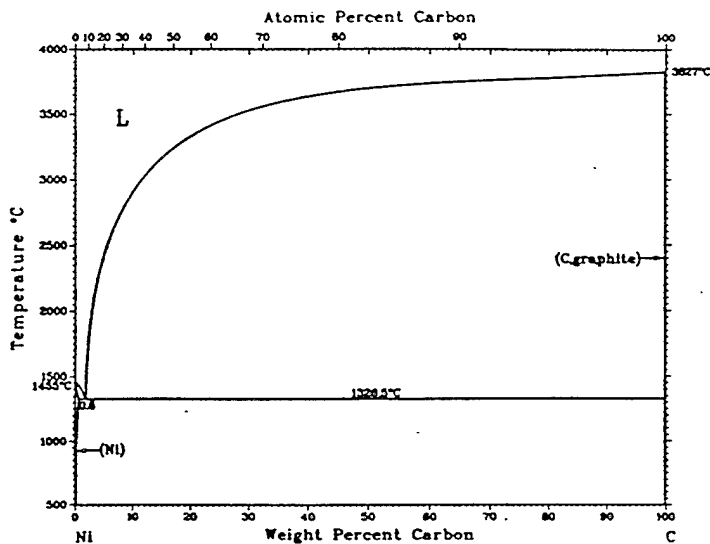


Phase	Composition, wt% Ni
(βTi)	0 to 12
(αTi)	0 to 0.3
ω(a)	-10
Ti <sub>2</sub> Ni	38.0
TiNi'(a)	-54 to 58
TiNi	54.6 to 62
γTiNi <sub>3</sub> (a)	-77
TiNi <sub>3</sub>	79
γTiNi <sub>3</sub> (a)	-86 to 90
(Ni)	88.4 to 100

(a) Metastable

(a)

# C-Ni



Phase	Composition, wt% C
(Ni)	0 to 0.6(a)
(C, graphite)	-100
Metastable phase	
Ni <sub>3</sub> C	...

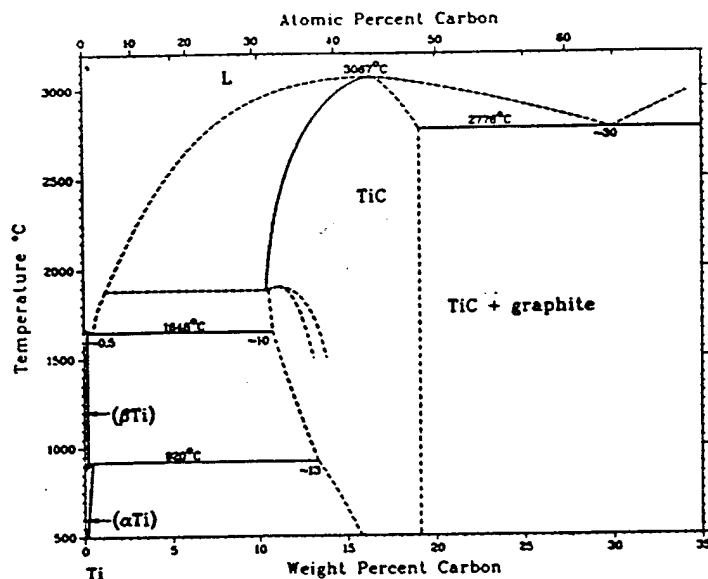
(a) Can be extended to 1.6 wt% C at 1314 °C

(b)

Figure 4-2

- (a) Binary Ni-C phase diagram
- (b) Binary Ti-Ni phase diagram

# C-Ti



(c)

Figure 4-2: (c) Binary Ti-C phase diagram

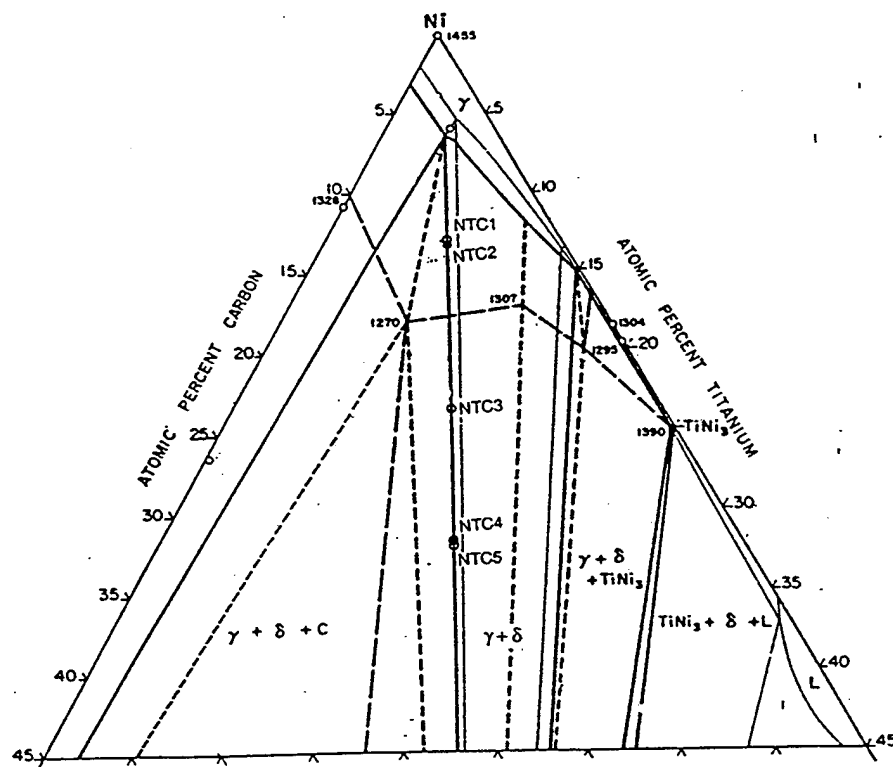
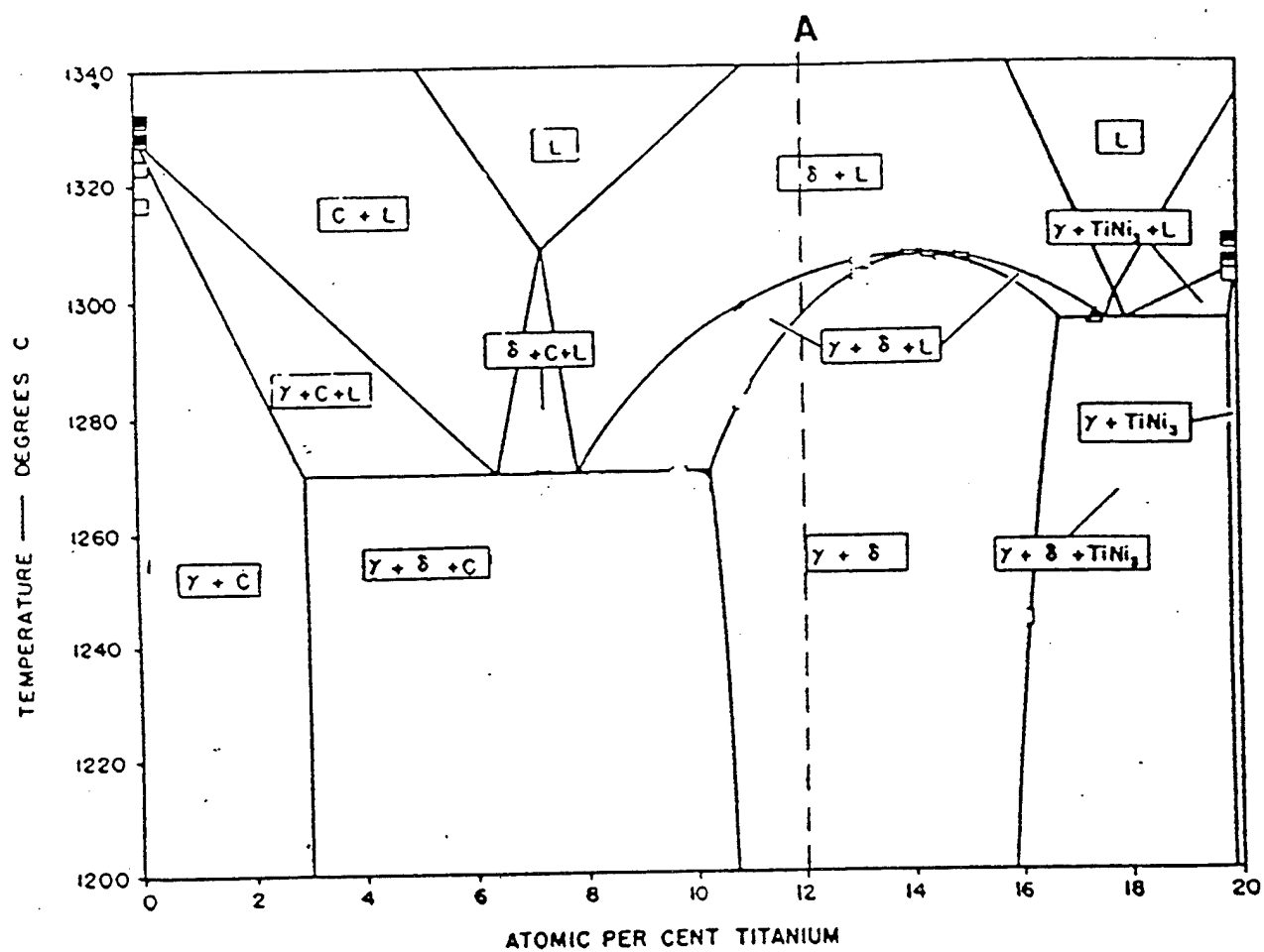
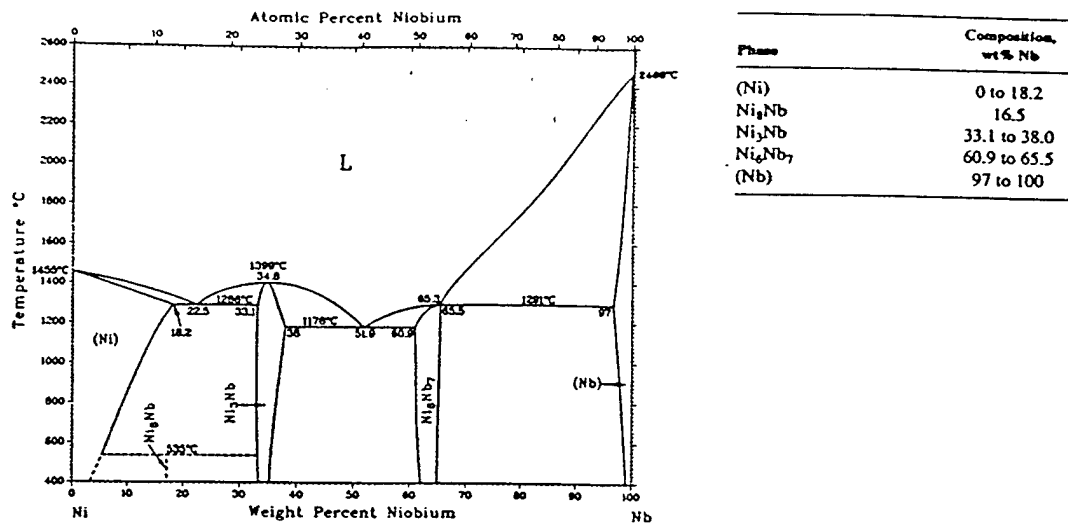


Figure 4-3 Isothermal section of Ni-Ti-C ternary at 1200 °C. Points marked indicate expected final compositions of RGI runs.

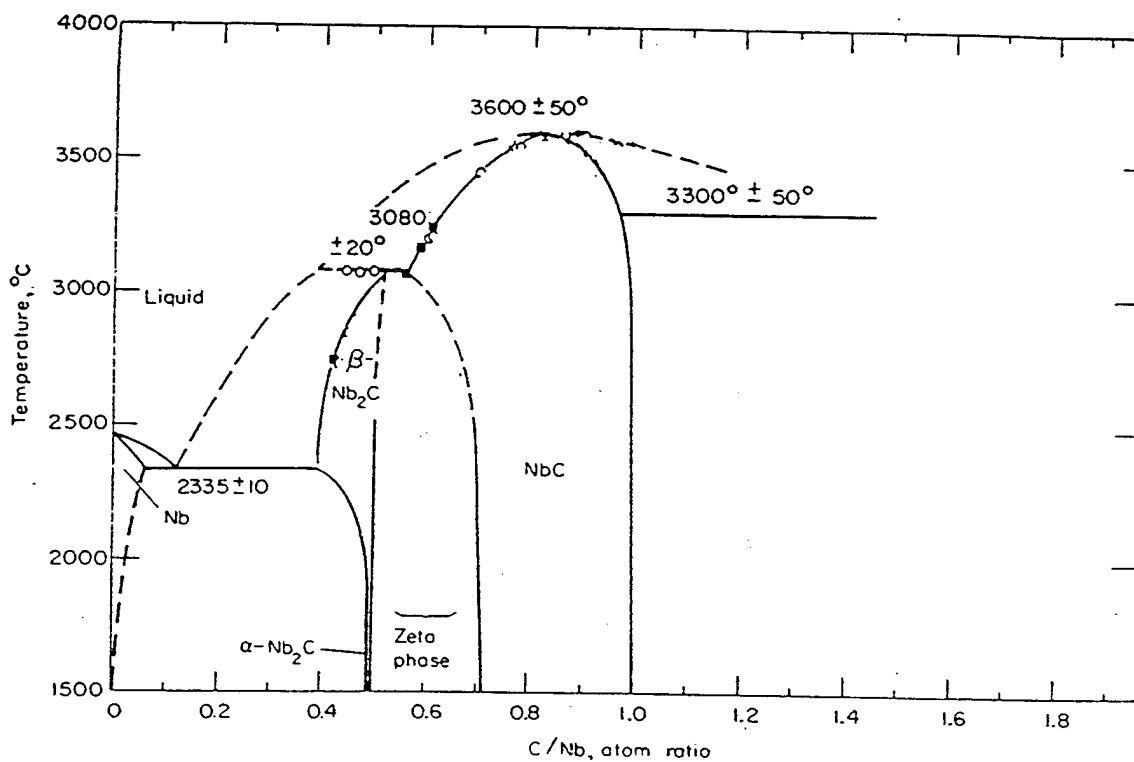


**Figure 4-4** Vertical section of Ni-Ti-C ternary between Ni-20 at.% C and Ni-20 at.% Ti

# Nb-Ni



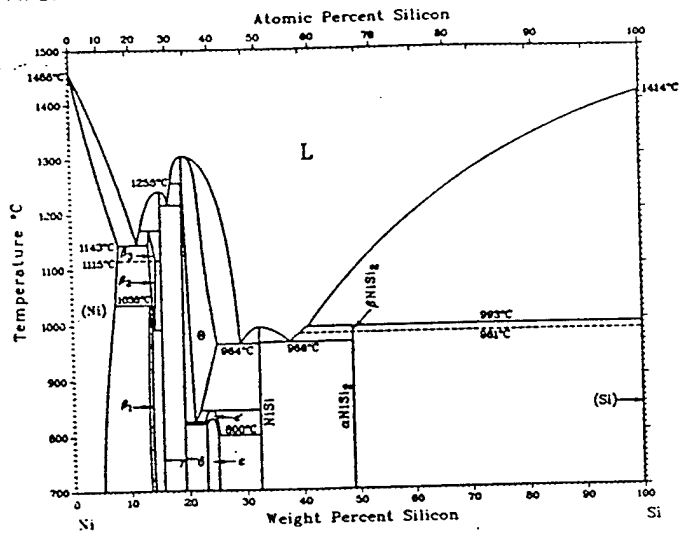
(a)



(b)

Figure 4-5 (a) Binary Ni-Nb phase diagram  
(b) Binary Nb-C phase diagram

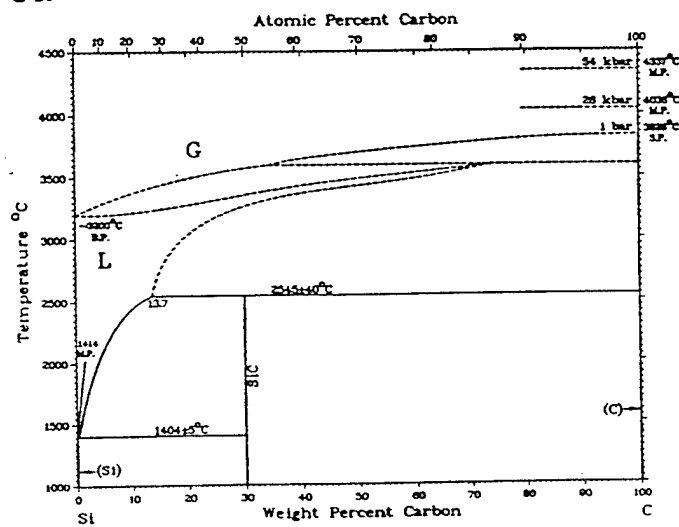
# Ni-Si



Phase	Composition, wt% Si
(Ni)	0 to 8.2
$\beta_1$ ( $\text{Ni}_4\text{Si}$ )	12.4 to 13.4
$\beta_2$ ( $\text{Ni}_3\text{Si}$ )	-13.4 to 14.1
$\beta_2$ ( $\text{Ni}_3\text{Si}$ )	-13.4 to 14.1
$\gamma$ ( $\text{Ni}_{11}\text{Si}_{12}$ )	15.6
$\theta$ ( $\text{Ni}_2\text{Si}$ )	19.4 to 25
$\delta$ ( $\text{Ni}_2\text{Si}$ )	19.3
$\epsilon$ ( $\text{Ni}_3\text{Si}_2$ )	23 to 25
NiSi	32.4
$\beta\text{NiSi}_2$	48.9
$\alpha\text{NiSi}_2$	48.9
(Si)	-100

(a)

# C-Si



Phase	Composition, wt% C
(Si)	0
SiC or $\beta\text{SiC}$	30
(C)	100
Metastable	
$\alpha\text{SiC(a)}$	30
Amorphous	22 to 40
High pressure	
SiC II	...

(a) Other SiC polytypes have been reported. (b) Hexagonal

(b)

Figure 4-6

- (a) Binary Ni-Si phase diagram  
(b) Binary Si-C phase diagram

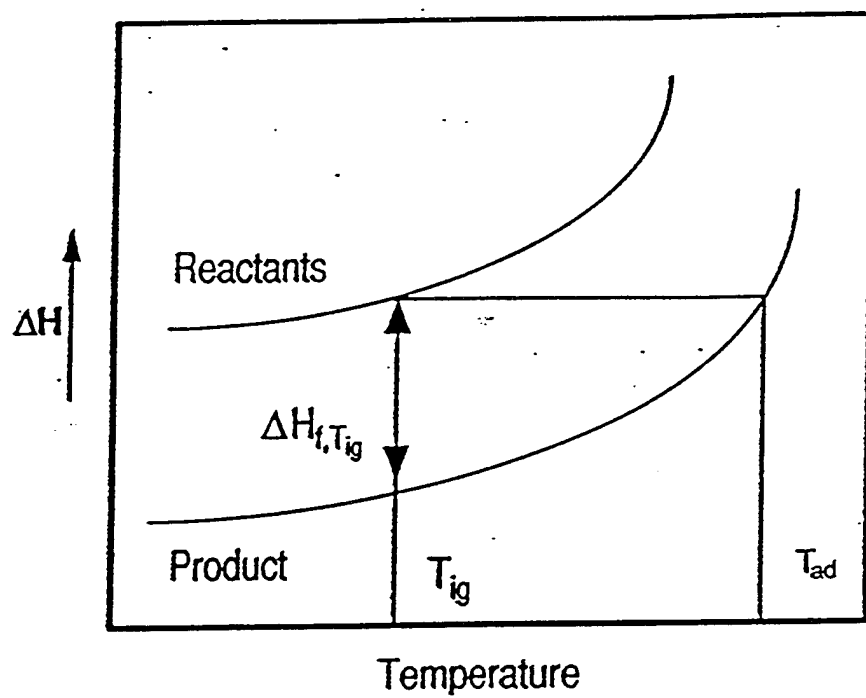


**Figure 4-7** Schematic of enthalpy-temperature curve for reactants and products during SHS reaction.



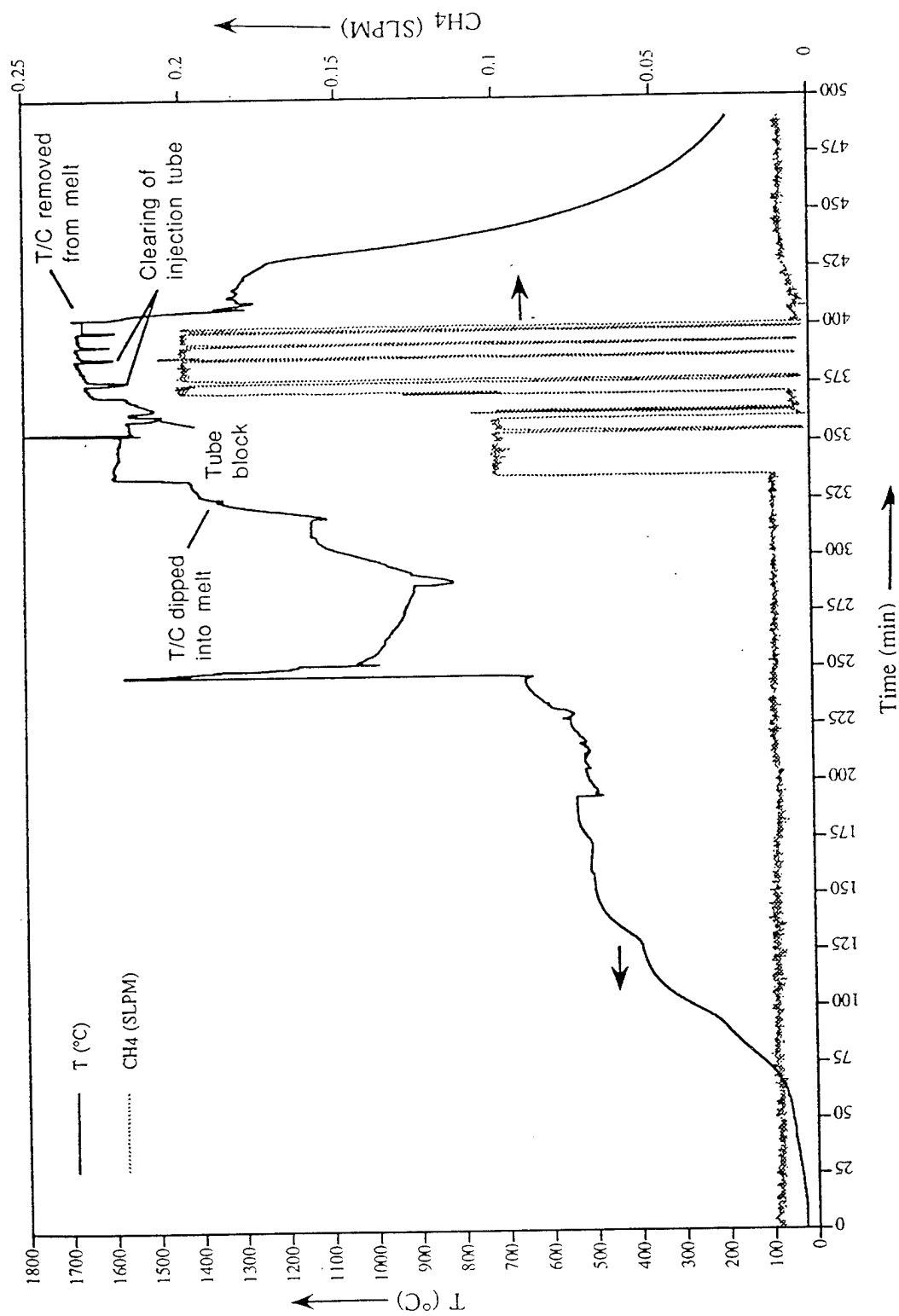


**Figure 4-8** Typical temperature and CH<sub>4</sub> flow rate variation with time during RGI runs [run NTC2]

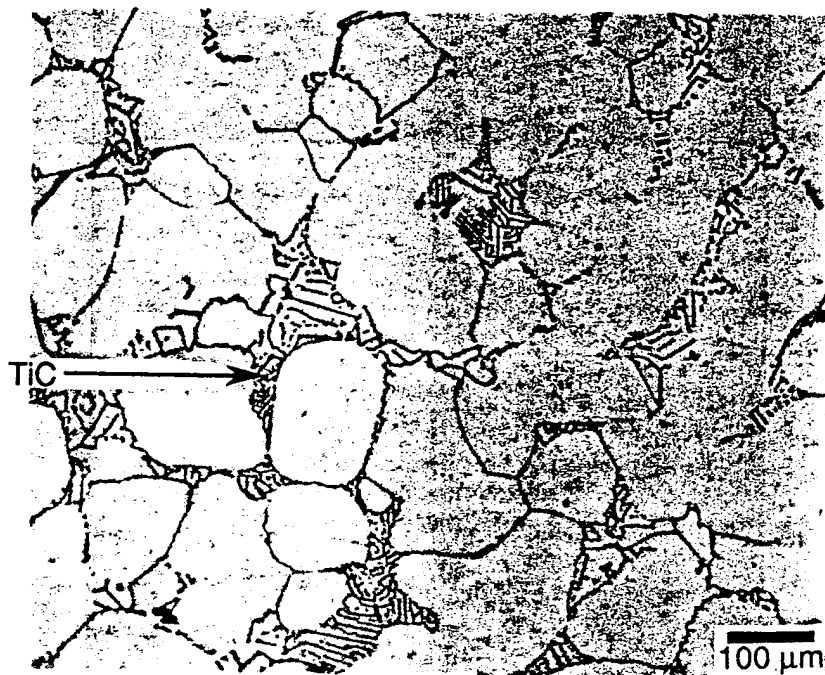


**Figure 4-9** Micrograph of sample NTC2, bulk, showing lamellar TiC.

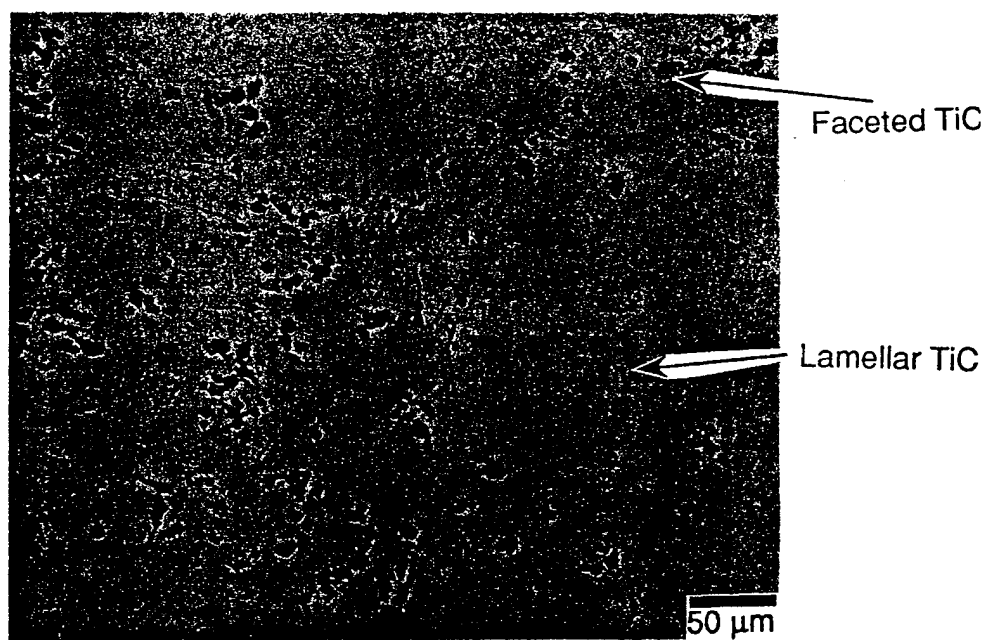


**Figure 4-10** Micrograph of sample NTC4, top half, showing both angular and eutectic TiC.

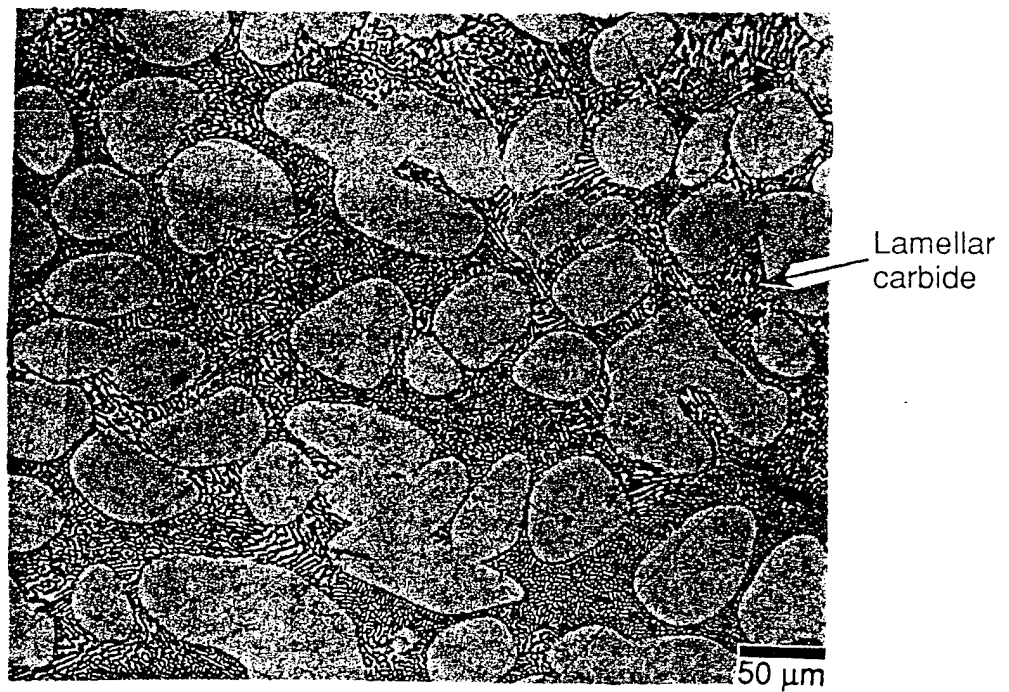


**Figure 4-11** Micrograph of sample NNC, bulk, showing primary Ni dendrites surrounded by eutectic carbides.

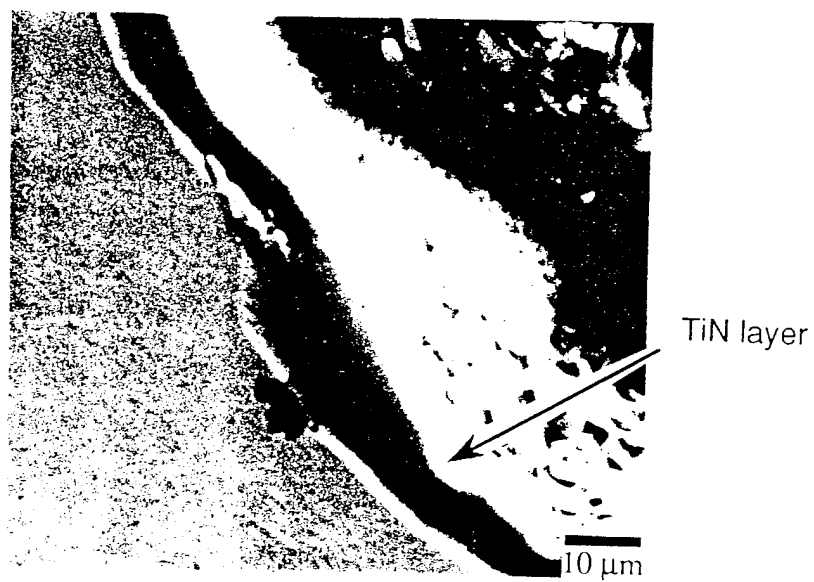


**Figure 4-12** Micrograph of sample NTN, surface, showing layer of TiN.

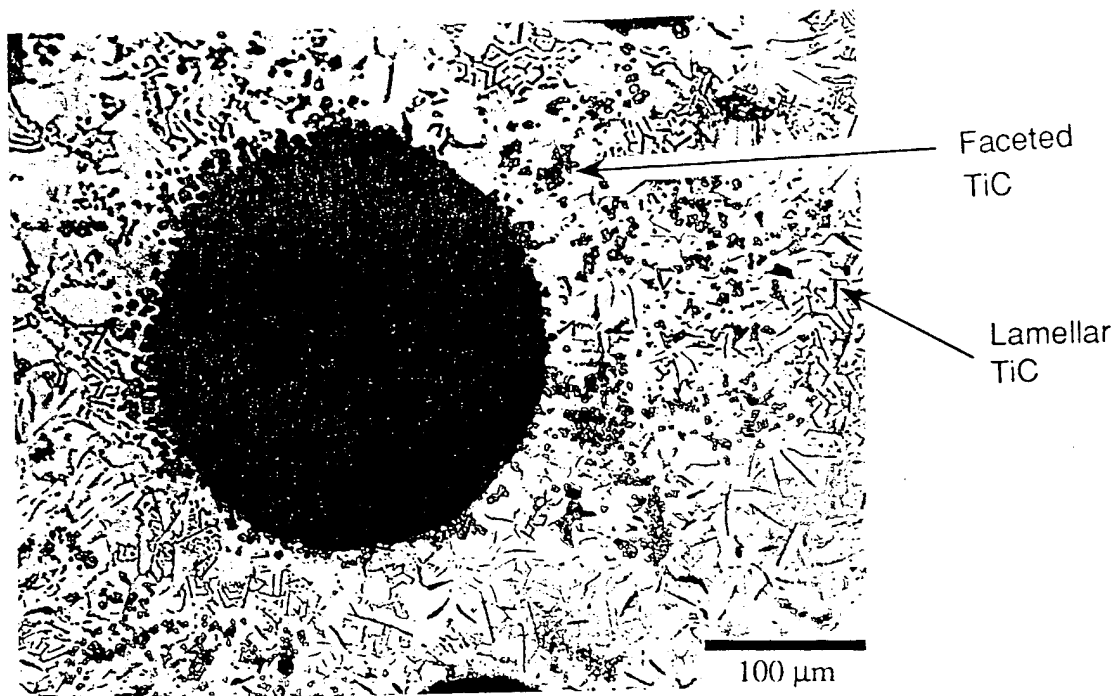


**Figure 4-13** Micrograph of sample NTC1, top half, showing entrapped bubble surrounded by angular TiC particles.

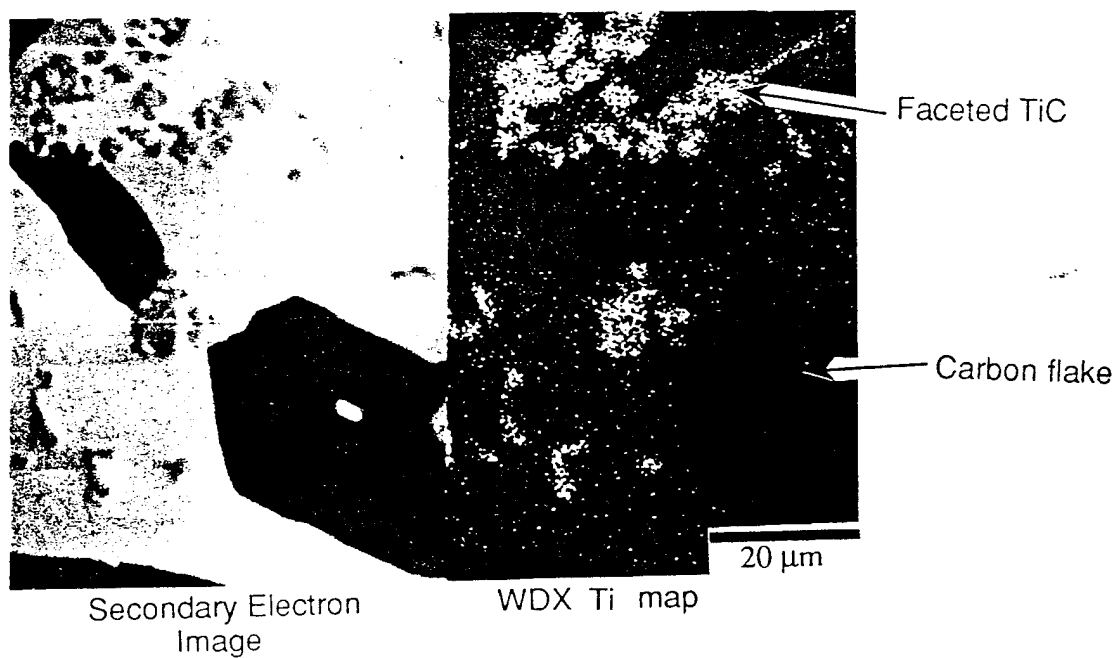


**Figure 4-14** WDX Ti elemental map of sample NTC2, bottom half, clearly identifying TiC particles.



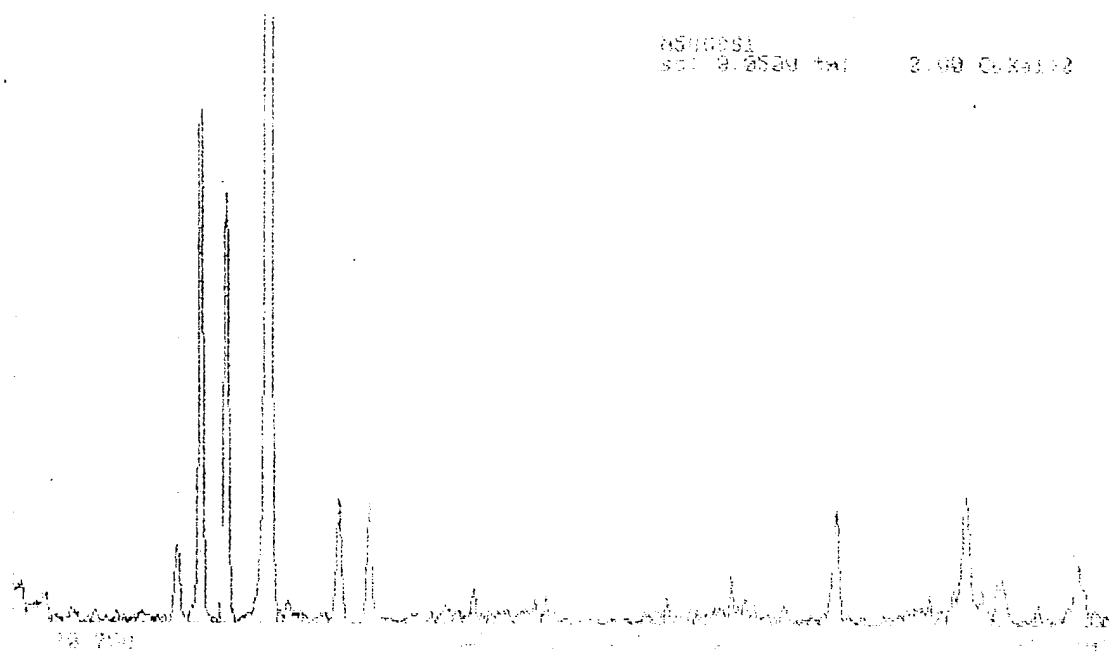


**Figure 4-17** XRD pattern of sample NTC4, bottom half, showing high intensity peaks of Ni<sub>3</sub>Ti.

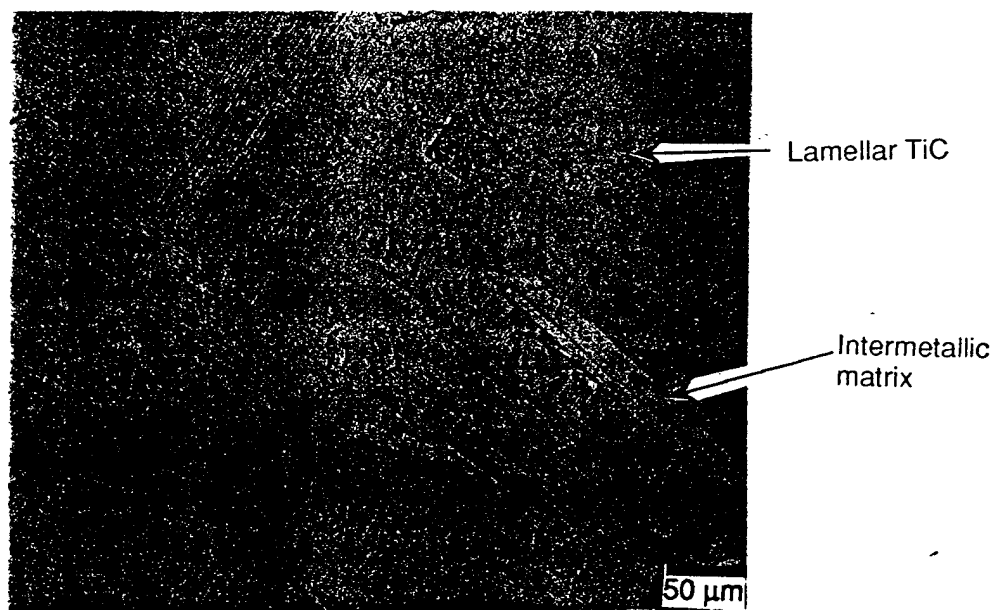
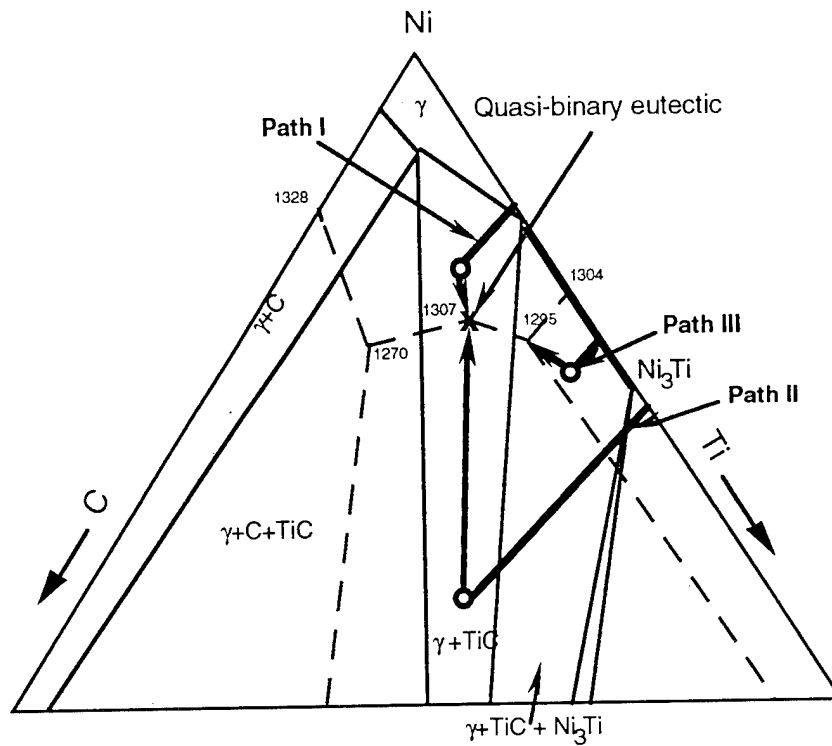


**Figure 4-18** Micrograph of sample NTC4, bottom half, showing eutectic carbides in intermetallic (Ni<sub>3</sub>Ti) matrix.



Path I :  $L \rightarrow L + \gamma \rightarrow \gamma + \text{TiC}$

Path II :  $L \rightarrow L + \text{TiC} \rightarrow \text{TiC} + \gamma$

Path III :  $L \rightarrow L + \text{Ni}_3\text{Ti} \rightarrow L + \text{Ni}_3\text{Ti} + \text{TiC} \rightarrow \text{Ni}_3\text{Ti} + \text{TiC} + \gamma$

● Indicates precipitation of primary phase, i.e. penetration of liquidus

— — Projection of liquidus surface intersections

— — Composition path on carbon addition

➔ Path of liquidus composition

**Figure 4-19**

Schematic of Ni-Ti-C ternary isothermal section at 1200 °C. Thick lines represent paths of composition points with addition of carbon. Also gives solidification sequence.





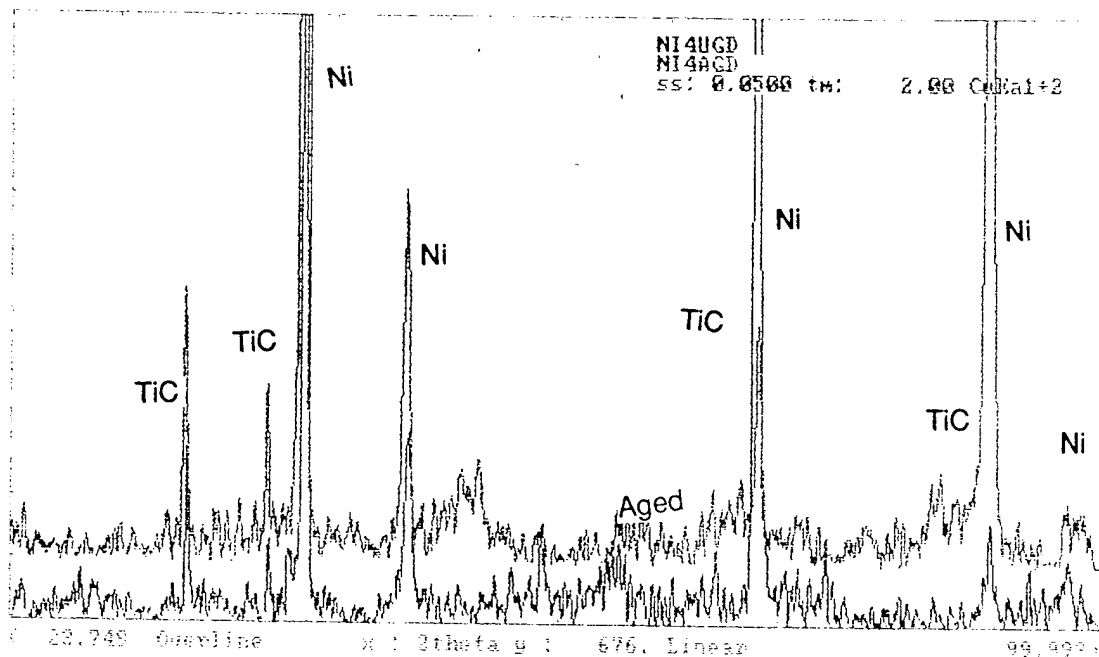


**Figure 4-22**

XRD pattern of aged sample NTC2, bulk, superimposed on pattern of as-cast sample. Note increase in TiC peak intensity.

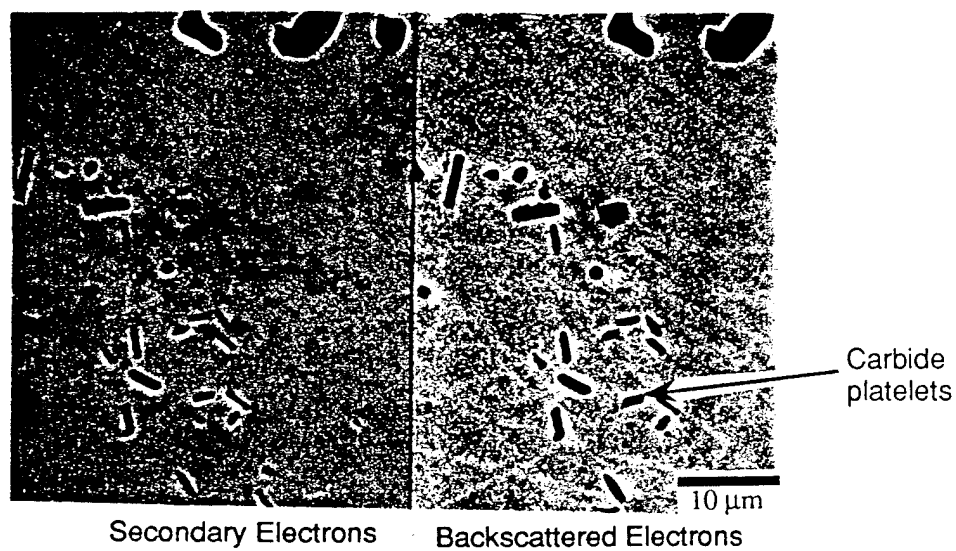


**Figure 4-23**

Backscattered electron image of region in the middle of Ni dendrites in aged sample NTC2. Note precipitation of carbide platelets on ageing.

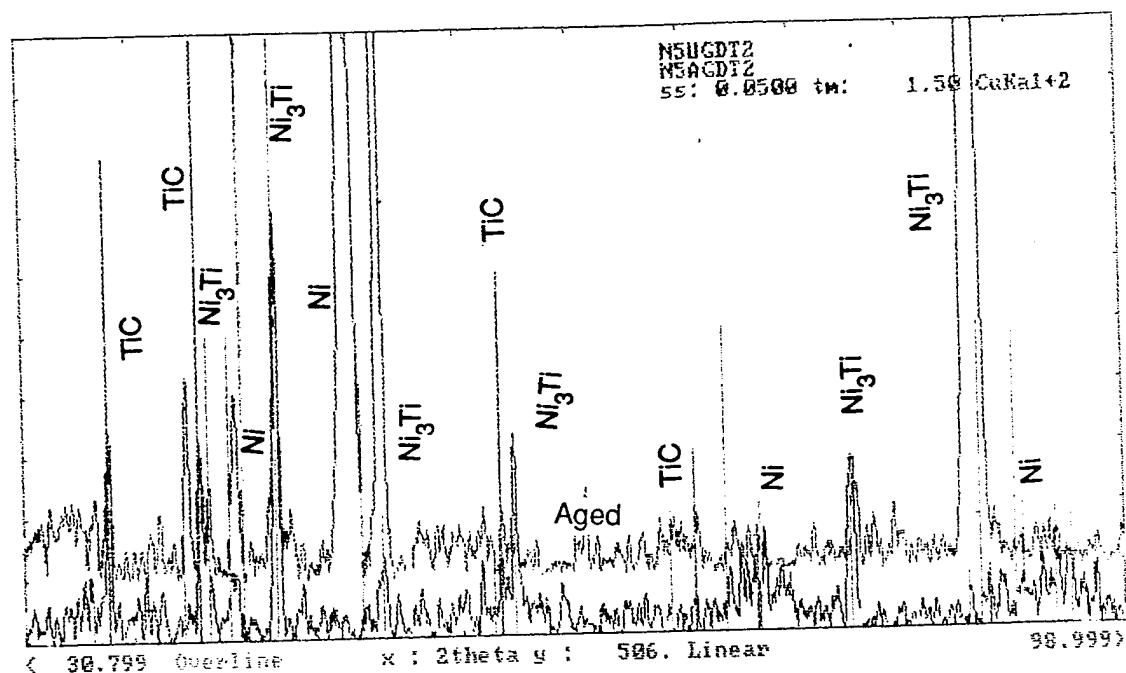


**Figure 4-24** XRD pattern of aged sample NTC4, top half, superimposed on pattern of as-cast sample. Note increase in  $\text{Ni}_3\text{Ti}$  peak intensity.

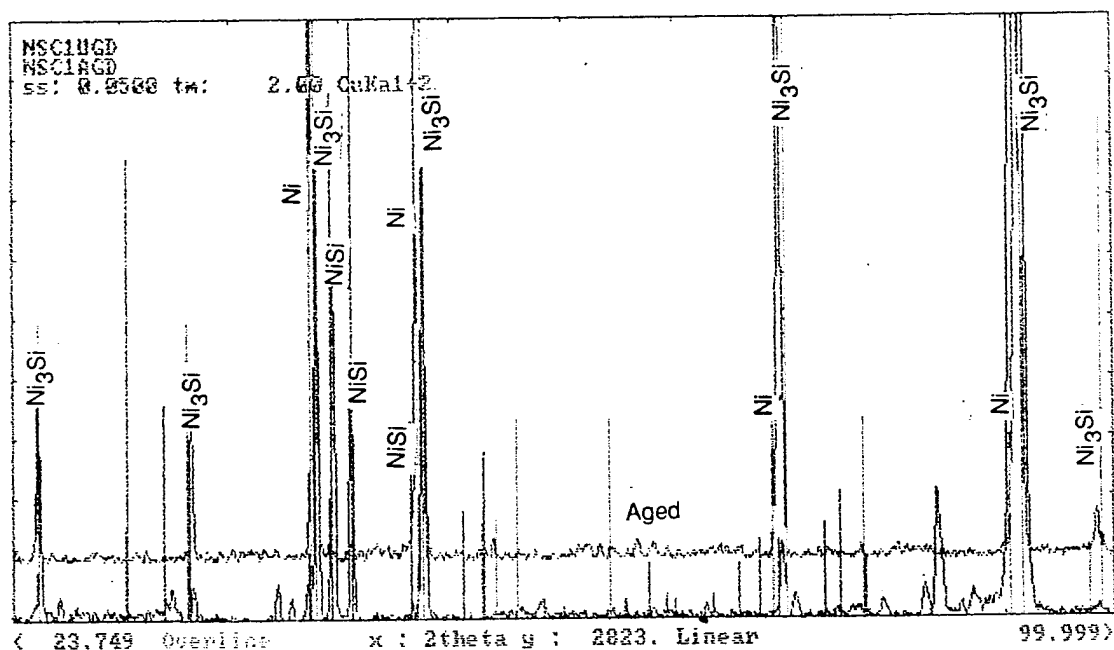


**Figure 4-25** XRD pattern of aged sample NSC, bulk, superimposed on pattern of as-cast sample. Note disappearance of  $\text{NiSi}$  peaks.

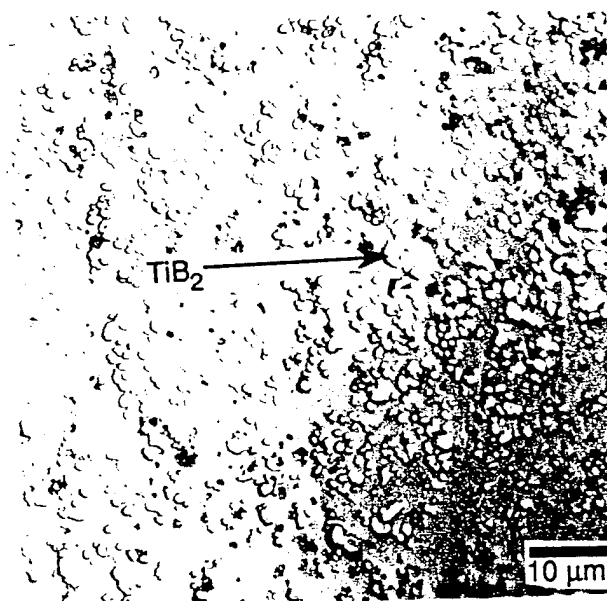


**Figure 4-26** Micrograph of TiB<sub>2</sub>/NiAl composite powder showing micron-sized TiB<sub>2</sub> particles.

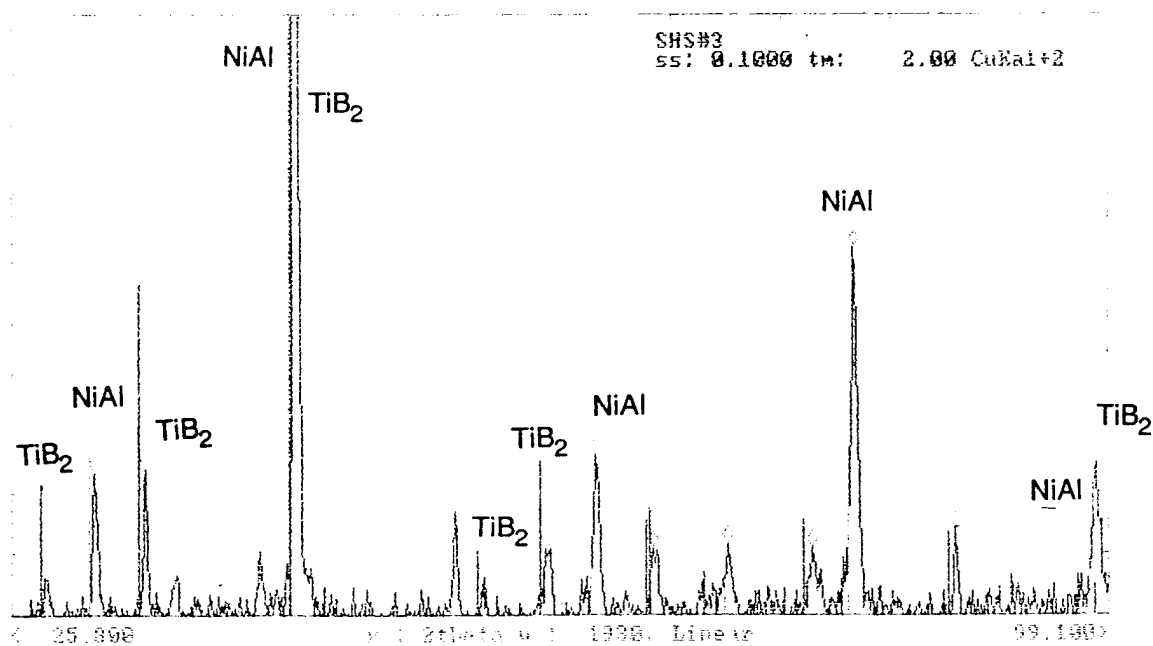


**Figure 4-27** XRD pattern of TiB<sub>2</sub>/NiAl composite powder. Note absence of intermetallic phases other than NiAl.

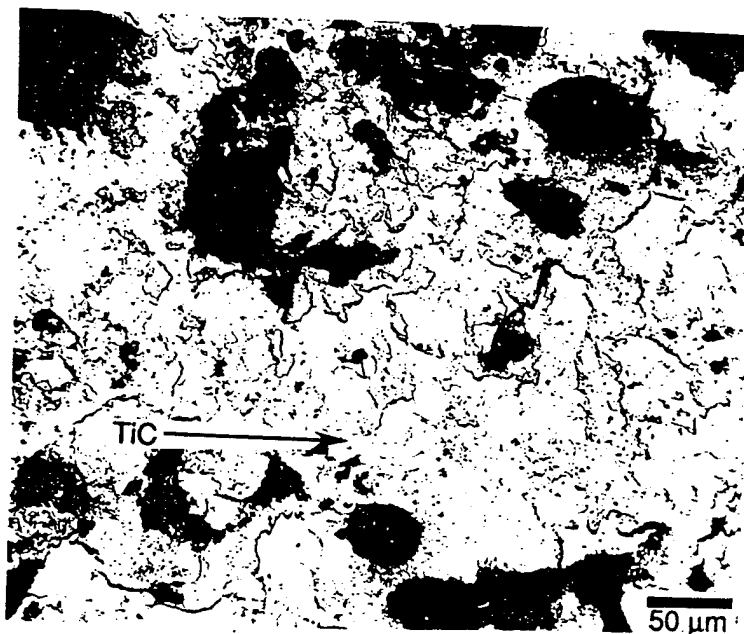


**Figure 4-28** Micrograph of TiC/FeAl composite powder showing large TiC particles.

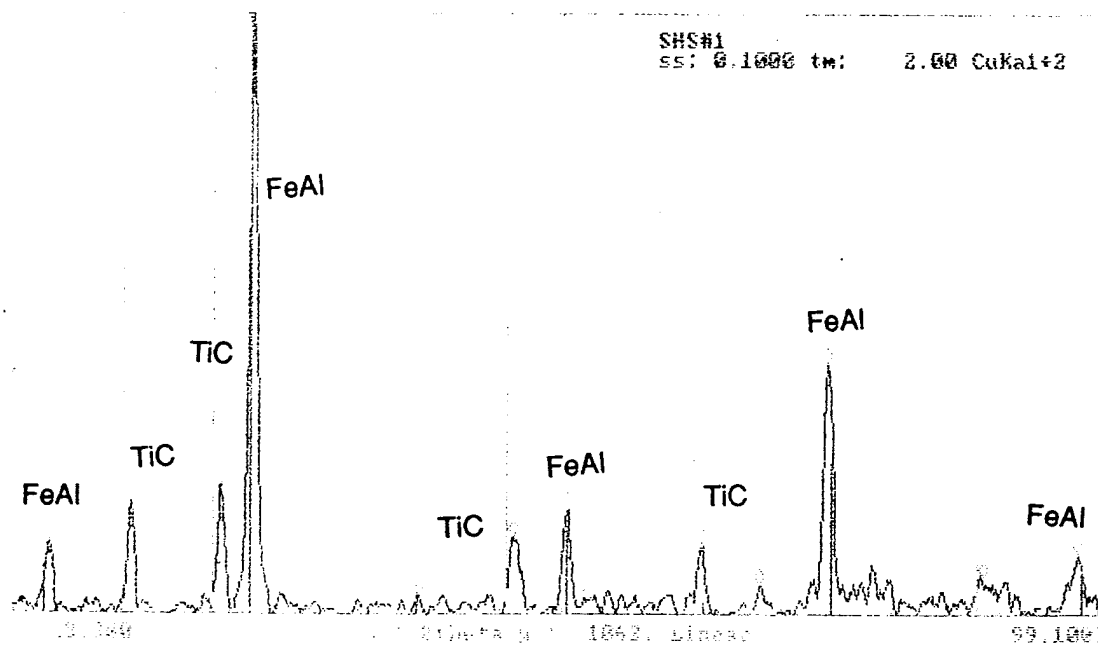


**Figure 4-29** XRD pattern of TiC/FeAl composite powder.

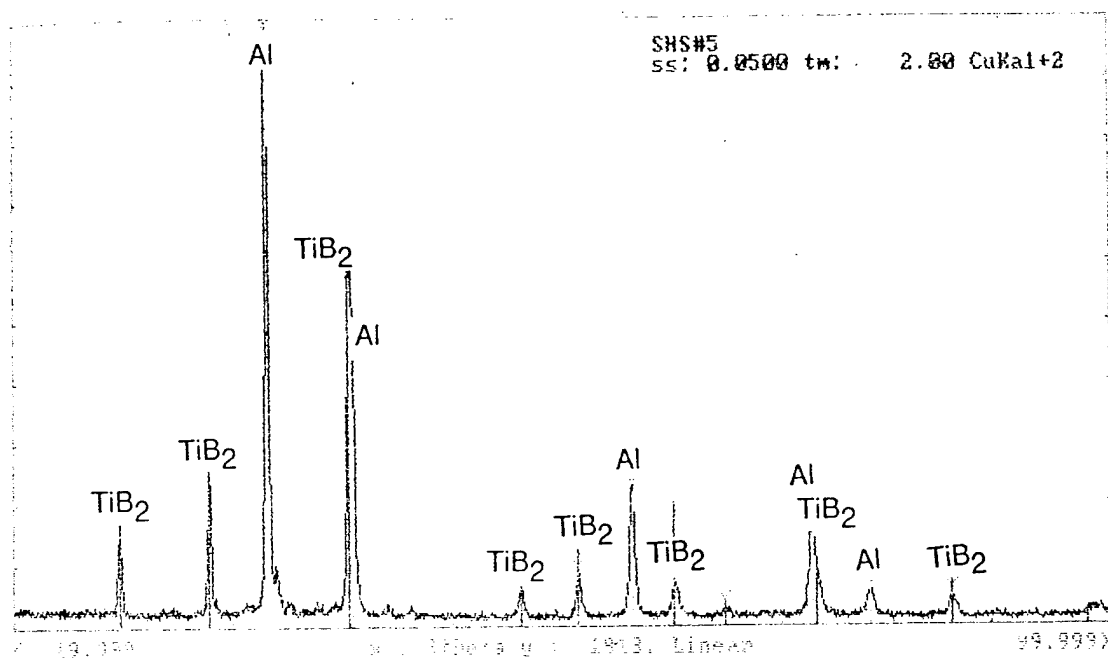


**Figure 4-30**

XRD pattern of  $\text{TiB}_2/\text{Al}$  composite powder.

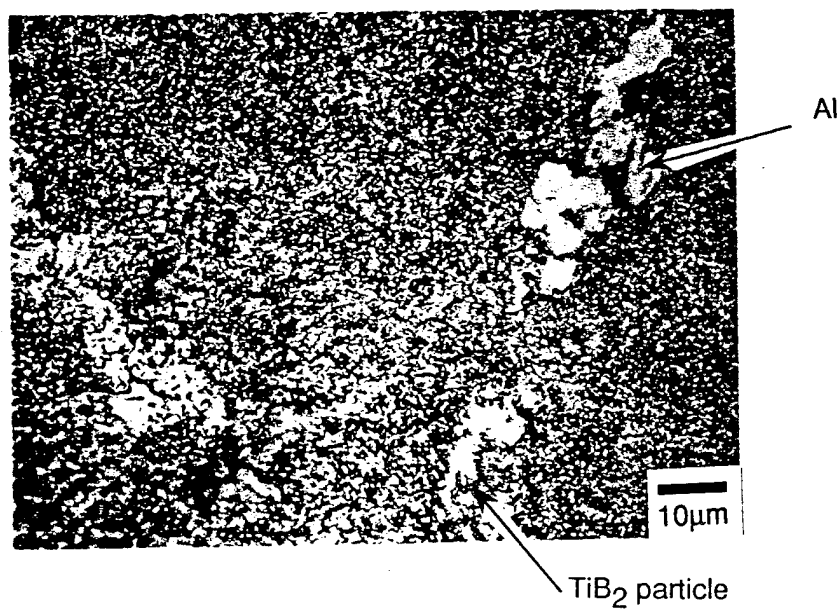


**Figure 4-31**

Micrograph of  $\text{TiB}_2/\text{Al}$  composite powder showing some large particles of Al.

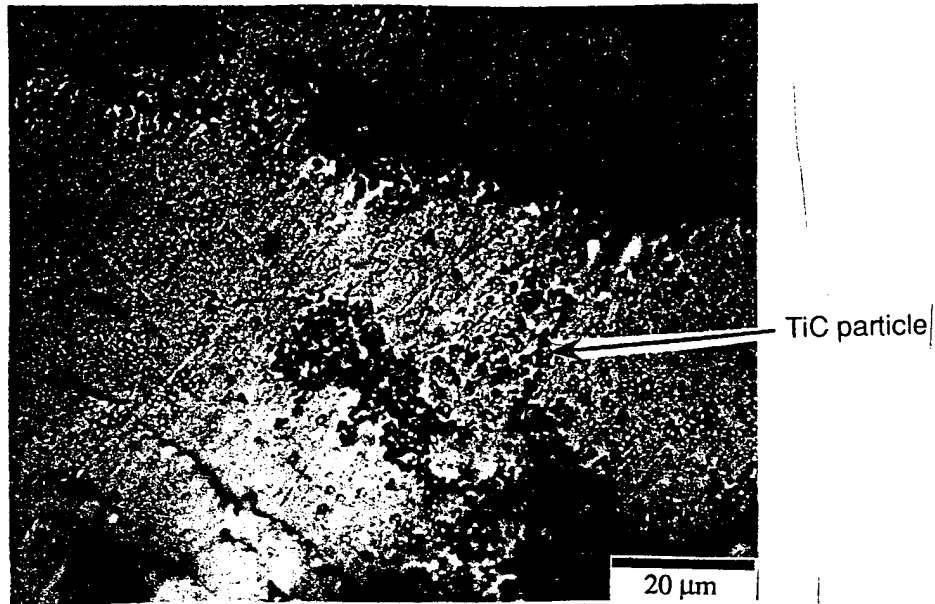


**Figure 4-32**

Micrograph of TiC/Al composite powder showing clusters of TiC particles.

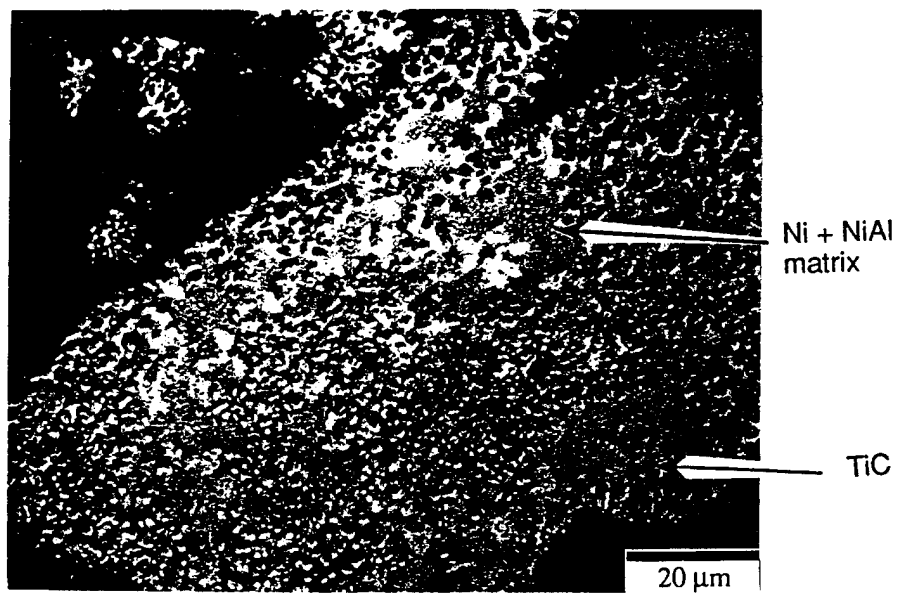


**Figure 4-33**

Micrograph of TiC/NiAl composite powders showing uneven distribution of TiC particles.

## CHAPTER V.

### CONCLUSIONS

#### I.A. Reactive Gas Injection Processing of TiC/Al

The goal of that research was to study the thermodynamics, kinetics and mechanism of the process of TiC formation in Al matrix via Reactive Gas Injection technique. Based on the analysis of the available literature, theoretical studies and results of the experiments conducted the following conclusions are made.

The RGI process was compared with the other existing in-situ techniques for the synthesis of MMC composite materials. The main advantages of the RGI are thermodynamic stability of the composites, nascent interfaces, fine reinforcement size as well as economical processing due to rapid kinetic of reinforcement formation and nonexpensive starting materials, net shape forming and continuous processing. The disadvantages of the RGI are mainly due to the high melt viscosity, which prevents the fabrication of composites with high volume fractions of reinforcement and causes the formation of inhomogeneties due to the poor mixing of the viscous melts. The selection of reinforcements is also limited due to thermodynamic reasons: in order to produce stable reinforcements there should be a large difference in change of free energy of carbide formation between the matrix metal and reinforcement precursor metal.

The study on relative TiC and  $\text{Al}_4\text{C}_3$  stability over the range of temperatures concludes that in liquid state, i.e. at any temperature above 1025 K (752°C), TiC is stable and  $\text{Al}_4\text{C}_3$  is not expected to form in excess of Ti in the Al-Ti-C system. However, since the free energy change for the reaction:  $4/3\text{Al} + \text{C} = 1/3\text{Al}_4\text{C}_3$  is negative at all the temperatures below 2000 °C, aluminum carbide will form in the presence of excess carbon. This is valid for liquid and solid aluminum. At temperatures below 1025 K, the reaction:  $3\text{TiC} + 13\text{Al} = \text{Al}_4\text{C}_3 + 3\text{TiAl}_3$  becomes thermodynamically feasible and titanium carbide converts to  $\text{Al}_4\text{C}_3$  and  $\text{Al}_3\text{Ti}$  on isothermal heat treatment.

The experiments conducted in the flow reactor demonstrate that the degree of methane decomposition is somewhat lower than predicted by thermodynamics, but still is within the range of 0.95- 0.99 at temperatures higher than 900°C. During RGI process, the decomposition of  $\text{CH}_4$  starts in the injection tube nozzle and continues in the melt and by the time a bubble reaches the melt surface, methane is fully decomposed. The analysis shows that it takes over a hundred seconds for 20 nm carbon particles, homogeneously nucleated in the bubble, to come in contact with the melt. By the time bubble approaches the melt surface only a fraction of the total carbon content in the bubble would diffuse to the bubble/melt interface and react with Ti; thus the rest of

carbon dissipates in the surrounding atmosphere during the bubble eruption and deposits on the furnace walls.

The processing envelope for conversion of C and Ti to TiC has been determined. Minimum TiC platelets size is limited by the nucleation process and corresponds to 0.1  $\mu\text{m}$  in diameter. Maximum size of reinforcement is determined by coarsening kinetics of carbides and the particles vary in size from 10 to 20  $\mu\text{m}$ . Maximum volume fraction of reinforcement is limited by the melt viscosity and does not exceed 40 volume percent. For the range of volume fractions, the average TiC particulate size is 1-3  $\mu\text{m}$ . The average TiC size does not increase significantly with time. TiC particle size increased by 15  $\mu\text{m}$  in 8 hours, which signifies that the process of TiC coarsening is quite slow.

The TiC formation mechanism follows the solution-reprecipitation route for fine soluble particles and interfacial reaction route for graphitic surfaces. The interfacial reaction of TiC formation at the solid carbon particle is 5 orders of magnitude slower than carbon dissolution process. Thus, the two processes are taking place simultaneously, but since the interfacial reaction is much slower, by the time a significant carbide layer can build up on a carbon particle, the particle may completely dissolve. It leads to the conclusion that the TiC forms predominantly via solution-reprecipitation mechanism, i.e. carbon goes in the Al-Ti solution, reacts with Ti (reaction time of TiC formation in the solution is estimated to be 0.2 seconds) and then precipitates from the melt. Due to the lack of data it was not possible to estimate the nucleation time and the nucleus size, but it is logical to assume that nucleation is not a limiting stage in the process of TiC formation.

### **I.B. Reactive Gas Injection Processing of AlN/Al**

Aluminum nitride synthesis in molten aluminum alloy was achieved by two methods, namely, direct and indirect nitridation. Direct nitridation experiments produced AlN/Al-Mg-Si metal matrix composites via nitrogen-bearing gas injection, with the aid of Mg and Si at temperatures above 1000°C. Indirect nitridation included solid-liquid displacement reaction, and reactive gas injection method. The first was by mixing magnesium nitride with molten aluminum at 1000°C. The reaction between magnesium nitride and aluminum is a liquid-solid interfacial reaction. Agitation and/or gas stirring must be carefully employed to develop intimate contact of  $\text{Mg}_3\text{N}_2$  and Al in order to provide for uniform composite. Early gas injection and stirring resulted in segregation of  $\text{Mg}_3\text{N}_2$  from Al, while late gas injection results in agglomeration of AlN particles formed. The second method of forming AlN via *in situ* generated  $\text{Mg}_3\text{N}_2$  was also successful. This approach has the promise of synthesizing micron and



submicron sized AlN. Volumetric concentrations of AlN as high as 15% are obtained. Enhanced mechanical and wear properties of aluminum alloy can be achieved with this cost effective liquid-gas phase synthesis route.

### **I.C. SHS Processing of TiC/Al, TiB<sub>2</sub>/Al, (TiC+TiB<sub>2</sub>)/Al**

Al matrix *in situ* composites with 30 vol.% of hard ceramic particles (TiC and/or TiB<sub>2</sub>) were successfully fabricated employing SHS technique. This is the first study to report the SHS processing of Al base MMCs with such a low volume fraction of the ceramic reinforcement. The result is significant, and it denotes that, employing SHS, it is possible to obtain Al matrix *in situ* composites with compositions ranging from 30 to 100 vol.% of TiC and/or TiB<sub>2</sub> particles.

Employing SHS processing route, very fine-scale ceramic reinforcements ranging from tens of nanometers up to 1-2  $\mu\text{m}$ , were obtained in the Al matrix. The micron-scale TiC and TiB<sub>2</sub> particles were formed by the surface reaction between Ti dissolved in the Al melt and carbon or boron powder particles. A certain amount of unreacted carbon remained in the SHS-processed samples, presumably as a result of the carbon black powder agglomeration. It is believed, that full conversion of C, as well as a more homogeneous microstructure of the SHS-processed materials may be achieved, if attrition milling is employed for the blending and refining of the starting powders. The mechanism of formation of the nanometer-scale TiC and TiB<sub>2</sub> precipitates remains to be elucidated but may be postulated to involve solution and reprecipitation.

It was shown that, by employing high pressure consolidation at temperatures not exceeding 300°C, full density can be achieved in the porous SHS-processed Al matrix composites containing 30% of TiC and/or TiB<sub>2</sub> particles. According to [43], this consolidation route should also be feasible for SHS-processed Al base MMCs with much higher volume fractions (up to 80 vol.%) of hard ceramic particles.

Room and elevated temperature mechanical properties (yield stress, microhardness) were obtained in the high pressure consolidated SHS-processed composites, comparable to the best rapidly solidified Al base alloys with the same volume fraction (~30%) of the second phase. These high properties were attributed to the superposition of Orowan-type hardening due to the high density of nano-scale ceramic particles, strengthening by formation of dislocation tangles around micron size particles, and submicron grain boundary hardening. According to the preliminary results, SHS-processed Al matrix MMCs exhibit wear resistance superior to the rapidly solidified Al base alloys with the similar room temperature mechanical properties,

apparently due to the presence in the former of the dispersion of micron-scale hard ceramic particles.

Alongside with the high yield strength, appreciable room and elevated temperature ductility was observed in the SHS-processed Al base composites. The high levels of elevated temperature ductility provide the possibility for these materials to be consolidated and shaped by the conventional hot processing methods, *i.e.* hot pressing, extrusion, forging. It was observed that at temperatures up to at least 500°C, no coarsening of microstructure occurred in the materials obtained. In order to better utilize the heat released during exothermic SHS reactions, the application of pressure shortly after the passage of the combustion wave while the sample is still at a relatively high temperature, may be attempted. Thus, cemented carbide alloys prepared by the application of pressure after the passage of the combustion wave were reported to be fully dense [20]. This approach may be further developed into the concept of the continuous manufacturing process, where the synthesized material is continuously densified immediately after the passage of the combustion wave at a rate equal to the combustion velocity. Al matrix *in situ* composites, with their low SHS combustion velocities (due to the strong heat dissipation in the "inert" metal matrix), as well as MMCs on the whole, may be an ideal choice for the utilizing of the continuous manufacturing process approach.

## II. RGI Process Model

A kinetic model of the process of TiC formation has been developed. The model predicts the degree of Ti and C conversion to TiC, (*i.e.*  $V_f$  of TiC) as a function of reaction time. The model revealed three main stages in the kinetics of conversion, *i.e.* initial, intermediate and final. (i) A slow incubation stage with no significant change in Ti concentration due to the lack of carbon in the system. Thus the reaction of TiC formation in this stage is considered to be a first order chemical reaction with carbon being a limiting element. (ii) At the intermediate stage the rate of Ti conversion reaches its maximum. At near equivalent C and Ti concentrations the rate of TiC formation depends on both Ti and C concentrations, *i.e.* reaction of TiC formation becomes a second order chemical reaction. (iii) At the final stage the reaction of TiC formation again becomes a first order chemical reaction, with titanium being a limiting element due to the lack of titanium in the system. This is predicted for a batch operation and can be modified for continuous MMC production.

On the basis of the analytical solution of the model several useful conclusions can be drawn for the synthesis and manufacturing technology. For each combination of reaction rate

and rate of carbon supply, i.e. for each value of  $F$ , there are optimal processing conditions leading to the highest degree of Ti conversion and the least quantities of free carbon in the melt.

The ideal processing should contain two steps:

Steps I: Introduction of carbon into the melt for the required time, which depends on the value of  $[Ti]_0$  and the flow rate of methane.

Steps II: Holding the melt at high temperature to allow the reaction of TiC formation to proceed to completion.

It was found that at the temperatures higher than Ti melting temperature, the dependence of reaction rate on temperature becomes very weak. The dependence of the reaction rate of TiC formation on temperature corresponds to that of the diffusion coefficients of the components in the melt. In this case the process of TiC formation in the liquid solution is not an activated process and does not obey the Arrhenius law. Thus the process rate is determined by the diffusion of Ti and C to each other and nucleation and growth kinetics. Therefore a reaction rate constant for the reaction of TiC formation in Al matrix via RGI technique can be measured at only one temperature and applied to the liquid reactions occurring at the other processing temperatures. Diffusion limited, TiC formation rate constant was calculated for the processing temperature of  $1300^{\circ}\text{C}$  to be  $1.64 \times 10^2 \text{ cm}^3/\text{g sec}$ .

The results of the theoretical model are in rather good agreement with the experiment, assuming that the rate constant does not strongly depend on temperature. The disagreement between the model and experiment is observed at high volume fractions of reinforcement. It can be explained by the increment of the melt viscosity; to include this effect a correction for reaction rate constant should be made.

### **III. *In-Situ* Processing of Ni-matrix Composites**

Reactive Gas Injection technique was used to produce carbide and nitride particulate reinforcements in an Ni alloy melt through methane injection. Composites of TiC/Ni, NbC/Ni and SiC/Ni were either produced or attempted. The reaction mechanism was developed based on experiments with the TiC/Ni system leading to the conclusions below.

TiC/Ni composites with TiC volume fractions below ~20 % can be produced by methane injection into the corresponding Ni-Ti alloy melt. The morphology of TiC in low volume fraction composites is eutectic lamellar. The thickness of the lamellae vary between 1 and 10  $\mu\text{m}$ . Equilibrium ageing experiments ( $1200^{\circ}\text{C}$  / 24 hours / Ar atmosphere) performed on these samples resulted in precipitation of TiC platelets inside the Ni dendrites. These platelets had a

thickness of  $<1\text{ }\mu\text{m}$  and were  $1\text{--}5\text{ }\mu\text{m}$  long. Higher volume fraction TiC/Ni composites (20-30 vol.%) exhibited non-homogeneous microstructures. TiC was formed in two morphologies-angular and eutectic lamellar.

Based on the microstructures observed and examination of available phase diagrams, a reaction mechanism was developed for the formation of TiC in Ni. The reaction sequence is: (i) decomposition of methane to give free carbon; (ii) dissolution of carbon in the Ni-Ti alloy melt and (iii) precipitation of TiC during solidification

An NbC/Ni composite casting was produced by the RGI process. The microstructure was again eutectic lamellar, suggesting a carbide formation reaction that is similar to that of low volume fraction TiC/Ni composites.

An SiC/Ni composite was attempted. This experiment resulted Ni-Ni<sub>3</sub>Si with no carbides. It was deduced that formation of the SiC/Ni composite was thermodynamically and kinetically unfavorable at the attempted level of reinforcement.

An attempt to produce TiN/Ni composite resulted in the formation of a layer of TiN of thickness  $3\text{--}5\text{ }\mu\text{m}$  on the surface and sides of the casting. Therefore, the TiN formation reaction was a surface reaction between the N<sub>2</sub> in the atmosphere and Ti in the melt. Synthesis of Si<sub>3</sub>N<sub>4</sub>/Ni was not successful. It is assumed that the formation of Si<sub>3</sub>N<sub>4</sub> was thermodynamically and kinetically unfavorable. The formation kinetics of nitrides can possibly be enhanced by the use of more reactive nitrogen bearing gases such as ammonia.

The SHS processing technique was used to produce intermetallic matrix composites (NiAl, FeAl) reinforced with carbides, nitrides and borides. This technique is very successful in producing chemically clean intermetallic and metallic matrix composites. This is evidenced by the absence of any intermediate or undesirable phases in the corresponding XRD patterns.

Intermetallic matrix composites of TiB<sub>2</sub>/NiAl and TiC/FeAl were produced by mixing elemental precursors and initiating the exothermic formation reactions. The TiB<sub>2</sub> particle size was between  $1\text{ and }3\text{ }\mu\text{m}$  while the TiC particle size was  $10\text{--}40\text{ }\mu\text{m}$ . This is thought to be due to the higher reaction temperature ( $1920\text{ }^{\circ}\text{C}$ ) for the TiC/FeAl composite compared to the TiB<sub>2</sub>/NiAl ( $1850\text{ }^{\circ}\text{C}$ ). The distribution of TiB<sub>2</sub> in NiAl was relatively uniform while TiC in FeAl was formed as large clusters. The reaction mechanism is believed to be the dissolution of the ceramic precursors in a transient molten phase followed by reaction and precipitation of the ceramic particles. Comparison of the above microstructures with those of TiB<sub>2</sub>/Al and TiC/Al showed similarities as far as particle size ( $1\text{ }\mu\text{m}$ ) and distribution were concerned. The TiC/Al composite showed clusters of TiC particles on the surface of the Al powders. This is believed to

be due to the low solubility of carbon in Al, which changes the reaction mechanism from solution reprecipitation ( $\text{TiB}_2/\text{Al}$ ) to Ti diffusion to solid carbon particles ( $\text{TiC}/\text{Al}$ ).

The in-situ processes used in the above work have demonstrated a general success in producing the required composite materials. While the RGI process seems to be well-suited for the production of wear-resistant materials (since the particle sizes are  $>10\text{ }\mu\text{m}$ ), the SHS process produces much finer reinforcements ( $\sim 1\text{ }\mu\text{m}$ ). Pursuit of the SHS route for intermetallic matrix composites and the RGI process for metal matrix composites should result in the development of economically viable production routes for the respective composites.

## **Acknowledgement**

The authors gratefully acknowledge program support from the Office of Naval Research - Materials Division, Aluminum Company of America, Dr. E.A. Shtessel, Exotherm Corporation, Camden, NJ for synthesis of the SHS samples and Dr. E.Y. Gutmanas, Technion, Israel for his help and advice in high pressure consolidation of the SHS-processed materials.

## References

1. M.J. Koczak and K.S. Kumar, "In situ process for producing a composite containing refractory material", *U.S. Patent 4,808,372*, 1989.
2. P. Sahoo and M. J. Koczak, *Mater. Sci. Eng.*, **A131**, pp. 69-76, 1991.
3. M.K. Premkumar and Chu, private communication.
4. P. Sahoo and M.J. Koczak, *Mater. Sci. Eng.*, **A144**, pp. 37-44, 1991.
5. V. Shtesev, S. Sampath, M.J. Koczak, *In-Situ Composites: Science and Technology*, Edited by M. Singh and D. Lewis, The Minerals, Metals, Materials Society, 1994.
6. S.C. Khatri and M.J. Koczak, *Mater. Sci. Eng.*, **A162**, pp. 153-162, 1993.
7. Q. Hou, R. Mutharasan., *Mater. Sci. Eng.*, Feasibility of Aluminum Nitride Formation in Aluminum Alloys, to be published, 1994.
8. V.I. Shapovalov, Poristye Pronitsaemye Spechennye Materialy [Sintered Permeable Porous Materials], *Metallurgia Publishing House, Moscow*, p.168, 1982
9. V.I. Shapovalov, Porous Materials, *MRS Bulletin*, Vol.XIX, **4**, pp.24-28, 1994
10. B.C. Giessen, *U.S. Patent 4,540,546*, Sep. 10, 1985.
11. J.White, T.C. Willis, I.R. Hughes and S.A. Court, Dispersion Strengthen Aluminum Alloys, edited by Y.W. Kim, *Metallurgical Society of AIME*, Warrendale, PA, 1988.
12. J.White, I.G. Palmer, I.R. Hughes and S.A. Court, Aluminum-Lithium Alloys V", edited by T.H. Sanders, Jr, and E.A. Starke, Jr, *Materials and Component Engineering Publications*, Birmingham, UK, pp.1635-1646, 1989.
13. T.C. Willis, *Met. and Mater.* **4**, p.485, 1988
14. Z.A. Munir, *Ceram. Bull.*, **67**, (2), pp. 342-349, 1988.
15. H. C. Yi and J. J. Moore, *JOM*, **42**, (8), pp. 31-35, 1990.
16. H. C. Yi, J. J. Moore and A. Petric, *Metall. Trans.*, **23A**, pp. 59-64, 1992.
17. H.J. Feng, H.C. Yi and J.J. Moore in *High Temperature Materials Chemistry - V*, W. B. Johnson and R. A. Rapp (eds.), pp. 123-134, The Electrochemical Society, Inc., NJ, 1990.
18. W.R. Wrzesinski and J.J. Rawers, *J. Mater. Sci. Lett.*, **9**, pp. 432-435, 1990.
19. D.E. Clark, I. Ahmad and R.C. Dalton, *Mater. Sci. Eng.*, **A144**, pp. 91-97, 1991.
20. J.M. Brupbacher, L. Christodoulou and D.C. Nagle, *U.S. Patent 4,710,348*, Dec.1, 1987.
21. Lenel F.V. Powder Metallurgy, Princeton, NJ: *Metal Powder Industries Federation*, 1980.
22. T. Donomoto, K. Funatani, N. Miura and N. Miyake, Paper 30252, *Society for Automotive Engineers*, Warrendale, PA, 1983.

23. S. Sampath, *Master's Thesis*, Drexel University, p. 9, 1993.
24. R. Mirta, M.E. Fine and J.R. Weertman, Jr., *Scripta Metall.* 1993 ( to be published)
25. I. Barin, *Thermochemical Data of Pure Substances* (VCH Verlagsgesellschaft, Weinheim, Germany, 1989), pp. 17, 26,71, 72, 1520, 1528
26. H.Yokokawa, N. Sakai, T.Kawada, M. Dokiya:*Metall.Trans.A*, **22A**, 3075-76, 1991
27. F.D.Richard, *Physical Chemistry of Melts in Metallurgy*, **1**, Academic Press, NY p.75
28. M.K. Aghajanian, M.A. Rocazella, J.T. Burke and S.D. Keck, *J. Mater. Sci.* , **26**, pp. 447-454, 1991.
29. CRC Handbook of Chemistry and Physics, 70th Edition, CRC Press Inc., 1989-1990.
30. Outokumpu HSC Chemistry for Window, User Guide Outokumpu Research Oy, Pori, Finland, 1994 .
31. H.A. Wriedt: *Bull. Alloy Phase Diagrams*, **7** , p. 329-33, 1986
32. T.V. Dubovik, V.S. Polishchuk, and G.V. Samsonov, *Zh. Prikl. Khim.* 37(8), pp.1820-30, 1964.
33. G. Marukawa, T. Oikawa, A. Hamada (Showa Denko K. K.) U.S. 3,551,143 (Cl. 75-138; C 22c) 29 Dec. 1970, Japan. Appl. 10 Oct. 1963; 8pp.
34. H.Scholz et al, *J. Mater. Sci.* **25**, pp. 1-9, 1990.
35. D.F.Chernega et al, UDC 669.715, 456-460.
36. Marc Costantino and Carlo Firpo, *J. Mater. Res.*, **6** (11), pp. 2397-2403, 1991.
37. A.G. Merzhanov and I.P.Borovinskaya, *Dokl. Akad. Nauk SSSR* , **204** , pp.336, 1972.
38. A.G. Merzhanov and I.P. Borovinskaya, *Comb. Sci. Technol.*, **10** , pp. 195, 1975.
39. J. Subrahmanyam and M. Vijayakumar, *J. Mater. Sci.*, **27** , pp.6249, 1992.
40. E.Y. Gutmanas, A. Rabinkin and M. Roitberg, *Scripta Metall.*, **13** , p.11, 1979.
41. E.Y. Gutmanas, *Powder Metall., Int.* **15**, p. 129, 1983.
42. E.Y. Gutmanas, *Progress in Mater. Sci.*, Vol.34 , p. 261, 1990.
43. E.Y. Gutmanas, in E. Arzt and L. Schultz (eds.) *New Materials by Mechanical Alloying Techniques*, DGM Informationsgesellschaft, Oberursel, p. 129, 1989.
44. S. Sampath, S. Khatri, E. Shtessel and M.J. Koczak, in V.A. Ravi and T.S. Srinivatsan (eds.), *Processing and Fabrication of Advanced Materials for High Temperature Applications II*, TMS, Warrendale, PA, p.223, 1993.



45. S.D. Dunmead, D.W. Readey, C.E. Semler and J.B. Holt, Report No. UCRL-98773, Lawrence Livermore National Laboratory, 1988.
46. J.B. Holt, Report No. UCRL-53258, Lawrence Livermore National Laboratory, 1982.
47. A. N. Tabachenko, T.A. Panteleeva and V.I. Itin, *Combustion Explos. Shock Waves USSR*, 20 , p. 387, 1984.
48. Y. Choi, M.E. Mullins, K. Wijayatilke and J.K. Lee, *Metall. Trans., A* 23 p. 2387, 1992.
49. O. Botstein, E.Y. Gutmanas and A. Lawley, in *Progress Powder Metall.*, Vol. 41, MPIF, Princeton, p.123, 1986.
50. C. Schuster, H. Nowotny and C. Vaccaro, *J. Solid State Chemistry*, 32 , p. 213, 1980.
51. A. Jarfors, H. Fredriksson and L. Froyen, *Mater. Sci. Eng., A135*, p.119, 1991.
52. M. Hansen, *Constitution of Binary Alloys*, McGraw Hill, New York, 1958.
53. R.C. Dorward, in A.V. Clack (ed.), *Light Metals*, Vol.1, TMS-AIME, New York, NY, p.105, 1973 .
54. C.J. Simensen, *Metall. Trans. A* , 20A , p.191, 1989.
55. A. Banerji and W. Reif, *Metall. Trans. A*, 17A , p. 2127, 1986.
56. S. Ezz, M.J. Koczak, A. Lawley and M.K. Premkumar, in G.J. Hildeman and M.J. Koczak (eds.), *High Strength Powder Metallurgy Aluminum Alloys II*, TMS-AIME, Warrendale, PA, p.287, 1986.
57. J.M. Papazian and P.N. Adler, *Metall. Trans. A* , 21A , p. 401, 1991.
58. G. Bao, J.W. Hutchinson and R.M. McMeeking, *Acta Met.all. Mater.*, 39 , p.1871, 1991.
59. S.V. Kamat, J.P. Hirth and R. Mehrabian, *Acta Met.all.* 37, p. 2395, 1989.
60. O. Botstein, E.Y. Gutmanas and A. Lawley, in *Modern Dev. Powder Metall.*, Vol.39, MPIF, Princeton, p.761, 1985.
61. E.Y. Gutmanas, private communication.
62. J. Yang, S.M. Pickard, C. Cady, A. Evans and R. Mehrabian, *Acta Met.all. Mater.*, 39 , p.1863, 1991.
63. S. Khatri, V. Shtessel, M. Koczak, A. Divecha and J. Kerr, *In-Situ Composites: Science and Technology*, Edited by M. Singh and D. Lewis, The Minerals, Metals, Materials Society, p.115, 1994.
64. A.S. Shteinberg and V. A. Knyazik, *International Union of Pure and Applied Chemistry*, 4 (7), pp.965-976, 1992
65. T. Rosenquist, "Principles of Extractive Metallurgy," p. 527, McGraw-Hill, 1974.
66. E.R. Stover and J. Wulff, *Trans. of AIME* , 215, pp. 127-136, 1959.

67. ASM Handbook, vol. 3, "Alloy Phase Diagrams", ASM International, 1992.
68. W.C. Bellamy and E.E. Huckle, *J. Metals* , **22**, p. 43-50, 1970.
69. E.K. Storms in "The Refractory Carbides", pp. 61-81, Academic Press, 1967.
70. Z.A. Munir and J.B. Holt (eds.), "Combustion and Plasma Synthesis of High Temperature Materials", VCH Publishers, Inc., 1990.
71. J. J. Moore in "Minerals and Metallurgical Processing", pp. 152-159, August 1991.
72. J. Szekely and N.J. Themelis, "Rate Phenomena in Process Metallurgy", Wiley, New York, p. 686, 1971.
73. A.K. Misra, *Metall. Trans.* , **22A**, pp. 715-721, 1991.
74. R.E. Tressler, T.L. Moore and R.L. Crane, *J. Mater. Sci.* , **8**, pp. 151-161, 1973.
75. J.L. Chermant and M. Coster, *J. Microscopy*, **109**, Pt. 3, pp. 269-281, April 1977.